



# THE UNIVERSITY *of*ADELAIDE

FACULTY OF SCIENCES  
DEPARTMENT OF PHYSICS

---

Extensive air shower asymmetry and  
cosmic ray mass composition with the  
upgraded Pierre Auger Observatory

---

Fraser Bradfield

*Supervisors:*

Prof. Bruce DAWSON  
Dr. Jose BELLIDO

May 2022



---

# Contents

---

<b>Abstract</b>	vii
<b>Declaration</b>	ix
<b>Acknowledgements</b>	xi
<b>Introduction</b>	2
<b>1 Cosmic rays</b>	3
1.1 A brief history of cosmic rays . . . . .	3
1.2 Energy spectrum . . . . .	5
1.2.1 Features of the energy spectrum . . . . .	6
1.3 Acceleration mechanisms . . . . .	7
1.3.1 Fermi acceleration . . . . .	7
1.3.2 Diffusive shock acceleration . . . . .	9
1.4 Candidate sources . . . . .	10
1.5 Composition of cosmic rays . . . . .	12
1.6 Anisotropy . . . . .	14
<b>2 Extensive air showers and methods of detecting UHECRs</b>	17
2.1 Extensive air showers . . . . .	17
2.1.1 Electromagnetic cascades . . . . .	19
2.1.2 Hadronic component . . . . .	21
2.2 Detection methods . . . . .	23
2.2.1 Surface detector arrays . . . . .	23
2.2.2 Fluorescence detection . . . . .	24
2.3 UHECR experiments . . . . .	26
2.3.1 Volcano Ranch . . . . .	26
2.3.2 Haverah Park . . . . .	26
2.3.3 SUGAR . . . . .	27
2.3.4 AGASA . . . . .	28
2.3.5 Fly's Eye and HiRes . . . . .	28
2.3.6 Telescope Array . . . . .	29
2.3.7 FAST . . . . .	30
<b>3 The Pierre Auger Observatory</b>	33
3.1 Communications and CDAS . . . . .	33
3.2 The surface detector . . . . .	34

---

3.2.1	WCD design . . . . .	35
3.2.2	Calibration of the SD . . . . .	36
3.2.3	Trigger system of the SD . . . . .	37
3.2.4	SD event reconstruction . . . . .	39
3.3	The fluorescence detector . . . . .	43
3.3.1	Hybrid detection . . . . .	45
3.4	Early enhancements - AMIGA and HEAT . . . . .	45
3.5	AugerPrime . . . . .	46
3.5.1	The scintillator surface detector . . . . .	47
<b>4</b>	<b>Parameterising the signal asymmetry in the Pierre Auger Observatory’s surface detectors</b>	<b>49</b>
4.1	CORSIKA . . . . .	50
4.2	The <u>Offline</u> software framework . . . . .	51
4.3	Initial investigation . . . . .	51
4.4	Parameterising WCD and SSD signal asymmetry . . . . .	55
4.5	Finding the maximum difference between the asymmetry parameterisations . . . . .	66
4.6	Conclusions . . . . .	69
<b>5</b>	<b>Causes of asymmetry in particle density</b>	<b>73</b>
5.1	Co-ordinate system . . . . .	73
5.2	Sources of asymmetry . . . . .	74
5.2.1	Geometrical effects . . . . .	75
5.2.2	Asymmetry induced by attenuation . . . . .	78
5.3	Separating geometry and attenuation . . . . .	78
5.3.1	Measuring the electromagnetic particle density in vertical showers . . . . .	80
5.3.2	Comparing regular and “rotated” showers . . . . .	85
5.3.3	Removing geometrical effects . . . . .	93
5.4	Conclusions . . . . .	94
<b>6</b>	<b>Predicting the asymmetry in muon particle density</b>	<b>97</b>
6.1	Muon production curve . . . . .	99
6.2	Opening angle and energy distributions . . . . .	101
6.3	The Monte Carlo model . . . . .	103
6.4	Results . . . . .	106
6.5	Conclusions . . . . .	113
<b>7</b>	<b>Using asymmetry to improve <math>X_{\max}</math> estimates from LDF slope parameters</b>	<b>115</b>
7.1	LDF slope parameters versus distance to $X_{\max}$ . . . . .	115
7.2	Parameterising $\beta$ as a function of $\theta$ and $X_{\max}$ using dense rings . . . . .	122

7.3	Applying the dense ring calibration to regular showers . . . . .	127
7.4	Calibrating using ensemble LDFs . . . . .	133
7.5	Conclusions . . . . .	136
<b>8</b>	<b>Summary and outlook</b>	<b>139</b>
<b>A</b>	<b>Residual/WCD asymmetry parameterisation plots from Chapter 4</b>	<b>143</b>
<b>B</b>	<b>Inclined atmospheres</b>	<b>151</b>
B.1	Using an inclined atmosphere to calculate slant depths . . . . .	154
	<b>Acronyms</b>	<b>157</b>
	<b>References</b>	<b>159</b>



---

# Abstract

---

The Pierre Auger Observatory, the largest detector in the world for observing cosmic rays, is currently undergoing a significant upgrade. The addition of scintillator detectors to the observatory's ground array aims to improve our ability to determine cosmic ray mass composition at the highest energies. One phenomenon which may provide hints to mass composition is asymmetry, the systematic difference in signal between detectors of equal perpendicular distance from the axis of an inclined extensive air shower at different azimuthal angles. In this work, the asymmetry in the water Cherenkov and surface scintillator detectors of the Pierre Auger Observatory is parameterised in simulations for proton and iron primaries. The largest difference between the two parameterisations is found to be for the scintillator detector at zenith angles  $> 50^\circ$  and energies  $\sim 2 \times 10^{19}$  eV. The causes of asymmetry in particle density are also investigated. For the electromagnetic component of extensive air showers, atmospheric attenuation is shown to give a non-negligible contribution to the overall asymmetry. A test of the understanding of these causes is demonstrated via a basic model for the asymmetry in muon particle density. Finally, the asymmetry parameterisations are utilised to improve upon the technique of reconstructing  $X_{\max}$  from the slope parameters of lateral distribution functions in simulations.



---

# Declaration

---

I certify that this work contains no material which has been accepted for the award of any other degree or diploma in my name, in any university or other tertiary institution and, to the best of my knowledge and belief, contains no material previously published or written by another person, except where due reference has been made in the text. In addition, I certify that no part of this work will, in the future, be used in a submission in my name, for any other degree or diploma in any university or other tertiary institution without the prior approval of the University of Adelaide and where applicable, any partner institution responsible for the joint award of this degree.

I give permission for the digital version of my thesis to be made available on the web, via the University's digital research repository, the Library Search and also through web search engines, unless permission has been granted by the University to restrict access for a period of time.

I acknowledge the support I have received for my research through the provision of an Australian Government Research Training Program Scholarship.

Signed: 

Date: 24/05/2022



---

# Acknowledgements

---

First and foremost, I would like to thank my supervisors, Dr. Jose Bellido and Professor Bruce Dawson, for their support and guidance throughout this project. I have thoroughly enjoyed my time working with you both and hope to take the many lessons I have learnt from you into the future.

I would also like to thank all the members of the Auger research group, past and present. It has been a friendly and stimulating environment to work in over the last two years. Special mention goes to Tristan and Brad, both of whom were always willing to listen and help with any problems I encountered, no matter how small. Their coding advice, particularly early on in my project, has also been extremely helpful.

Lastly, to my friends and family, mum and dad in particular, thank you for your love and constant encouragement. Without you, this thesis would not have been possible.



---

# Introduction

---

Cosmic rays, the highest energy particles known in the universe, have been a frontier of science ever since their discovery more than 100 years ago. Despite our best efforts however, the origin, production mechanisms and composition of the highest energy cosmic rays, those above  $10^{18}$  eV, remain a mystery. Part of the difficulty in studying cosmic rays of these energies is their low flux at Earth. This necessitates an enormous collecting area for any experiment aiming to observe these particles. Such experiments detect cosmic rays indirectly, measuring the properties of the cascade of secondary particles that originates from their interaction with an air molecule, known as an extensive air shower.

The largest cosmic ray detector in the world is the Pierre Auger Observatory, located in the Mendoza province of Argentina. The observatory stretches across some  $3000\text{ km}^2$  and utilises a hybrid design consisting of over 1600 ground based water Cherenkov detectors, overlooked by 27 fluorescence telescopes. The water Cherenkov detectors sample the secondary particles from extensive air showers at ground level, whilst the fluorescence telescopes detect the fluorescence light emitted by atmospheric nitrogen molecules which have been excited by the particle cascade.

One of the key, unsolved questions regarding cosmic rays of the highest energies is their composition. Whilst the most accurate and precise techniques of determining mass composition currently use fluorescence detectors, their low duty cycle means there is limited capacity for measurement. This naturally leads to the idea of using ground based arrays, which have duty cycles of nearly 100%, for mass composition studies. Improving the capabilities of its own ground array in this area is the primary motivation for the upgrade currently taking place at the Pierre Auger Observatory. Known as “Auger Prime”, the upgrade includes the deployment of scintillator detectors on top of every water Cherenkov detector. The differing response of each detector type to the components of extensive air showers aims to open up more possibilities for determining the primary mass of the highest energy cosmic rays.

Utilising an observable from extensive air showers known as asymmetry may allow mass composition information to be extracted from ground array measurements. Asymmetry is a phenomenon where detectors of equal perpendicular distance from the axis of an inclined extensive air shower have, on average, systematically different signals depending on their location relative to the axis of the incoming shower. In principle, the magnitude of asymmetry may depend on the composition of the

primary cosmic ray. The extent, causes and possible applications of asymmetry and how it relates to mass composition will be addressed in this thesis.

This thesis is organised as follows,

**Chapter 1:** Gives a brief description of the history of cosmic ray research and an overview of significant observations and results.

**Chapter 2:** Details the main method used to detect high energy cosmic rays, extensive air showers, and how the properties of these showers are measured. Also describes a selection of past/current cosmic ray experiments.

**Chapter 3:** Provides a broad summary of the components of the Pierre Auger Observatory, with the inner workings of the surface detector and its reconstruction of extensive air shower properties addressed in greater detail.

**Chapter 4:** Introduces the concept of asymmetry and parameterises the amplitude of the asymmetry in proton and iron showers for both the water Cherenkov and scintillator detectors in simulations.

**Chapter 5:** Investigates and attempts to separate two of the main causes behind the asymmetry in electromagnetic particle density, namely geometrical effects and the attenuation of extensive air shower particles.

**Chapter 6:** Constructs a simple model for the production and propagation of muons in an extensive air shower to test the understanding of asymmetry gathered in Chapter 5.

**Chapter 7:** Applies the asymmetry parameterisations from Chapter 4 to improve upon the technique of extracting  $X_{\max}$  from the fitted slope parameters of lateral distribution functions.

**Chapter 8** Concluding remarks.

# Cosmic rays

---

Cosmic rays are extremely high energy particles originating outside of Earth. Their energies can surpass even those from the largest man-made particle accelerators by several orders of magnitude, making them an exciting frontier for the discovery of new physics. To better understand cosmic rays, and in turn the most extreme processes in the universe, three fundamental questions must be answered,

- Origin: Where do they come from?
- Composition: What are they made of?
- Sources: What astrophysical mechanisms are able to produce particles of such high energy?

For cosmic rays with energies above  $10^{18}$  eV, known as Ultra High Energy Cosmic Rays (UHECRs), definitive answers to the above still largely elude us. However, significant strides in our understanding have certainly been made since the field of cosmic ray research began more than a century ago. The following chapter contains a short overview of these discoveries along with a brief timeline of research.

### 1.1 A brief history of cosmic rays

Observations of the ionizing property of cosmic rays can be traced back to the 18<sup>th</sup> century. In 1785 Charles-Augustin de Coulomb saw that when a metallic conductor was placed in air it would gradually lose its charge [1]. The same phenomenon was observed fifty years later by Michael Faraday and then again in 1887 by W. Linss [2, 3]. In 1900, German scientists Elster and Geitel deduced that the leakage of charge was caused by the presence of positively and negatively charged ions in the atmosphere. The source of the ions however, remained unknown [3].

In the first decade of the 20<sup>th</sup> century, scientists conducted many experiments to probe the origin of the mysterious ionization. Changes in altitude, pressure, temperature and shielding were all investigated, yet no firm conclusions were drawn [1]. One of the first to suggest an extra-terrestrial origin was Charles Thomas Rees Wilson in 1901. He attempted to validate his theory by measuring the ionisation

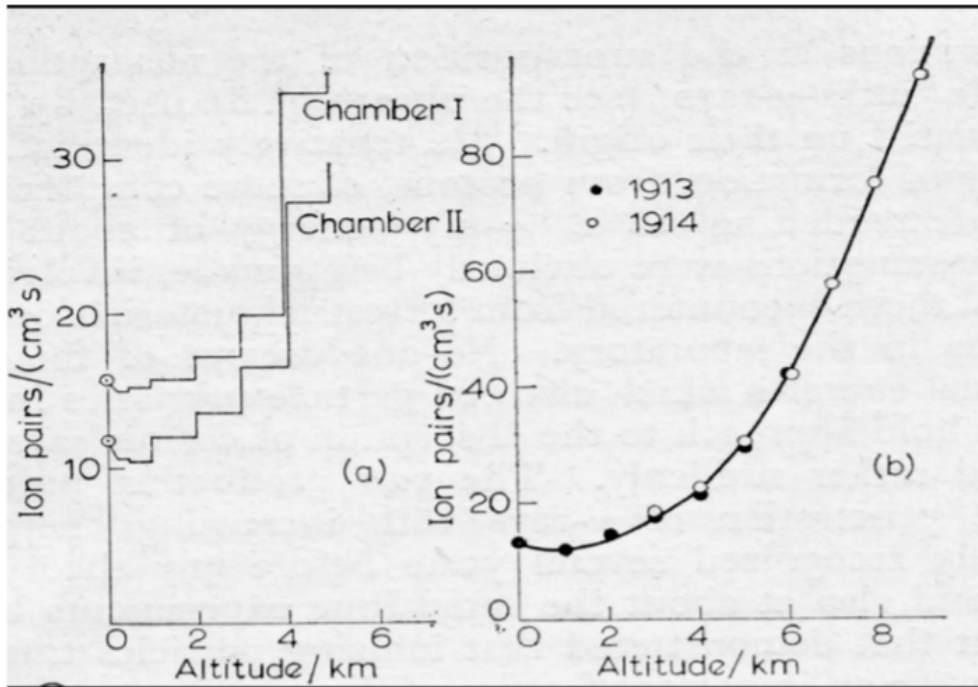


**Figure 1.1:** Results of Hess' balloon flight in August 1912 (left) showing an increase in ionisation with altitude. Results confirming Hess' initial findings taken by Kolhörster in 1913/1914 are shown on the right. From [5].

rate in tunnels, expecting to observe a decrease. Unfortunately for Wilson he saw no change, leaving him to conclude that the ionisation was due to natural radiation from the Earth [4].

The breakthrough came in 1912 from the balloon flights of Austrian physicist Victor Hess. An amateur balloonist, Hess conducted several flights over the course of roughly two years during which he measured the ionization rate as a function of altitude [1]. The results of his flight in August 1912 and their confirmation in the following years by Werner Kolhörster, are shown in Figure 1.1. The evidence showed that, despite an initial decrease, above 2 km the ionization rate increased with altitude [6]. Hess concluded that the ionization was of extraterrestrial origin, winning him the 1936 Nobel Prize [1].

Follow up studies to determine the composition of cosmic rays found their make up to be primarily positively charged nuclei, with this subset being mostly protons [7]. Later, in the 1930's, Pierre Auger and Roland Maze conducted an experiment to investigate the phenomenon of separated detectors recording measurements almost simultaneously. Auger's conclusion was that primary particles above  $10^{15}$  eV were colliding with atmospheric molecules and initiating cascades of secondary particles [8]. Since then, successively larger observatories have been constructed to measure the cascades generated by these high energy cosmic rays.

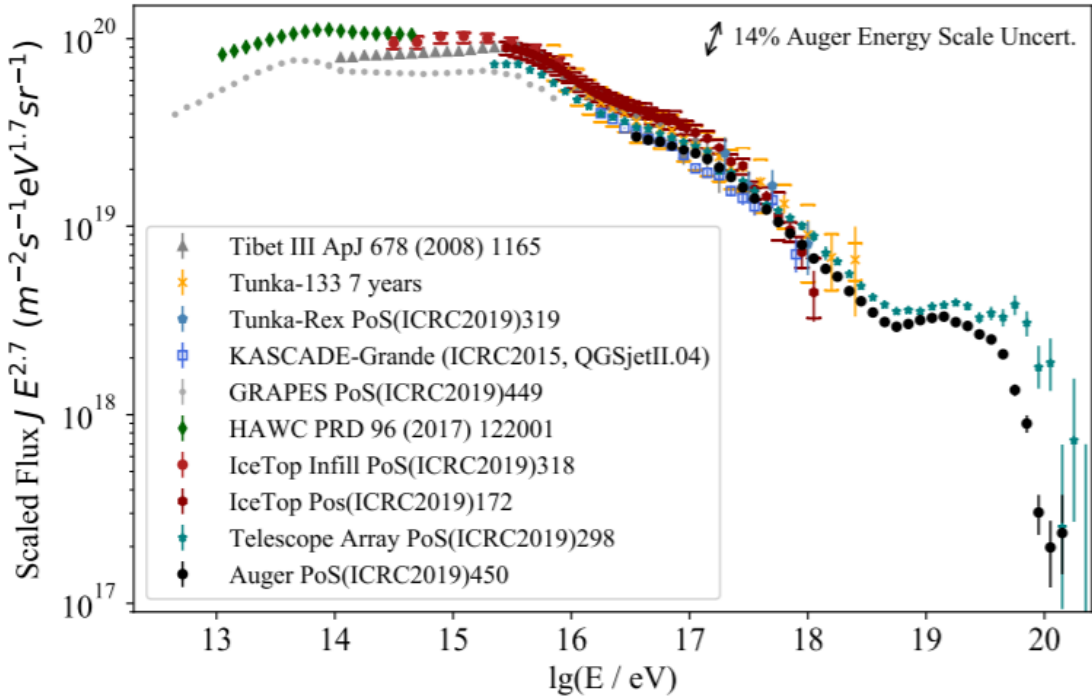


**Figure 1.2:** An all particle cosmic ray energy spectrum. Each experiment listed uses indirect methods to measure the primary energy. From [9].

## 1.2 Energy spectrum

The energy spectrum of cosmic rays provides hints to the origin, acceleration mechanisms and makeup of these astrophysical messengers. The spectrum describes how many particles are observed at Earth as a function of energy, and takes the form of a power law,

$$\frac{dN}{dE} \propto E^{-\gamma} \text{ m}^2 \text{s}^{-1} \text{sr}^{-1} \text{eV}^{-1} \quad (1.1)$$

In Equation 1.1,  $N$  is the flux of cosmic rays arriving at Earth,  $E$  is their energy and  $-\gamma$  is known as the “spectral index”. The power-law nature of the spectrum indicates that the acceleration processes are non-thermal [10]. On average, a value of  $\gamma = 3$  describes the spectrum fairly well, with small deviations from this value giving insights into potential limits of and changes to acceleration mechanisms [7]. To highlight these features it is typical to multiply the flux by the energy raised to some power, as done in Figure 1.2. The steepness of the spectrum makes observing UHECRs very difficult. For comparison, a flux of 1 particle/m<sup>2</sup>/second above 10<sup>14</sup> eV drops to approximately 1 particle/km<sup>2</sup>/century above 10<sup>20</sup> eV. Thus whilst satellites and balloon flights are sufficient to study lower energy cosmic rays, studies of those at the highest energy typically involve ground based arrays stretching across tens, hundreds or even thousands of square kilometers.

### 1.2.1 Features of the energy spectrum

For cosmic ray energies up to approximately  $3 \times 10^{15}$  eV, the value of  $\gamma$  is roughly 2.7. Past this energy the spectrum steepens to a value of  $\gamma \approx 3.1$ . This steepening is called the “knee”. In Hillas’ model [11], the knee indicates the end of galactic cosmic rays accelerated by supernova remnants (SNRs), with the energy of the break point being proportional to the charge of the species [9]. In an “all-particle” spectrum (spectrum including cosmic rays of all masses) the knee is associated with the maximum energies attainable by protons via this method. Another, possibly connected cause, is that above  $3 \times 10^{15}$  eV the gyro-radius of protons in the galactic magnetic field is comparable to the size of the galactic disc. Hence protons of this energy can no longer be confined to the galaxy and thus are far less likely to reach Earth [10].

The steepness of the spectrum increases again around  $10^{17}$  eV, shifting to  $\gamma \approx 3.3$ . Known as the “second knee”, the origin of this feature is still unclear, though recent measurements by the Pierre Auger Observatory have shown it to be a gradual softening of the spectrum [12]. One theory is that the second knee corresponds to heavy primaries, up to  $Z = 92$  (uranium), reaching their energy limit via SNR acceleration. This matches roughly with the location of the second knee being  $E_{2nd} \approx 92 \times E_k$  where  $E_k$  is the energy of the first knee [7]. Additionally, the lowest energy extra-galactic cosmic rays may be contributing to the structure of the second-knee [13].

At about  $3 \times 10^{18}$  eV the spectrum flattens back to  $\gamma \approx 2.6$ . This part of the spectrum is known as the “ankle” and is thought to have two possible explanations. The first is that it represents a transition from primarily galactic cosmic rays to those from extra-galactic sources. The second proposes that the ankle is generated by a modification of the source spectrum of extra-galactic protons and that the transition from galactic to extra-galactic cosmic rays actually occurs at a lower energy. Specifically, these protons could interact with and lose energy to cosmic microwave background (CMB) photons via [9, 14]

$$p + \gamma_{CMB} \rightarrow p + e^+ + e^-$$

Finally, there is a suppression of flux above energies of  $4 \times 10^{19}$  eV. Shown by the Pierre Auger Collaboration to be significant to more than  $20\sigma$  [14], the suppression could be due to the Greisen–Zatsepin–Kuz’mín (GZK) effect. This effect involves cosmic ray protons above  $\sim 6 \times 10^{19}$  eV losing energy via pion production when interacting with CMB photons. The relevant processes are

$$p + \gamma_{CMB} \rightarrow n + \pi^+$$

$$p + \gamma_{CMB} \rightarrow p + \pi^0$$

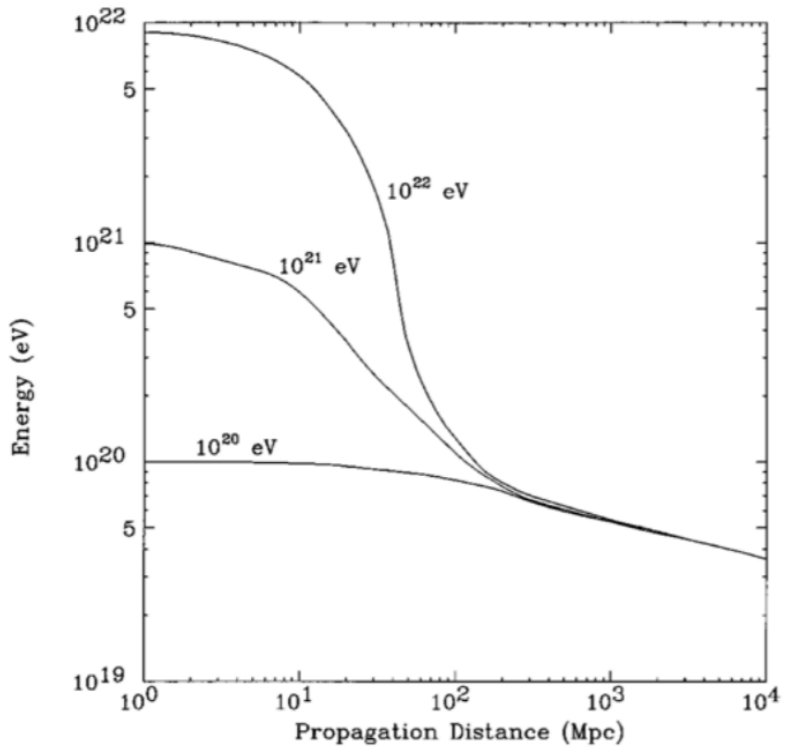


**Figure 1.3:** The reduction in energy experienced by cosmic ray protons as they propagate due to the GZK effect. All higher energy protons converge to approximately  $10^{20}$  eV after travelling roughly 100 Mpc. From [16].

As shown in Figure 1.3, these interactions would cause a rapid decrease in energy for any cosmic ray with  $E > 10^{20}$  eV. This creates a cutoff where, after  $\approx 100$  Mpc, any higher energy cosmic ray will converge to  $E \approx 10^{20}$  eV.

An alternative, albeit far less interesting, explanation for the suppression is that sources of cosmic rays cannot accelerate particles to higher energies [15].

## 1.3 Acceleration mechanisms

Many models have been proposed attempting to explain the acceleration of cosmic rays to the energies we observe. One of particular importance is that of Fermi acceleration, an idea proposed in 1949 by Enrico Fermi [17]. An improvement to this model, called diffusive shock acceleration (DSA) [18], can be shown to provide an energy spectrum which aligns closely with the measured spectrum .

### 1.3.1 Fermi acceleration

The original proposition by Fermi was that cosmic rays are accelerated through elastic collisions with magnetized gas clouds in the interstellar medium (ISM). The basic idea is that a cosmic ray will enter a cloud, be randomly scattered by the associated magnetic field and then exit the cloud with, on average, a higher energy.

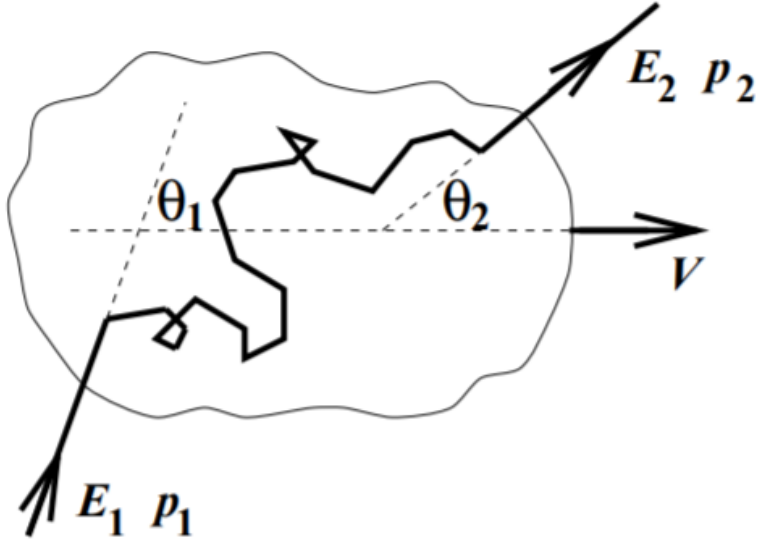


**Figure 1.4:** Schematic of the original idea proposed by Fermi for the acceleration of cosmic rays. An incoming cosmic ray with energy  $E_1$  and momentum  $p_1$  is scattered by magnetic irregularities in a gas cloud before exiting the cloud with new energy  $E_2$  and momentum  $p_2$ . From [19].

A schematic of this process is shown in Figure 1.4. Quantitatively, consider a cosmic ray of energy  $E_1$  incident on an ISM gas cloud travelling with velocity  $v$ . The cosmic ray enters the cloud at an angle  $\theta_1$  with respect to the velocity of the cloud and then exits at an angle  $\theta_2$  with energy  $E_2$ . In the frame of reference moving with the cloud, these quantities are denoted as  $E'_1$ ,  $\theta'_1$ ,  $\theta'_2$  and  $E'_2$  respectively. By the Lorentz transformation laws we can write

$$E'_1 = \gamma_{\text{cloud}} E_1 (1 - \beta_{\text{cloud}} \cos \theta_1) \quad (1.2)$$

The energy of the cosmic ray after scattering in the lab frame is given by the reverse Lorentz transformation as

$$E_2 = \gamma_{\text{cloud}} E'_2 (1 + \beta_{\text{cloud}} \cos \theta'_2) \quad (1.3)$$

Since the scattering is elastic  $E'_2 = E'_1$ . Substituting Equation 1.2 into 1.3 gives

$$E_2 = \gamma_{\text{cloud}}^2 E_1 (1 - \beta_{\text{cloud}} \cos \theta_1)(1 + \beta_{\text{cloud}} \cos \theta'_2) \quad (1.4)$$

Considering the fractional change in energy  $= \Delta E/E_1 = (E_2 - E_1)/E_1$ , we find

$$\frac{\Delta E}{E_1} = \frac{1 - \beta \cos \theta_1 + \beta \cos \theta'_2 - \beta^2 \cos \theta_1 \cos \theta'_2}{1 - \beta^2} - 1 \quad (1.5)$$

To calculate the **average** fractional energy change the average values of the quantities  $\cos \theta'_2$  and  $\cos \theta_1$  must be determined. Since the cosmic ray is randomly

scattered within the cloud its exit direction is random and thus

$$\langle \cos \theta'_2 \rangle = 0 \quad (1.6)$$

The average value of  $\cos \theta_1$  will depend on the relative velocities of the incoming cosmic rays compared to the cloud. Calculation gives

$$\langle \cos \theta_1 \rangle = -\beta/3 \quad (1.7)$$

Substituting these values into Equation 1.5 leaves us with

$$\left\langle \frac{\Delta E}{E_1} \right\rangle = \frac{1 + \frac{1}{3}\beta^2}{1 - \beta^2} - 1 \approx \frac{4}{3}\beta^2 \quad (1.8)$$

where we have made the approximation that  $\beta \ll 1$ . This is valid as typical speeds for these gas clouds are  $\sim 15$  km/s [19].

From Equation 1.8 the fractional change in energy is positive, showing that cosmic rays could be accelerated to high energies through this process after many scatterings. However, the dependence on  $\beta^2$  means this process is very slow, making it an unlikely candidate for accelerating cosmic rays to the highest of energies. Physically speaking, this is because the large velocity of the cosmic rays compared to the cloud make head-on collisions only slightly more likely than tail-end collisions.

### 1.3.2 Diffusive shock acceleration

In diffusive shock acceleration Fermi's original idea of cosmic rays scattering of magnetized gas clouds is expanded to include the presence of an astrophysical shock, such as a supernova. ISM clouds are present either side of the shock and scatter cosmic rays back and forth across the shock front, as shown in Figure 1.5. In crossing from one side of the shock to the other, the cosmic ray will gain energy more efficiently due to experiencing head-on collisions more often.

The same fractional energy gain from Equation 1.5 applies to this method, however the average value will be different due to the new definitions of  $\cos \theta_1$  and  $\cos \theta'_2$ . The average values of these quantities are now

$$\langle \cos \theta_1 \rangle = -2/3 \quad (1.9)$$

$$\langle \cos \theta'_2 \rangle = 2/3 \quad (1.10)$$

Thus for diffusive shock acceleration we have

$$\left\langle \frac{\Delta E}{E_1} \right\rangle = \frac{1 + \frac{4}{3}\beta + \frac{4}{9}\beta^2}{1 - \beta^2} - 1 \approx \frac{4}{3}\beta \quad (1.11)$$

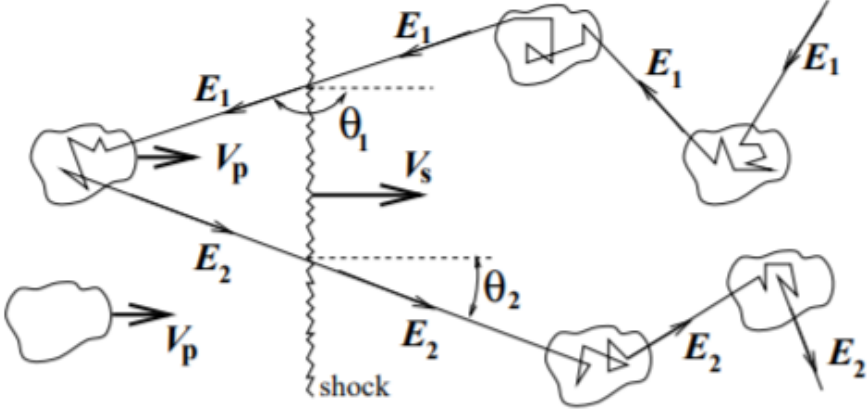


**Figure 1.5:** Diagram depicting the process of diffusive shock acceleration. Cosmic rays are scattered back and forth across a shock by ISM gas clouds. This process is more efficient for gaining energy due to the higher probability of head-on collisions. From [19].

The greater efficiency is shown quantitatively by the first order dependence on  $\beta$ , as opposed to the second order dependence found in the original mechanism. Calculation of the energy spectrum produced by DSA yields an  $E^{-2}$  dependence. This spectrum would be further steepened by an energy dependent escape of cosmic rays from the galaxy, bringing it roughly in line with the measured spectrum of  $E^{-2.7}$  below the knee [19].

## 1.4 Candidate sources

The energy spectrum and propagation mechanisms of cosmic rays provide useful clues to the astrophysical sources which could produce them. For instance, if we consider the origins of UHECRs, sources unable to accelerate particles to at least  $10^{18}$  eV can be ruled out. Furthermore, if diffusive shock acceleration is the primary method by which cosmic rays are accelerated, astrophysical shocks must be present within the vicinity of any candidate source. Additional constraints can be placed on the type of environment needed to confine cosmic rays to allow them to reach the ultra high energies we observe at Earth.

One necessary, though not sufficient, constraint is for the candidate astrophysical object to have a radius,  $R$ , larger than the gyro radius,  $r_g$ , of the cosmic ray it is accelerating. For a cosmic ray of momentum  $p$  and charge  $Z_e$ , propagating in a magnetic field of strength  $B$ , the gyro radius is given by

$$r_g = \frac{p}{Z_e B} \quad (1.12)$$

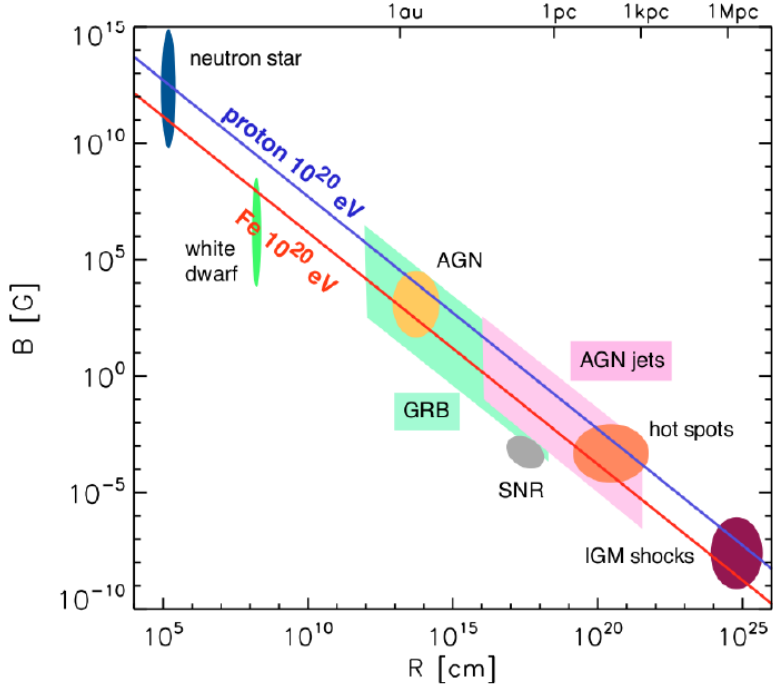


**Figure 1.6:** The classic Hillas plot, showing potential sources of cosmic rays based on their size,  $R$ , and magnetic field strength,  $B$ . From [20].

Since the particles being accelerated are already highly relativistic,  $p \approx E/c$ . Thus for a cosmic ray to be contained by the source we require that

$$R > \frac{E}{cZ_e B} \quad (1.13)$$

Equation 1.13 can be rearranged to give the maximum energy attainable by a cosmic ray at a given source. Considering the case of diffusive shock acceleration we find

$$E_{\max} \approx 10^{18} \text{ eV} Z_e \beta_s \left( \frac{R}{\text{kpc}} \right) \left( \frac{B}{\mu\text{G}} \right) \quad (1.14)$$

where  $\beta_s$  is the shock velocity (units of  $c$ ) [7, 21]. The containment requirements in Equation 1.14 naturally give rise to what is known as the “Hillas Plot”, a diagram displaying the dimensions and magnetic field required of an astrophysical source to accelerate cosmic rays to an energy  $E_{\max}$ . An example is shown in Figure 1.6. Sources with properties which don’t extend above the red (blue) line cannot accelerate an iron (proton) primary to  $10^{20}$  eV. The list of sites which may be able to accelerate both primaries to this energy is quite small and does not include SNRs. Possible sources are Active Galactic Nuclei (AGN) and their jets, Gamma Ray Bursts (GRBs), neutron stars, and Inter-Galactic Medium (IGM) shocks [20]. A detailed discussion of the various sources can be found in [22].

It is important to stress again that the Hillas criterion (Equation 1.14) by itself is not a sufficient requirement for an astrophysical object to be a candidate source

of cosmic rays. Shocks, for example, must also be present. Moreover the energy loss processes which occur at these extreme energies, such as interactions with low-energy photons in the vicinity of the source, further complicate trying to identify possible sources [21].

One piece of information the Hillas criterion does allow us to infer is that the lack of measured galactic-plane anisotropy (see Section 1.6) indicates that cosmic rays of the highest energies come from sources which are extra-galactic, such as AGN. This is because protons accelerated to  $10^{20}$  eV by a galactic source would have a gyro radius of  $\sim 100$  kpc within the galaxy. This is considerably larger than the radius of the Milky Way at  $\sim 16$  kpc. Therefore, these protons would be expected to travel in nearly straight lines towards Earth, creating a clear “hotspot”. Since no evidence of such an excess has been observed, the sources for such particles are assumed to be located outside our galaxy.

## 1.5 Composition of cosmic rays

Determining what nuclei constitute the majority of cosmic rays at various energies can provide information on what types of sources are producing these particles. At lower energies, where direct detection methods are viable and the composition can be accurately determined, it has been shown that the relative abundance of galactic

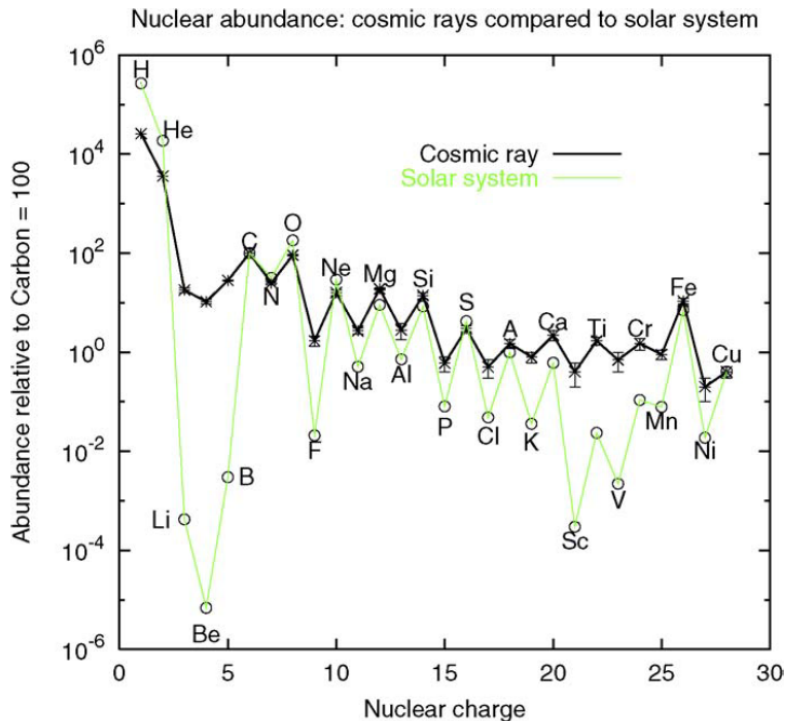


**Figure 1.7:** Relative abundance of nuclei in the solar system compared with the abundance of galactic cosmic rays. From [23].

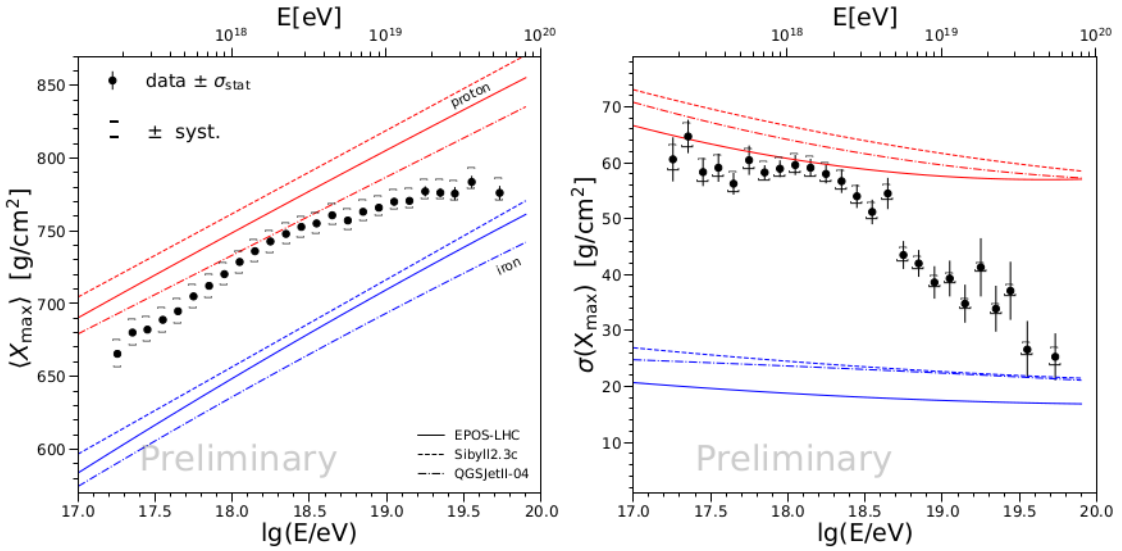


**Figure 1.8:**  $X_{\max}$  means (left) and standard deviations (right) as a function of energy measured by the Pierre Auger Observatory. From [25].

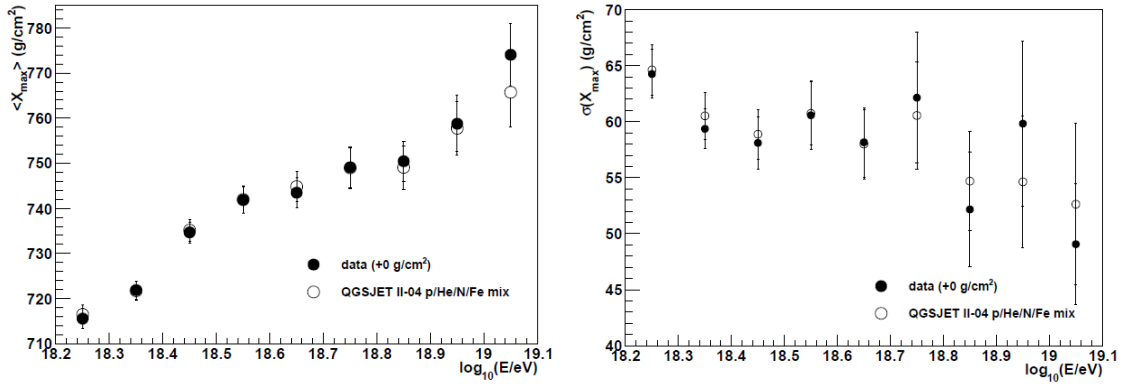


**Figure 1.9:**  $X_{\max}$  means (left) and standard deviations (right) as a function of energy measured by the Telescope Array experiment. The white points are predictions from the QGSJet-II.04 model for a mixed composition (see text). From [26].

cosmic rays of different primaries matches closely with the abundance in the solar system. This is shown in Figure 1.7. The small discrepancies are explained by cosmic spallation, a process where larger nuclei are broken down into smaller nuclei through collisions in the interstellar medium [24].

For higher energy cosmic rays, the flux is too low to measure the primary directly. Thus indirect methods must be used to measure the properties of large particle cascades initiated when a primary cosmic ray strikes an atmospheric molecule. These cascades are known as extensive air showers (EASs) and are discussed in detail in Chapter 2. For now it suffices to note that the fluctuations in the development of EASs do not allow for the primary composition to be determined on an event by event basis. However by looking at ensembles of showers and their average properties

one can estimate the abundance of primaries in 4 mass groups, namely protons (hydrogen), helium, nitrogen and iron. At the highest energies, this is typically done using a shower parameter known as  $X_{\max}$  (see Section 2.1), essentially a measure of where in a shower’s development the greatest number of particles is observed. The key point is that the  $X_{\max}$  distributions of lighter primaries, such as proton, have both larger means and standard deviations than heavier primaries like iron. Figure 1.8 shows measurements of the mean and standard deviation of  $X_{\max}$  distributions as a function of energy from the Pierre Auger Observatory. The lines plotted indicate predictions based on various hadronic interaction models. When compared with the models, there is a clear change in behaviour around the “ankle” region, where the average composition begins to become heavier [25].

Measurements of the  $X_{\max}$  moments have also been made by the Telescope Array (TA) experiment, albeit over a smaller energy range, and are shown in Figure 1.9. Whilst the data is not directly comparable due to different analysis methods, the conclusions are. TA finds the mean and standard deviation of  $X_{\max}$  distributions for cosmic rays between energies of  $10^{18.2}\text{--}10^{19.1}$  eV to be compatible with the Auger result, however a lighter composition cannot be entirely ruled out [27]. The best fit to their data consists of a mixture containing 57% proton, 18% helium, 17% nitrogen and 8% iron using the QGSJet-II.04 hadronic interaction model [26].

## 1.6 Anisotropy

Deviations from an isotropic distribution are known as anisotropies. With regard to cosmic rays, anisotropy in arrival directions is the third key observable, alongside mass composition and the energy spectrum, which provide clues to sources and acceleration mechanisms. Anisotropy studies are the only definitive method to reveal the location of possible sources [28]. This is made difficult however by intervening galactic and extra-galactic magnetic fields which cause charged particles, such as cosmic rays, to take elaborate curved trajectories before arriving at Earth. Only those of the highest energies travel in sufficiently straight lines to perform “cosmic ray astronomy” [27].

Fortunately, the last decade has seen an unprecedented number of measurements of high energy cosmic rays with which to perform searches for anisotropy. This is thanks to the enormous exposure of the previously mentioned Pierre Auger Observatory and Telescope Array. Both experiments have performed searches for large scale anisotropies and local hotspots. The most statistically significant discovery is a large scale dipole anisotropy observed by Auger for events with a reconstructed primary energy  $> 8$  EeV. The result is shown in Figure 1.10. The amplitude of the dipole is  $6.5^{+1.3}_{-0.9}\%$  with a significance of  $5.2\sigma$ . In galactic coordinates, the peak in intensity is in the direction  $(l, b) = (233^\circ, -13^\circ)$ , indicating an extra-galactic origin for these UHECRs. [29].

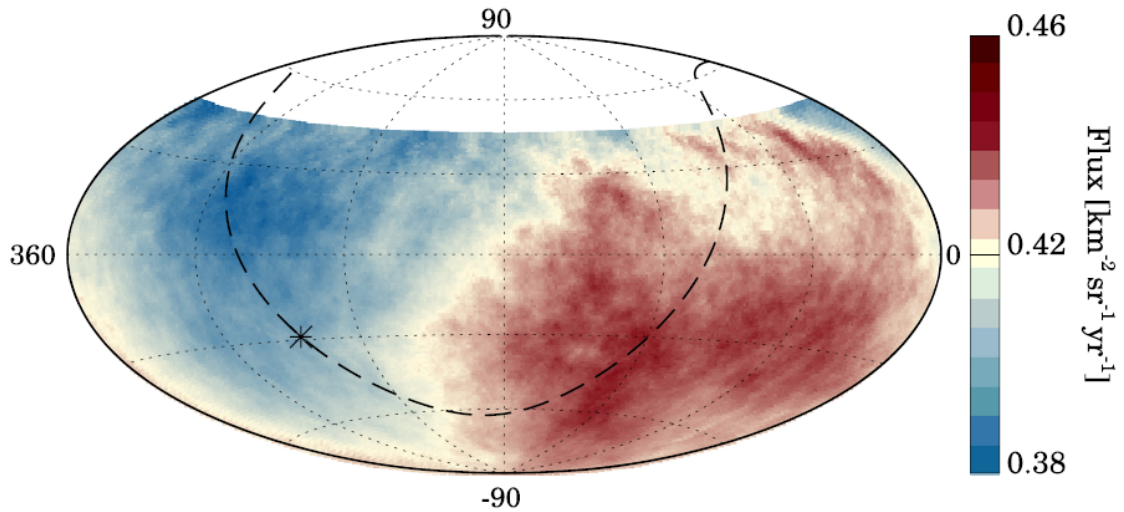


**Figure 1.10:** The large scale dipole anisotropy measured by the Pierre Auger Observatory. Plot is in equatorial coordinates. The star denotes the galactic centre. From [29].

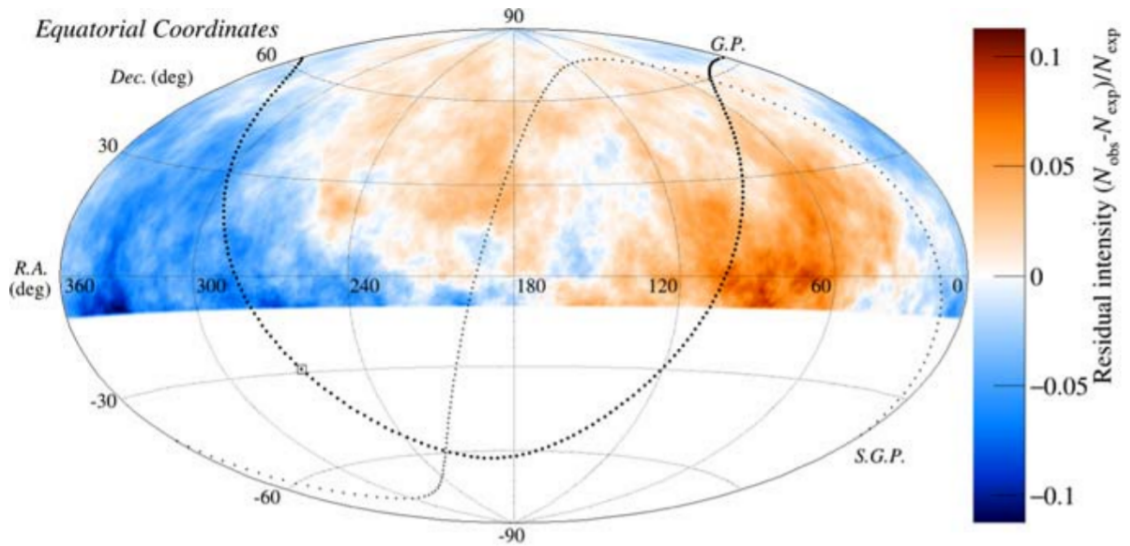


**Figure 1.11:** Result from the follow up search for a large scale dipole anisotropy by the Telescope Array experiment. In the common declination band with Auger, the phase and amplitude of the fitted dipole support the result of an extra-galactic origin for these cosmic rays [30].

This observation motivated a similar search by TA. Their result is shown in Figure 1.11. Overall, the smaller exposure and thus limited statistics of TA mean their result is compatible with an isotropic distribution at the  $2\sigma$  significance level. However, in the region of sky able to be observed by both observatories, the fitted dipole has an amplitude and phase in agreement with the Auger result [30]. When the data from Auger and TA are combined, a full sky fit of the dipole can be performed, as done in [31]. The fitted dipole is again compatible with the initial results from Auger, but now with smaller uncertainties on the dipole components.

Other results from anisotropy searches include Auger’s finding of a correlation between the position of nearby astrophysical objects and the arrival directions of cosmic rays above energies of 20 EeV. The most significant result was the correlation between cosmic rays above 38 EeV and starburst galaxies, with a significance level of  $4.5\sigma$  [32]. As for local hotspots, Auger observes an excess of cosmic rays above 37 EeV from the vicinity of Centaurus A, which incidentally coincides with the positions of some starburst galaxies. The current significance level of the result is  $3.9\sigma$  [32]. TA has also observed a hotspot, reporting an excess of UHECR above 57 EeV in the direction of the Ursa Major cluster at a significance level of  $2.9\sigma$  [33]. Though none of these results can be considered discoveries, they are nonetheless promising and have potential to be improved with further exposure.

# Extensive air showers and methods of detecting UHECRs

---

For cosmic rays with energies above roughly  $10^{15}$  eV direct methods of detection become infeasible. This is due to the nature of the cosmic ray energy spectrum (see Section 1.2) and the significantly lower flux above this energy, less than 1 particle/m<sup>2</sup>/year. Instead, indirect methods must be utilised to infer the energy, arrival direction and composition of these cosmic rays. Indirect techniques involve measuring the properties of so called “extensive air showers” (EASs) and comparing the predictions of simulations to real data [34]. This chapter will explain the basic physics, terminology and primary methods of detecting EASs, as well as provide a summary of UHECR experiments.

## 2.1 Extensive air showers

When a cosmic ray breaches Earth’s atmosphere, it inevitably collides with an atmospheric particle, usually a nucleus of nitrogen or oxygen [34]. This interaction generates a cascade of further “secondary particles” collectively known as an extensive air shower. The secondary particles in an EAS consist primarily of electrons/positrons, photons, muons and hadrons. These particles are concentrated around what is known as the “shower axis”, defined as the path the original cosmic ray would have taken if it had not interacted. The angle of the shower axis with respect to the vertical is called the zenith angle of the shower and is typically labelled  $\theta$ . The “development” of an EAS is the variation in the total number of secondary particles during the cascade. This is often referred to as the longitudinal development of a shower. Since the production of new particles depends on interactions with air nuclei the longitudinal development depends on the amount of matter traversed. Thus a useful quantity to describe the level of development is atmospheric slant depth,  $X$ . Typically measured as a column density in g cm<sup>-2</sup>, the atmospheric slant depth at a particular height above ground,  $h$ , for a shower with zenith angle  $\theta$ , is the integral of the atmospheric density,  $\rho(z)$ , from  $h$  to the top of the atmosphere

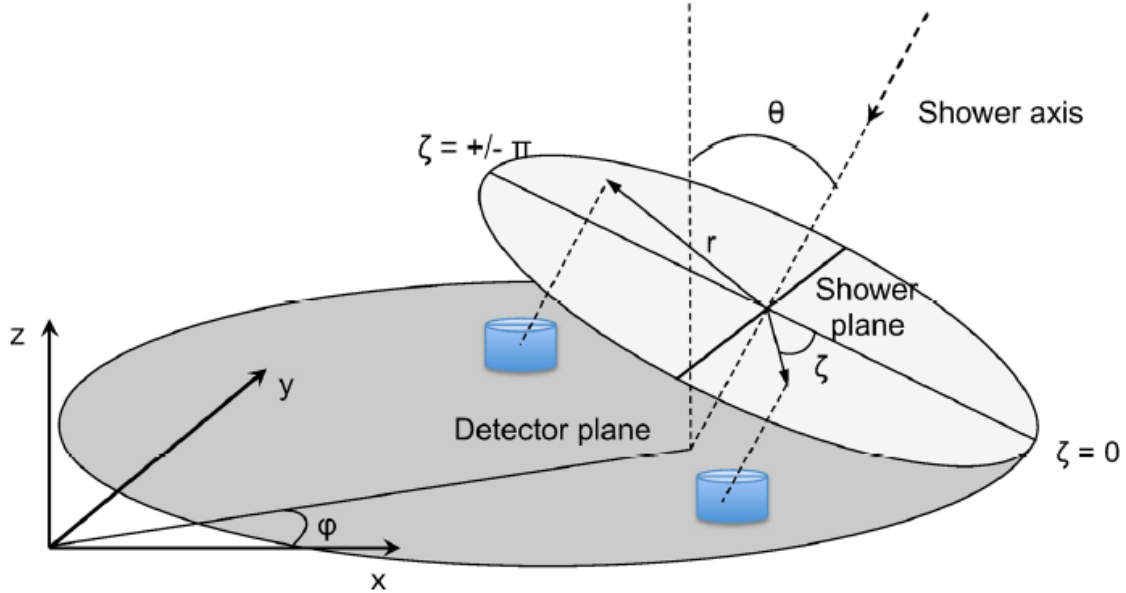


**Figure 2.1:** Geometry of an EAS. From [35].

scaled by  $1/\cos \theta$  (assuming Earth's surface is flat, valid for  $\theta < 60^\circ$ ).

$$X = \frac{1}{\cos \theta} \int_h^\infty \rho(z) dz \quad [\text{gcm}^{-2}] \quad (2.1)$$

A closely related quantity is the rate of energy deposited by EAS particles into the atmosphere with respect to atmospheric slant depth,  $\frac{dE}{dX}$ . The value of  $X$  at which  $\frac{dE}{dX}$  is a maximum is called  $X_{\max}$  and is an important parameter for mass composition studies.

The point of intersection between the shower axis and the ground is the “shower core”, whilst the plane that is perpendicular to the shower axis is known as the “shower plane”. The shower plane is a useful construct as the density of secondary particles in a cosmic ray air-shower depends mainly on the distance to the shower axis, which differs from the distance to the core in non-vertical ( $\theta > 0^\circ$ ) showers. Thus positions on the ground are usually projected parallel to the shower axis onto the shower plane. Points in the shower plane are expressed in polar coordinates, with  $r$  the distance from the shower axis and  $\zeta$  the azimuth. Convention is to take  $\zeta = 0^\circ$  to be directly beneath the shower axis and for  $\zeta$  to lie in the range  $(-\pi, \pi)$ . Figure 2.1 shows a basic diagram of the geometry of an EAS.

The types of secondary particles that make up an EAS can be split into three main components; electromagnetic, hadronic and muonic. A basic depiction of how the three components arise from the initial interaction of a cosmic ray with an air molecule is shown in Figure 2.2. The electromagnetic and hadronic components will now be discussed in detail.

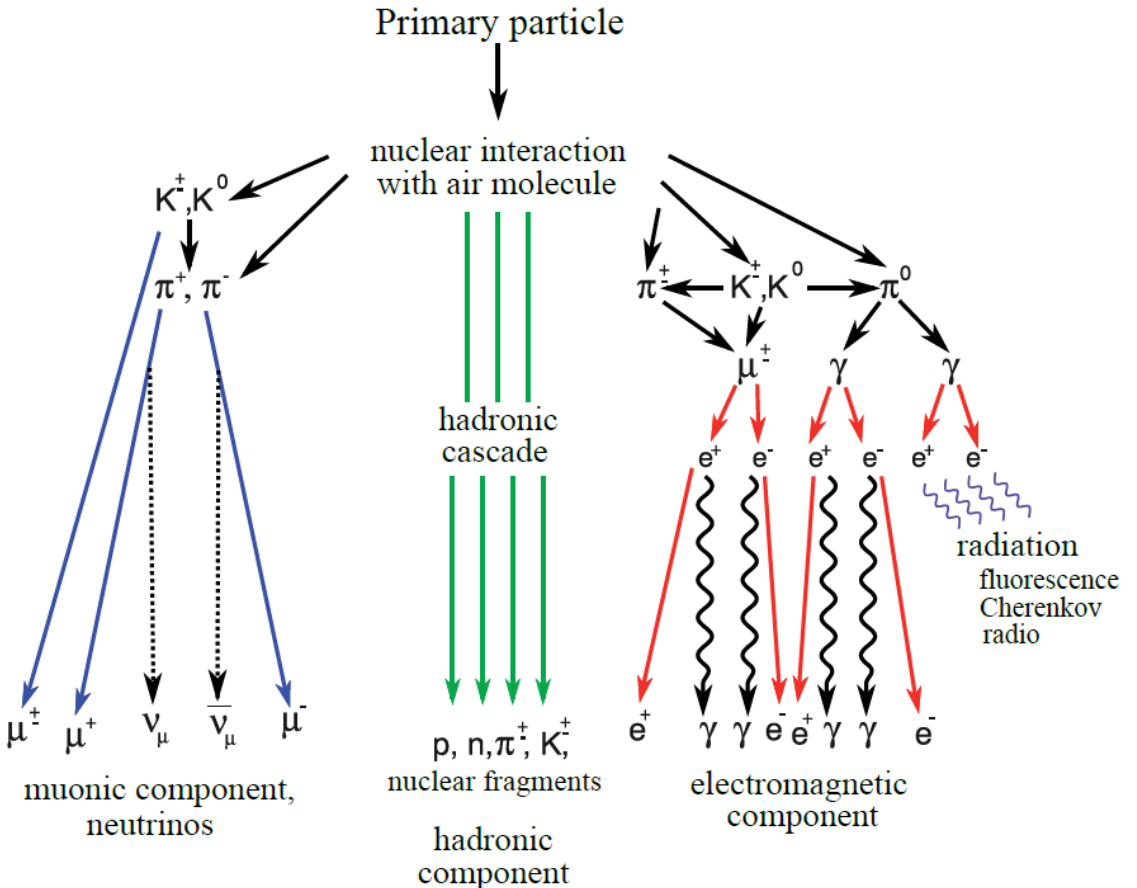


**Figure 2.2:** Schematic of how the different components of an extensive air shower are produced from the interaction of a cosmic ray with an air molecule. From [36].

### 2.1.1 Electromagnetic cascades

The simplest theory of electromagnetic (EM) cascades was described by Heitler in 1954 [38]. Though he and others went on to introduce further complexity to their models, only the simplest case will be outlined here. Importantly, this simple case still describes the most critical aspects of these showers, and clearly shows the physics involved in the shower development [37]. It should be noted that the following explanation of the Heitler model is derived largely from Matthews [37], who explores it in greater detail.

The Heitler model considers the interactions of electrons, positrons and photons within a cascade. In the model, each particle travels a distance  $d = \lambda_r \ln 2$  before “splitting” into two new particles. Here,  $\lambda_r$  is the radiation length in the medium, approximately  $37 \text{ g cm}^{-2}$  in dry air [34]. For  $e^-$  and  $e^+$ , a “splitting” involves radiation of a photon via bremsstrahlung,

$$N + e \rightarrow N + e + \gamma \quad (2.2)$$

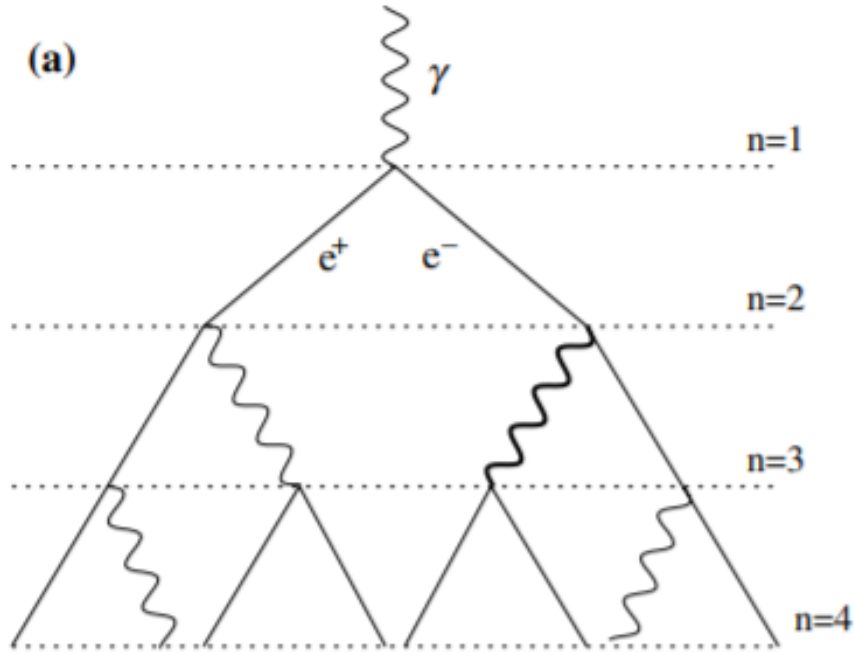


**Figure 2.3:** A diagram of Heitler’s model of an electromagnetic cascade. Explanation of the model is provided in the text. From [37].

where  $N$  is an air nucleus. Photons on the other hand split into an electron and positron via pair production, again in the presence of an air nucleus,



Figure 2.3 shows a schematic view of this process. After splitting, the outgoing particles are assumed to have half the energy of the incoming particle. For  $n$  splittings the EM shower travels a depth

$$x = n\lambda_r \ln 2 \quad (2.4)$$

and consists of  $N = 2^n$  particles. However, the production of particles is not indefinite and halts at a critical energy,  $E_c^e$ , where energy losses due to collisions become greater than radiative losses. In Earth’s atmosphere  $E_c^e \approx 85$  MeV.

Now consider an EM particle with energy  $E_0$  initiating a cascade. After some critical number of splittings,  $n_c$ , all particles in the cascade will have an energy  $E = E_c^e$  and thus the number of particles in the cascade will be a maximum,  $N = N_{\max}$ . Hence,

$$E_0 = E_c^e N_{\max} \quad (2.5)$$

To determine the atmospheric slant depth corresponding to the maximum number of particles,  $X_{\max}$ , note that  $N_{\max} = 2^{n_c}$  and so  $n_c = \ln(N_{\max}) / \ln 2$ . Applying Equation 2.5,

$$n_c = \ln(E_0/E_c^e) / \ln 2 \quad (2.6)$$

Using Equations 2.4 and 2.6 we find

$$X_{\max} = n_c \lambda_r \ln 2 = \lambda_r \ln \frac{E_0}{E_c^e} \quad (2.7)$$

Note this value for  $X_{\max}$  only applies to purely electromagnetic showers. To describe how  $X_{\max}$  changes with initial energy  $E_0$ , a quantity called the *elongation rate* is used. It is defined as

$$\Lambda \equiv \frac{dX_{\max}}{d \log_{10} E_0} \quad (2.8)$$

From Equation 2.7 and using the value of  $\lambda_r = 37 \text{ g cm}^{-2}$ ,

$$\Lambda = \ln(10) \lambda_r \approx 85 \text{ g cm}^{-2}$$

Though simplistic, the Heitler model's predictions of  $\Lambda \approx 85 \text{ g cm}^{-2}$  and a proportional relationship between the natural log of the primary energy and maximum shower size (Equation 2.7) are verified by simulations and experiments [37].

### 2.1.2 Hadronic component

A generalisation of the Heitler model by Matthews provides a basic understanding of hadronic cascades [37]. In Matthews' model, hadrons interact after traversing a fixed distance  $\lambda_I \ln 2$  where  $\lambda_I \approx 120 \text{ g cm}^{-2}$  is the interaction length of pions in air. Two thirds of the particles produced in each interaction are charged pions, with the remaining third being neutral pions. The neutral pions will decay to two photons, sparking EM cascades, whilst the charged pions will continue to traverse the atmosphere and interact until their energy falls below some critical value,  $E_c^\pi$ . A diagram of this process is shown in Figure 2.4. Upon reaching  $E_c^\pi$ , all charged pions are assumed to decay into muons via

$$\pi^+ \rightarrow \mu^+ + \nu_\mu \quad \text{and} \quad \pi^- \rightarrow \mu^- + \bar{\nu}_\mu$$

Suppose now a cosmic ray proton of energy  $E_0$  interacts with an atmospheric molecule, producing a hadronic shower. The number of charged pions,  $N_\pi$ , after  $n$  interactions is given by  $N_\pi = (N_{\text{ch}})^n$ , where  $N_{\text{ch}}$  is the number of charged particles produced in a typical hadronic interaction. If each interaction divides the energy amongst the produced particles equally, each of these pions would have an energy

$$E_\pi = \frac{(\frac{2}{3})^n E_0}{(N_{\text{ch}})^n} \quad (2.9)$$

For a primary particle with  $E_0 = 10^{17} \text{ eV}$ , it takes approximately six interactions for  $E_\pi$  to fall below the critical energy, at which point 90% of the energy of the shower has been converted to electromagnetic particles [34, 37]. At this point the number of charged pions is a maximum and since the charged pions decay to muons at the critical energy we have  $N_\mu = N_{\pi,\max}$ .

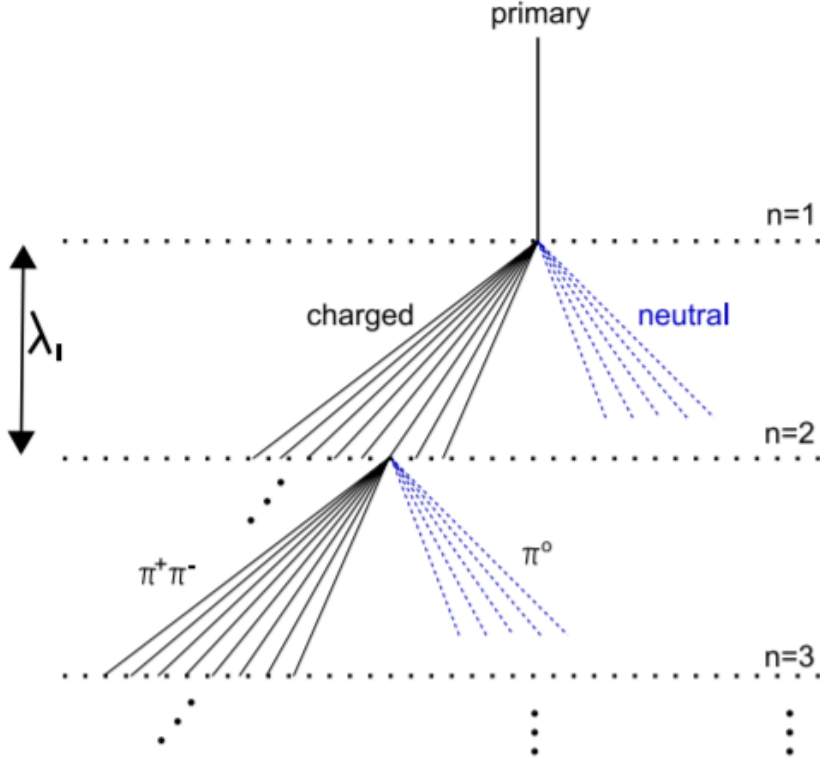


**Figure 2.4:** A depiction of the hadronic version of the Heitler model developed by Matthews. The neutral pions, represented by dashed lines, do not re-interact, but decay to photons. From [39].

Analogous to Equation 2.5, the energy of the primary particle is simply given by the maximum shower size for each component multiplied by the associated critical energy. Matthews takes the critical energies to be 85 MeV and 20 GeV for the EM and hadronic component respectively. Note in Matthews' model only electrons/positrons contribute to the energy in the EM component. This is corrected for with an order of magnitude estimate,  $N_e = N_{\max}/10$ . Altogether, this gives the following parameterisation for the initial energy,

$$E_0 = 0.85 \text{ GeV} (N_e + 24N_\mu) \quad (2.10)$$

The structure and coefficients of Equation 2.10 have been shown to agree closely with simulations [37]. Matthews also provides a formula for the  $X_{\max}$  of a proton primary with energy  $E_0$ ,

$$X_{\max} = 470 + 58 \log_{10}(E_0/1 \text{ PeV}) \quad [\text{gcm}^{-2}] \quad (2.11)$$

Although Equation 2.11 is a systematic underestimation of  $X_{\max}$ , due to only considering the first generation of photon showers arising from  $\pi^0$  decays, the predicted elongation rate of  $58 \text{ g cm}^{-2}$  per decade of energy agrees very closely with simulations [37].

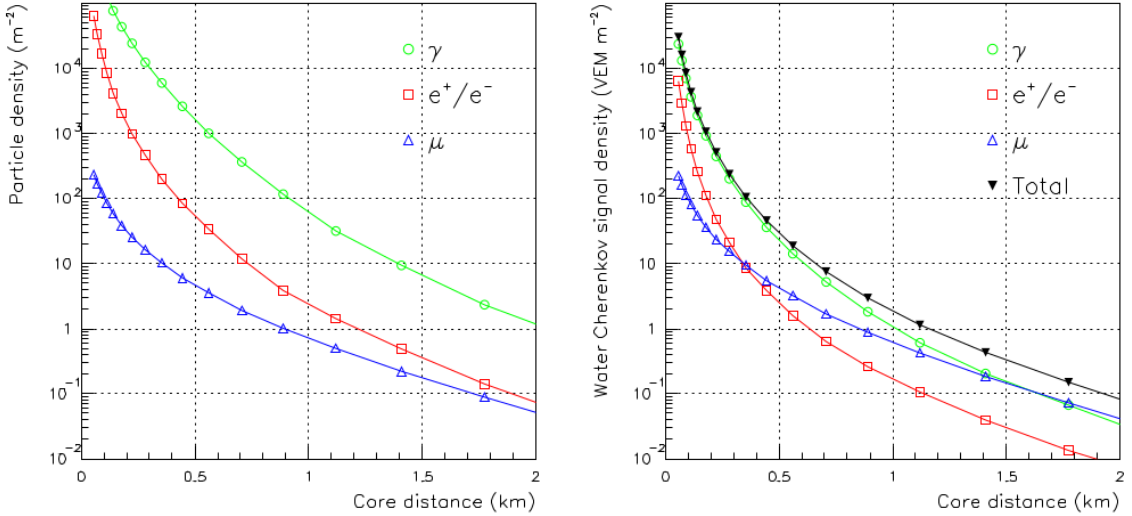


**Figure 2.5:** The lateral distributions of photons (green), electrons/positrons (red) and muons (blue) in a simulated  $10^{19}$  eV proton shower. The left plot shows the density of particles at ground level, whilst the right plot shows the particle density convolved with the response of a 1.2 m deep water Cherenkov detector. From [40].

## 2.2 Detection methods

There are several methods of detecting extensive air showers, each with its own advantages and disadvantages. The two most common techniques for UHECR detection are surface detector arrays and fluorescence detection.

### 2.2.1 Surface detector arrays

Surface detector arrays are the oldest method of studying high energy cosmic rays and have the advantage of being able to operate constantly. The basic principle is that several detectors are spread over a large area to measure the secondary particle density at ground. The majority of particles detected are either photons, electrons or muons, due to their broad lateral distributions. Figure 2.5 shows an example of these distributions for a  $10^{19}$  eV proton shower.

To reconstruct the properties of the original cosmic ray, at least three detectors are required to trigger. With three detectors the location of the shower core can be reconstructed. The direction of the shower is then calculated based on the timing of the signal pulses in each of the three detectors. With the shower core and direction known, the measured signals can be plotted as a function of radius in the shower plane, to which a lateral distribution is then fit. The parameters of the fit allow for the energy of the primary particle to be estimated based on simulation models. Naturally the greater number of detectors triggered in an event, the more precise these reconstructed parameters become. The number of detectors which trigger largely comes down to the spacing of the array. For a given number of detectors,

decreasing the spacing will allow for more detectors to be triggered in each event. However this sacrifices a larger collecting area, meaning fewer showers overall will be detected. Balancing these two considerations is critical for ground arrays to obtain the desired precision and statistics for meaningful analysis.

The two most common types of detector used in ground arrays are scintillation detectors and water Cherenkov detectors. Scintillation detectors utilize the property of luminescence. When the scintillating material is struck by ionizing radiation, such as the secondary particles within an EAS, optical light is produced. This light is detected by a photomultiplier tube (PMT) and subsequently converted to an electrical signal. Scintillation detectors are equally sensitive to muons and electrons and can detect photons if they pair-produce in the scintillating medium.

The other common detector type is the water Cherenkov detector. As the name suggests, these detectors rely on Cherenkov light to detect EAS particles. Cherenkov light is produced when a charged particle passes through a medium faster than the speed of light in that medium. Since the refractive index of water is 1.33, particles must travel faster than  $0.75c$  in the detector to produce Cherenkov light. The majority of electrons and muons in an EAS satisfy this requirement. For EAS photons to be detected they must undergo pair-production to produce electrons with the velocity required to produce Cherenkov light. One bias of water Cherenkov detectors is an increased sensitivity to muons. This is because muons are far more energetic, allowing them to pass through the entirety of the detector whilst producing Cherenkov light. Electrons on the other hand do not have enough energy to penetrate through the entire volume of water, thus they only emit Cherenkov light for a short period of time [41].

The reliance on hadronic models to estimate the primary energy, particularly when these models do not have access to the ultra-high energy range being considered, is a significant disadvantage of the surface detector array method. Additionally, estimating mass composition is difficult and often requires isolating different components of the air-shower. Examples of surface array layouts are given in Section 2.3.

### 2.2.2 Fluorescence detection

When a cosmic ray initiates an EAS its energy is converted into secondary particles. One method of estimating the energy of the primary particle is to measure the energy deposited by these secondary particles into the atmosphere. This type of measurement is known as a “calorimetric measurement” as the atmosphere is acting as a calorimeter. EAS particles deposit energy into the atmosphere by ionising or exciting air molecules, predominantly nitrogen. When nitrogen molecules transition back to their ground state a common mode is via emission of fluorescence light. The emission is isotropic and mainly between 300 nm and 400 nm in wavelength, as shown in Figure 2.6. As the number of fluorescence photons is proportional to

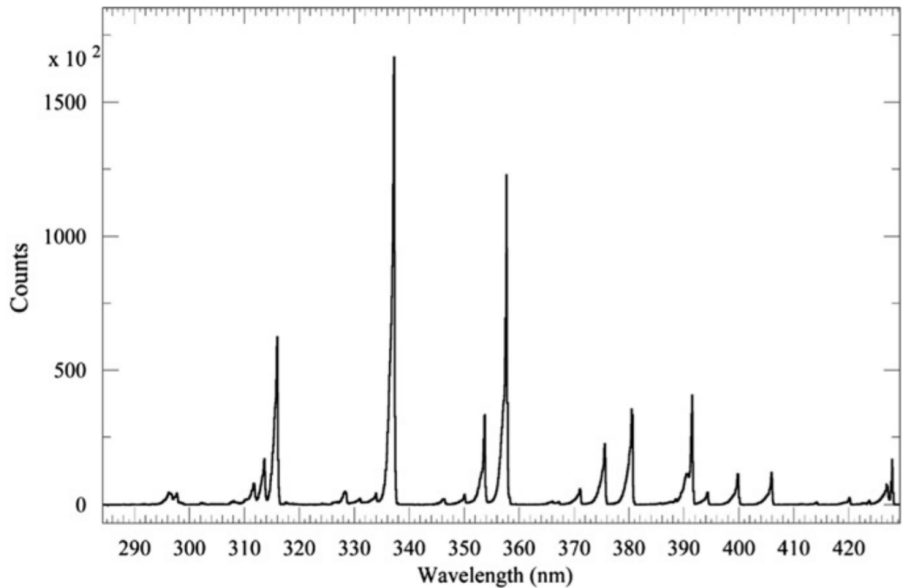


**Figure 2.6:** Fluorescence spectrum of nitrogen in dry air. Measurements taken at 800 hPa and 293 K. From [43].

the energy deposited, measuring the emitted light can determine the energy of the primary particle. Current equipment is sensitive enough to measure the fluorescence light produced by showers greater than  $10^{17}$  eV in energy [42].

The challenge of fluorescence detection can be likened to trying to observe a 100 W light bulb travelling at the speed of light 30 km away, all amidst sources of background noise [42]. Hence detectors must possess high temporal resolution and be extremely sensitive to ultraviolet (UV) light. This is typically achieved by filtering out non-UV light sources and using a large mirror to focus the fluorescence light onto a grid of PMTs. Each PMT is called a “pixel”. As the EAS develops the fluorescence light will pass through several pixels. This trace and the timing of the pulses in each pixel can be used to reconstruct the direction of the shower. From the reconstructed geometry and fluorescence emission measurements, an energy deposit profile can be made. Integrating this profile gives the total energy of the shower, whilst the maximum value of the profile gives  $X_{\max}$ . The reconstruction of each parameter can be improved by having the same shower seen by multiple telescopes, called a stereo event. This removes dependency on the timing of pixel pulses for the geometry reconstruction, improving the accuracy of the estimated core location and shower direction. In turn, better measurements of the total energy and  $X_{\max}$  can be made.

Using a surface detector array in conjunction with fluorescence telescopes, known as hybrid detection, can also enhance geometry reconstruction. This typically involves using a ground array to estimate the time at which the shower front reaches the ground, removing possible degeneracy in the timing fit from a single fluorescence telescope. Hybrid reconstruction has the additional benefit of being able to calibrate

the energy measurements of the surface detector with the calorimetric readings from the fluorescence detector.

A fraction of secondary particles in an EAS will not deposit their energy into the atmosphere. Some of these particles will be detected by surface arrays at ground level whilst others are largely undetectable, such as neutrinos. Thus, for a fluorescence detector, corrections to the energy estimate of the primary cosmic ray must be made. The correction factor for this “invisible energy” varies between 1.07 to 1.17 and is dependent on the primary mass and the hadronic interaction model used to describe the shower development. An additional correction must be made for the (typically) small fraction of Cherenkov light scattered towards the detector [42].

A significant downside to the fluorescence detection method is the low duty cycle of approximately 10 – 15%, as measurements can only be made on clear nights with little or no moon. This means a set of fluorescence detectors will observe far fewer events than a surface detector array with the same effective area. However, the methods of determining the primary energy and  $X_{\max}$  are far more direct with fluorescence detection. The hybrid detection approach is one way of compensating for the weaknesses of either detection technique. This method is utilised by the two largest cosmic ray detectors in the world, the Telescope Array experiment (see Section 2.3.6) and the Pierre Auger Observatory (see Chapter 3).

## 2.3 UHECR experiments

### 2.3.1 Volcano Ranch

Volcano Ranch was a cosmic ray observatory located near Albuquerque, New Mexico, that operated from 1959 to 1978. The project was headed by John Linsley from the Massachusetts Institute of Technology and consisted of nineteen  $3.3 \text{ m}^2$  plastic scintillators measuring secondary particles from cosmic ray air showers [44]. The scintillators were arranged in a hexagonal pattern with an initial spacing of 442 m, enclosing an area of  $2 \text{ km}^2$ . The spacing was later increased to 884 m giving an enclosed area of  $8.1 \text{ km}^2$ . The comparatively large size of the array at the time allowed for the extension of the cosmic ray energy spectrum above  $10^{18} \text{ eV}$  [45]. The highest energy event recorded at Volcano Ranch was  $10^{20} \text{ eV}$  [46]. This was evidence of cosmic rays originating from extra-galactic sources as no objects within our galaxy were believed to be able to accelerate a proton to such an energy at the time. Figure 2.7 shows the layout of the experiment and the estimated location of the highest energy event recorded.

### 2.3.2 Haverah Park

Situated in Haverah Park, England, this ground array made use of water Cherenkov detectors to detect extensive air showers. The array was a collaborative effort by

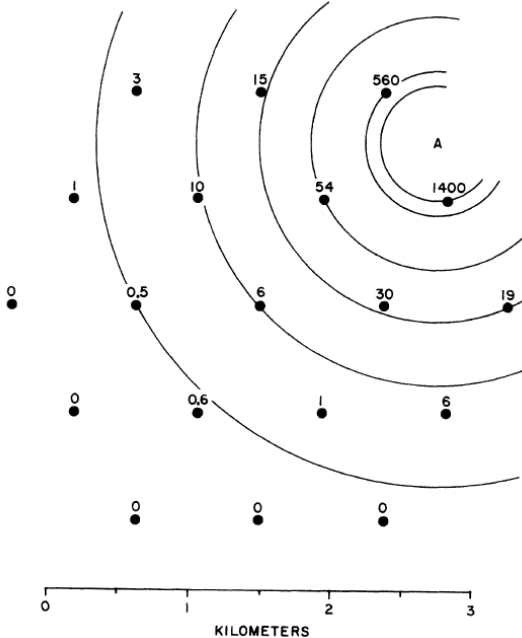


**Figure 2.7:** Layout of the Volcano Ranch array in 1962. The small circles are scintillators with the adjacent numbers representing the estimated particle density ( $\text{particles}/\text{m}^2$ ) from the highest energy event recorded. *A* indicates the estimated core location of the event. From [46].

the Universities of Durham, Leeds and London, and collected data from 1962-1987. The array initially consisted of just 4 detectors, with a central detector surrounded by 3 others arranged in a triangle formation [47]. In 1968 the number of detectors was increased by placing several sub-arrays of 4 detectors roughly 2 km from the original site. Haverah Park demonstrated that water Cherenkov detectors were a viable method for the long term detection of cosmic ray air-showers, as evidenced by its 20+ year run time. The measured energy spectrum showed a flattening around  $10^{19}$  eV [48] i.e. just above the region of the now well measured “ankle”.

### 2.3.3 SUGAR

The Sydney University Giant Air-shower Recorder (SUGAR) was the first large scale cosmic ray detector in the southern hemisphere and measured the muon content in extensive air-showers. The experiment was located near the town of Narrabri in New South Wales, Australia, and operated between 1968 and 1979. The array consisted of 54 underground detector stations arranged in a rectangular grid spread over  $70 \text{ km}^2$ . These stations were autonomous and consisted of two liquid-scintillators, each with an area of  $6 \text{ m}^2$ , separated by 50 m in the north-south direction. The majority of stations were spaced by 1600 m to detect high energy showers. However smaller grids with 800 m and 400 m spacing were utilised for recording smaller showers [49]. To reconstruct the primary energy of an EAS, SUGAR invoked models relating the

number of muons recorded to the energy [50]. Data from SUGAR also showed a flattening in the energy spectrum around the ankle region, in agreement with other experiments at the time [49].

### 2.3.4 AGASA

The Akeno Giant Air Shower Array (AGASA) was built in 1990 and operated until 2004. During this period, it was the largest cosmic ray observatory in the world. Located 120 km west of Tokyo in Akeno, Japan, the array was spread over 100 km<sup>2</sup> and consisted of 111 scintillation detectors, each with an area of 2.2 m<sup>2</sup>. In addition there were 27 muon detectors of various sizes [51]. The size of the array allowed it to probe the highest energy cosmic rays. Initial results from AGASA showed a surprising lack of a GZK cutoff in the energy spectrum. However this result was later retracted in 2006 after an error in the analysis process was found, bringing the results more in line with experiments of similar collecting area, such as HiRes [52].

### 2.3.5 Fly’s Eye and HiRes

The Fly’s Eye detector and the subsequent upgraded version, HiRes, both utilised the fluorescence detection technique to analyse the properties of EASs. The Fly’s Eye operated between 1982 and 1992 and was located at Dugway, Utah [52]. The first detection site, known as Fly’s Eye I, consisted of 67 spherical mirrors, each with a diameter of 1.5 m and focusing light onto 12 or 14 PMTs. With a total of 880 PMTs, each covering a region of sky 5.5° in diameter, Fly’s Eye I was able to image the entire night sky. A second detector, Fly’s Eye II, was completed in 1986 and situated 3.4 km away. This detector had only 36 mirrors, all pointing towards the direction of Fly’s Eye I and covering half the night sky. This allowed for stereo detection and improved the geometry reconstruction for showers seen by both detectors [53].

The Fly’s Eye stereo energy spectrum showed a clear dip at  $3 \times 10^{18}$  eV, the location of the “ankle”. Direct measurements of  $X_{\max}$  allowed Fly’s Eye to show a change in composition with energy around this region. Starting from predominantly heavy primaries at  $\sim 0.1$  EeV, the composition was observed to gradually transition towards lighter nuclei up to 15 EeV. The results were explained by a model where galactic cosmic rays were primarily heavy nuclei and extra galactic cosmic rays were primarily light nuclei. The highest energy event ever recorded by a cosmic ray experiment was also observed at Fly’s Eye, with an energy of  $3.2 \times 10^{20}$  eV [54]. The profile of the event is shown in Figure 2.8.

Completed in 1997, the High Resolution Fly’s Eye I (HiRes I) was a significant upgrade to the original Fly’s Eye experiment, improving resolution and sensitivity. This was achieved by using 5.1 m diameter mirrors focusing light onto 256 PMTs, each viewing a roughly 1° by 1° region of sky. HiRes I was located at the same site

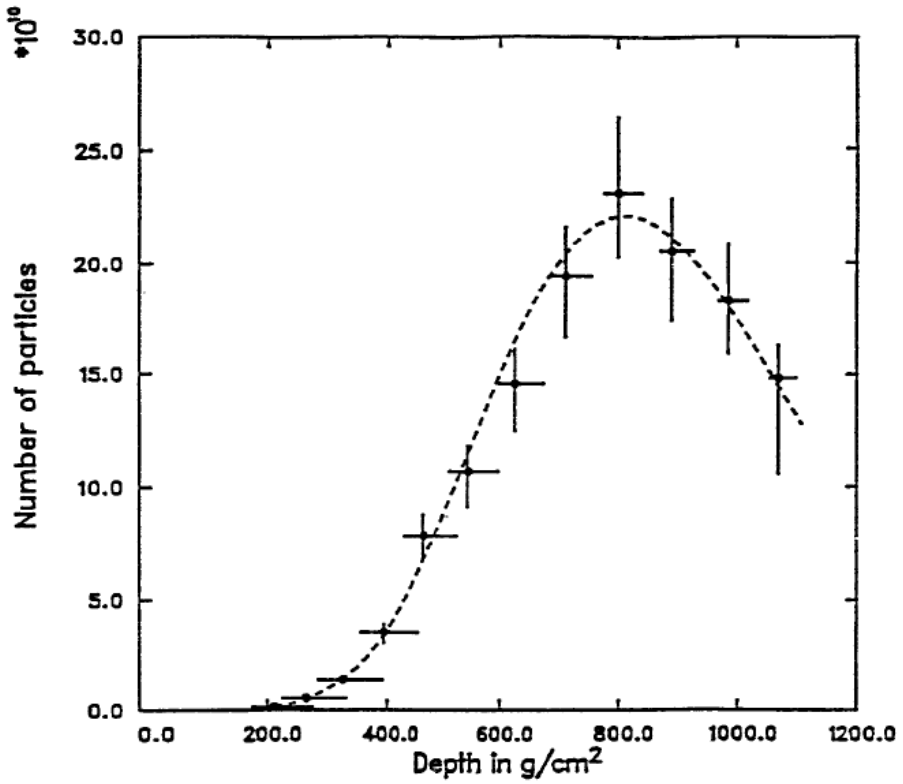


**Figure 2.8:** Profile of the highest energy cosmic ray event ever recorded with  $E \approx 3.2 \times 10^{20}$  eV. The event was observed by the Fly's Eye experiment on the 15<sup>th</sup> of October, 1991. From [54].

as the original Fly's Eye I, and consisted of 22 telescopes covering 360° in azimuth and 3-17° coverage in elevation. A second site, HiRes II, was established in 1999. It was located 12.6 km away from HiRes I and had 42 detectors. Similar to Fly's Eye II, this site was able to provide stereo reconstruction when used in conjunction with HiRes I. HiRes II also possessed full 360° coverage in azimuth but with an extended range in elevation, from 3-31°[52, 55]. The improvements in HiRes allowed it to observe the suppression in flux predicted by the GZK cutoff [52]. HiRes also showed predominantly light composition at the highest cosmic ray energies [56].

### 2.3.6 Telescope Array

The Telescope Array experiment (TA) is a current experiment designed to study UHECRs. The observatory is located in Millard County, Utah, and began data acquisition in 2008. TA utilises the hybrid detection technique, with 38 fluorescence telescopes distributed over 3 sites overlooking a ground array of 507 plastic scintillators. The scintillators have an area of 3 m<sup>2</sup> and consist of two 12 mm layers of scintillating material, separated by 1 mm of stainless steel. The ground array is spread over 678 km<sup>2</sup> with a grid spacing of 1.2 km between detectors. Each fluorescence detection site has a coverage of 108° in azimuth (114° for the Middle Drum

site) and 3-33° in elevation. Every telescope is equipped with a 3.3 m diameter mirror and a grid of 256 PMTs [57]. Examples of results from TA on the cosmic ray energy spectrum, mass composition and anisotropy can be found in Chapter 1.

### 2.3.7 FAST

The Fluorescence detector Array of Single-pixel Telescopes (FAST) is a next generation cosmic ray detector. The goal of FAST is to observe cosmic ray air showers above energies of  $10^{19.5}$  eV with unprecedented statistics. To achieve the enormous collecting area required, whilst also minimising costs, the FAST collaboration has designed a simplified, cost-effective fluorescence telescope. These telescopes have a smaller light collecting area and far fewer pixels compared to current designs, allowing many more units to be produced for the same cost. The telescopes consist of a mirror 1.6 m in diameter focusing fluorescence light onto four PMTs. The field of view of each telescope is 30° by 30°, such that a station of 12 FAST telescopes would cover 360° in azimuth. Simulations of the detector suggest the optimal spacing between stations to be 20 km, with stations arranged in a hexagonal pattern. An example layout is shown in Figure 2.9.

Currently, there are three prototype FAST telescopes installed at TA and one prototype installed at the Pierre Auger Observatory. Shower reconstruction is achieved via a two step process. First, a neural network provides a first guess at the true shower parameters. This guess is then passed to a top-down reconstruction method where the measured PMT traces are compared to simulated ones and the best fit shower parameters are found [58].

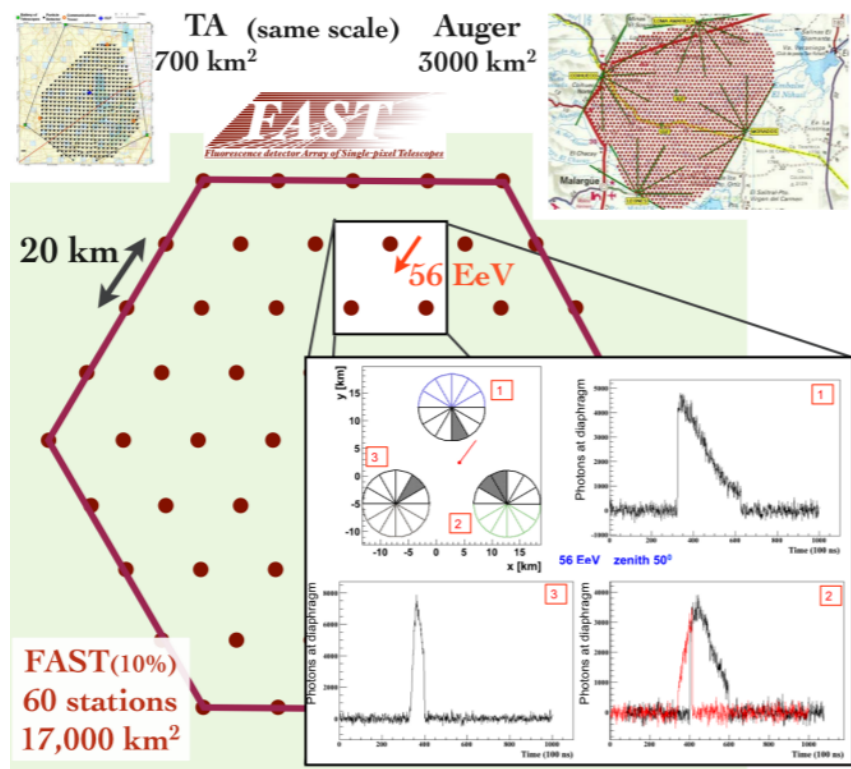


**Figure 2.9:** Schematic of a proposed layout for FAST. The sizes of TA and the Pierre Auger Observatory are shown for reference. Results from a simulation of a cosmic ray with energy 57 EeV incident on the detector is also shown. From [59].



# The Pierre Auger Observatory

---

The Pierre Auger Observatory, located near the city of Malargüe in the Mendoza province of Argentina, is currently the largest detector in the world designed to study cosmic rays. After initial conception by Jim Cronin and Alan Watson in 1991, construction of the observatory began in 2002 and was completed in 2008 [60]. The goal of the observatory is to study the energy spectrum, arrival directions and mass composition of UHECRs with high statistics [61]. To achieve this, the observatory utilises a hybrid detection system consisting of a fluorescence detector (FD) and a surface detector (SD) array. The layout of these detectors is shown in Figure 3.1. The following chapter will discuss the main components of the observatory, primarily focusing on the SD as it is this detector around which much of the work in this thesis is based.

### 3.1 Communications and CDAS

The sheer size of the SD array and large amounts of data needed to be sent and received requires a robust communication system. Two complementary networks are currently employed for this purpose. The first is a microwave network which operates in the 7 GHz band and is responsible for transferring data from communications towers at each FD site to the Central Data Acquisition System (CDAS), located at a central campus in Malargüe. Each communications tower holds 8 “base” stations, each of which is responsible for coordinating communications to and from SD stations in a given section of the array. The second network, a wireless Local Area Network (LAN), is what allows each SD station to communicate with their associated base station. This network operates in the 902–928 MHz range. By dividing the array into sectors, the processing load across the array is distributed efficiently and the failure of a single base station does not cause data loss from the rest of the observatory [62].

The purpose of these communication systems is to provide array-wide connection with the CDAS. The CDAS plays a number of critical roles including storing SD data, processing SD-only and hybrid event triggers, monitoring SD performance and providing configuration/control tools for the SD. The CDAS is completely separate

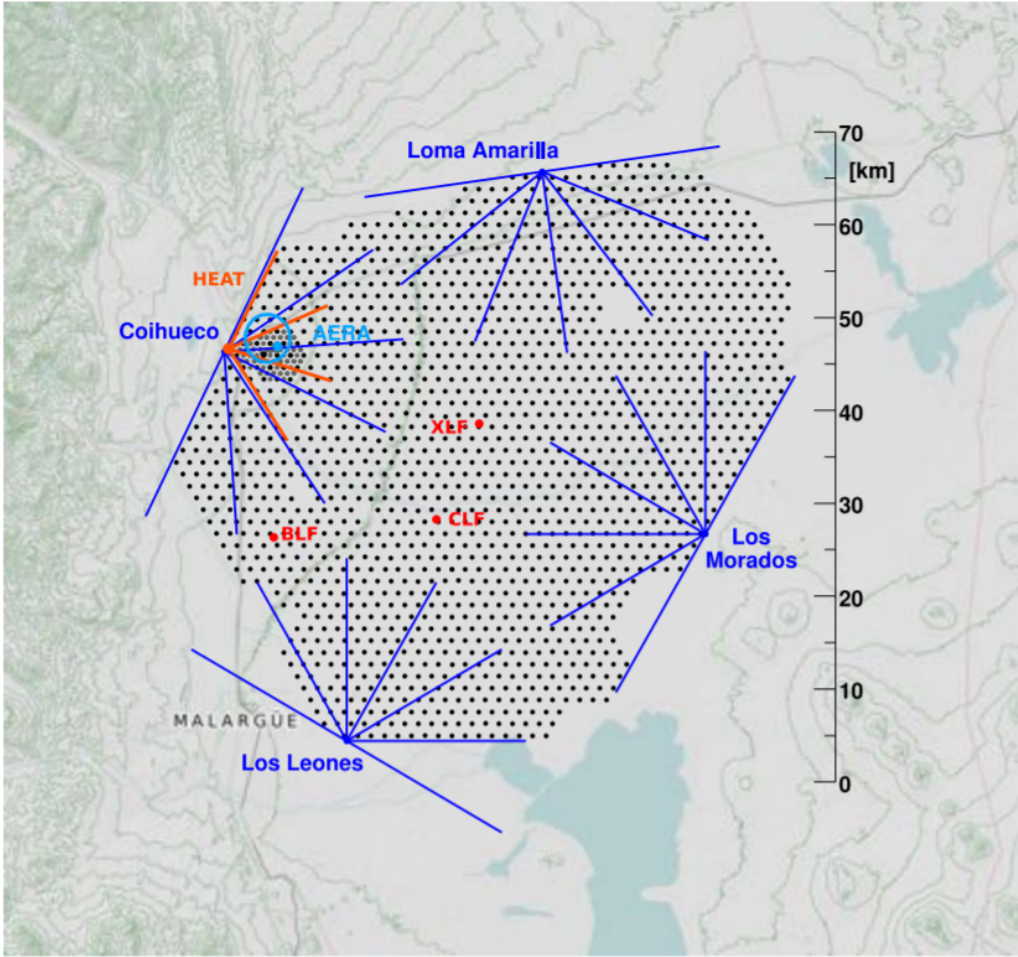


**Figure 3.1:** Layout of the Pierre Auger Observatory. Each black dot represents one of the 1660 stations that make up the SD. The 4 housings for the fluorescence telescopes are shown in blue, with each telescope having a 30° field of view in azimuth. Other components shown include the infill array and HEAT upgrades to the observatory, along with the central and extreme laser facilities (CLF & XLF) in the middle of the array. From [61].

from the FD data acquisition system, only receiving alerts for the purpose of hybrid triggering [62].

## 3.2 The surface detector

The SD array of the Pierre Auger Observatory is spread across 3000 km<sup>2</sup> of semi-desert terrain and consists of 1660 water Cherenkov detectors (WCDs). Shown to be a robust method of detecting cosmic rays by previous experiments (see Section 2.3.2), WCDs were chosen for their durability, low cost and nearly uniform exposure to primary cosmic rays with zenith angles < 60°. The elevation of each tank above sea level ranges between 1340 m and 1610 m, with an average elevation of roughly 1400 m. This equates to  $\sim 880 \text{ g cm}^{-2}$  of atmospheric overburden [63].

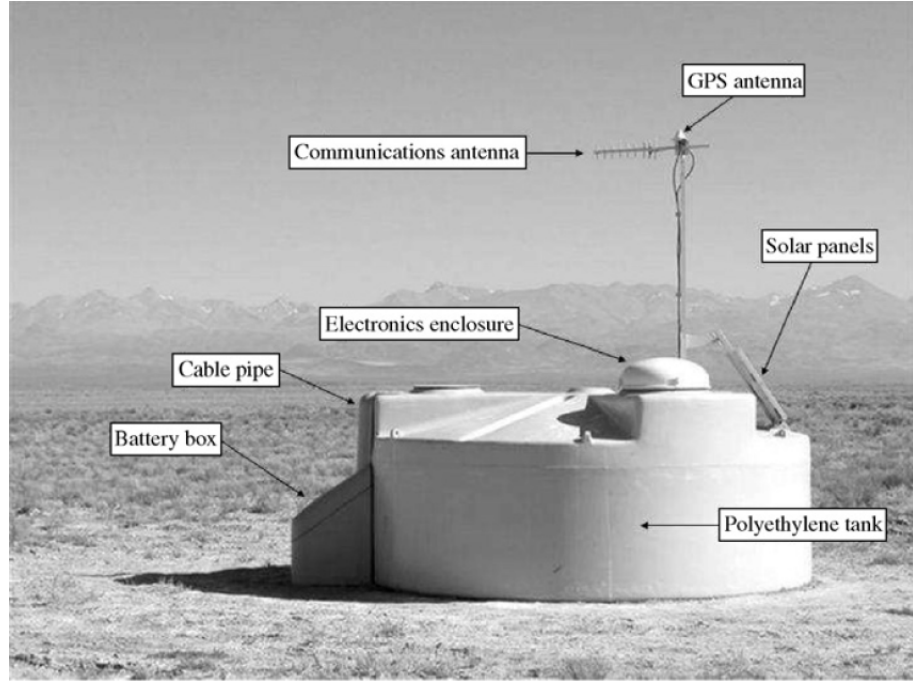


**Figure 3.2:** Image of a water Cherenkov detector with the component parts labelled. From [63].

An initial design goal for the SD was to have 5 triggered stations for any shower with energy above  $10^{19}$  eV. This requirement was met by arranging the tanks in a triangular grid pattern with a spacing of 1.5 km. A desirable outcome of such spacing is that measured data from the observatory overlaps with existing data from other experiments, allowing for useful comparisons and cross-checks. For showers with zenith angles  $< 60^\circ$  the current threshold for full efficiency of the regular SD array is  $3 \times 10^{18}$  eV, slightly lower than that of the FD [63].

### 3.2.1 WCD design

Each water Cherenkov detector is a cylindrical, polyethylene tank 1.2 m high and 3.6 m in diameter. This particular height was chosen to enhance the muon signal in the detectors. On the interior, the tanks have a sealed liner with a reflective inner surface, whose purpose is to diffusely reflect Cherenkov light. Each tank contains 12 tons of purified water and three 9-inch photomultiplier tubes. The PMTs are located at the top of the tank, oriented downwards to look through clear polyethylene into the purified water. The large dynamic range of the PMTs allows them to measure signals close to and far away from the shower core. These signals are digitised by a flash analog to digital converter (FADC) operating at 40 MHz. A solar panel is attached to the tank to provide power to the PMTs and electronics [63]. A photo of a tank with labelled components is shown in Figure 3.2.

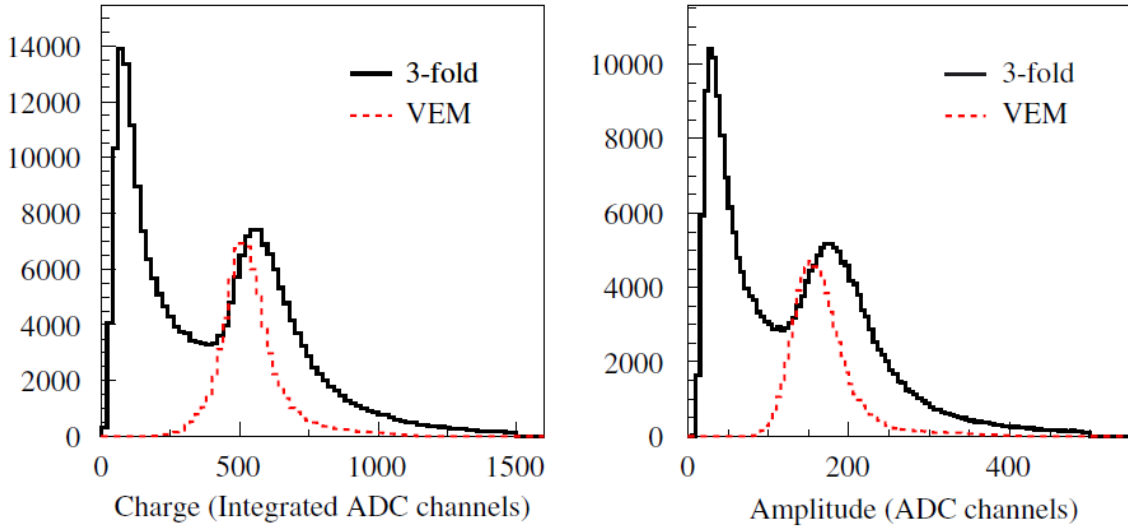


**Figure 3.3:** Histograms of the charge and pulse height from the summed signal of all 3 PMTs in an SD station. The black lines represent background muons and the dashed red lines show central, vertical muons selected with a muon telescope. From [64].

### 3.2.2 Calibration of the SD

To ensure the signals from an extensive air shower are accurately recorded, every WCD automatically records the parameters required for calibration every minute. Upon an event trigger, the previous minute of calibration data is sent to the CDAS. There, the primary signals measured by the detectors are converted into a station independent unit known as a vertical equivalent muon (VEM). This corresponds to the average “charge” measured by a PMT from the Cherenkov light emitted by a muon passing vertically through the centre of the tank. Note that “charge” refers to the integrated PMT pulse over time [64].

In normal operation the WCDs are not able to isolate a single vertical muon, thus the charge histogram of background muons passing through the detector is used to determine the conversion. An example of such a histogram is shown in the left panel of Figure 3.3. The solid black line is a histogram of the sum of the charges measured by the 3 PMTs, whilst the dashed red line has been produced outside of regular data taking by using a muon telescope to select only central, vertical muons. The charge value of the central peak in the vertical muon charge histogram,  $Q_{\text{VEM}}$ , corresponds to 1 VEM and hence is the value needed for calibration. The second peak in the charge histogram of background muons,  $Q_{\text{VEM}}^{\text{peak}}$ , has been shown to correspond to approximately  $1.09 Q_{\text{VEM}}$ . Thus any integrated FADC signal can be converted to VEM units by simply dividing by  $Q_{\text{VEM}}^{\text{peak}}/1.09$ . In practice,  $Q_{\text{VEM}}^{\text{peak}}$  is found by fitting a polynomial to the second peak. The accuracy of the conversion is about 3% [64].

The other purpose of calibration is to set stable trigger thresholds. This is also done using the flux of background muons, in this case with the pulse height or

“current” histogram measured by the PMTs. An example is shown in the right panel of Figure 3.3. The second peak in the pulse height histogram of background muons,  $I_{\text{VEM}}^{\text{peak}}$ , is used as the reference unit for threshold levels [64]. This value will be referred to in the following section on the SD trigger system.

### 3.2.3 Trigger system of the SD

The SD uses a hierarchical trigger system to decide whether detected signals should be classified as an event. The design of the system is such that the array is fully efficient for the detection of EASs above energies of  $3 \times 10^{18}$  eV with zenith angles between  $0^\circ$  and  $60^\circ$ . The first two triggers are performed locally by individual stations and filter out the background particle flux. The lowest level trigger, T1, has two modes. The first is a threshold (TH) trigger which looks for all 3 PMTs to have signals above  $1.75 I_{\text{VEM}}^{\text{peak}}$ . The second mode is a time over threshold (ToT) trigger and requires 2 out of the 3 PMTs to be above  $0.2 I_{\text{VEM}}^{\text{peak}}$  for a period of at least 13 FADC bins (325 ns) in a 3  $\mu\text{s}$  sliding window. The rate of triggering for each mode is approximately 100 Hz and 2 Hz respectively.

If the requirements for a T1 trigger are met, the second level trigger, T2, is checked. The T2 trigger also has two modes and reduces the rate of events per detector to roughly 20 Hz. All ToT-T1 triggers automatically pass the T2 trigger, whilst the TH-T1 triggers must pass a higher threshold of having all 3 PMTs above  $3.2 I_{\text{VEM}}^{\text{peak}}$ . Smaller signals between  $1.75 I_{\text{VEM}}^{\text{peak}}$  and  $3.2 I_{\text{VEM}}^{\text{peak}}$  are not immediately discarded however, as they may be used if the criteria for the third level trigger, T3, are met. If the T2 condition is passed, the timestamp and type of T2 is sent to the CDAS for the preparation of an array level trigger [65].

The third level trigger, T3, looks for spatial and temporal coincidences of T2 triggers across the array. Similar to the T1 and T2 triggers, the T3 trigger has two modes. The first requires at least 3 stations to pass the ToT condition, with at least one of these stations having one of its closest and one of its second closest neighbours triggered. The name for this type of trigger is “*ToT2C<sub>1</sub>&3C<sub>2</sub>*”, where  $C_n$  represents the  $n^{\text{th}}$  set of neighbours for a station. Thus the name states that this trigger is a ToT trigger where 2 stations (including the central one) are within  $C_1$  and 3 stations are within  $C_2$ . Additionally, each station must trigger within  $(6+5C_n)$   $\mu\text{s}$  of the central one for this mode to be satisfied.

The second mode is a 4 fold coincidence of stations passing any T2 trigger mode. The required spatial distribution of triggered stations is  $2C_1\&3C_2\&4C_4$ . The same timing condition as in *ToT2C<sub>1</sub>&3C<sub>2</sub>* is implemented for this mode. Example layouts of the spatial requirements for each T3 trigger mode are shown in Figure 3.4. Upon the formation of a T3, all stations passing either T1 or T2 level triggers within 30  $\mu\text{s}$  of the T3 send their data to the CDAS for storage. Combined, the T3 triggers select roughly 3800 events per day [65].

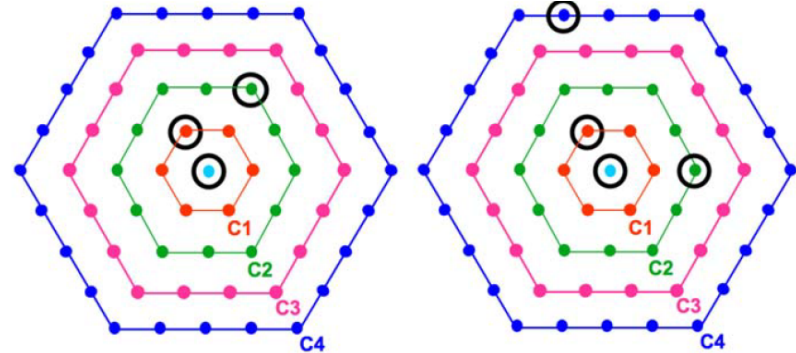


**Figure 3.4:** Examples of possible T3 spatial configurations. The left layout shows an event passing the  $ToT2C_1\&3C_2$  trigger. The right layout is an example of the 4-fold  $2C_1\&3C_2\&4C_4$  trigger. From [65].

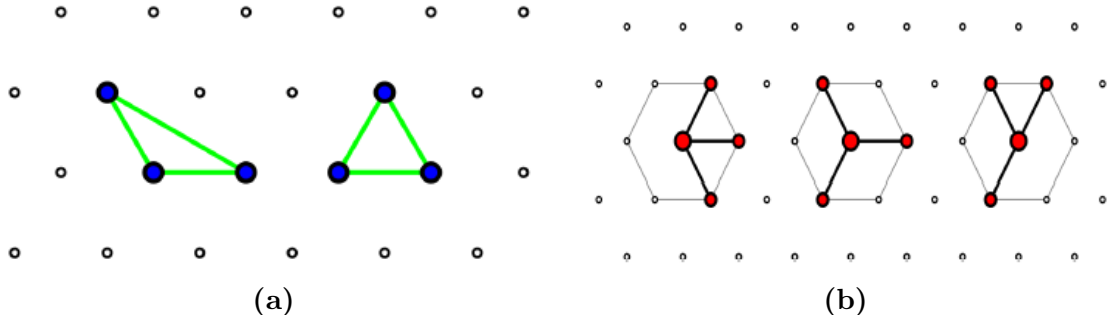


**Figure 3.5:** Possible configurations for events passing the T4 trigger. 3ToT trigger layouts are shown in (a). 4C1 layouts are shown in (b). From [66].

The T4 or “physics” trigger is used to select real showers from stored T3 data. Once again there are two sets of criteria. The “3ToT” mode requires 3 stations passing the T2-ToT trigger to be arranged in a triangular pattern, as shown in Figure 3.5a, whilst the “4C1” mode is satisfied if 4 stations passing any T2 trigger are arranged in one of the configurations shown in Figure 3.5b. Both modes must also meet a timing requirement, namely for the timing of the station signals to fit to a plane shower front moving at the speed of light. Events which pass the T4 trigger are able to have their arrival direction, core position and energy reconstructed 99.9% of the time.

The last trigger level is T5. T5 is a fiducial trigger, selecting only events in which the “hottest” station, that is the station with the greatest integrated signal in an event, has all 6 of its neighbours working at the time of the event (not necessarily triggered). This is known as a “6T5” trigger and the reason for employing it is to remove events which land on the edge of the array or in an area with faulty stations. Such events may have a biased reconstruction, affecting estimates of the shower geometry and thus energy [65].

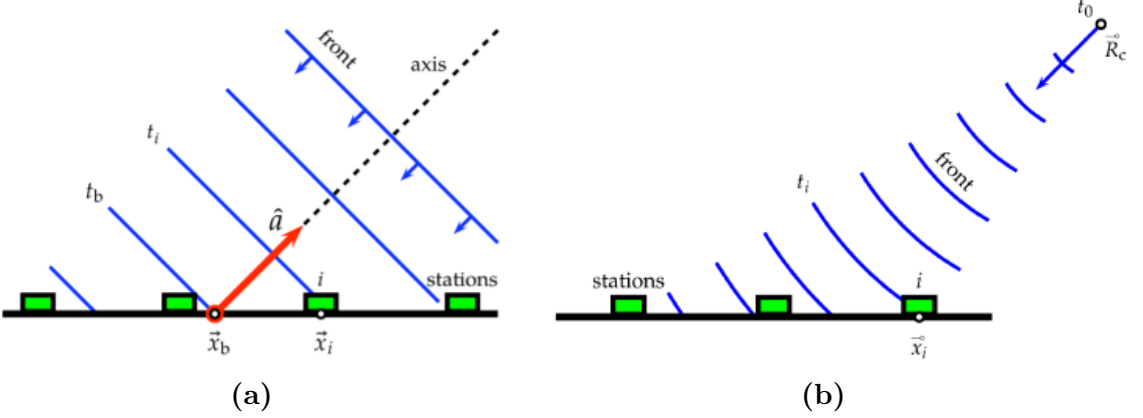


**Figure 3.6:** Diagrams of the plane shower front (a) and spherical shower front (b) models used to estimate the shower geometry. From [68].

### 3.2.4 SD event reconstruction

The SD reconstruction of the properties of an EAS employed by the Pierre Auger Observatory largely follows the outline given in Section 2.2.1. This section adds some additional details and focuses only on “vertical showers”, that is showers with zenith angles  $< 60^\circ$ . Showers with greater zenith angles are known as “horizontal showers” and must be reconstructed differently due to the large amount of atmosphere they pass through [67].

The process to fully reconstruct the shower geometry and primary energy occurs in a number of steps. The key components are outlined below, after which is a description of how they combine to perform the complete reconstruction.

#### Shower geometry

Shower geometry refers to the location of the shower core and direction of the shower axis. The initial estimate of the shower geometry is made using a plane shower front model moving at the speed of light. Here, the shower core is given by the signal weighted barycentre,  $\vec{x}_b$ , and the time of intersection between the shower core and ground is given by the weighted bary-time,  $t_b$ . Thus, for some shower axis direction  $\hat{a}$ , where  $\hat{a}$  points from the ground towards the direction of the incoming shower, the estimated trigger time,  $t_i$ , for a station located at  $\vec{x}_i$  can be written as

$$ct_i = ct_b - \hat{a} \cdot (\vec{x}_i - \vec{x}_b) \quad (3.1)$$

A schematic view is given in Figure 3.6a. From here, an analytical solution for  $\hat{a}$  is derived by using a “seed-triangle” - a set of 3 stations consisting of one station and its two nearest neighbours all passing a station level trigger arranged in a triangle pattern. The seed-triangle with the greatest sum of the three station signals is used to find a first estimate of  $\hat{a}$  [68].

Using the values of  $\vec{x}_b$  and  $\hat{a}$  as initial guesses for the shower core and shower axis respectively, a spherical model is then used to obtain a more accurate approximation of the shower geometry. A schematic for this model is shown in Figure 3.6b. The estimated trigger time of a station is now

$$ct_i = ct_c - |\vec{R}_c - \vec{x}_i| \quad (3.2)$$

where  $\vec{R}_c$  is the virtual origin of the shower front and  $t_c$  is the unknown time at which the shower core intersects the ground.  $\vec{R}_c$  can be written in terms of the shower axis  $\hat{a}$  as

$$\vec{R}_c = \vec{x}_c + R_c \hat{a} \quad (3.3)$$

Here,  $R_c$  is the radius of curvature of the spherical front at the impact point (shower core)  $\vec{x}_c$ . A chi-squared minimization procedure can be performed on the difference in predicted and observed trigger times to find the best fit of the parameters  $\hat{a}_x$ ,  $\hat{a}_y$ ,  $t_c$ , and, in the case of 5 or more stations,  $R_c$ . Events with only 3 or 4 stations have their  $R_c$  value fixed to a predefined parameterisation [68].

## Lateral distribution

The lateral distribution function (LDF) describes how the signal measured by a station changes with respect to the distance from the shower axis,  $r$ , as measured in the shower plane. The current LDF fitted to WCD signals takes the form

$$S(r) = S(r_{\text{opt}}) f_{\text{NKG}}(r) \quad (3.4)$$

where  $S(r_{\text{opt}})$  is a normalisation, often referred to as the “shower size”, and  $f_{\text{NKG}}$  is a modified Nishimura-Kamata-Greisen (NKG) function describing the shape of the LDF. The functional form of  $f_{\text{NKG}}$  is

$$f_{\text{NKG}}(r) = \left( \frac{r}{r_{\text{opt}}} \right)^\beta \left( \frac{r + r_s}{r_s + r_{\text{opt}}} \right)^{\beta + \gamma} \quad (3.5)$$

Regarding Equation 3.5,  $r_s$  is fixed to be 700 m,  $r_{\text{opt}}$  refers to the distance at which the uncertainty in the LDF shape is minimised, and  $\beta$  and  $\gamma$  are variable shape parameters. For the layout of Auger,  $r_{\text{opt}}$  has been shown to be  $\approx 1000$  m. Thus  $f_{\text{NKG}}(1000) = 1$  and so  $S(1000)$  is the measure of the shower size. The lateral distribution of signals for a sample event is shown in Figure 3.7a, with the corresponding fit to these signals shown in Figure 3.7b

For the majority of events, the multiplicity and spatial distribution of triggered stations doesn't allow for the shape of the LDF to be accurately determined. Hence, an *average* LDF based on data-derived parameterisations of  $\beta$  and  $\gamma$  is usually fitted. The parameterisations are in terms of  $S(1000)$  and zenith and come from subsets of events with satisfactory *lever-arms*. Specifically, parameterisations of  $\beta$  are from events which have 2, 3 or  $\geq 4$  stations in the range 400-1600 m, with two of the stations being separated by at least 900, 800 or 700 m respectively. Parameterisations

of  $\gamma$  come from similarly restricted events, except the range in which the stations must be distributed is 1000-2000 m [68].

When fitting the LDF, a maximum likelihood method is used to find the most probable values of  $S(1000)$  and core position  $\vec{x}_c$  for the given event.  $\beta$  may also be fitted if the station layout meets the lever-arm conditions outlined above. The uncertainties on the station signals used in this method come from a signal uncertainty model developed for the SD. This model has the baseline assumption of Poisson statistics, where the uncertainty in signal scales with its square root. This is because the uncertainties primarily arise from sampling fluctuations (variation in the number of particles sampled at a fixed distance from the shower axis). However, a linear dependence on zenith is also present, attributed to the larger relative fraction of muons detected by the WCDs at higher zenith angles. Further details on the fitting procedure and signal uncertainties can be found in [68].

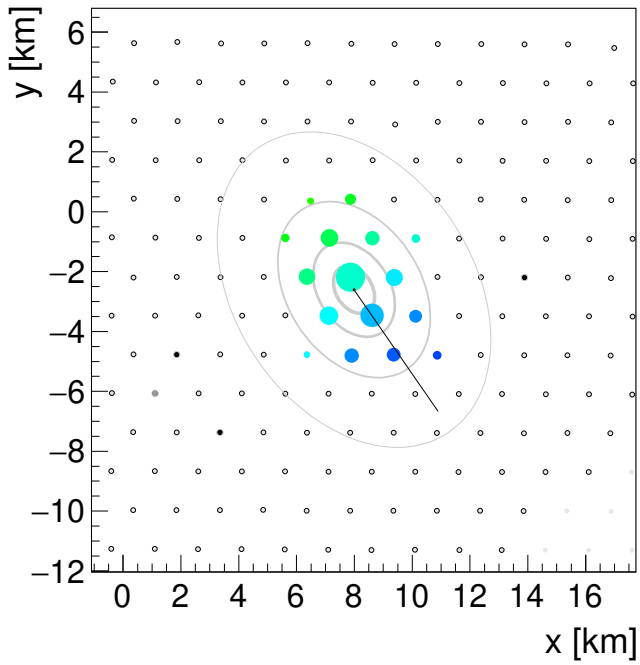
## Fit process

A full reconstruction combines the results of the shower geometry and lateral distribution fits as follows. First, an initial plane shower front is fit to the station timings, with the core,  $\vec{x}_c$ , estimated by the station weighted barycentre. This gives a first guess of the shower axis,  $\hat{a}$ , which is subsequently improved using the spherical front approximation. The shower axis is used to define the shower plane and hence give the initial station radii in the fit to the lateral distribution of signals. An iterative procedure is then performed, where the shower core and  $S(1000)$  (and possibly  $\beta$ ) are fit simultaneously. The resulting shower core location from the fit is then used to re-estimate  $\hat{a}$ , and thus the station distances, before performing the fit again. This process converges quickly to optimal values of  $S(1000)$ ,  $\vec{x}_c$  and  $\hat{a}$  [68]. The resolution of these properties generally increases with station multiplicity. The uncertainty in the shower axis direction, for example, goes from  $< 1.6^\circ$  for more than 3 stations to  $< 0.9^\circ$  for more than 6 stations [61].

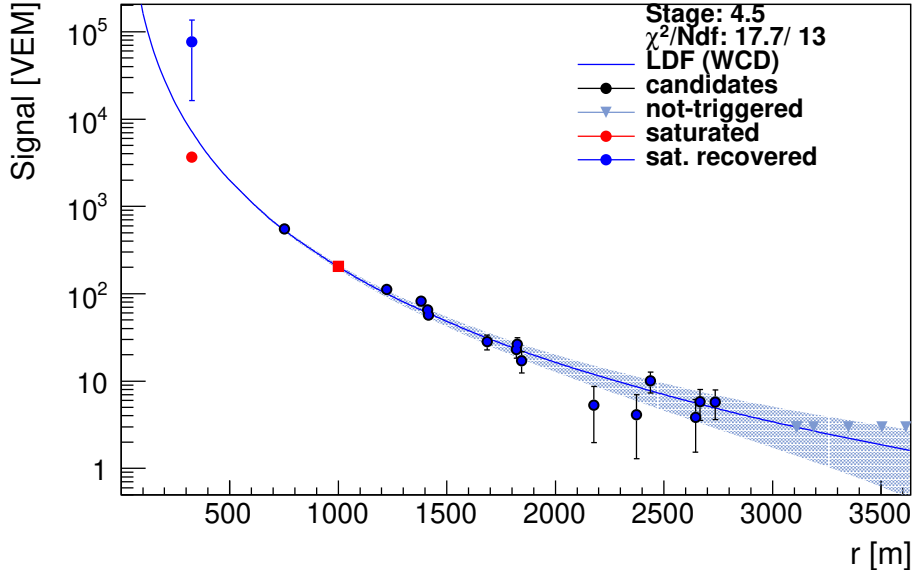
## Energy reconstruction

To reconstruct the energy of the primary cosmic ray the  $S(1000)$  size estimator is used. Since inclined showers have a significantly attenuated electromagnetic component,  $S(1000)$  is zenith dependent and hence is first normalised to the value it would have if the shower had arrived with a zenith angle of  $38^\circ$  (the median of the zenith angle distribution between 0 and  $60^\circ$ ). This value is known as  $S_{38}$ . The conversion is performed using the Constant Intensity Cut method which relies on the assumption of an isotropic flux of cosmic rays [69]. For a given  $S(1000)$  and  $\theta$ ,

$$S_{38} = \frac{S(1000)}{1 + ax + bx^2 + cx^3} \quad (3.6)$$



(a)



(b)

**Figure 3.7:** (a) An example lateral distribution of signals. Triggered stations are coloured, with the color scale corresponding to the start time of the signal in each station. The size of each circle is proportional to  $\log(S)$  where  $S$  is the measured signal. The black line indicates the projection of the shower axis onto the ground. (b) A fit to the signals of the same event. The different possible states of stations are shown in the legend. The red square indicates  $S(1000)$ . Plots are from the Offline EventBrowser.

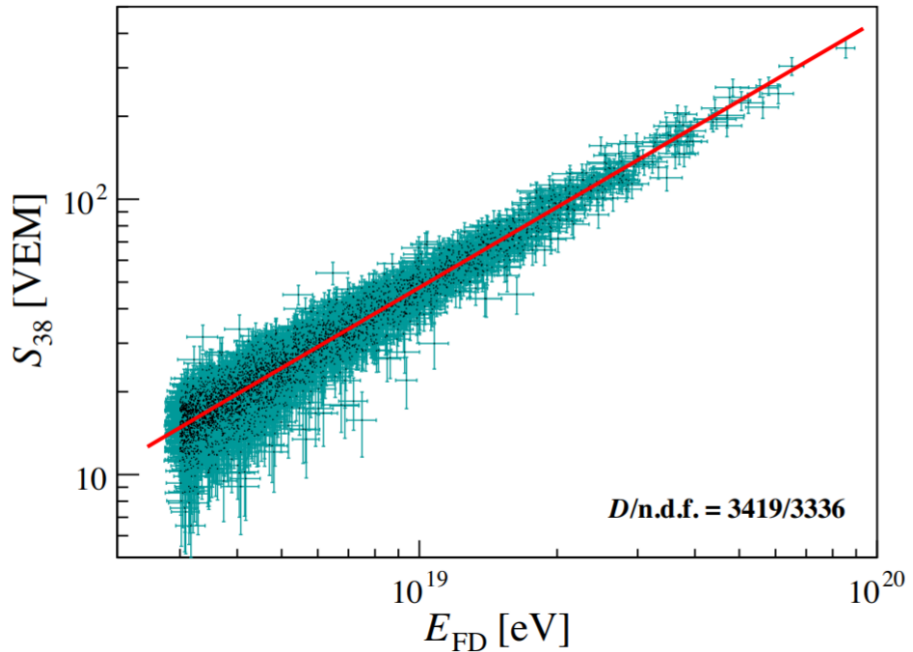


**Figure 3.8:** Relationship between the FD energy and  $S_{38}$  used to calibrate the SD energy. Measurements are from Golden Hybrid data. From [70].

where the parameters  $a$ ,  $b$  and  $c$  come from the result of a fit to  $S(1000)$  as a function of  $x = \cos^2 \theta - \cos^2 38^\circ$ . Hybrid data (see Section 3.3.1) is then used to calibrate the value of  $S_{38}$  to the energy as measured by the FD. A plot of this calibration is shown in Figure 3.8. The fitted function (red line) is a power law and takes the form [70],

$$E_{SD} = 0.186 \left( \frac{S_{38}}{\text{VEM}} \right)^{1.031} \text{ EeV} \quad (3.7)$$

The resolution of this estimate is roughly 15% above 1 EeV [14].

### 3.3 The fluorescence detector

The fluorescence detector of the Pierre Auger Observatory consists of 27 fluorescence telescopes overlooking the SD array. Their purpose is to measure the fluorescence light emitted by atmospheric nitrogen molecules which have been excited by charged particles from an EAS. The first 24 telescopes deployed were spread evenly over four sites: Los Leones, Los Morados, Loma Amarilla and Coihueco. Each of these telescopes has a field of view of  $30^\circ \times 30^\circ$  in azimuth and elevation, giving full  $180^\circ$  coverage in azimuth at each site (see Figure 3.1). Three additional telescopes were added to Coihueco in 2009 as one of the observatory's first major upgrades, HEAT (see Section 3.4).

When in operation, light collected by an FD telescope must first pass through a UV filter, which accepts wavelengths between 290-410 nm, before being focused by a  $10\text{ m}^2$  spherical mirror onto a 440 pixel camera. Each camera pixel is the

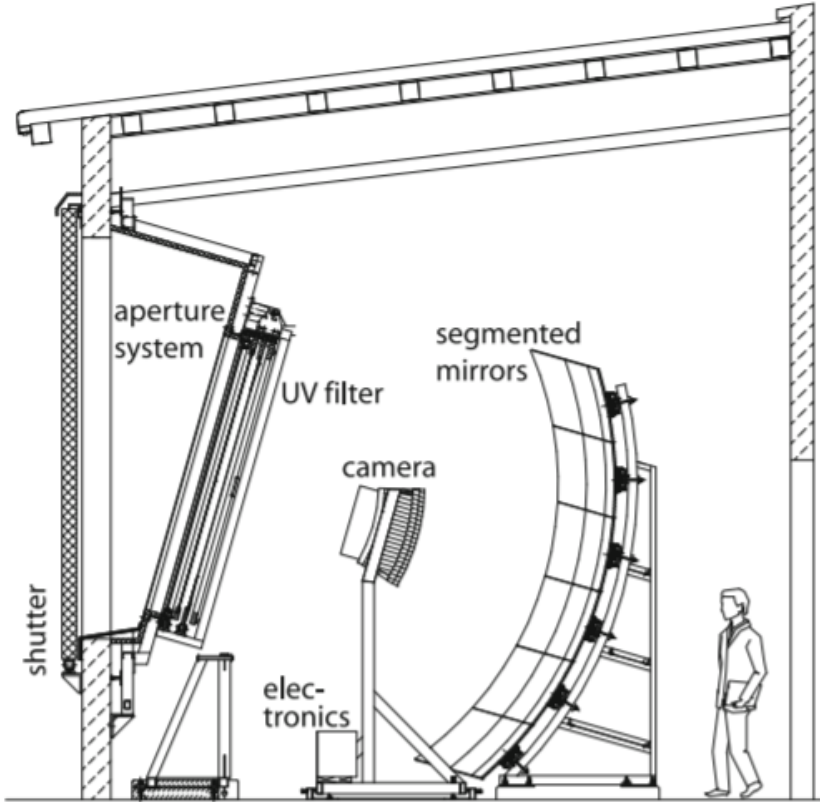


**Figure 3.9:** Schematic view of a fluorescence telescope of the Pierre Auger Observatory. From [43].

photo-cathode of a photomultiplier, with pulses in the PMTs digitised every 100 ns. Similar to the SD, a hierarchical trigger system is utilised to decide whether these pulses constitute a real air shower. Each telescope is housed in a climate controlled room and has a shutter which can be closed to prevent damage to the equipment [43]. A schematic view of an individual telescope is shown in Figure 3.9.

The reconstruction of FD events follows the description given in Section 2.2.2. One extra detail worth mentioning is the functional form fit to the longitudinal profile of the shower. In 2019, the Pierre Auger Collaboration modified the original Gaisser-Hillas function [71] by recasting the shape parameters of the fit so as to reduce their degeneracy. The current function is

$$\frac{dE}{dX}(X) = \left( \frac{dE}{dX} \right)_{\max} \left( 1 + \frac{R}{L}(X - X_{\max}) \right)^{1/R^2} \exp \left( -\frac{X - X_{\max}}{RL} \right) \quad (3.8)$$

In this function,  $L$  describes the width of the shower profile and  $R$  describes the asymmetry of the shower profile. The  $X$  value which maximises Equation 3.8 is  $X_{\max}$ , whilst the calorimetric energy is determined by integrating the function from 0 to  $\infty$ . Above 10 EeV, the energy estimate has a statistical uncertainty of 8%,

with the total systematic uncertainty for energy measurements being 14% [72].  $X_{\max}$  measurements have a resolution of approximately  $20 \text{ g cm}^{-2}$  [73].

A crucial component in obtaining an accurate measurement of the longitudinal profile is the atmospheric monitoring that takes place across the observatory. Measurements of the aerosol content are made by laser facilities located in the centre of the array and cross-checked by LIDARs operating at each FD site. The pressure, temperature and humidity of the atmosphere is provided at 3-hourly intervals by the Global Data Assimilation System (GDAS). A cloud detection system is also present, handled by the LIDARs and cloud cameras at each site, with complementary information obtained from satellites in geostationary orbit [74]. These systems allow the effect of atmospheric fluctuations to be taken into account when reconstructing showers with the FD.

Currently, the FD operates for 15% of the year, a small fraction compared to the near 100% up-time of the SD [60]. This is because the FD cannot operate with excessive background light or in poor weather conditions. Thus the presence of the sun, nearly full moon, rain/snow or even high wind speeds contribute to the off time of the FD. Because of these strict operational requirements, each detectors exposure must be constantly monitored [43].

### 3.3.1 Hybrid detection

Events observed by both the SD and FD are referred to as hybrid events and are the highest quality data the observatory measures. For this reason, hybrid data is used for mass composition studies and for calibrating the energy measurements of the SD array (see Section 3.2.4) to be used for studies of the cosmic ray energy spectrum. Hybrid data is collected when satisfactory trigger levels for the FD are met, initiating data acquisition from the SD. This information is sent to the CDAS where it can be stored and later processed for hybrid reconstruction.

For a hybrid reconstruction, the shower geometry is reconstructed using the timing information from both the SD and FD, giving uncertainties in the shower direction and core location of  $0.6^\circ$  and 50 m respectively [43]. This is achieved by first using the triggered pixels in the FD to define the plane in which the shower axis lies. The orientation of the axis is then determined using the timing of the FD pixels and the arrival time of the shower at ground as measured by the station with the greatest signal. The energy reconstruction technique is the same as used for the FD.

## 3.4 Early enhancements - AMIGA and HEAT

One of the fist enhancements to the Auger SD array was the Auger Muon and Infilled Ground Array (AMIGA). It began construction in 2008, with the goal of gaining insight into the cosmic ray energy spectrum between  $10^{17} \text{ eV}$  and  $10^{18} \text{ eV}$ . The AMIGA

upgrade is embedded within the original 1.5 km array and stationed within the field of view of the Coihueco FD site [75]. Currently, 71 additional identical WCD tanks have been deployed with a spacing of 750 m, spanning approximately 27 km<sup>2</sup>. Recently, 12 more tanks were embedded within the 750 m array with 433 m spacing [76]. The AMIGA upgrade also plans to bury muon detectors with an area of 30 m<sup>2</sup> underground, at a depth of  $\approx 2.3$  m, next to each 750 m tank. Their purpose is to measure the muon component of detected EASs. This will allow for better reconstruction of the primary particle's properties, particularly the mass composition measurement [75].

In combination with AMIGA was a low energy extension to the FD in 2009; the addition of High Elevation Auger Telescopes (HEAT). These telescopes were added to the Coihueco site and are very similar to the original detectors in design, but with the key ability to be tilted upwards by 29°. This enables them to see in the elevation range 30° to 58° and allows for the hybrid detection of showers down to energies of 10<sup>17</sup> eV. In addition, unbiased lower energy measurements of  $\langle X_{\max} \rangle$  are possible with this hybrid approach [61, 75]. The other significant difference between HEAT and the original detectors is the electronics kit. With double the sampling rate, HEAT telescopes are able to better track showers with higher angular velocities, a necessary capability to study lower energy showers [61].

### 3.5 AugerPrime

The latest upgrade to the Pierre Auger Observatory is known as “AugerPrime”. There are many motivations and goals for this upgrade, the primary one being to further our understanding of the mass composition of UHECRs by having a mass measurement for every event recorded. This may lead to insights into the acceleration mechanisms and sources of cosmic rays.

Other notable objectives include discovering the origin of the flux suppression seen in the energy spectrum, determining the fraction of proton cosmic rays at the highest energies, and investigating hadronic multi-particle production at energies unobtainable with current accelerator technology [60]. The upgrade consists of the following,

- Scintillator detectors deployed on top of every WCD
- Each SD station, now comprising of a WCD and a scintillator, will have their electronics board upgraded
- A duty cycle increase of the FD telescopes by 50%
- Finalising the installation of the underground muon detectors as part of AMIGA

Altogether, these upgrades will provide the observatory with more data, due to the increase in FD duty cycle, higher quality measurements from the SD, and



**Figure 3.10:** (Left) A top-down view of the 24 scintillator bars in the right-hand module of a scintillator. The bars are interconnected with WLS fibres and transport photons to a PMT, located in the bottom left of the picture. From [77]. (Right) The final scintillator unit, equipped with a roof for protection. From [66].

enhanced sensitivity to the mass composition of primary cosmic rays. Regarding this last point, the different responses to secondary particles produced in an EAS from the WCDs and scintillator detectors will allow for the muonic and electromagnetic components of the shower to be separated on an event by event basis. The addition of scintillator detectors will also be useful for direct comparisons of data between the Pierre Auger Observatory and the Telescope Array experiment in the northern hemisphere.

### 3.5.1 The scintillator surface detector

The scintillator surface detector (SSD) will consist of scintillator detectors placed on top of every WCD in the SD array. At the time of writing, more than 80% of tanks have a scintillator installed, however only around 6% also have the upgraded electronics board (also known as the upgraded unified board (UUB)) to service the upgraded detectors [76]. The small section of the array with both the SSD and UUB installed is called the pre-production array and is currently taking data with the SSD.

The scintillators contain two modules, each with an area of roughly  $2\text{ m}^2$  and consisting of 24 plastic scintillator bars. Each bar is 160 cm long, 1 cm thick and 5 cm wide. Fluorescence photons produced in the scintillator have their wavelength shifted to the visible range of the electromagnetic spectrum due to the materials used to make each scintillator bar - polystyrene (Polystyrene Dow Styron 663 W) mixed with dopants PPO (1%) and POPOP (0.03%). Inside, two small kidney shaped holes run along the length of the bar and provide a path for optical fibres to transport photons to the PMT [60]. The chosen optical fibers are Y-11 (300) MSY from Kuraray [78] with a 1.00 mm diameter. These fibres are wavelength-shifting (WLS) fibres and shift any blue light to green light. The two scintillator modules containing the bars are placed inside an aluminium frame and covered with protective sheets of

aluminium and polystyrene-aluminium for protection. Altogether, the final unit has a scintillating area of  $3.84\text{ m}^2$  [60]. Photos of the scintillator bars and final housed detector are shown in Figure 3.10.

As for triggering and calibration, the SSD does not at-present have a triggering system, instead relying on the trigger system of the SD to decide when to send data to the CDAS. Calibration of the SSD is done in a similar fashion to the SD, relying on the signal produced by vertical muons impinging on the detector. Currently, results from simulations are being used for the calibration while the measurements required for a data-driven calibration are being finalised. The unit for calibration is the “Auger minimum ionising particle (MIP)”, defined as the average signal produced by a vertical, through-going muon, randomly incident on the detector. In terms of the number of photo-electrons (PE) produced at the photo-cathode of the PMT, recent simulations have shown  $1\text{ Auger MIP} = 31.3 \pm 0.3\text{ PE}$  [66].

---

# Parameterising the signal asymmetry in the Pierre Auger Observatory’s surface detectors

---

As part of the “Auger Prime” upgrade to the Pierre Auger Observatory, scintillator detectors are currently being installed on top of every water Cherenkov detector. The primary reason for adding scintillators is to have two types of ground based particle detectors with different responses to the components of extensive air showers. Since different primary cosmic rays are believed to generate slightly different distributions of secondary particles, the idea is to exploit these differences for mass composition studies. One property of air showers which could be utilised to assist in mass determination is “asymmetry” - a phenomenon where detectors equal distances from the shower core (when projected into the shower plane) will, on average, have systematically different signals for inclined showers. Specifically, stations located between  $-90 < \zeta/\text{°} < 90$  (the *upstream* or *early* region) will, on average, have greater signals than stations located at  $|\zeta/\text{°}| > 90$  (the *downstream* or *late* region). Figure 4.1 shows a basic 2D diagram indicating the upstream and downstream regions for an inclined shower. The magnitude and causes of asymmetry, and how these link to mass composition, is the main focus of this thesis.

In the literature there are two main reasons often cited as the source of asymmetry, namely the attenuation of air shower particles and geometrical effects related to the inclination of the shower and shape of the detector. A detailed look into some of these causes is the focus of Chapter 5. For now, it suffices to say that the complete picture is rather complex and a detailed understanding isn’t needed to simply analyse the magnitude of the asymmetry. Parameterising the amplitude of the asymmetry in both the water Cherenkov detector and scintillator detector signals is the goal of this chapter. Note that from this point onwards, “WCD” will be used to refer to both the entire collection of water Cherenkov detectors and individual tanks where appropriate. Since we would like to know how the magnitude of asymmetry differs with mass composition, the parameterisations will be done on a large number of simulated extensive air showers of which the primary particle is known. The software used to create the simulated air showers, COsmic Ray SImulations

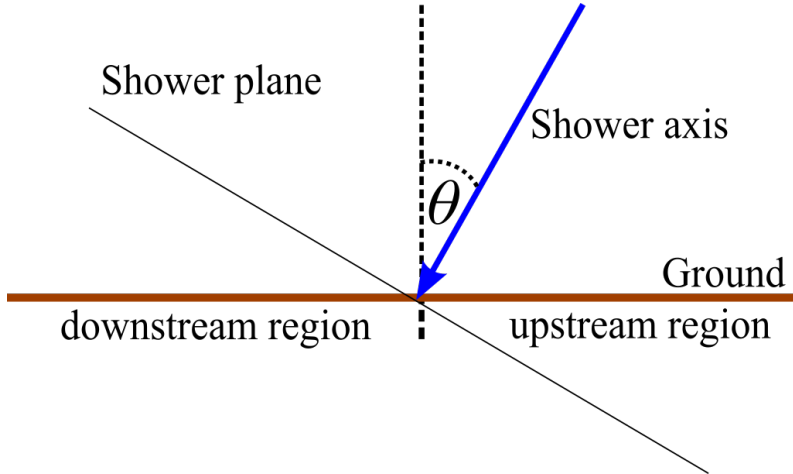


**Figure 4.1:** A 2D representation of the so called “upstream” and “downstream” regions for an inclined extensive air shower. For a station located in the upstream or downstream region, when its position is projected into the shower plane parallel to the shower axis, the absolute value of its  $\zeta$  coordinate is  $< 90^\circ$  or  $> 90^\circ$  respectively.

for Kascade (CORSIKA) and the Offline framework used to model the detector response to air showers will now be briefly described.

## 4.1 CORSIKA

CORSIKA [79] is a program originally designed for simulating extensive air showers for the KASCADE array experiment, located in Germany. Its utility has made it a widespread tool for many cosmic ray studies, including those performed by the Pierre Auger Observatory. CORSIKA is designed to simulate the interactions and decay of secondary particles from air showers generated by cosmic rays of primary energies between  $10^{11}$  and  $10^{20}$  eV. The secondary particles tracked include nuclei, hadrons, electrons, muons and photons. The properties of these particles, such as position, momentum, type and arrival time, are recorded any time they pass an observation level set by the user. Whilst multiple observation levels can be set, it is typical to only have one level, that being the height above sea level of the experiment one is interested in simulating showers for.

CORSIKA provides many different options and functionalities to the user, one of the most important being the option to choose different models to describe the high and low energy interactions of particles. These models are updated when new particle accelerator data are released. Another option, called “thinning”, assists in the simulation of high energy showers. In such showers the total number of particles may reach hundreds of billions, requiring an enormous amount of computational effort to completely simulate. However by setting a threshold energy below which not all particles which interact are tracked (based on the energy of the primary), only a small fraction of particles need to be considered, with those that are assigned weights

corresponding to their probability of having been selected. In general, particles with higher energies are more likely to continue to be tracked. A de-thinning process, where particles are restored to having unity weight, is necessary when considering the detector response of a sparse ground array such as the SD of the Pierre Auger Observatory.

All simulated air showers used for analysis in this thesis were generated with CORSIKA. The specific details regarding the options used to simulate each set of showers will be described as needed.

## 4.2 The Offline software framework

In order to analyse the data from both real and simulated events, the Pierre Auger Collaboration has designed the Offline software framework [80]. The software is used to reconstruct measured events and to simulate the response of the observatory's detectors to a simulated air shower. Offline is written in C++ and is modular in its design, meaning the user can select which modules to run in order to perform a certain task. The framework of Offline has 3 core components;

- Collection of modules: The modules are essentially self-contained algorithms which constitute a single processing step in the analysis. A wide variety of applications can be achieved by combining the various modules in different ways. An XML-based language has been constructed to handle the sequencing of the modules and the module options.
- Event data: The event data contains all raw, calibrated, reconstructed and simulated data. Modules are able to read and write to the Event data, allowing communication between different modules. The data is arranged in a collection of classes, structured based on the hierarchy of the observatory instruments.
- Detector description: This data is read-only and is retrieved by modules to provide information on the detector configuration and performance at any particular time. Atmospheric conditions are also contained in the detector description.

All CORSIKA showers used in this study have been reconstructed with the Offline software.

## 4.3 Initial investigation

Before beginning a full scale parameterisation, the asymmetry in proton and iron showers (for both the WCD and SSD) was investigated for a specific energy range and radius. This was done as a check of the method and to gain some insight into the level of difference in asymmetry that could be expected between proton/iron and

Primaries	Proton, Iron
$\log(E/\text{eV})$	19 - 19.5, flat in $\log(E/\text{eV})$
$\theta/^\circ$	0-60, flat in $\sin^2 \theta$
$\phi/^\circ$	0 - 360, uniformly distributed
Had Int. Models	QGSJet-II.04

**Table 4.1:** Properties of the showers used for this initial study. There were a total of 417 unique proton showers and 500 unique iron showers.

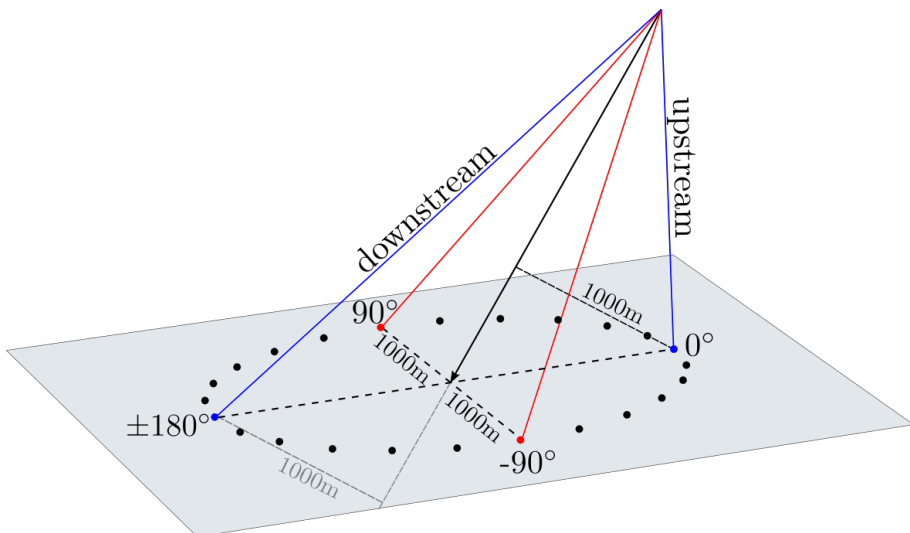


**Figure 4.2:** A schematic of a dense ring on the ground containing 24 stations. All stations are located at a distance of 1000 m from the shower core when projected into the shower plane. The angles listed show the values of  $\zeta$  the corresponding coloured stations would have when projected into the shower plane. Modified from [81].

between the WCD/SSD. Roughly 400 proton and 500 iron showers were simulated, with energies between  $19 < \log(E/\text{eV}) < 19.5$ , zenith angles ranging from  $0 - 60^\circ$  and a randomly assigned azimuth. The hadronic interaction model chosen was QGSJet-II.04. The properties of this small library of showers is summarised in Table 4.1.

When simulating the detector response to one of these showers, the spacing of the regular Auger SD array didn't allow for signals at equal distances in the shower plane, for many different values of  $\zeta$ , to be measured. Thus these simulations made use of "dense rings". A dense ring of tanks is simply a set of tanks simulated on the ground which, when their positions are projected into the shower plane, are at an equal distance from the shower core and spaced evenly in  $\zeta$ . A schematic diagram is shown in Figure 4.2. For our case, a ring of 12 tanks at 1000 m in the shower plane was used to obtain a profile of the signal asymmetry at this distance for every individual shower. The first tank was placed directly beneath the shower axis, at  $\zeta = 0^\circ$ , with subsequent tanks separated by  $30^\circ$ .

Signal fluctuations within the dense rings were too large for the asymmetry in any individual shower to be accurately measured. As such the showers were binned in zenith, specifically 7 bins equally spaced in  $\sin^2 \theta$ , so as to give roughly equal statistics in each bin. Additionally, because each shower had a different energy and thus different value of  $S(1000)$ , the average signal in each dense ring was used to normalise the individual signals of each of the 12 tanks/scintillators. In each zenith bin, the average relative signal and corresponding standard error for every value of  $\zeta$  ( $0^\circ, -30^\circ, 30^\circ, \dots, -150^\circ, 150^\circ, -180^\circ$ ) was found for both detectors, before a cosine function of the form

$$S(1000, \zeta) / \langle S(1000, \zeta) \rangle = 1 + b \cos \zeta \quad (4.1)$$

was fit to each set of points. Here,  $S(1000, \zeta)$  is the recorded signal in VEM (or MIP) at 1000 m in the shower plane as a function of  $\zeta$  and  $b$  is the asymmetry amplitude, a fitted parameter which will be fully parameterised in the following section. If a shower did not trigger all 12 tanks in the dense ring then it was not included in the average relative signal calculations. This is because the true signal in the non-triggered tanks may have been above 0 VEM but still less than the trigger threshold. Example plots which include the results for both detectors are shown in Figure 4.3 for proton (top panel) and iron (bottom panel). The  $b$  values for the proton WCD/SSD fits in this example were  $0.220 \pm 0.008$  and  $0.39 \pm 0.01$ , whilst the iron WCD/SSD values were  $0.175 \pm 0.007$  and  $0.30 \pm 0.01$ .

The amplitude of the asymmetry,  $b$ , in each zenith bin for both the proton and iron showers is summarised in Figure 4.4. From this plot, we see a clear increase in the magnitude of the asymmetry with zenith angle (in both detectors) for both proton and iron primaries up to the second to last bin, which corresponds to  $\sim 50^\circ$ . The noticeable drop in the asymmetry amplitude in the final bin for each primary/detector type is possibly due to these showers “running out” of electromagnetic particles, which are generally considered to be the primary cause of asymmetry. This may be because of the large amount of atmospheric depth needed to be traversed at large zenith angles. Another observation is that the asymmetry in the SSD signals is larger than the WCD signals. This is likely due to muons, which typically show less asymmetry than electromagnetic particles, contributing a larger fraction of the overall signal in the WCD than the SSD. Regarding the amplitude of the asymmetry for the WCD, it is evident that the asymmetry is somewhat greater when measuring showers initiated by proton primaries than iron primaries for zenith angles  $\gtrsim 30^\circ$  ( $\sin^2 \theta \gtrsim 0.3$ ). Again this is probably because of muons, specifically that they constitute a larger portion of the total number of particles in an iron shower than a proton shower.

Finally, iron showers measured by the SSD show a slightly larger asymmetry than proton showers for zenith angles below  $\sim 40^\circ$  ( $\sin^2 \theta \sim 0.4$ ). The reason for this is not immediately obvious, however it may be related to the average  $X_{\max}$  of

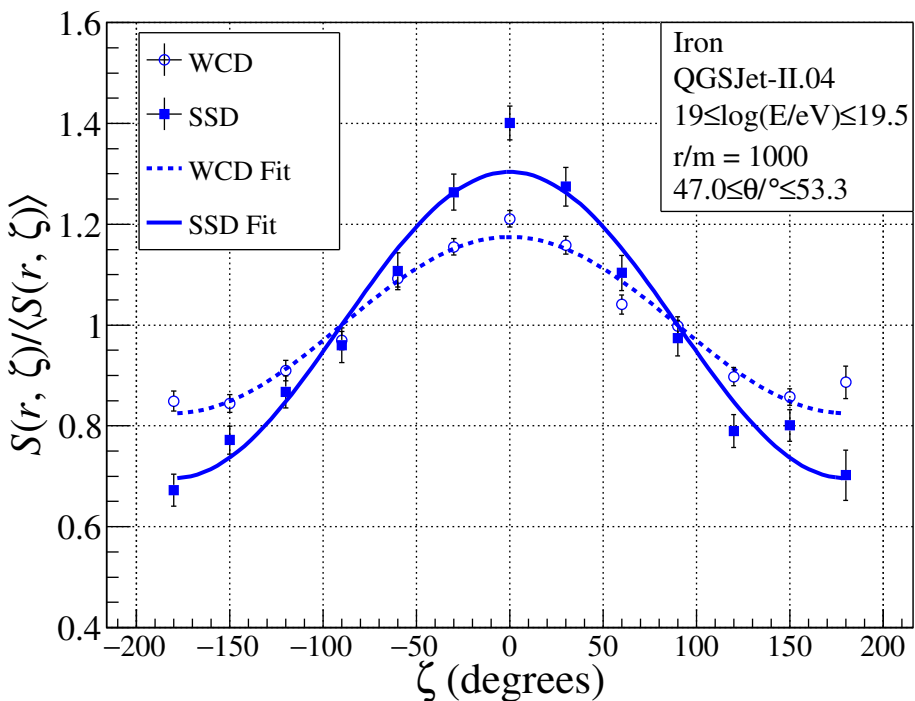
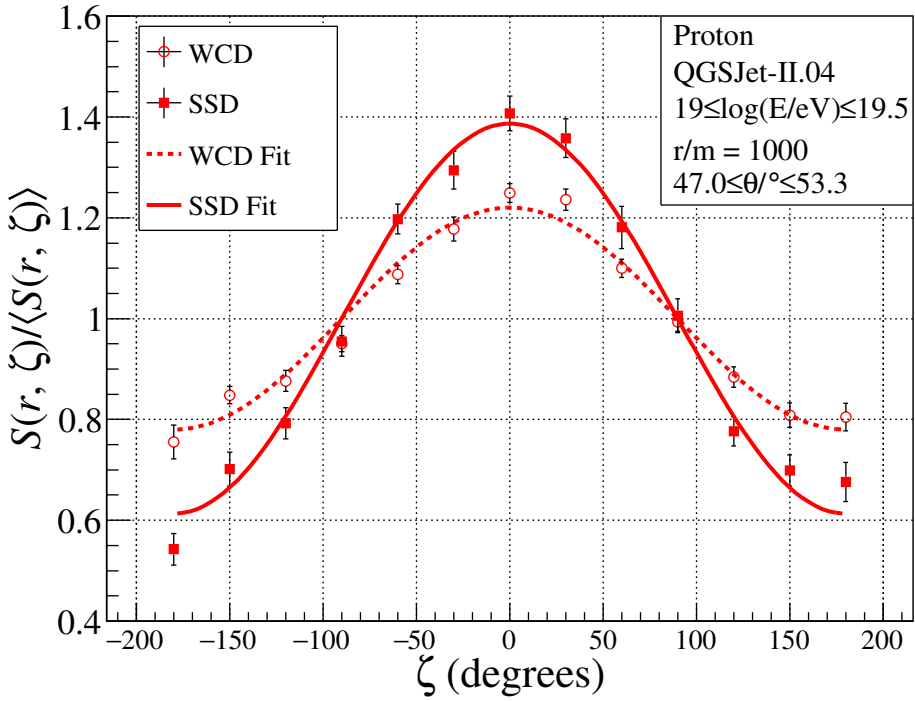


**Figure 4.3:** The normalised signal of a dense ring of WCD/SSD detectors at 1000 m in the shower plane, averaged over many showers, for proton primaries (top) and iron primaries (bottom). The magnitude of the asymmetry in the SSD signals is larger for both primaries

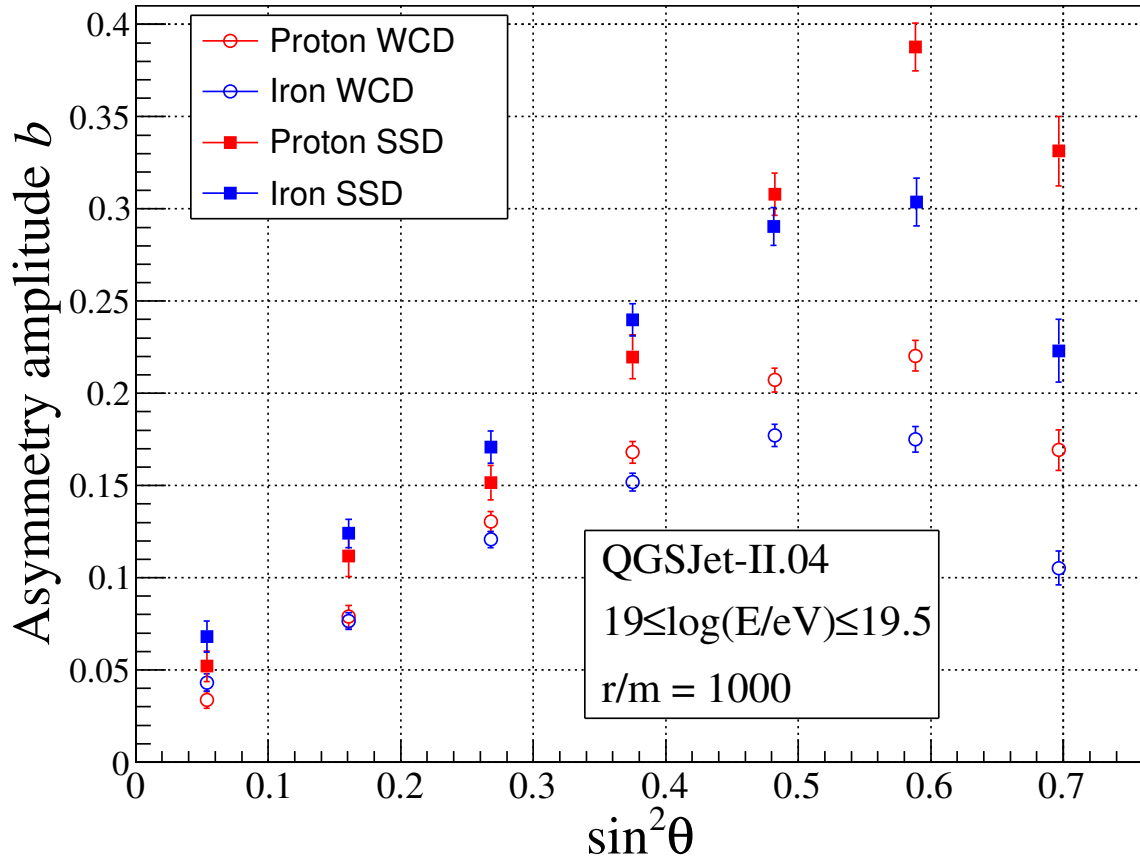


**Figure 4.4:** A summary plot showing the amplitude of the asymmetry,  $b$ , as a function of  $\sin^2 \theta$  for proton and iron primaries and WCD/SSD detectors.

iron showers being shallower (higher in the atmosphere) than proton showers, which would allow the electromagnetic component of the iron showers to develop more, potentially increasing the asymmetry induced from attenuation based effects (see Chapter 5). The reason we may not be observing this for the WCD is the stronger response to muons which show less asymmetry.

Having demonstrated the method of calculating signal asymmetry for a particular choice of energy bin and radius, along with gaining a basic understanding of the level of asymmetry to be expected from different primaries/detector types, we now move on to a full parameterisation for  $b$ .

#### 4.4 Parameterising WCD and SSD signal asymmetry

The parameterisation of the amplitude of the signal asymmetry,  $b$ , was performed in bins of  $\log(S(1000))$ ,  $\sin^2 \theta$  ( $\theta$ =zenith angle) and radius. Note for the sake of clarity

and ease of reading the standard notation to describe the signal at 1000 m,  $S(1000)$ , will be replaced with  $S_{1000}$  throughout the remainder of the chapter. The reason for choosing  $\log(S_{1000})$  was that it can be directly measured or inferred from SD data, whereas the estimate of the energy of a primary cosmic ray requires a calibration to be performed with the fluorescence detectors (see Section 3.2.4). The binning decided upon was

- 4 equally sized bins in  $\log(S_{1000})$  between  $1 \leq \log(S_{1000}) \leq 2.5$
- 7 equally sized bins in  $\sin^2 \theta$  between  $0 \leq \sin^2 \theta \leq 0.75$
- 16 equally sized bins in radius between  $450 \leq r/\text{m} \leq 2050$

To obtain enough statistics in each bin, approximately 3000 proton and 3000 iron showers ranging between  $18.5 \leq \log(E/\text{eV}) \leq 20$  in energy and  $0 - 60^\circ$  in zenith were simulated and reconstructed through Offline. To accommodate the number of radius bins required, the Offline simulation was made to contain a set of dense rings every 100 m from 500 m to 2000 m, with 12 tanks in each ring. The properties of this set of showers is summarised in Table 4.2.

Primaries	Proton, Iron
$\log(E/\text{eV})$	18.5 - 20, flat in $\log(E/\text{eV})$
$\theta/^\circ$	0-60, flat in $\sin^2 \theta$
$\phi/^\circ$	0 - 360, uniformly distributed
Had Int. Models	QGSJet-II.04

**Table 4.2:** Properties of the showers used for the parameterisation of  $b$ , the amplitude of the asymmetry. Approximately 3000 unique proton showers and 3000 unique iron showers were used.

The first step in determining a parameterisation for  $b$  was to produce the fundamental asymmetry plots for every bin of  $\log(S_{1000})$ ,  $\sin^2 \theta$  and radius, similar to those in Figure 4.3. One important note is that not every shower in a particular  $\log(S_{1000})$  and zenith bin would trigger all 12 tanks in every dense ring out to 2000 m. This was especially the case with lower energy showers. As done in the initial investigation, if a shower did not trigger all 12 tanks in a dense ring then the data from the tanks in the ring which were triggered was not used. For this reason, several bins were filled with little to no data. To avoid fitting to these cases, which may be biased towards only including showers with deeper  $X_{\max}$  values, a cut was applied. The cut was, for a bin of  $\log(S_{1000})$  and  $\sin^2 \theta$ , if a radius bin did not have 80% of all possible showers in that bin triggering all 12 tanks then it would not be fit to and thus not be used in the subsequent parameterisation of  $b$ .

The values and errors in  $b$  for each bin were then able to be plotted as functions of zenith or radius to see what kind of functional form would be needed for the

parameterisation. Fortunately, similar work had already been performed by another member of the Pierre Auger Collaboration, Quentin Luce. Luce has parameterised the asymmetry in the WCD in simulations, and used it to correct the estimate of the shower core location [82]. However at the time of writing the exact values of his parameterisation have not been published. As such, in this work we aim to provide an eventual cross check for his results as well as parameterise the asymmetry in the new scintillator detectors.

For Luce's parameterisation, he used the following function for the signal LDF

$$S(r, \zeta) = S_{1000} f_{\text{LDF}}[1 + b(r, \theta, \log(S_{1000})) \cos \zeta] \quad (4.2)$$

to describe the signal measured in the shower plane at some radius,  $r$ , and azimuth,  $\zeta$ . We can see this is identical to the regular LDF but with the addition of a  $(1 + b(r, \theta, \log(S_{1000})) \cos \zeta)$  term. It is the function  $b(r, \theta, \log(S_{1000}))$  which we must parameterise. The form used by Luce was

$$b(r, \theta, \log(S_{1000})) = k(\theta, \log(S_{1000})) \operatorname{erf}\left(\frac{r}{r_0(\theta, \log(S_{1000}))}\right) \quad (4.3)$$

where

$$k(\theta, \log(S_{1000})) = \frac{k_0 + k_1 \sin^2 \theta}{1 + \exp\left(-\frac{\sin^2 \theta - k_2(\log(S_{1000}))}{k_3(\log(S_{1000}))}\right)} \quad (4.4)$$

and

$$r_0(\theta, \log(S_{1000})) = r_1(\log(S_{1000})) + r_2(\log(S_{1000})) \sin^4 \theta \quad (4.5)$$

Note the parameters  $k_2, k_3, r_1$  and  $r_2$  are all functions of  $\log(S_{1000})$ . To see where this functional form comes from, consider Figure 4.5, which shows the asymmetry amplitude of the SSD plotted as a function of  $\sin^2 \theta$  for  $r = 1000$  m and for different bins of  $\log(S_{1000})$ . The functional form of  $k(\theta, \log(S_{1000}))$  has been fit to each set of points, with each of the  $k_i$  parameters freely fit. The shape and magnitude of each series of points is similar to what we observed in Figure 4.4, and the functional form appears to fit quite well, capturing the initial increase at low zenith angles as well as the turnover at larger zenith angles. Moreover, the turnover point of the function seems to shift to the right with energy, giving some justification for the parameters of the fit to be energy dependent.

The necessity of the  $r_0(\theta, \log(S_{1000}))$  part of the parameterisation for  $b$  can be seen when  $b$  is plotted against radius for different bins of  $\sin^2 \theta$ . An example is shown in Figure 4.6 for the energy range  $2.125 \leq \log(S_{1000}/\text{MIP}) \leq 2.5$ . Here we have fit the function

$$k_0 \operatorname{erf}\left(\frac{x}{r_1}\right) \quad (4.6)$$

with free parameters  $k_0$ , which acts like  $k(\theta, \log(S_{1000}))$ , and  $r_1$ . The value of  $k_0$

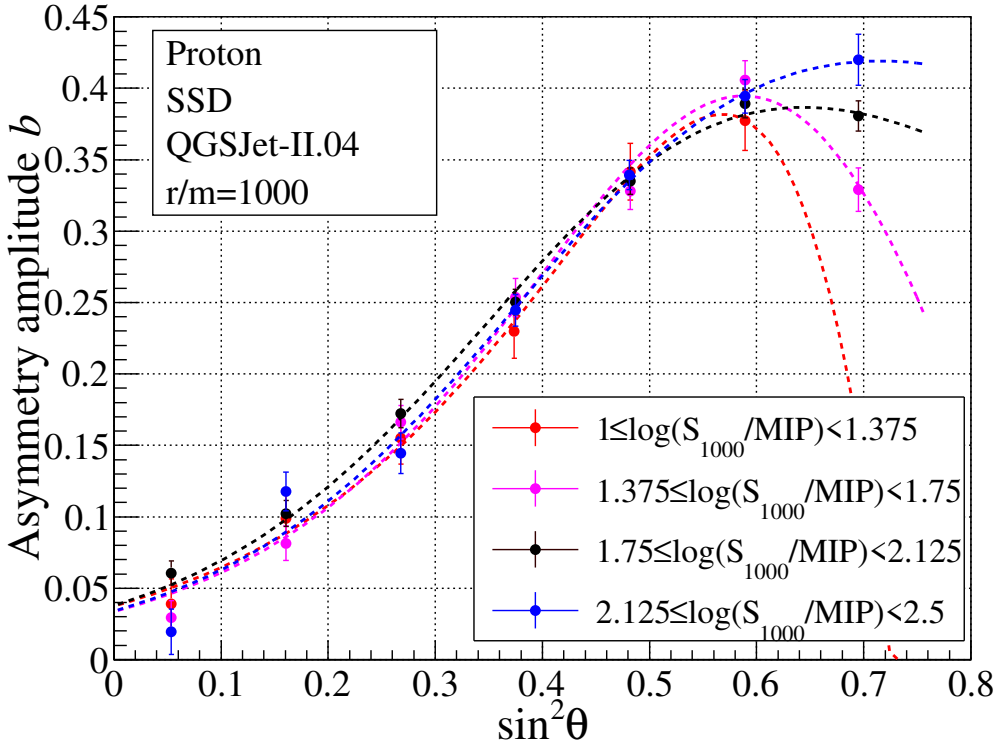


**Figure 4.5:** The SSD asymmetry amplitude,  $b$ , plotted as a function of  $\sin^2 \theta$  for the different energy bins. The function  $k(\theta, \log(S_{1000}))$  has been fit to each set of data points, with the color of the fit set to the same color as the corresponding data.

naturally increases with zenith. Also note how the flattening off point, which is dependent on  $r_1$ , decreases with zenith angle. This is the reason for including the  $r_2(\log(S_{1000})) \sin^4 \theta$  term in  $r_0(\theta, \log(S_{1000}))$ .

Finally, we can consider how the shape of the radial profile of  $b$  varies with energy. The example shown in Figure 4.7 is for the zenith angle range  $0.43 \leq \sin^2 \theta \leq 0.54$ . Overall, there does not appear to be any clear differences between each set of data points. Also notice the aforementioned lack of data points in the lower energy bins for some of the larger radii. Despite this, the  $r_1$  and  $r_2$  parameters will still be allowed to vary with  $\log(S_{1000})$  in order to get the best overall fit for each  $\log(S_{1000})$  bin.

After this analysis and some further testing, some slight modifications to Equation 4.3 were made in order to simplify the fitting process. The function we used to parameterise the asymmetry is identical to Equation 4.3 but with

$$k(\theta, \log(S_{1000})) = \frac{k_0(\log(S_{1000}))(1 - \sin^2 \theta)}{1 + \exp\left(-\frac{\sin^2 \theta - k_2(\log(S_{1000}))}{k_3(\log(S_{1000}))}\right)} \quad (4.7)$$

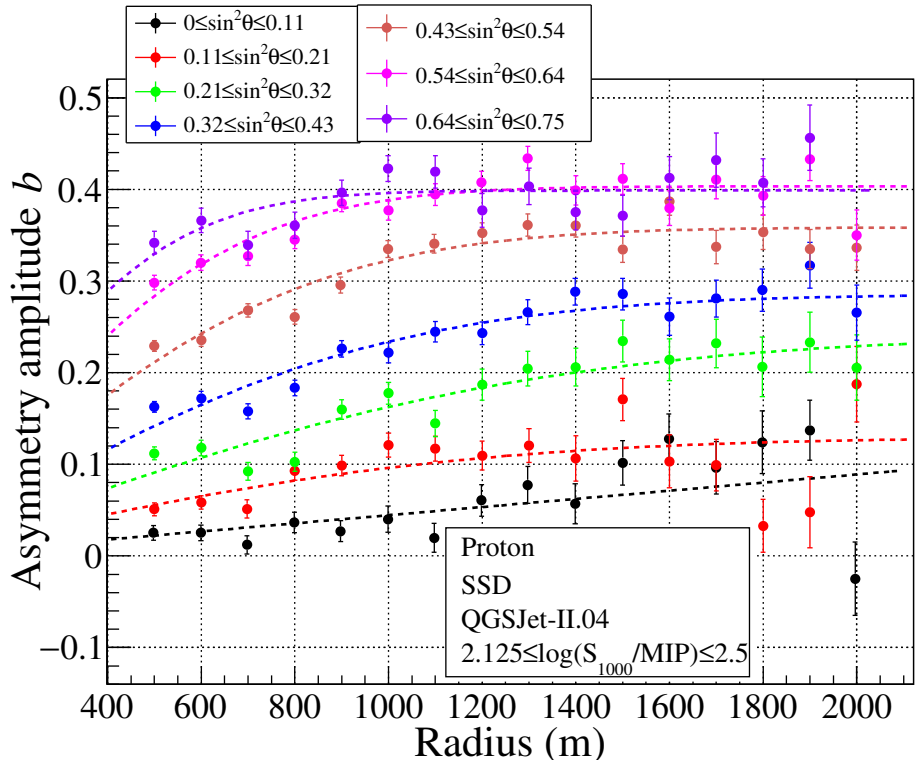


**Figure 4.6:** The SSD asymmetry amplitude  $b$  plotted as a function of radius for the different zenith angle bins.

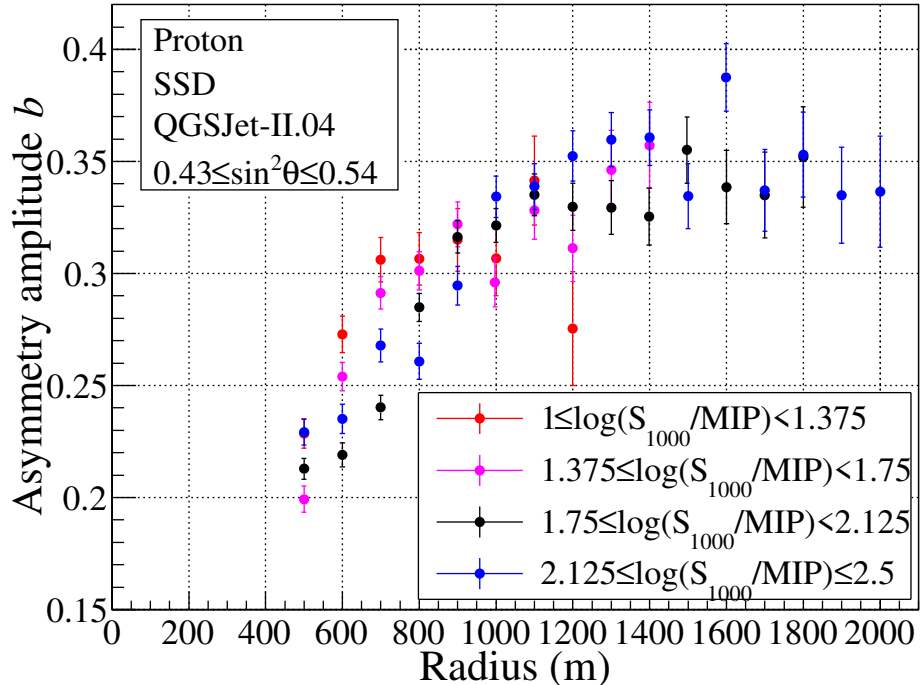


**Figure 4.7:** The SSD asymmetry amplitude  $b$  plotted as a function of radius for the different  $\log(S_{1000})$  bins. No clear difference is seen between each set of points.

These changes were made because allowing  $k_0$  to vary with energy improved the overall fits and  $k_1$  was found to be very close to the negative of  $k_0$ . From here, the values of  $b$  for each energy bin were plotted as a function of  $\sin^2 \theta$  and radius in a 3 dimensional graph. An example is shown in Figure 4.8. This example is for proton primaries in the energy bin  $2.125 \leq \log(S_{1000}) \leq 2.5$  for the SSD. The points are coloured such that the white/black points represent the points which lie above/below the fitted surface respectively. Having analysed the 2D projections of such a graph it is clear to see how the surface combines the changes in shape of  $b$  with  $\sin^2 \theta$  and radius. The residuals of the fit to the data are shown using a histogram in Figure 4.9. Considering the empirical nature of the function, the mean and RMS of this distribution is quite good. However, for other choices of detector and primary (WCD/iron), these residual distributions have larger RMS values. Upon inspection of all the fits performed, it was found that, for the WCD, there was tendency for the fits to overestimate/underestimate the data at low/high radii, indicating that the functional form may not have been entirely correct. This issue wasn't as obvious for the SSD fits however, signalling that the errors on the asymmetry amplitudes may have been too small. It is likely a combination of these effects causing the wide residual distributions. The residual distributions for each primary and detector type can be found in Appendix A.

After fitting 2D surfaces to each energy bin, as in Figure 4.8, the parameters of the fit were extracted and plotted as a function of  $\log(S_{1000})$  (taking the middle of each bin of  $\log(S_{1000})$ ). The results for proton and iron showers as detected by the SSD are shown in Figures 4.10 and 4.11 respectively. The equivalent WCD results can be found in Appendix A. Polynomial functions of the form  $a + bx + cx^2$  have been fit to each parameter plot, with the choice of degree dependent on the shape of the graphs. Despite the seemingly curved nature of some of these plots, using a quadratic fit was generally avoided as it would have over-fitted the data. Only the  $r_1$  and  $r_2$  parameters of the iron WCD parameterisation utilised a quadratic fit.

Special mention must be made regarding Figure 4.11, the parameterisation of the iron SSD fit parameters. The best possible fit parameter values are those shown in black. Taking these as correct however would have implied the shape of the data for each parameter to be noticeably different to both the proton SSD fits and those for the proton/iron WCD parameterisations. We didn't believe this should be the case. Thus, before fitting, we decided to manually fix the value and error of the  $r_2$  parameter in the third  $\log(S_{1000})$  bin to values more consistent with the other parameterisations. The  $r_2$  value chosen was -1000, with an error of 80 (similar error bar to the other points in the graph). This had the effect of forcing the other parameters to shift in a direction consistent with the shape of the data in the other parameterisations. This implies there are probably compensating/degenerate effects between the parameters, one aspect which should be improved upon in future, more robust parameterisations. To obtain our final parameterisation of the iron SSD

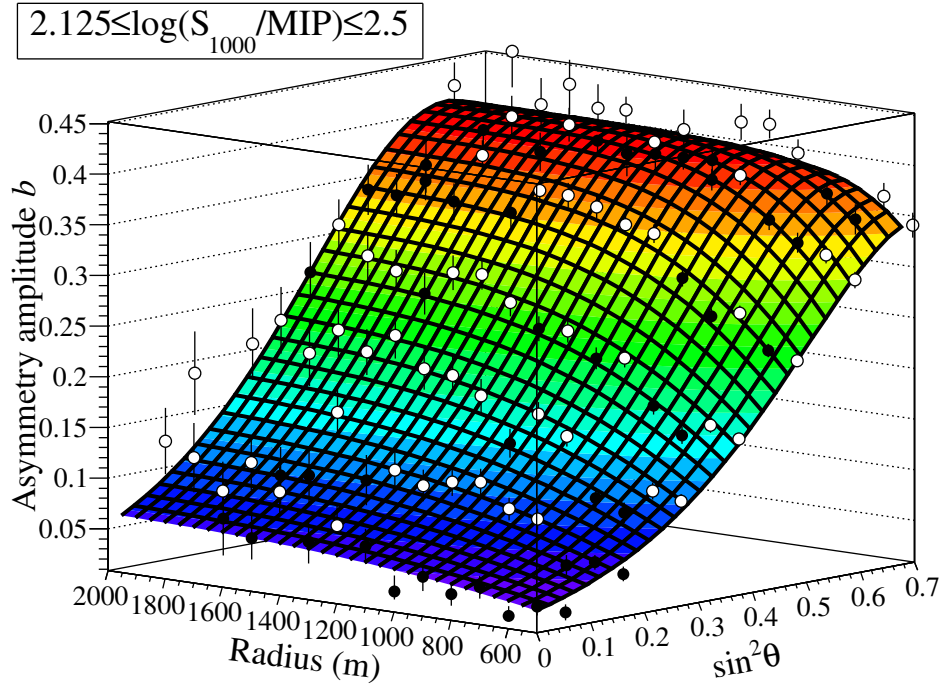


**Figure 4.8:** An example of a surface fit to the proton SSD asymmetry amplitude data in the  $\log(S_{1000})$  bin  $2.125 \leq \log(S_{1000}) \leq 2.5$ , plotted as a function of radius and  $\sin^2 \theta$ . Black points lie below the fit, white points lie above it.

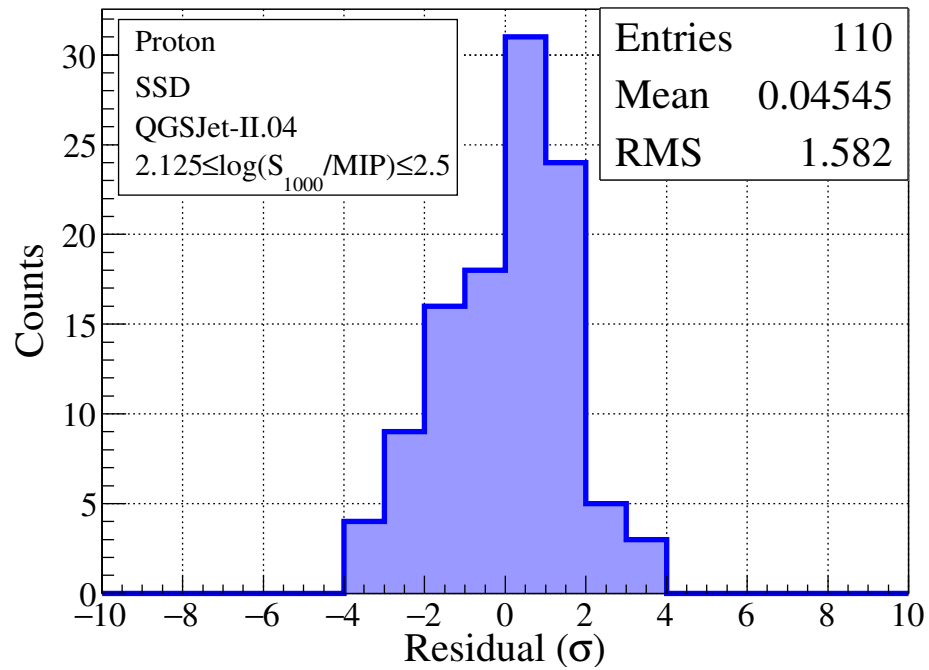


**Figure 4.9:** The residuals, in terms of  $\sigma$ , for the data and fit in Figure 4.8.

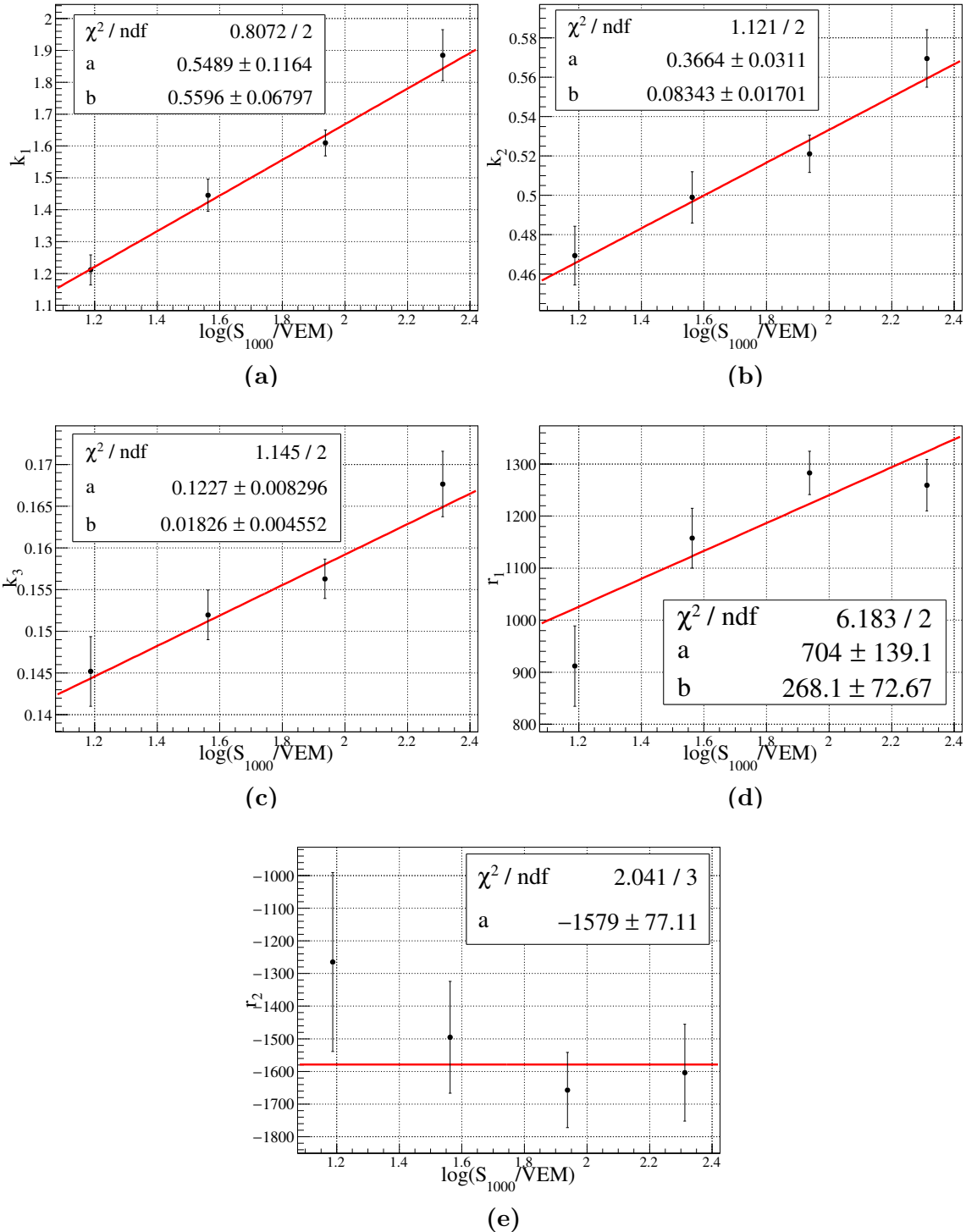


**Figure 4.10:** Parameterisations of the parameters of the function  $b(r, \theta, \log(S_{1000}))$  for proton showers as measured by the SSD.

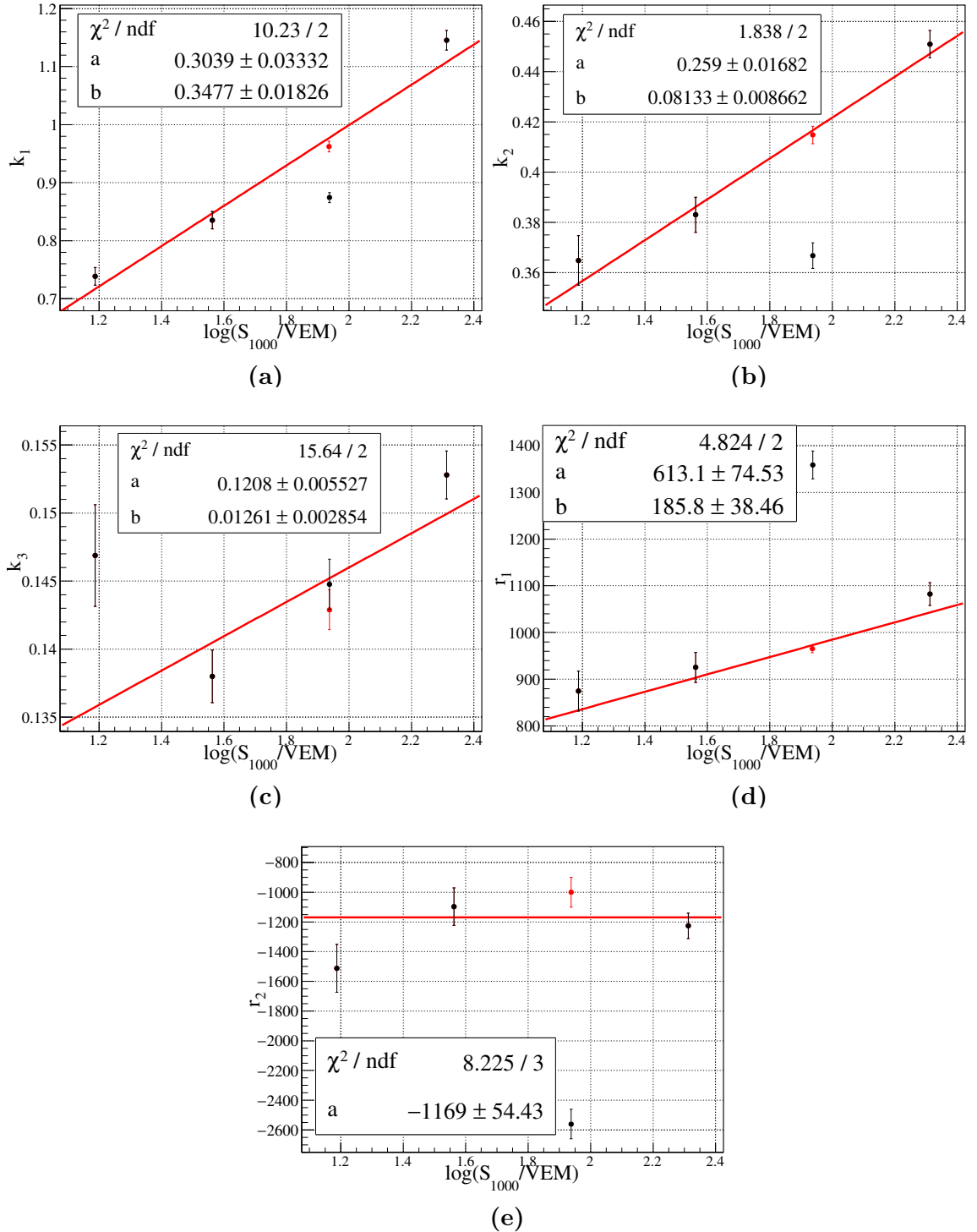


**Figure 4.11:** Parameterisations of the parameters of the function  $b(r, \theta, \log(S_{1000}))$  for iron showers as measured by the SSD. The points fit to are the 1st, 2nd and 4th black points, and the single red point. See the text for explanation.

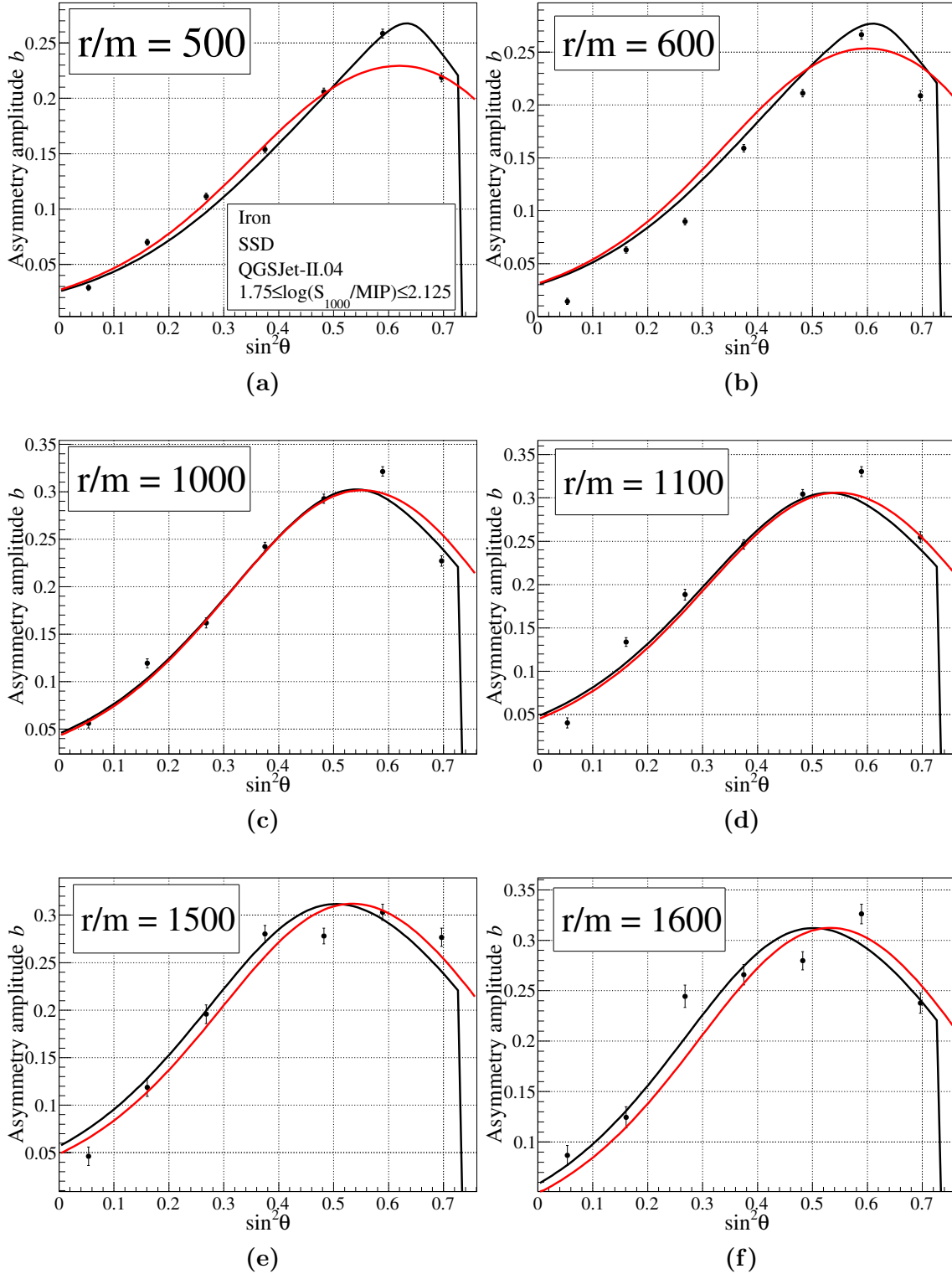


**Figure 4.12:** Plots comparing the best possible fit (black) and the manually adjusted fit (red) to the iron SSD asymmetry amplitude data. The comparisons are made for different radial bins, namely 500, 600, 1000, 1100, 1500 and 1600 m.

parameters, we fitted to the data shown excluding the black point in the third  $\log(S_{1000})$  bin.

To compare how different the fit results were using the best possible black point or the adjusted red point, several radial slices were taken from the corresponding  $\log(S_{1000})$  plot and the  $b$  values plotted as a function of  $\sin^2 \theta$ . The two possible fits have been overlayed and the results are shown in Figure 4.12. The black line is the best fit to the data and the red fit is the adjusted fit. We can see that at early radii the best possible fit captures the larger value at  $\sin^2 \theta \approx 0.59$ . Around 1000 m the two fits are very similar. Further out there seems to be a systematic shift of the red fit to the right. Overall though, these differences are quite small and the red line captures much of the same behaviour and to similar accuracy around the distance which is often of interest, 1000 m. Therefore, we feel reasonably confident that manually adjusting the fit, allowing us to get a reasonable parameterisation, was a valid decision.

Tables 4.3, 4.4, 4.5 and 4.6 show our final results for the parameters which make up the parameterisation of the asymmetry amplitude for the proton SSD/WCD and iron SSD/WCD respectively.

Parameter	a	b	c	$\chi^2/\text{NDF}$
k1	$0.5 \pm 0.1$	$0.56 \pm 0.07$	0	0.4
k2	$0.37 \pm 0.03$	$0.08 \pm 0.02$	0	0.56
k3	$0.123 \pm 0.008$	$0.018 \pm 0.005$	0	0.57
r1	$700 \pm 100$	$270 \pm 70$	0	3.0915
r2	$-1580 \pm 80$	0	0	0.68

**Table 4.3:** Table of the parameterisations for the fit parameters of  $b$  as a function of  $\log(S_{1000})$  for proton showers detected by the SSD.

Parameter	a	b	c	$\chi^2/\text{NDF}$
k1	$0.27 \pm 0.03$	$0.25 \pm 0.02$	0	0.84
k2	$0.25 \pm 0.02$	$0.10 \pm 0.01$	0	0.96
k3	$0.096 \pm 0.007$	$0.029 \pm 0.004$	0	2.3
r1	$700 \pm 100$	$150 \pm 50$	0	0.25
r2	$-1400 \pm 400$	$-300 \pm 200$	0	0.042

**Table 4.4:** Table of the parameterisations for the fit parameters of  $b$  as a function of  $\log(S_{1000})$  for proton showers detected by the WCD.

Parameter	a	b	c	$\chi^2/\text{NDF}$
k1	$0.30 \pm 0.03$	$0.35 \pm 0.02$	0	5.1
k2	$0.26 \pm 0.02$	$0.081 \pm 0.009$	0	0.92
k3	$0.121 \pm 0.006$	$0.013 \pm 0.003$	0	7.8
r1	$610 \pm 80$	$190 \pm 40$	0	2.4
r2	$-1170 \pm 50$	0	0	2.7

**Table 4.5:** Table of the parameterisations for the fit parameters of  $b$  as a function of  $\log(S_{1000})$  for iron showers detected by the SSD.

Parameter	a	b	c	$\chi^2/\text{NDF}$
k1	$0.195 \pm 0.009$	$0.132 \pm 0.005$	0	12
k2	$0.17 \pm 0.01$	$0.096 \pm 0.005$	0	0.79
k3	$0.098 \pm 0.005$	$0.021 \pm 0.003$	0	1.5
r1	$3000 \pm 300$	$-2600 \pm 300$	$700 \pm 90$	2.009
r2	$-6000 \pm 2000$	$5000 \pm 2000$	$-1400 \pm 500$	0.2899

**Table 4.6:** Table of the parameterisations for the fit parameters of  $b$  as a function of  $\log(S_{1000})$  for iron showers detected by the WCD.

## 4.5 Finding the maximum difference between the asymmetry parameterisations

We conclude this chapter by using the parameterisations from the previous section to find the phase space in which the difference in the amplitude of the asymmetry between proton and iron primaries (for both detector types) is a maximum. The reason for doing this is that, if these parameterisations match reality, then measuring the asymmetry in cosmic ray air showers in this phase space may allow us to distinguish whether the primaries being detected are lighter (proton-like) or heavier (iron-like). Unfortunately, additional work by Luce has shown that the asymmetry in real WCD signals is significantly less than that measured in simulations [83]. This doesn't necessarily mean the phase space which maximises the difference in asymmetry between proton and iron signals measured by the WCD is different for real data, nor that the magnitude of the asymmetry in the SSD is different in simulations than it is in reality. However it is far beyond the scope of this work to formally check these points. For this reason, we will simply present our findings for data derived from simulations, in the hope that either the results or the principle behind them can be utilised in future studies.

The simplest solution to the task was to use the inbuilt functionality of the analysis software ROOT to find the values of  $\log(S_{1000})$ ,  $\sin^2\theta$  and radius which maximised/minimised the difference between the 3 dimensional functions describing the amplitude of the asymmetry for proton,  $b_p$ , and iron,  $b_i$ . The results for both the

WCD and SSD are given in Table 4.7 below. The values of  $b_p$  for the given phase space values are shown for reference.

Detector (Min/Max)	$b_p - b_i$	$b_p$	$\log(S_{1000})$	$\sin^2\theta$	Radius (m)
WCD (Minimum)	-0.019	0.086	1.9	0.29	500
WCD (Maximum)	0.065	0.21	2.0	0.65	1500
SSD (Minimum)	-0.019	0.14	2.0	0.32	620
SSD (Maximum)	0.11	0.36	1.7	0.69	1900

**Table 4.7:** Table of the maximum/minimum values of the difference between the proton and iron asymmetry parameterisations ( $b_p - b_i$ ) and the phase space values where they occur. The values of  $b_p$  are shown for reference.

In terms of magnitude, the largest difference occurs in the SSD, where proton showers with  $S_{1000}=56$  MIP,  $\theta=56^\circ$  and radius = 1900 m have an asymmetry amplitude  $\approx 0.11$  greater than iron showers in the same phase space. The minimum value of  $b_p - b_i$  for the SSD is -0.19 and occurs at  $S_{1000}=100$  MIP,  $\theta = 34^\circ$  and radius = 600 m. In this region iron showers have an asymmetry amplitude slightly larger than proton showers. Probing the phase space associated with the maximum difference for the SSD may be difficult in reality, due to a possible lack of triggered stations at the large radial distance required. This is demonstrated by our parameterisations not having a data point at 1900 m for  $\log(S_{1000}) < 2.125$ . Restricting the search space for the maximum value to within  $r \leq 1500$  m yields identical results when rounded to 2 significant figures, with the maximum occurring at 1500 m. This seems to suggest the maximum difference does not depend significantly on the radius, only on the zenith angle and  $\log(S_{1000})$ .

The maximum value for the WCD shows proton showers have an asymmetry amplitude  $\approx 0.65$  greater than iron showers in the phase space corresponding to  $S_{1000} = 100$  VEM,  $\theta = 54^\circ$  and radius = 1500 m. This region is within the range of the data used to create the parameterisations. The minimum value of  $b_p - b_i$  for the WCD and the phase space in which it occurs is very similar to the SSD. Additionally, we see that our initial findings in Section 4.3 are reaffirmed, in that the maximum difference between proton and iron is occurring at large zenith angles. This may be due to the different  $X_{\max}$  distributions of either primary and how these affect the electromagnetic component of the showers (the main contributing factor to asymmetry) which reach ground at these zenith angles.

All that being said, for the array spacing of Auger, it would be ideal to have the maximum difference occurring close to 1000 m. Hence we found the maximum value of the difference between the proton and iron parameterisations at this distance. The results are given in Table 4.8. We see that, rounded to 2 significant figures, the results for the maximum are the same, with identical phase space values. This further supports our initial hypothesis that the difference in asymmetry, at least at large zenith angles and values of  $S_{1000}$ , is largely independent of the radius.

Detector	$b_p - b_i$	$b_p$	$\log(S_{1000})$	$\sin^2\theta$
WCD (Maximum)	0.065	0.21	2.0	0.65
SSD (Maximum)	0.11	0.36	1.7	0.69

**Table 4.8:** Table of the maximum values of the difference between the proton and iron asymmetry parameterisations at 1000 m, with the phase space values of  $\log(S_{1000})$  and  $\sin^2\theta$  where they occur.

To check this point, we have plotted the difference between the proton and iron parameterisations as a function of energy and radius for  $\sin^2\theta=0.65$  for the WCD, and  $\sin^2\theta=0.69$  for the SSD. The results are shown as 2D histograms in Figure 4.13. We observe that, for the WCD at this particular value of  $\sin^2\theta$ , the difference does not depend on radius, and only slightly on  $\log(S_{1000})$ , as indicated by the small range of values in the color bar. For the SSD the result is largely the same, however at larger values of  $\log(S_{1000})$  we do begin to see a non-trivial dependence on radius. We have also plotted the difference between the parameterisations as a function of zenith and energy for  $r=1000$  m, to visualise which of the two variables affects the difference the most. The resulting histograms are shown in Figure 4.14. For both the WCD and SSD, changing the zenith angle yields the largest change in the difference. Also note the difference in the  $\sin^2\theta$  values at which the WCD/SSD difference switches from negative to positive, around 0.25 and 0.35 respectively. There is a slight dependence on  $\log(S_{1000})$  however, which may support our theory about the differing  $X_{\max}$  distributions of the primaries causing the iron asymmetry to be larger at lower zenith angles.

In summary, the regions of phase space we suggest using to attempt to distinguish ensembles of showers as proton/iron-like with asymmetry alone are high zenith angle showers ( $> 50^\circ$ ) with values of  $S_{1000}$  around 50 MIP ( $\approx 2 \times 10^{19}$  eV) for the SSD and 100 VEM ( $\approx 3 \times 10^{19}$  eV) for the WCD. From the WCD parameterisations, the expected values of the asymmetry amplitude at the point of maximum difference for an ensemble of proton showers is 0.21, whilst for iron showers it is 0.14. For the SSD parameterisations, the expected asymmetry amplitudes are 0.35 for proton and 0.24 for iron. Note once again these values are for simulations - the differences in real data will likely be smaller and harder to measure precisely due to the lack of dense rings. The regions of phase space corresponding to the maximum difference in asymmetry may also be different. Future investigations should focus on understanding the difference between the asymmetry in simulated and real data, and seeing whether the knowledge gained from simulations can be applied to reality to assist in determining the mass composition of cosmic rays.

## 4.6 Conclusions

In this chapter we have successfully parameterised the asymmetry in the water Cherenkov and scintillator detectors of the Pierre Auger Observatory in simulations. The parameterisations were performed on proton and iron showers with the ultimate goal of determining if there was an exploitable difference between the two.

The amplitude of the asymmetry was found to be higher in the SSD than the WCD for both primaries, a result believed to be caused by the equal sensitivity of the scintillator to air shower particles, compared to the WCD bias towards muons. The maximum difference between the proton and iron parameterisations was found to be at very large zenith angles, above  $50^\circ$ , and not depend heavily on radius. At 1000 m, a convenient distance based on the size of the Auger ground array, results showed a maximum difference for the WCD occurring for values of  $S_{1000} \approx 100$  VEM and  $\theta \approx 54^\circ$  (corresponding to an energy  $\approx 3 \times 10^{19}$  eV), with the asymmetry amplitude being 0.14 for iron and 0.21 for proton. For the SSD, the maximum difference in asymmetry was found to be in the phase space  $S_{1000} \approx 56$  MIP and  $\theta \approx 56^\circ$  (roughly translating to an energy of  $2 \times 10^{19}$  eV), with the asymmetry amplitudes of iron/proton being 0.24/0.35 respectively. Furthermore, at this radius, the parameterisations showed the amplitude of the asymmetry in proton showers to be greater than in iron showers for zenith angles above  $\sim 30^\circ$  for the WCD and  $\sim 35^\circ$  for the SSD.

With simulations and the accuracy of dense ring measurements, one could certainly distinguish an ensemble of proton showers from an ensemble of iron showers at this radial distance based on the asymmetry amplitude. It may also be possible to distinguish individual showers as proton/iron, though this would need to be formally checked. As for whether determining mass composition using asymmetry alone is feasible with real data, and indeed whether the phase spaces of maximum difference are the same, remains to be seen. Based on this study's results, we believe it would not be possible to determine the primary of real, individual shower using this technique. The relatively low number of tanks in a real event compared to using dense rings as well as signal fluctuations mean it is unlikely any adequate level of precision in  $b$  could be obtained. However, with averages of showers in bins of  $\log(S_{1000})$  and  $\theta$  it may be possible to achieve decent precision in the mean value of  $b$ . The challenge then would be to interpret the result, especially in the likely event of mixed composition. This will be made even more difficult due to the difference in asymmetry Luce has shown is present between simulations and reality.

We hope the results of these parameterisations can be used as a cross check for future work and be improved upon. Beyond a simple comparison of the asymmetry amplitude to determine mass composition, the parameterisations have the potential to be used for correcting the core location (as done by Luce [82]) or correcting the signals in detectors to be the average value as would be measured by a dense ring

in simulations. This would improve LDF fits which could impact many different studies performed with the surface detector, including attempts to determine mass composition (see Chapter 7). Seeing whether the same patterns which have been found here hold in real data, and whether they are a viable method of determining mass composition, is a recommendation for future studies.

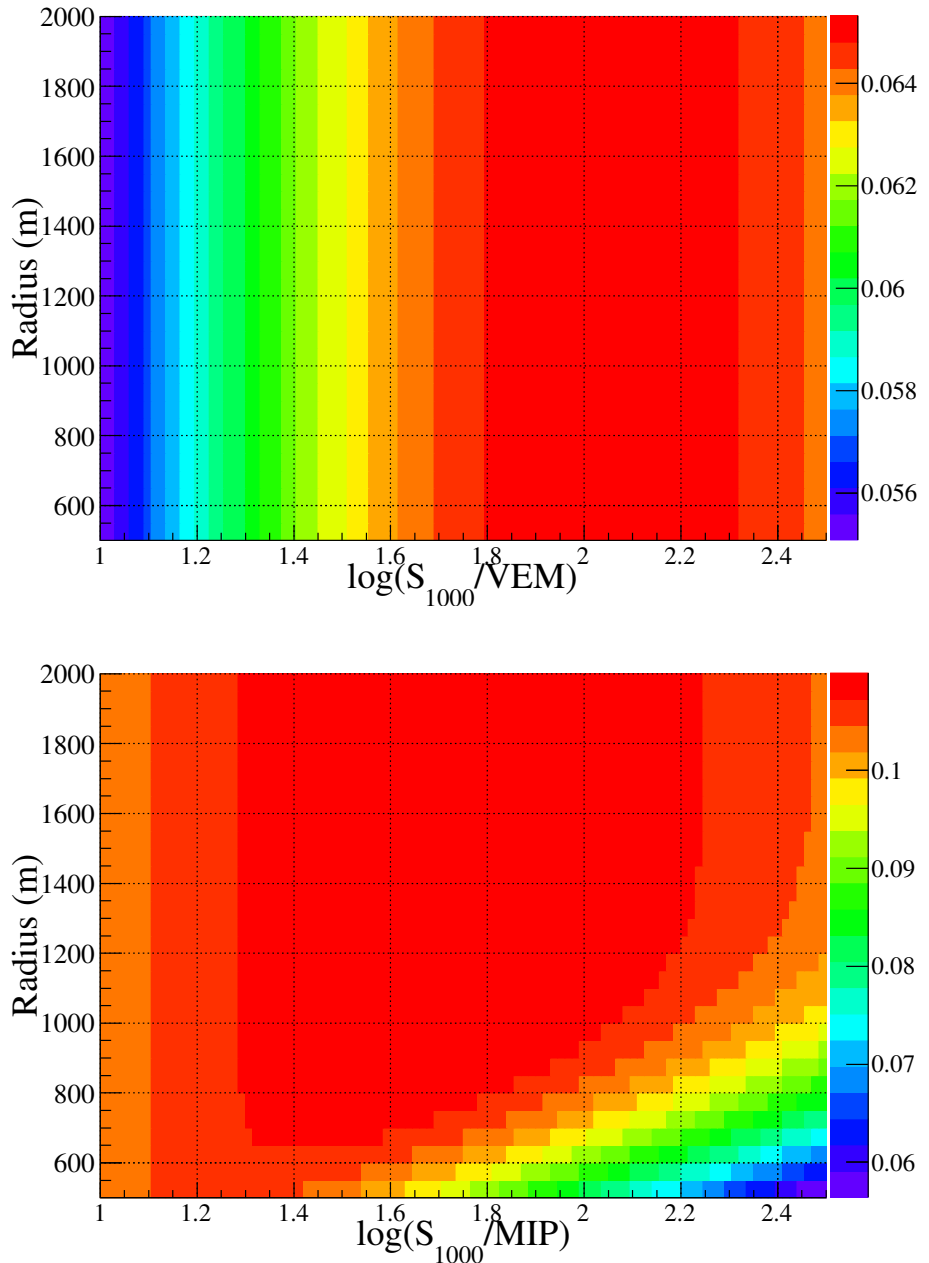


**Figure 4.13:** 2D histograms of the difference between the proton and iron parameterisations, evaluated at  $\sin^2 \theta=0.65$  for the WCD (top) and  $\sin^2 \theta=0.69$  for the SSD (bottom). The color bar or  $z$ -axis represents the difference (proton-iron). In the top plot we see that, for this zenith angle, the difference in asymmetry amplitude is rather independent of both radius and  $\log(S_{1000})$  (note the range of the color bar).

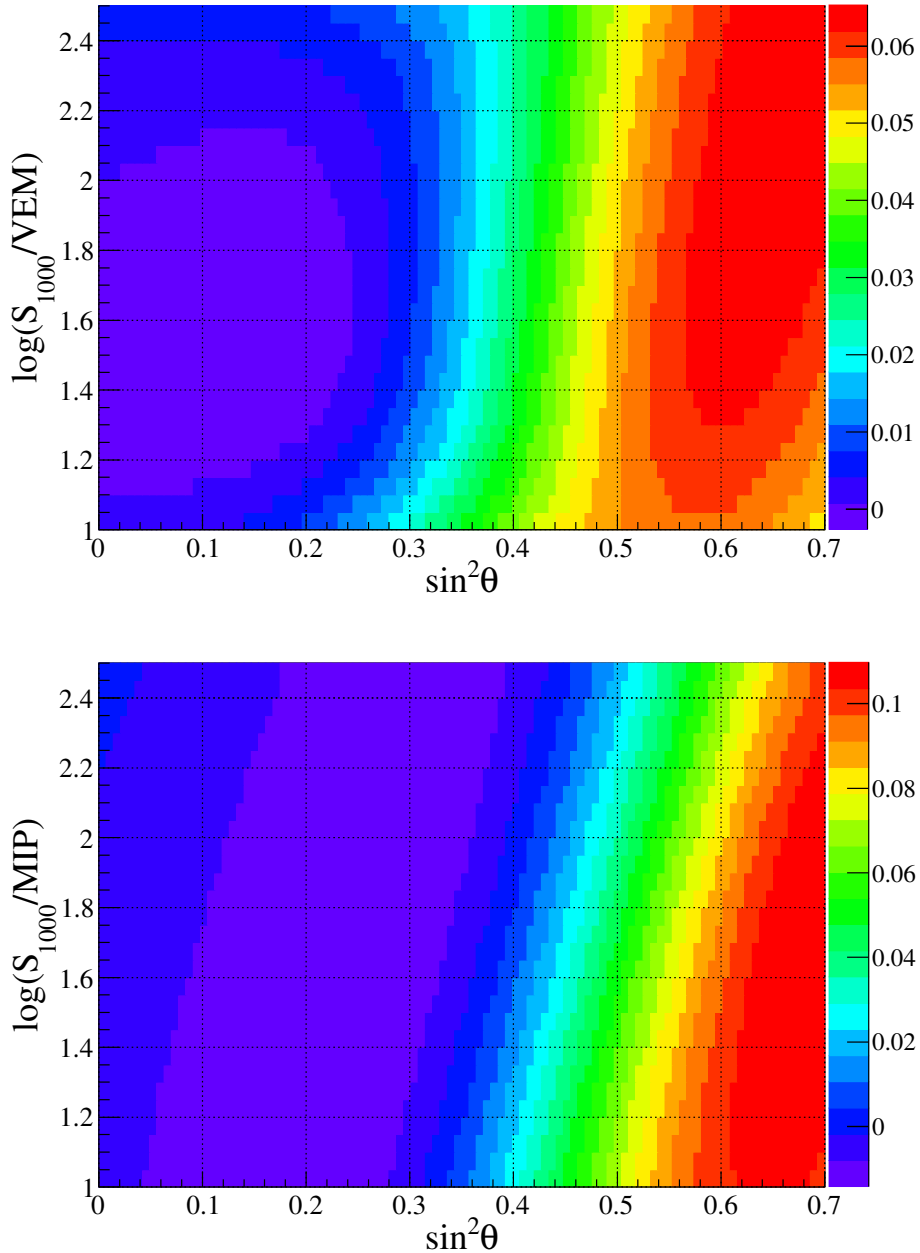


**Figure 4.14:** 2D histograms of the difference between the proton and iron parameterisations, evaluated at a constant radius  $r=1000$  m. The WCD result is shown in the top panel, the SSD result in the bottom panel. The color bar or  $z$ -axis represents the difference (proton-iron).

---

# Causes of asymmetry in particle density

---

In Chapter 4 the amplitude of the signal asymmetry in both the water Cherenkov and scintillator detectors of the Pierre Auger Observatory was parameterised. A clear difference was found between the two detectors, with the scintillator having a larger asymmetry. Additionally, both detectors measured greater asymmetry in proton showers than iron showers at larger zenith angles. The goal of this chapter is to better understand this result. Specifically, we would like to know what factors contribute to asymmetry and how, if at all, the relative contributions differ between proton and iron primaries. If this can be understood, then perhaps a method of determining the mass composition from asymmetry information can be found. Whilst the previous chapter investigated the asymmetry in measured signals, this chapter will focus on the asymmetry in pure particle numbers/particle density. This decision was made to eliminate the response of a detector as a possible source of asymmetry, thus helping to differentiate between other causes. Note that asymmetry effects related to how particles impinge on a particular detector shape (i.e. the “detector response”) will not be addressed in this thesis. See [84] for more information.

To begin, a co-ordinate system which can be used as a reference throughout the remainder of the chapter will be outlined.

## 5.1 Co-ordinate system

When analysing the geometry of an air shower there are two frames of reference to consider, the ground frame and the shower frame. Both frames share the same origin, namely the shower core. Using CORSIKA conventions, the ground frame has co-ordinates  $(x, y, z)$  where the positive  $x$  axis points in the direction of magnetic north and the positive  $y$  axis points west. Positive  $z$  is upwards. For simplicity we will assume all showers come from the positive  $x$ -direction. The shower frame is given co-ordinates  $(x', y', z')$  and is simply a rotation of the ground frame by the inclination of the shower,  $\theta$ , in the clockwise direction. Thus the  $z'$  axis points upwards along the shower axis and the  $x'$  and  $y'$  axes form the shower plane. Points in the shower plane will also be referred to in polar coordinates, where  $r$  is the distance from the core and

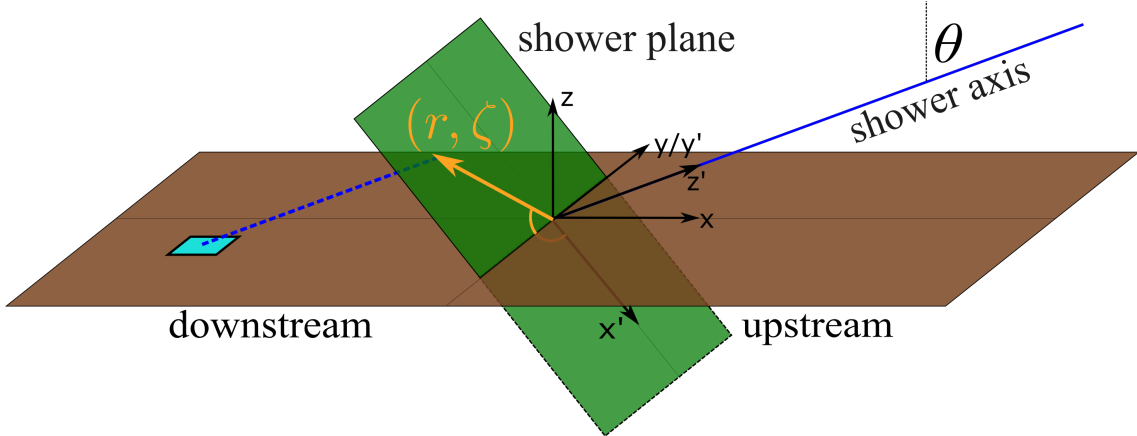


**Figure 5.1:** A schematic of the coordinate system which will be used throughout the remainder of the chapter. As an example, the position of the light blue square has been projected into the shower plane along the direction of the shower axis. Its shower plane coordinates are given by  $r$  and  $\zeta$ , shown on the diagram.

$\zeta$  the azimuthal angle ranging from  $0$  to  $\pm 180^\circ$ . Zero degrees is defined to be beneath the shower axis. Lastly, the ground region corresponding to positive/negative  $x$  values is the *upstream/downstream* region respectively. A diagram of the co-ordinate system is shown in Figure 5.1.

## 5.2 Sources of asymmetry

For a truly vertical shower,  $\theta = 0^\circ$ , the ground frame and shower frame are identical. Thus by symmetry (about the shower axis), we expect equal particle density contours on the ground to be circles centred on the shower core. Minor deviations from this arise due to the deflection of muons by the geomagnetic field and shower to shower fluctuations. However, these effects are minor and we generally refer to a shower with  $\theta = 0^\circ$  as having no asymmetry.

For showers with zenith angles  $> 0^\circ$ , one might expect the equal particle density contours on the ground to be ellipses, again with the shower core as the centre. This is in fact not quite true, as, whilst the contours are elliptical, their centres are shifted in the upstream direction, towards where the shower came from. Thus if these elliptical contours were to be projected into the shower plane along the direction of the shower axis, the resulting circular contours would be offset towards the positive  $x'$  direction. This phenomenon is what we call asymmetry. Examples of the equal particle density contours *on the ground* for a vertical and inclined shower are shown in Figure 5.2. The change in shape and systematic shift upstream for all contours in the inclined shower is clear, with the effect being greatest for the contours furthest from the core, corresponding to lower densities. The common belief is that there are two main causes for this observed shift (asymmetry in particle density);

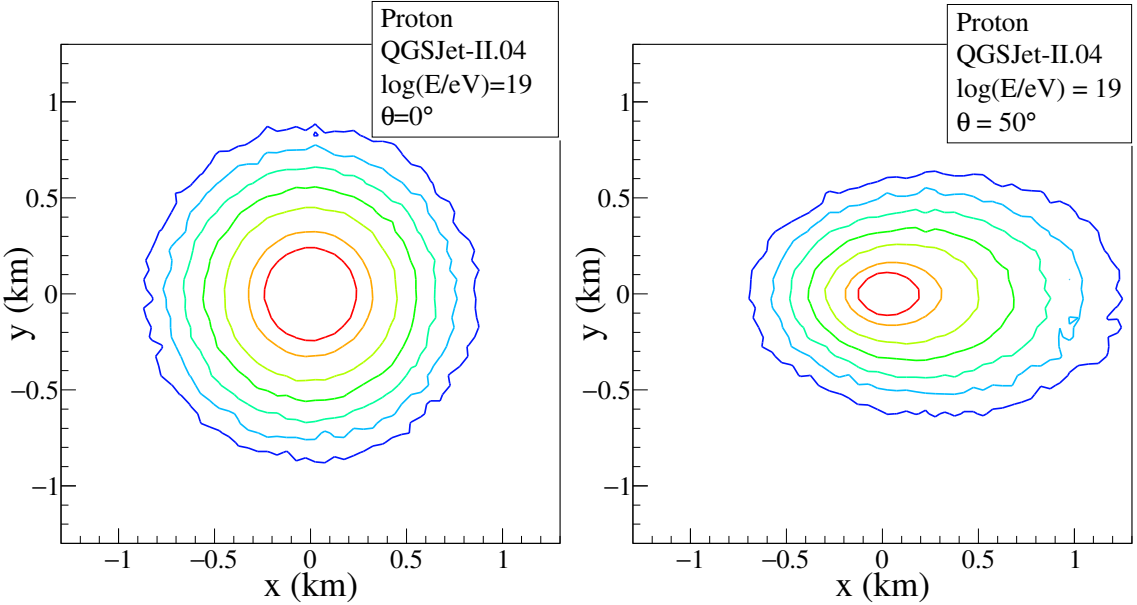


**Figure 5.2:** Contours of equal particle density on the ground for a simulated  $0^\circ$  (left) and  $50^\circ$  (right) proton shower, both with energy  $10^{19}$  eV. The contour levels are identical for both showers. The simulations were performed with CORSIKA with the geomagnetic field on. The inclined shower was made to arrive from magnetic north i.e. the positive  $x$  direction ( $\phi=0$ ).

1. Geometrical effects related to the inclination of the shower
2. Attenuation of air shower particles

How these two factors contribute to asymmetry will now be described.

### 5.2.1 Geometrical effects

When trying to understand the geometrical causes of asymmetry it is necessary to envision a geometrical model which approximates the shape and propagation of an air shower. This allows one to consider the trajectories of air shower particles and their subsequent contact point with the ground in a simple way. Ultimately, it is the act of rotating what we assume to be an axis-symmetric shower which gives rise to the geometrical effects causing asymmetry. This is demonstrated in the following examples where the difference in density between two regions on the ground at the same distance from the shower core is determined.

For an axis-symmetric or cylindrical shower geometry, where particles are symmetric about the shower axis and the size of the shower front remains constant, one can assume that particles effectively travel parallel to the shower axis. This assumption is only valid for showers at a point of development well past the shower maximum. Schematics of this model for a vertical and inclined shower are shown

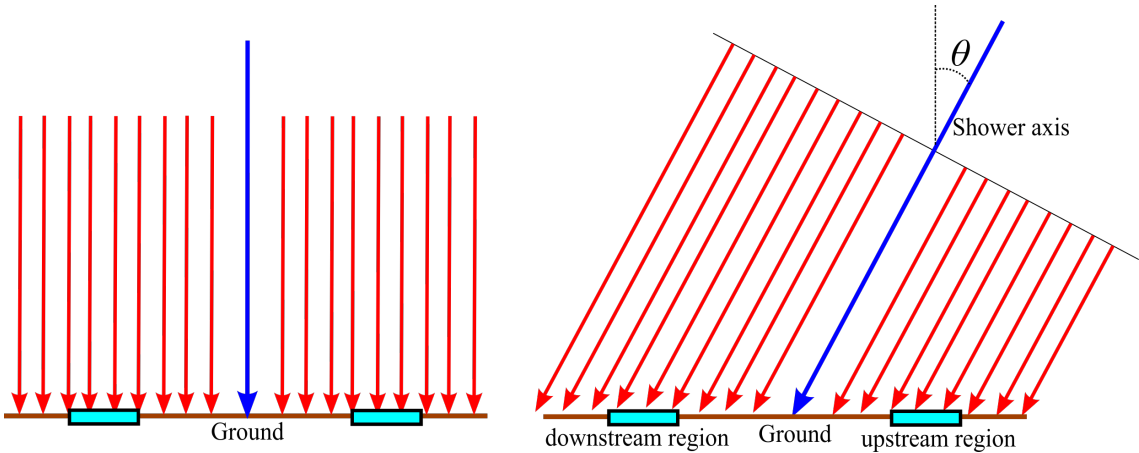


**Figure 5.3:** A cylindrical model for the geometry of an extensive air shower. Particles (red) effectively travel parallel to the shower axis (blue) and the size of the shower front remains constant. The difference in flux through the light blue regions is 0 in both the vertical and inclined cases.

in Figure 5.3. Comparing the flux of particles (red arrows) through the light blue regions either side of the shower core, we see that there is no difference, thanks to all particles travelling parallel to each other. This also means the equal particle density contours produced on the ground *are* ellipses centred on the shower core, which become circles centred around the shower axis when projected back into the shower plane. Hence, in this model, there are no geometrical effects which give rise to asymmetry.

Now consider a conical model of shower development where all the particles are emitted from a single point on the shower axis, each with a random opening angle uniformly distributed between 0 and  $\alpha$  (measured with respect to the shower axis). The particles are assumed to travel in straight lines to ground. This is slightly more realistic than the previous model, with schematics of the vertical and inclined versions shown in Figure 5.4. A clear difference in density (flux of red arrows) between the two light blue regions appears when the vertical shower is rotated. This is simply a result of the inverse square law and is an example of what we mean when we refer to “geometrical effects”. When the densities of the regions are projected into the shower plane the shower axis direction is used since, in reality, we do not have any knowledge of the directions of the particles. Hence, upon projection, a purely geometrical asymmetry arises. The contours of constant density on the ground for this model are ellipses with their centres shifted upstream, a fact easily seen by considering the points on the ground which are equal distances from the point of production.

Another simple model one might consider is for particles to be continuously emitted along the shower axis, each at some fixed angle. An example of the resulting locations of particles on the ground for a vertical and inclined shower is shown in

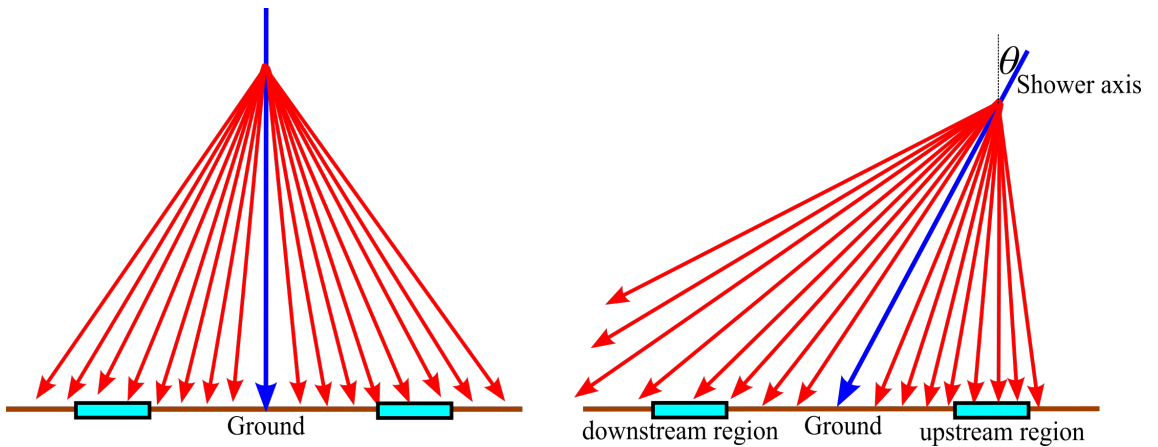


**Figure 5.4:** A conical model of shower development where all particles are emitted from a single location with a range of opening angles between 0 and  $\alpha$ . Inclining a symmetric, vertical shower under this model causes there to be a greater density in the light blue upstream region.

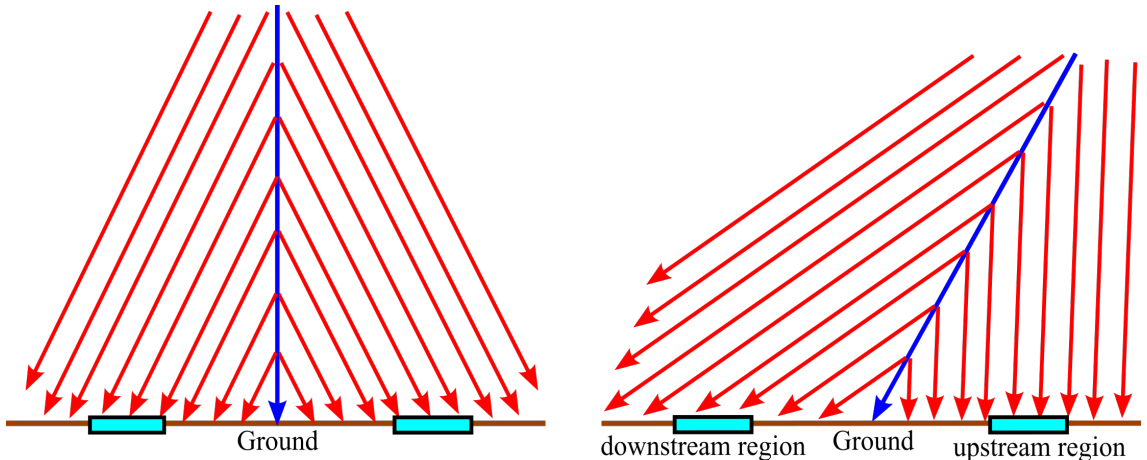


**Figure 5.5:** A simple air shower model where particles are emitted continuously along the shower axis at a fixed angle. Like the conical model, rotating the vertical version of the shower induces a greater density in the light blue upstream region.

Figure 5.5. Here, we see that once again the density of particles is higher in the blue upstream region. In this case however, the reason is not the inverse square law but simply the angle of incidence of the downstream particles being shallower. If the flux of particles incident perpendicular to a surface is  $F$  then rotating the incident particles by an angle  $\beta$  to the normal leaves a flux of  $F \cos \beta$  through the surface. This is another example of a “geometrical effect”, since an inclined shower will have  $\beta$  greater on the downstream side, causing the density in the downstream light blue region to be smaller. This leads to a geometrical asymmetry after projection into the shower plane. For this model, the density in the upstream and downstream regions differs by a constant amount.

In reality, none of these models properly describe how particles in an air shower propagate. Electrons and photons in particular do not travel in the straight lines presented in these illustrations and are instead scattered multiple times between their production point and ground. They also are not necessarily produced on the shower axis. Furthermore, the opening angle distributions are not uniform and change depending on the production height, another variable factor. However, these models are useful for visualising how the geometry of an air shower affects asymmetry and are reasonable first approximations, especially for muons which generally travel away from the shower axis without scattering on their way to ground.

### 5.2.2 Asymmetry induced by attenuation

Asymmetry also arises from a difference in the level of attenuation experienced by the flux of particles travelling downstream/upstream. No matter the geometrical model one uses to describe a shower, particles landing in the downstream region at a set distance from the shower core generally travel through more atmosphere to reach the ground than particles landing in the upstream region at the same distance. This means “downstream particles” lose more energy and are more likely to decay or stop than “upstream particles”. The effect of this asymmetry is more striking for the electromagnetic component of air showers than the muonic component, as the electromagnetic component attenuates faster. Whilst conceptually understanding how attenuation gives rise to asymmetry is relatively straightforward, when trying to model asymmetry one must realise its effects are coupled with the geometry of the shower i.e. how far and in what direction each particle must travel from production point to ground.

## 5.3 Separating geometry and attenuation

With the basic understanding outlined in the previous section, the goal was to quantitatively separate the geometrical and attenuation effects underpinning asymmetry. In searching for a method to differentiate the two, an internal paper to the Pierre Auger Collaboration, written by former members Xavier Bertou and Pierre Billoir, [85] was found. Published in 2000, the paper attempts to demonstrate that the cause of asymmetry cannot purely be the attenuation of electromagnetic particles. Whilst details of the procedures used are sparse, the ideas presented seemed worth implementing, with the results they achieved providing a useful cross-check.

As a reference for the following analysis, a plot of the density of electromagnetic air shower particles for a shower with the median zenith angle of  $38^\circ$  is shown in Figure 5.6. The shower has an energy of  $10^{19}$  eV and is from a proton primary. Here, the density has been sampled in 12 segments on the ground, which, when projected into the shower plane, are equally sized, spaced by  $30^\circ$  in azimuth, and form an annulus with a central radius of 1000 m and width of 100 m. The weighted number

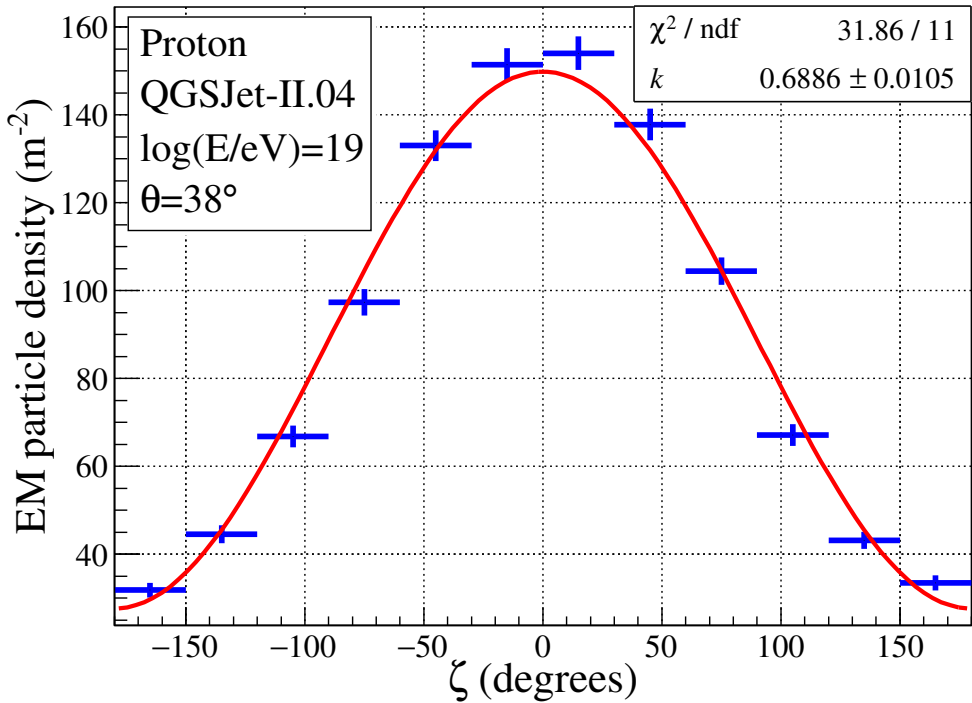


**Figure 5.6:** The ground density of electromagnetic particles in a  $38^\circ$  shower, measured at 1000 m in the shower plane. The extreme upstream and downstream segments, centred at  $\pm 15^\circ$  and  $\pm 165^\circ$  respectively, show roughly a 5 fold difference in density. The results from fitting Equation 5.1 are shown in the top right.

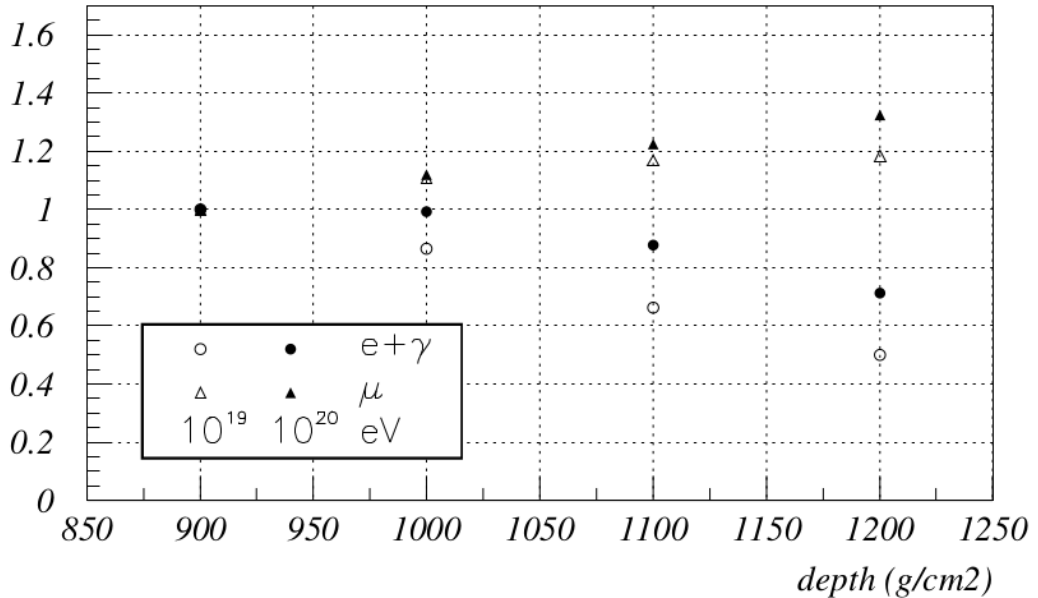


**Figure 5.7:** Results from [85] on the change in density of electromagnetic particles (circles) as a function of atmospheric depth traversed.

of particles in each ground segment has been counted before being divided by the area of the segment *on the ground* i.e.  $A = (\pi(1050^2 - 950^2)/12) \times \sec 38^\circ \text{ m}^2$ . This imitates what is done in real life where a signal, roughly equivalent to a density in the case of a scintillator detector, is measured on the ground and then projected into the shower plane. The errors,  $e_i$ , for each bin of the histogram were calculated as  $e_i = \sqrt{(\sum_{m=1}^n w_m^2)/A}$  where  $w_1, w_2, \dots, w_n$  were the weighted values used to fill the  $i^{th}$  bin. To keep a consistent measure of asymmetry across chapters, a function similar to that used in Chapter 4 for estimating the asymmetry amplitude in signals has been fit to the data, namely

$$\rho(\zeta) = \bar{\rho}(1 + k) \cos \zeta \quad (5.1)$$

The fit result is shown in red. Here,  $k$  is a free parameter describing the asymmetry amplitude in *particle density* and  $\bar{\rho}$  is the average value of the density. This slightly modified form allows us to plot the absolute value of the density whilst also finding the relative difference,  $k$ , between the average density and the density upstream or downstream. In Figure 5.6  $k = 0.69 \pm 0.01$ .

### 5.3.1 Measuring the electromagnetic particle density in vertical showers

The initial study presented in [85] was an investigation into the density of electromagnetic particles in vertical showers. The goal was to measure the density at different stages of longitudinal development, thereby giving a quantitative answer to how much attenuation contributes to asymmetry. By using vertical showers, no geometrical effects relating to the inclination of the shower were present. Additionally, the particles were extracted at atmospheric depths typically larger than the depth of shower maximum,  $X_{\max}$ . Thus the electromagnetic component of the shower fronts should have been decreasing in size with increasing atmospheric depth. Twenty proton showers at  $10^{19} \text{ eV}$  and  $10^{20} \text{ eV}$  were simulated, though the paper does not provide details on whether these showers had different values of  $X_{\max}$ , nor the location or size of the region in which the density was sampled. The results from the paper are shown in Figure 5.7. Although the limited information provided in [85] means we do not fully understand what is being shown in this plot, we can at least note the conclusion of Bertou and Billoir - that the density of electromagnetic particles decreases by approximately 15% per  $100 \text{ g cm}^{-2}$  and that this value is too small to explain the difference between the upstream and downstream densities in simulated inclined showers.

Before checking their conclusion for ourselves, it is perhaps useful to compare the Bertou/Billoir observations with the density measurements in Figure 5.6, which utilises the modern air shower simulation program CORSIKA. For a  $38^\circ$  shower, assuming the cylindrical model of air shower geometry, particles which land downstream in a segment corresponding to 1000 m in the shower plane will travel an

extra  $2 \times 1000 \tan 38^\circ \approx 1560$  m. This equates to roughly an additional  $160 \text{ g cm}^{-2}$ , which according to Figure 5.7 would only result in a decrease of roughly 25%. This percentage can be converted to an estimate of the asymmetry amplitude in electromagnetic particle density for a  $38^\circ$  shower assuming the only contributing factor is attenuation. Using Equation 5.1, we have that  $(1 + k)/(1 - k) = 0.25$  and so  $k=0.14$ . Measuring  $k$  for 25 showers of the same energy, zenith and primary as in Figure 5.6, which include both geometrical and attenuation effects, and averaging the result yields  $k = 0.70$ . This is significantly larger than the attenuation only estimate of  $k=0.14$ , making Bertou and Billoir's argument seem plausible. Nonetheless we decided to repeat their analysis with the aim of being as transparent as possible with the data sets and methods of measuring the particle density.

For the cross-check, a similar data set to that used by Bertou and Billoir was simulated using CORSIKA. The data consisted of 20 vertical ( $\theta = 0^\circ$ ) proton showers and 20 vertical iron showers, each of energy  $10^{19}$  eV with varying values of  $X_{\max}$ , simulated using the QGSJet-II.04 model with a thinning level of  $10^{-6}$ . Iron showers were included to observe the dependence on primary mass. The particles in each shower were sampled at observation levels corresponding to atmospheric depths of 900, 950, 1000, 1050, 1100, 1150 and  $1200 \text{ g cm}^{-2}$ . Such extreme vertical depths were obtained by modifying the atmospheric profile used by CORSIKA to that which would be seen by a  $30^\circ$  shower incident on a ground height equal to sea level. Details of this procedure can be found in Appendix B. At each observation level, the density was sampled by counting the weighted number of electromagnetic particles which landed in an annulus centred at 1000 m, with width 100 m, and then dividing the total by the area of the annulus. Two example plots of the density measurements versus the atmospheric depth of the observation levels are shown in Figure 5.8. Both showers are from proton primaries, with the first shower having an  $X_{\max} \approx 705 \text{ g cm}^{-2}$ , whilst the second shower has an  $X_{\max} \approx 850 \text{ g cm}^{-2}$ . In both cases a simple Gaussian with no restrictions on its parameters has been fitted to the data, allowing for interpolation between the data points.

As the observation levels are fixed, we see that different stages of development are captured for each shower, due to their  $X_{\max}$  values being different. This means the development we observe with fixed observation levels depends on  $X_{\max}$  and so the estimated amount of attenuation between the levels will also depend on  $X_{\max}$ , something not captured in the Billoir plot. Therefore, we decided to use the Gaussian fits to provide an estimate of the asymmetry amplitude for a shower with the median zenith angle of  $38^\circ$ . For a  $38^\circ$  shower the atmospheric slant depth at the ground height of Auger is  $880/\cos(38^\circ) \approx 1116 \text{ g cm}^{-2}$ . We can also estimate the slant depths for points directly upstream ( $\zeta = 0^\circ$ ) and downstream ( $\zeta = \pm 180^\circ$ ) of the shower core for such a shower which, when projected into the shower plane, are at  $r = 1000$  m. This is done by assuming a cylindrical geometry and then using the atmospheric profile of a  $38^\circ$  shower to calculate the slant depth based on the height of the point above/below the shower core as measured along the shower axis. Details

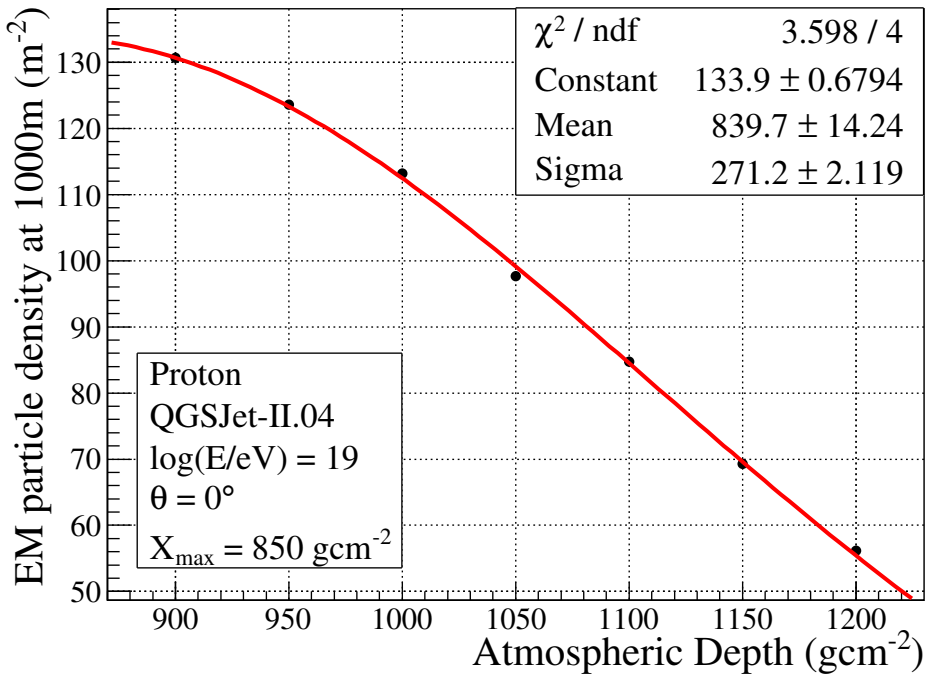
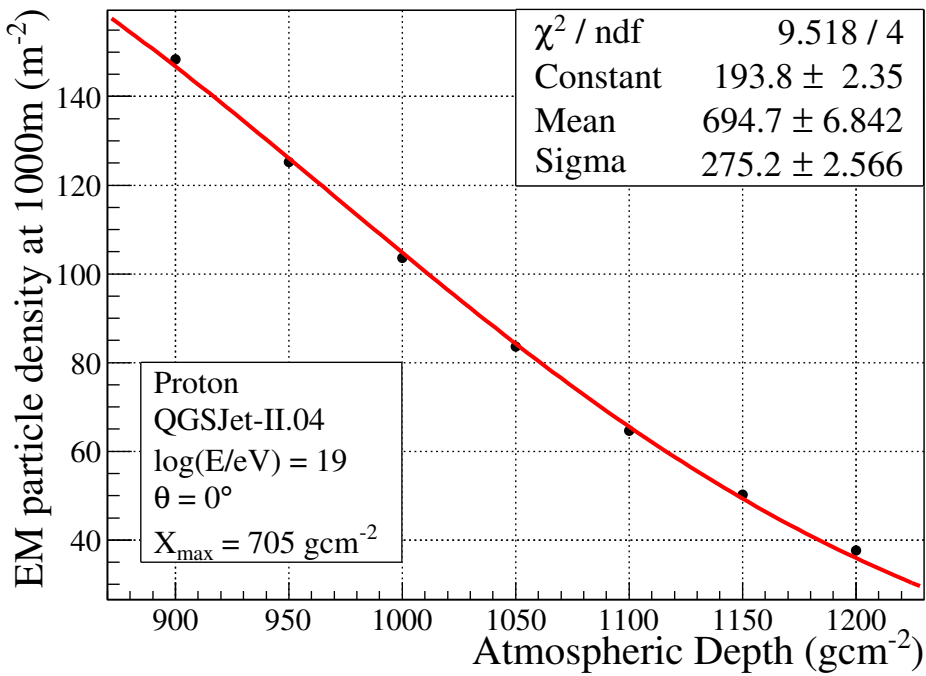


**Figure 5.8:** The electromagnetic particle density at different stages of shower development for two different vertical proton showers. The density is sampled in an annulus centred at 1000 m from the shower axis with a width of 100 m at each level (black dots). A Gaussian fit has been applied in both cases, with respective parameters shown.

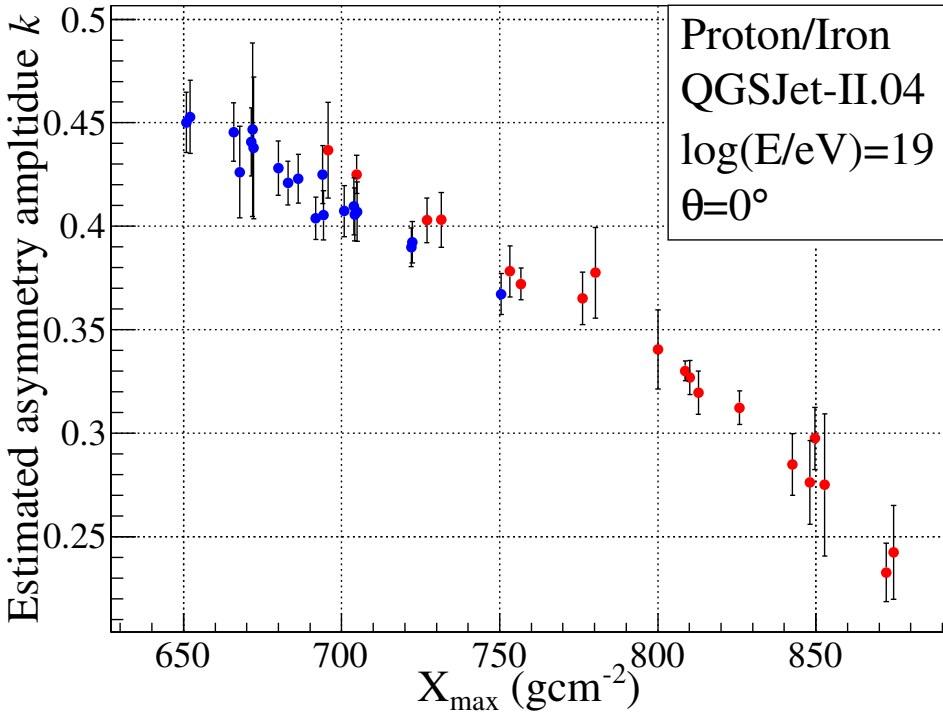


**Figure 5.9:** The estimated amplitude of the asymmetry in electromagnetic particle density for  $38^\circ$  showers, based purely on attenuation, as a function of  $X_{\max}$ .

of this calculation can also be found in Appendix B. The upstream/downstream values are  $1035$  and  $1198 \text{ g cm}^{-2}$  respectively. Using the Gaussian fits,  $G_i(x)$ , for  $i = 1 \dots 40$  (including proton and iron showers), the ratio  $R = G_i(1035)/G_i(1198)$  was calculated for each  $i$  and then converted into an asymmetry amplitude via  $k = (R - 1)/(1 + R)$ . The  $k$  values were plotted against the true  $X_{\max}$  of the shower, obtained from CORSIKA, giving the result shown in Figure 5.9. The red points represent proton showers, the blue points iron showers.

There is a clear decreasing linear trend between  $k$  and  $X_{\max}$  for both proton and iron showers. This demonstrates that the rate of attenuation of the electromagnetic component of air showers increases the further we are from  $X_{\max}$  (at least up until  $1200 \text{ g cm}^{-2}$ ). There also appears to be a small offset between the proton and iron points, highlighted by the  $X_{\max}$  region which contains both types of showers. In this region we see that, for the same  $X_{\max}$ , iron showers have a slightly lower asymmetry amplitude. The effect is likely due to the additional muon content of iron showers. The minimum amplitude for proton and iron primaries is around  $0.24$  and  $0.36$  respectively, whilst the maximum amplitude is around  $0.45$  for both. This is over  $60\%$  of the average value of  $0.7$  calculated for the electromagnetic component of regular  $38^\circ$  proton showers (Figure 5.6). Altogether this may indicate an additional contribution from geometrical effects is needed to push the estimated value of the

asymmetry in line with the CORSIKA output. It also shows that attenuation could be the dominant factor contributing to asymmetry in shallow showers at zenith angles around  $38^\circ$ . In addition, although small, the difference in asymmetry for proton and iron showers of the same  $X_{\max}$  may show a way to help distinguish between the two primaries. Combining estimates of the asymmetry amplitude for the SSD, whose signal is a closer proxy to particle density than the WCD, with accurate measurements of  $X_{\max}$  from the fluorescence detector may help constrain the mass composition of an ensemble of showers. Naturally many challenges would need to be overcome to achieve this, not least of which is reconciling any differences between asymmetry in real data and simulations. However the possibility of combining FD and SD data in such a manner for mass composition studies may justify investigating this point further in future work.

The main flaw in this analysis is the reliance on the cylindrical geometry assumption to estimate how much less/extra atmospheric depth has to be travelled by the upstream/downstream particles. Particles travelling upstream/downstream in inclined showers actually experience slightly different atmospheric profiles, which could mean we are underestimating the asymmetry amplitude. This is because the details of scattering processes such as Coulomb scattering and Bremsstrahlung depend on the local atmospheric density and for particles travelling downstream, whose trajectories are usually more inclined, the slower this density will change. This gives downstream travelling particles more chances to scatter and lose energy than upstream going particles, potentially increasing the asymmetry. If the production position, initial opening angle and scattering of electrons and photons could be taken into account, then a more accurate estimate of the extra atmospheric depth travelled through could be obtained, possibly leading to different estimates of the asymmetry amplitude. This issue, whilst outside the scope of this work, could be addressed in future studies.

Finally, without knowing exactly what is being shown in Bertou and Billoir's concluding plot (Figure 5.7), it is difficult to compare our results to theirs. However, our results for the expected asymmetry amplitude in electromagnetic particle density, based solely on attenuation, for  $38^\circ$  proton showers at 1000 m in the shower plane, vary between roughly 0.24-0.44. This is noticeably larger than the corresponding amplitude of the Bertou/Billoir estimate,  $k = 0.14$ . The results from this analysis incline us to believe that, at least for showers around  $38^\circ$  in zenith, attenuation is a significant, possibly the main, factor contributing to asymmetry in electromagnetic particle density, especially for shallow showers. An extension to this analysis would be to measure the densities at both smaller and larger atmospheric depths, allowing showers of different zenith angles to have their attenuation component of asymmetry extracted.

### 5.3.2 Comparing regular and “rotated” showers

Having seen that electromagnetic attenuation could perhaps be the primary cause of asymmetry, another method outlined in [85] for separating the geometric and attenuation components was checked. Bertou and Billoir describe the method as follows;

1. First, simulate an inclined shower with zenith angle  $\theta$ , recording the secondary particle positions at ground level. If the ground corresponds to a vertical atmospheric depth  $X_g$ , then such a shower will have travelled through an atmospheric slant depth of  $X = X_g \sec \theta \text{ g cm}^{-2}$ .
2. A vertical shower of the same energy and primary is then simulated and made to travel through the same amount of accumulated atmosphere as the inclined shower i.e.  $X \text{ g cm}^{-2}$ . This ensures the stage of development of the electromagnetic component of both air showers is similar at ground level, provided the  $X_{\max}$  values are close to each other.
3. Next, the vertical shower is rotated clockwise in the  $x - z$  plane by  $\theta$ . In other words, the positions of all the particles are rotated such that the particles appear to lie in the shower plane, with particles whose original  $x$  coordinate was negative now above the ground and those whose original  $x$  coordinate was positive below the ground. The momentum vector of each particle is also rotated.
4. All the particles in the rotated ground plane (shower plane) are then propagated back to the original ground along their own (rotated) direction, with no simulation of particle attenuation.

In theory, the result is two showers of the same zenith, energy, primary and  $X_{\max}$ , with the particle list of each recorded at the same atmospheric depth. The only difference is that one shower has both geometrical and attenuation affects contributing to the observed asymmetry (the original inclined shower), whereas the other should only experience a pure geometrical asymmetry (the rotated vertical shower). By propagating the final positions of the particles in both showers back into the shower plane along the direction of the shower axis, the asymmetries can be compared. The results achieved by Bertou and Billoir, who only tracked electromagnetic particles, are shown in Figure 5.10. The asymmetries in their results are clearly very similar. This implies that attenuation is not a significant effect. Thus Bertou and Billoir concluded the primary cause of asymmetry to be geometry.

Whilst this result is in clear contradiction with our conclusion from the previous section, the method appeared, at the time, worth trying. Hence the aim was to replicate the above process and compare the result to Bertou and Billoir’s observations. Unfortunately, the paper was again not specific in the details of what type of inclined shower was used to give the results in Figure 5.10 i.e. neither energy nor primary nor

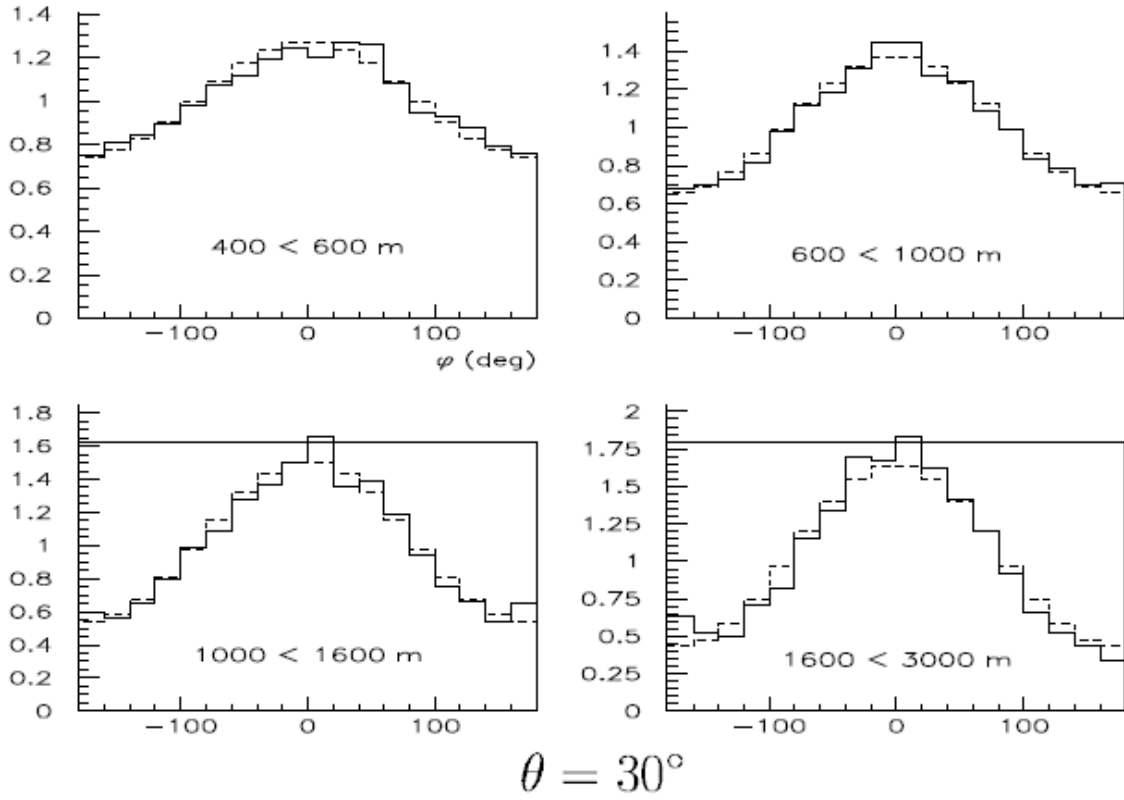


**Figure 5.10:** Results from [85] on the asymmetry in electromagnetic particle density observed in a simulated inclined shower (solid lines) to the prediction of a vertical shower at the same depth, after rotation and projection (dashed lines). The method by which the histograms have been normalised is not known.

$X_{\max}$  were stated. Though this made reproducing their exact procedure impossible, a proton shower of energy  $10^{19}$  eV and zenith angle  $30^\circ$  was simulated for the “regular” shower with which to compare to. The  $X_{\max}$  of the shower was  $792 \text{ g cm}^{-2}$ . A plot of the electromagnetic density profile at 1000 m for this shower is shown in Figure 5.11, with density calculations performed as explained for Figure 5.6. By fitting Equation 5.1, the asymmetry amplitude was estimated to be  $k = 0.52 \pm 0.01$ . Also note that CORSIKA was used for the shower simulations instead of AIRES, the software used by Bertou and Billoir. Before moving on, we briefly mention that the inclined shower profile (solid line) in the bottom left panel of Figure 5.10 has a very similar shape and asymmetry amplitude as our example shower in Figure 5.11. Thus any differences between the simulations of regular inclined showers in the old AIRES software and the current CORSIKA software shouldn’t cause major discrepancies.

### Simulating the vertical shower

The next step was to simulate a vertical shower travelling through the same slant depth as the regular inclined shower. For the chosen  $30^\circ$  shower, this was  $880/\cos(30^\circ)$

$\approx 1016 \text{ g cm}^{-2}$ . To change the atmospheric slant depth traversed by the shower, one option is to adjust the height of the observation level in CORSIKA. However this is not sufficient for simulating vertical showers which travel through the same atmospheric depth as very high zenith angle showers (e.g.  $50^\circ$ ). The solution is to manually adjust the parameters which define the atmosphere in CORSIKA. For our purposes, to make a vertical shower traverse the same depth as a shower of zenith angle  $\theta$ , incident on Auger ground at 1.452 km above sea level, the atmosphere *as seen by the inclined shower* was modelled and given to CORSIKA to use for simulating the vertical shower. This ensured the same atmospheric profile for both showers. Details of the method can be found in Appendix B.

## Transforming the vertical shower

With the ability to generate inclined atmospheres, vertical showers passing through an atmosphere which would be seen by a  $30^\circ$  shower were simulated with CORSIKA until one was produced with a similar  $X_{\max}$  as the regular inclined shower. Using this shower, the entire plane of ground particles was then rotated clockwise about the  $y$ -axis by the zenith angle of the regular inclined shower ( $30^\circ$  for this example). Thus the following transformation

$$\vec{x} = \begin{pmatrix} x \\ y \\ 0 \end{pmatrix} \rightarrow \begin{pmatrix} x_r \\ y_r \\ z_r \end{pmatrix} = \begin{pmatrix} \cos \theta & 0 & \sin \theta \\ 0 & 1 & 0 \\ -\sin \theta & 0 & \cos \theta \end{pmatrix} \begin{pmatrix} x \\ y \\ z \end{pmatrix} \quad (5.2)$$

was applied to the positions of the particles, whilst the transformation

$$\vec{p} = \begin{pmatrix} px \\ py \\ pz \end{pmatrix} \rightarrow \begin{pmatrix} px_r \\ py_r \\ pz_r \end{pmatrix} = \begin{pmatrix} \cos \theta & 0 & \sin \theta \\ 0 & 1 & 0 \\ -\sin \theta & 0 & \cos \theta \end{pmatrix} \begin{pmatrix} px \\ py \\ pz \end{pmatrix} \quad (5.3)$$

was applied to the momentum of each particle. Note that if, after the initial rotation, a particle had a momentum vector pointing upward, it was discarded. The particles in the rotated plane were then propagated back to the original ground along their own (rotated) momentum vectors. This was achieved by parameterising the trajectory of each particle as a line  $L$ ,

$$L = \begin{pmatrix} x_r + t \\ y_r + py_r/px_r \times t \\ z_r + pz_r/px_r \times t \end{pmatrix} \quad (5.4)$$

and then finding  $t$  such that the  $z$ -component of  $L$  was zero i.e. when  $z_r + pz_r/px_r \times t = 0$ . This gave  $t = -z_r \times px_r/pz_r$  and hence the new ground co-ordinates of each

particle were given by

$$\begin{pmatrix} x_r \\ y_r \\ z_r \end{pmatrix} \rightarrow \begin{pmatrix} x_g \\ y_g \\ z_g \end{pmatrix} = \begin{pmatrix} x_r - z_r \times px_r/pz_r \\ y_r + py_r/px_r \times -z_r \times px_r/pz_r \\ 0 \end{pmatrix} \quad (5.5)$$

The new positions of the electromagnetic particles at ground were then able to be studied for asymmetry just as for a regular shower. The density profile for the rotated vertical shower is shown in Figure 5.12.

Clearly our result is significantly different from the work of Bertou and Billoir. The “asymmetry” is now in the complete opposite direction, with a greater density of particles downstream. One possibility is that attenuation is even more important than originally believed for producing asymmetry and that purely geometrical effects actually cause the asymmetry to go in the opposite direction. However this goes against the basic understanding of asymmetry developed in Section 5.2, indicating a probable flaw in the method.

To gain insight into what could be causing this surprising result, the footprint of the vertical shower and location of particles which end up in the sampled region in the shower plane after transformation were plotted. The result is shown in Figure 5.13. The blue dots indicate the original location of the electromagnetic particles in the vertical shower and the green dots show which particles ended up in the orange ellipse after rotation and propagation back to ground. This orange region corresponds to the annulus in the shower plane of width 100 m and central radius 1000 m. From this we see that particles with a wide range of negative  $x$  values get transformed into the sampling region, whereas particles with positive  $x$  values generally have to be around the ellipse originally to be selected. Although initially surprising, considering what happens to a small subset of particles either side of the original vertical axis reveals what may be happening, a schematic of which is shown in Figure 5.14.

When the vertical shower is rotated, particles on what becomes the “upstream” side (positive  $x$  in this example) are more likely to be transformed inwards after rotation and projection. This is because it is more likely that particles have a positive radial component of momentum. This is illustrated in Figure 5.15, which shows a histogram of the radial components of the  $(x, y)$  momentum vectors for each electromagnetic particle (ignoring the  $z$ -component). The opposite is true for particles which end up downstream, in that they are more likely to be transformed further from the shower core. This means the high density of particles close to the core on the downstream side get transformed to a distance where they are within the orange ellipse shown in Figure 5.13. Meanwhile on the upstream side, particles near the orange region stay roughly where they are. This leads to the odd shaped green section of Figure 5.13.

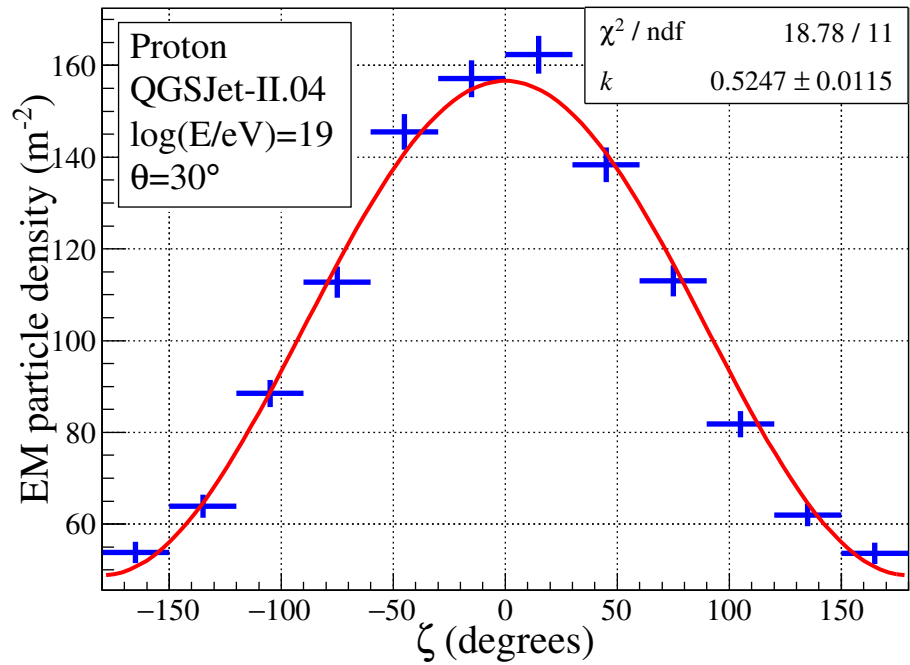


**Figure 5.11:** Histogram of the density of electromagnetic particles in a  $30^\circ$  shower, measured at 1000 m in the shower plane. The results from fitting Equation 5.1 are shown in the top right.

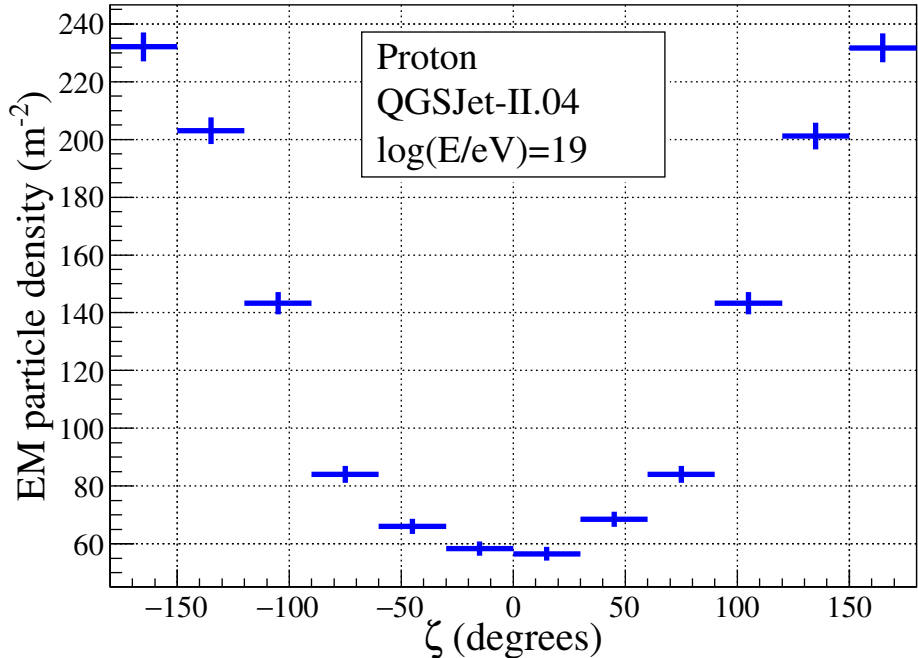


**Figure 5.12:** Histogram of the density of electromagnetic particles in the rotated vertical shower. The density is measured in an annulus at 1000 m in the shower plane as usual.

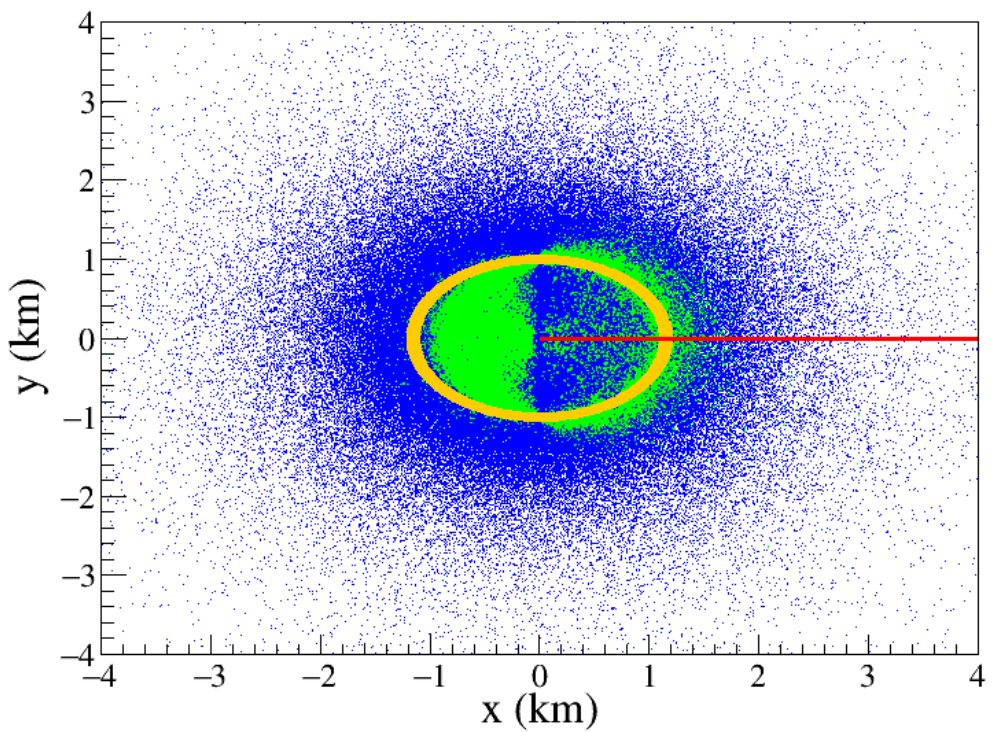


**Figure 5.13:** (Blue) Footprint of the electromagnetic particles which reach ground in the original vertical shower. (Green) The locations of the electromagnetic particles which are transformed into the orange region after rotation and propagation back to ground. It is these particles which are sampled for the density measurements in Figure 5.12. (Red) Direction of the shower axis after rotation i.e. the vertical shower is rotated to come from the positive  $x$  direction.

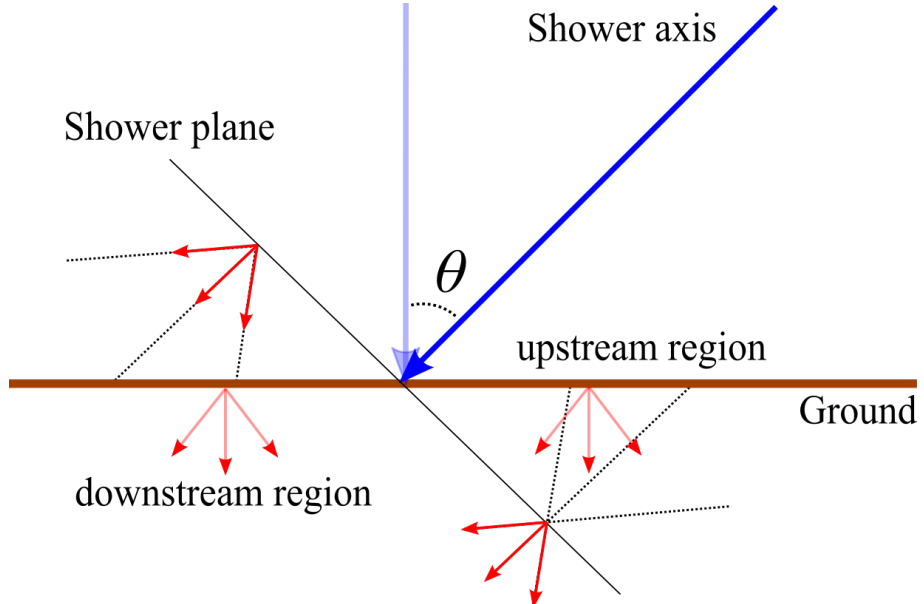


**Figure 5.14:** Illustration of how particles either side of the shower axis are shifted through the Bertou/Billoir transformations performed on a vertical shower. Outwards going particles on the upstream/downstream side are shifted inwards/outwards respectively.

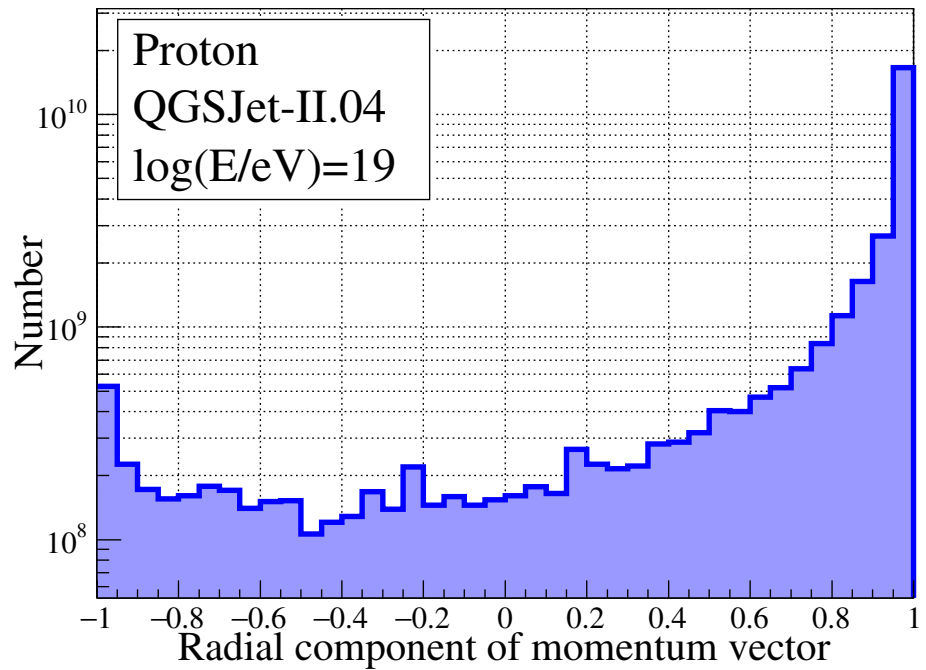


**Figure 5.15:** The radial component of the momentum vectors for each electromagnetic particle in the vertical shower before rotation. Significantly more particles are moving away from the shower axis.

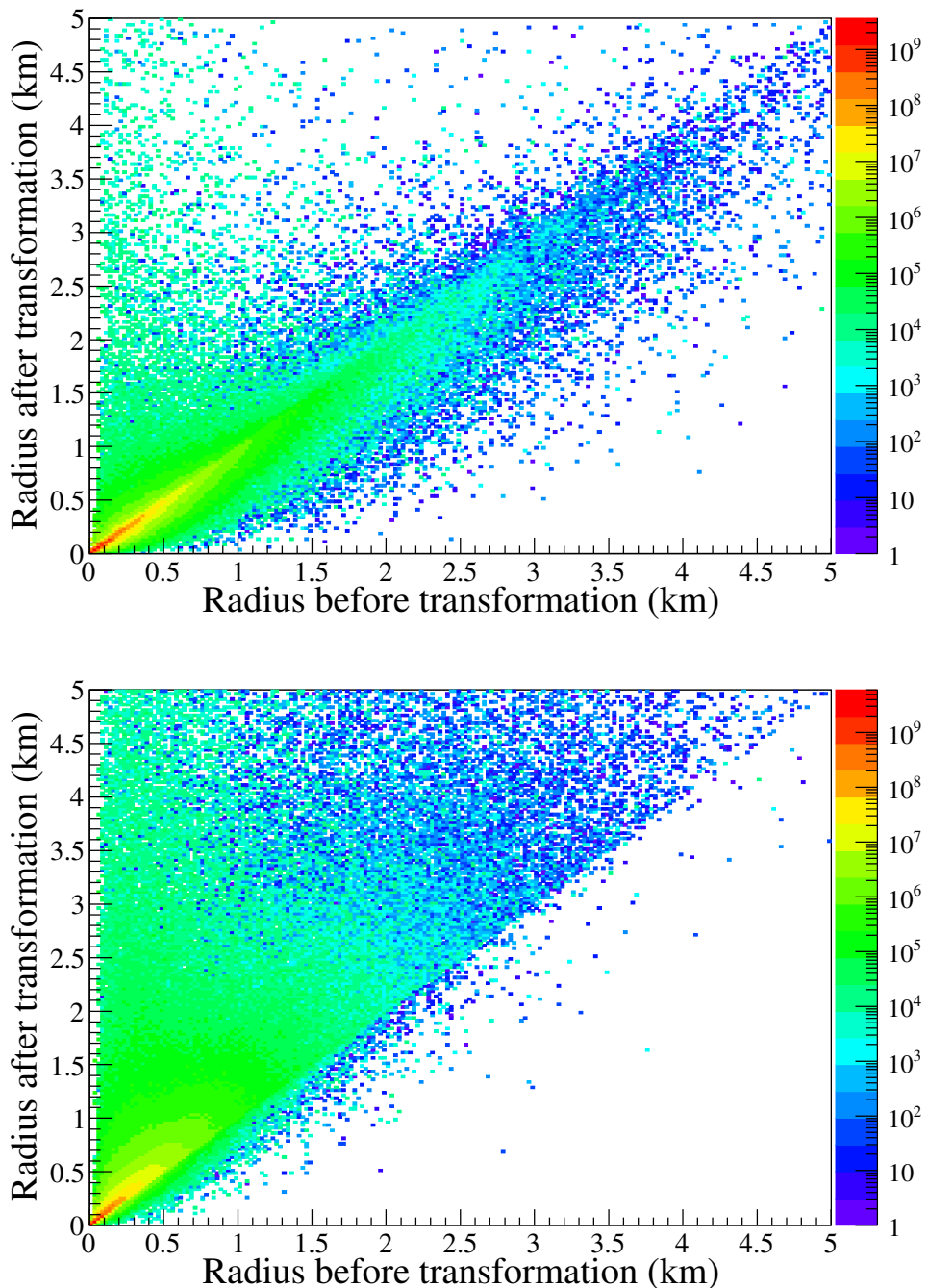


**Figure 5.16:** The radius of electromagnetic particles (on the ground) in a vertical shower before and after applying the Bertou/Billoir transformations. (Top) Particles with initially positive  $x$  co-ordinate. (Bottom) Particles with initially negative  $x$  co-ordinate. The color bar or  $z$ -axis indicates the number of particles.

To test this theory, the radii of the particles (on the ground) before and after transformation were plotted. The particles were separated into two groups - those with initially positive  $x$  values and those with initially negative  $x$  values. The results are shown in Figure 5.16. We can see that although the upstream side particles stay relatively close to their initial positions, the downstream particles almost always get shifted further from the shower core. This supports our hypothesis and provides a plausible reason as to what caused the “opposite asymmetry” effect seen in Figure 5.12.

Despite now having some intuition as to what is happening in the Bertou/Billoir procedure, it is still not clear why their results are so different. Regardless, the uncertainty as to whether the geometrical effects have been properly taken into account through this method mean a quantitative value for either the attenuation or geometrical component is not assigned here. Unfortunately this also means no additional insight into how the components differ between primaries can be given. Future variations of this study should, if possible, use the tools of modern air shower simulation programs to simulate showers in which the attenuation effects are “turned off” so to speak. Comparing the resulting asymmetry to that of normal shower would be insightful.

### 5.3.3 Removing geometrical effects

To complement the Bertou/Billoir method of attempting to remove attenuation based asymmetry effects, a method was devised to try and remove geometrical affects from an inclined shower. In this case, particles in a regular inclined shower were traced back to their position in the shower plane, the idea being this would essentially leave the footprint of a vertical shower - *except*, there will be fewer particles coming from the downstream side thanks to attenuation effects. The resulting asymmetry should then purely be the result of attenuation. Testing this method on the  $30^\circ$  shower used in the Bertou/Billoir method yields the histogram in Figure 5.17. Note for the sake of direct comparison only electromagnetic particles were considered. Also the density measurements were performed for the same  $r = 1000$  m, width=100 m annulus as done previously, except the area divided by was the area of each segment in the shower plane.

The shape of this distribution is noticeably narrower, and flatter for  $|\zeta| > 100^\circ$ , than a normal asymmetry profile, such as in Figure 5.11. For this reason fitting Equation 5.1 to the histogram was not a valid method of assigning an amplitude to the observed asymmetry. Instead, we simply note that the ratio of the upstream density to downstream density is approximately 9. This is considerably larger than the corresponding ratio of the original  $30^\circ$  shower, roughly 3 (Figure 5.11). The enormous asymmetry may actually agree with the results from the Bertou/Billoir method, though this is probably due to the identical assumption that we can ignore scattering effects and trace electromagnetic particles along their momentum direc-

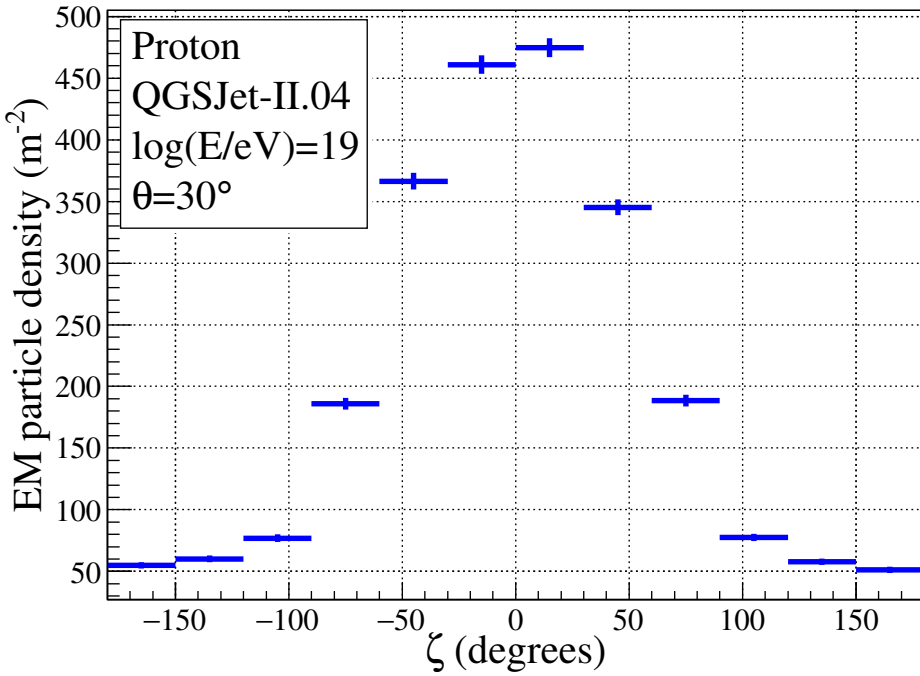


**Figure 5.17:** The electromagnetic particle density measured in the shower plane for the same  $30^\circ$  shower as in Figure 5.11 after tracing particles back along their own direction into the shower plane.

tion to some intersection point, whether that is the ground or the shower plane. Another factor which may be contributing to the extreme results seen in both methods is ignoring the *production* of new particles from existing particles, however this is difficult to check and will not be explored here. As trusting the output of this technique would also imply a negative contribution from geometrical effects to asymmetry, we again do not assign any values to the either the attenuation or geometrical components.

## 5.4 Conclusions

This chapter has investigated two primary causes of asymmetry, namely geometrical effects and attenuation effects, and tried to separate their contributions to the asymmetry observed in electromagnetic particle density. A summary of the methods used, their results and shortcomings is provided in the list of dot points below.

- **Measuring the electromagnetic particle density in vertical showers**

Of the methods used, only this technique, where electromagnetic particle densities in vertical showers were sampled at different depths and used to predict the asymmetry amplitude for a  $38^\circ$  shower, gave a reasonable, quantitative answer to the problem. Specifically, the amplitude of the asymmetry for proton

showers (in E.M. particle density) was found to range between 0.24-0.44 due to attenuation alone. For iron showers, the range of amplitudes was between 0.36-0.45. For both primaries, greater asymmetry was observed for shallower showers (smaller  $X_{\max}$ ). These asymmetry amplitudes were all lower than the value of 0.7 calculated for a regular 38° proton shower. The remaining contribution to asymmetry is believed to be from the geometrical effects outlined at the beginning of the chapter. This study showed that attenuation may be the dominant asymmetry causing effect in some cases. It also showed that there may be a possibility for future studies to leverage asymmetry in combination with FD measurements of  $X_{\max}$  to help constrain the mass composition of UHECRs, though several points will need to be checked and challenges overcome for this to be a realistic prospect.

The primary flaws in this method were the cylindrical geometry assumption made to estimate the atmospheric slant depths of the upstream/downstream regions, not accounting for the different atmospheric profiles seen by upstream/downstream going particles, and ignoring scattering and off-axis production.

- **Comparing regular and “rotated” showers (i.e. the Bertou/Billoir method)**

This method aimed to produce an inclined shower with no attenuation effects, via the rotation and propagation of particles in a vertical shower, and compare the resulting asymmetry to that of a regular inclined shower. Performing the method ourselves showed attenuation to be the dominant factor, however the extent of this was so large that accepting the result would force one to conclude that geometrical effects actually cause asymmetry to go in the opposite direction (greater density downstream). This goes against our fundamental understanding and thus is indicating a problem/s with the method - possibly that the assumptions of being able to track individual electromagnetic particles along straight lines and ignoring particle production are not valid.

- **Removing geometrical effects**

The last technique attempted aimed to isolate the attenuation component of asymmetry by tracing particles in an inclined shower back along their direction into the shower plane. This yielded very similar results to the Bertou/Billoir method, in that the resulting asymmetry was extremely large, to the extent of implying the geometrical component has a negative effect.

The flaws in this technique are believed to be the same as in the Bertou/Billoir method.

It is unlikely that any of the methods presented in this chapter completely separated the two effects, given that attenuation relies on knowing the atmospheric depth travelled through, which in turn is reliant on knowing the particle’s trajectory to ground i.e. geometry. Regardless of this or the shortcomings of each of the methods

tested, we feel confident in saying that the attenuation of electromagnetic particles is a significant component of the observed asymmetry in particle density in simulations. As such, the hypothesis stated in the previous chapter; that the difference between proton and iron in asymmetry largely comes down to the difference in the electromagnetic components, is supported. A natural extension to this work would be to perform the study in Section 5.3.1 for a number of different zenith angles, furthering our understanding of how the geometrical and attenuation components of asymmetry interact.

The work in this chapter leads to the question of whether we can check our understanding with a simple case. The following chapter looks to accomplish this by considering the asymmetry in muon particle density.

## Predicting the asymmetry in muon particle density

---

In the previous chapter the causes of asymmetry in the density of electromagnetic particles was investigated. The results indicated that, at least for showers around  $38^\circ$ , the difference in atmospheric attenuation experienced by particles travelling upstream vs. downstream is a significant factor in shaping the asymmetry profile of a shower. However, directly measuring the contribution of geometric effects to the overall asymmetry was not able to be achieved, due to the shortcomings of the techniques used. To clearly see how geometrical effects impact asymmetry a simpler case is studied here, namely the asymmetry in muon particle density. The trajectory of muons through the atmosphere is far more straightforward than that of electromagnetic particles, and can be easily modelled with only a few assumptions. These are that

- (a) Muons travel in approximately straight lines from their production point to ground. This is a reasonable approximation as muons generally experience little scattering during propagation and, for zenith angles  $< 60^\circ$ , the earth's magnetic field has only a small deflection on a muons original trajectory [86].
- (b) Muons are produced on the shower axis. The pions from which muons decay typically remain within  $\sim 50\text{ m}$  of the shower axis. Hence, relative to the several kilometer scale of air showers, it is justified to approximate a muons production position as lying on the shower axis. [86].

These assumptions allow for both the production point and resulting ground position of a muon to be estimated, provided one knows the original production height and momentum of the muon. This means that the geometrical component of the asymmetry in muon particle density can be predicted using a Monte Carlo (MC) simulation where these parameters are sampled from known distributions. The goal of this chapter is to use information from CORSIKA and the above assumptions to create a simple Monte Carlo simulation which predicts the asymmetry in muon particle density with and without atmospheric attenuation. Our expectation is that, due to the rate of attenuation in the muonic component of extensive air showers being relatively low, geometrical effects should dominate any observed asymmetry. To build the Monte Carlo model, the following distributions must be known,

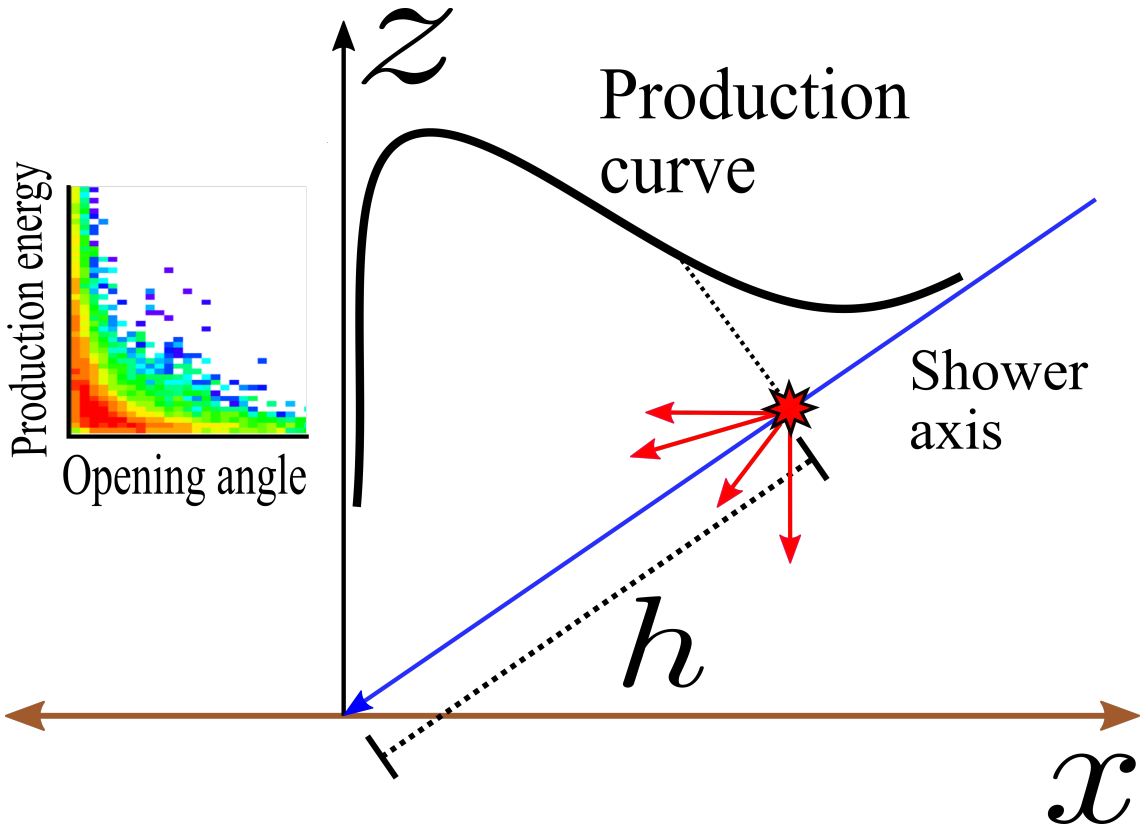


**Figure 6.1:** A 2D representation of how the muon model will operate. Starting from the ground, the production histogram, illustrated by the black curve, will give the number of muons to produce at some distance along the shower axis,  $h$ . For each distance the opening angles and production energies of the simulated muons will be given by sampling from the corresponding opening angle and energy distribution for that particular distance. A mock distribution is shown to the left of the  $z$  axis. A random value of  $\phi$  between 0 and  $2\pi$  will also be assigned, fully defining the outgoing momentum vector of the muon.

1. The production of muons as a function of distance along the shower axis (0 m is at the shower core)
2. The two-dimensional distribution of muon opening angles and production energies as a function of distance along the shower axis. The opening angle is defined to be the angle the muons momentum vector makes with the shower axis.

Naturally, this information varies depending on a shower's energy, primary mass and zenith angle. For this reason, the initial investigation only attempted to predict the asymmetry in muon particle density for a single CORSIKA shower. The simulated shower was generated using the CORSIKA options "MUPROD" and "EHISTORY" to record the production positions and initial momenta of all muons produced in the shower (including those which didn't reach the ground). This information was then used to create the required distributions and subsequently a Monte

Carlo program which would sample from these distributions to generate a new, muon only, air shower. When generating the new shower, the number of muons produced at each point along the shower axis was given by the production histogram, with the opening angle and initial kinetic energy of each muon given by sampling from the associated 2D-histogram so as to maintain the proper correlation. Figure 6.1 shows an example of this process. By following the particles in straight lines to the ground, with and without the simulation of attenuation, the result of the Monte Carlo would be two lists of muons and their properties at ground, similar to the output of a CORSIKA simulation. These particle lists could then be analysed for asymmetry as done in the previous chapter.

The method of forming the required distributions will now be described. Note that plots of example distributions will be for a CORSIKA shower with proton primary, hadronic interaction model QGSJet-II.04, thinning level  $10^{-6}$ , zenith angle =  $40^\circ$ , energy =  $1.0 \times 10^{19}$  eV and  $X_{\max} = 763 \text{ g cm}^{-2}$ .

## 6.1 Muon production curve

To build the production histogram of muons as a function of distance along the shower axis, the point on the shower axis closest to the muon production location was found and subsequently converted to a distance. For an individual muon, let the production position be  $\vec{\mu} = (\mu_x, \mu_y, \mu_z)$ , and the closest position on the axis be  $\vec{p} = (t \sin \theta, 0, t \cos \theta)$  for some yet to be determined value of  $t$ . Note that we have assumed the shower is coming directly from east and has a zenith angle of  $\theta$ . The value of  $t$  here is the length of  $\vec{p}$  and thus is the distance along the shower axis we desire. To find  $t$ , consider the vector  $\vec{v} = \vec{\mu} - \vec{p}$ , which will be orthogonal to  $\vec{p}$ . Therefore

$$\vec{v} \cdot \vec{p} = (\mu_x - t \sin \theta, \mu_y, \mu_z - t \cos \theta) \cdot (t \sin \theta, 0, t \cos \theta) = 0 \quad (6.1)$$

Upon rearranging we find that

$$t = \mu_x \sin \theta + \mu_z \cos \theta \quad (6.2)$$

Thus  $\mu_x \sin \theta + \mu_z \cos \theta$  is the distance along the shower axis for the *estimated* production point of the muon. An example histogram of the distribution of distances is shown in Figure 6.2. The histogram has been filled using the weights of each muon as given by CORSIKA. The number of muons used to fill the histogram is represented by the “Entries” statistic, whilst the integral of the histogram ( $\sim 1.9 \times 10^8$ ) corresponds to the total weighted number of muons. The same applies for the subsequent histograms. We can see that the majority of muons are produced at distances  $< 15$  km from the ground as measured along the shower axis, with the first muons produced at around 32 km. To check the approximation of muons being produced on the shower axis, a histogram of the magnitude of  $\vec{v}$  (the distance

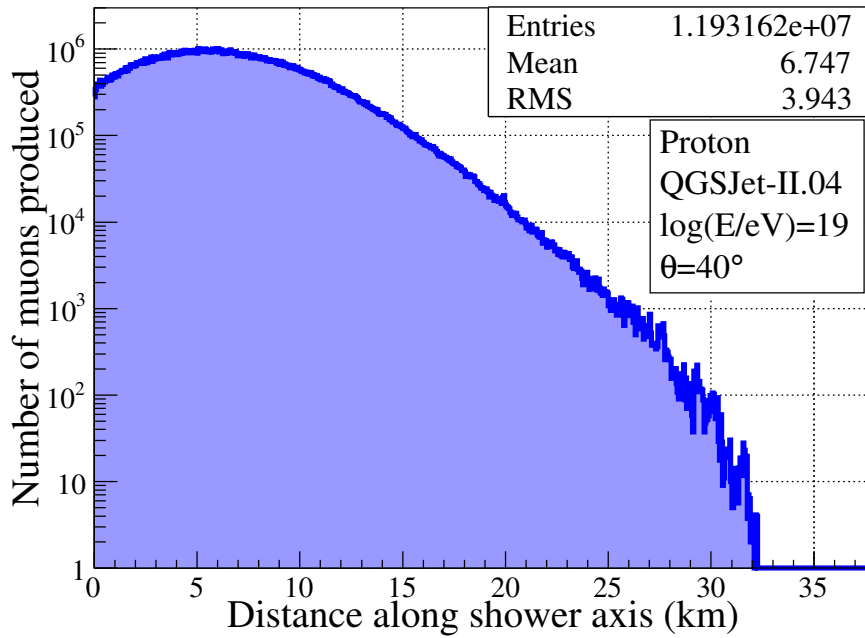


**Figure 6.2:** A histogram of the estimated number of muons produced in an extensive air shower at different distances along the shower axis. 0 m is taken to be the location of the shower core at Auger ground. Each bin is 50 m wide.

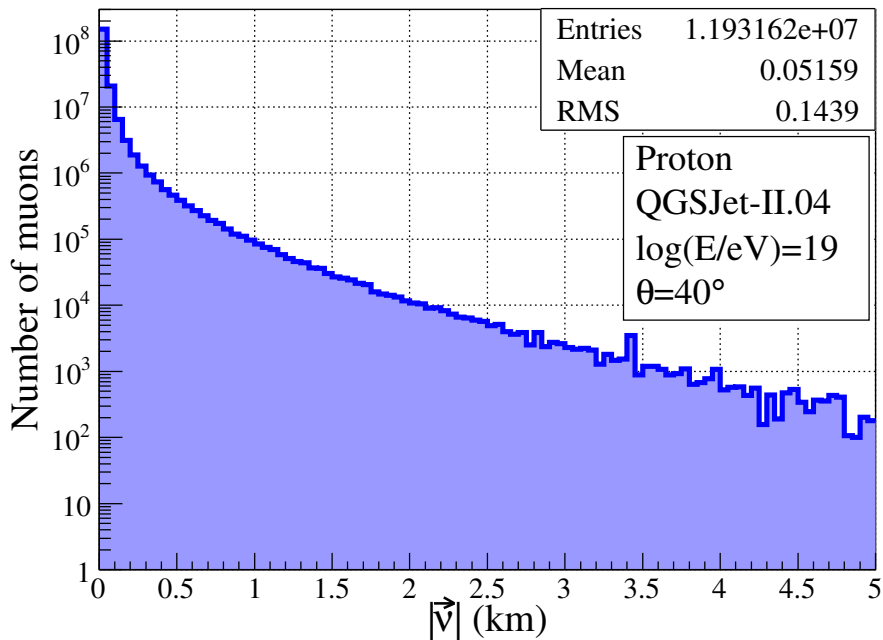


**Figure 6.3:** A histogram of the distances between the muon production location as given in CORSIKA and the closest point to this position on the shower axis i.e. the estimated production point. The bin widths are 50 m.

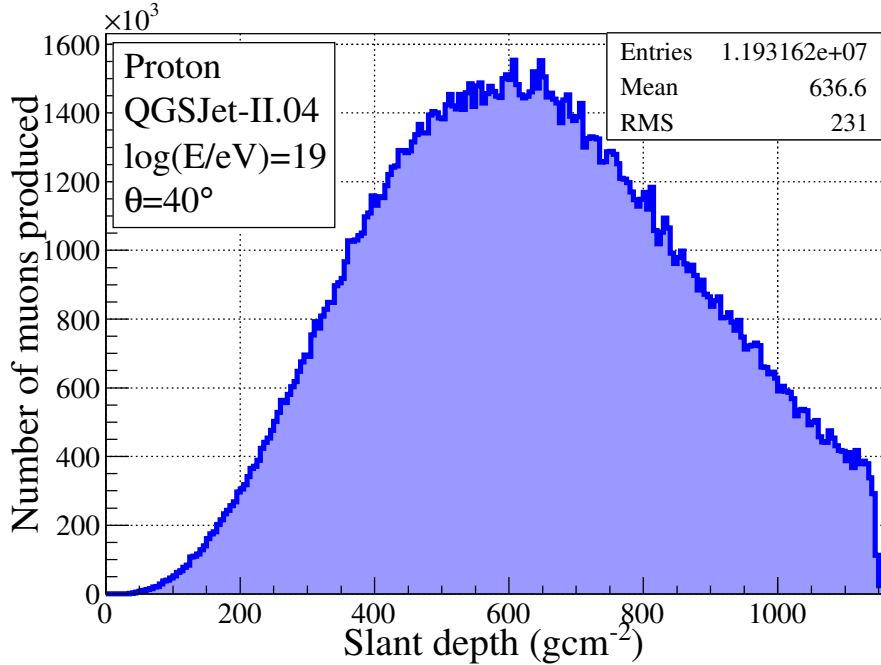


**Figure 6.4:** A histogram of the muon production curve in terms of atmospheric slant depth.  $0 \text{ g cm}^{-2}$  refers to the top of the atmosphere. The bin widths are  $5 \text{ g cm}^{-2}$ .

between the true production point from CORSIKA and the estimated production point) is shown in Figure 6.3. Approximately 90% of muons are produced within 100 m of the shower axis. Muons further out than this are likely the result of sub-showers initiated further away from the axis. Lastly, by converting the *vertical height* of  $\vec{p}, p_z$ , to an atmospheric slant depth via

$$X = M(p_z)/\cos \theta \text{ g cm}^{-2} \quad (6.3)$$

we arrive at the production curve as a function of slant depth, shown in Figure 6.4. Here,  $p_z$  is being measured from sea level and  $M(p_z)$  is the vertical atmospheric depth above  $p_z$ . The function  $M(h)$  is the atmospheric column density profile at Malargüe, Argentina in April. Details on this function and atmospheric profiles in general can be found in Appendix B. Although not used directly in the Monte Carlo model, this figure is provided as a reference.

## 6.2 Opening angle and energy distributions

To accurately simulate the geometrical and attenuation effects in the Monte Carlo model, the opening angle and kinetic energy at production for muons in each bin of the histogram in Figure 6.2 were recorded. These components were calculated using the momentum at production of each muon,  $\vec{P}$ , and the vector defining the shower

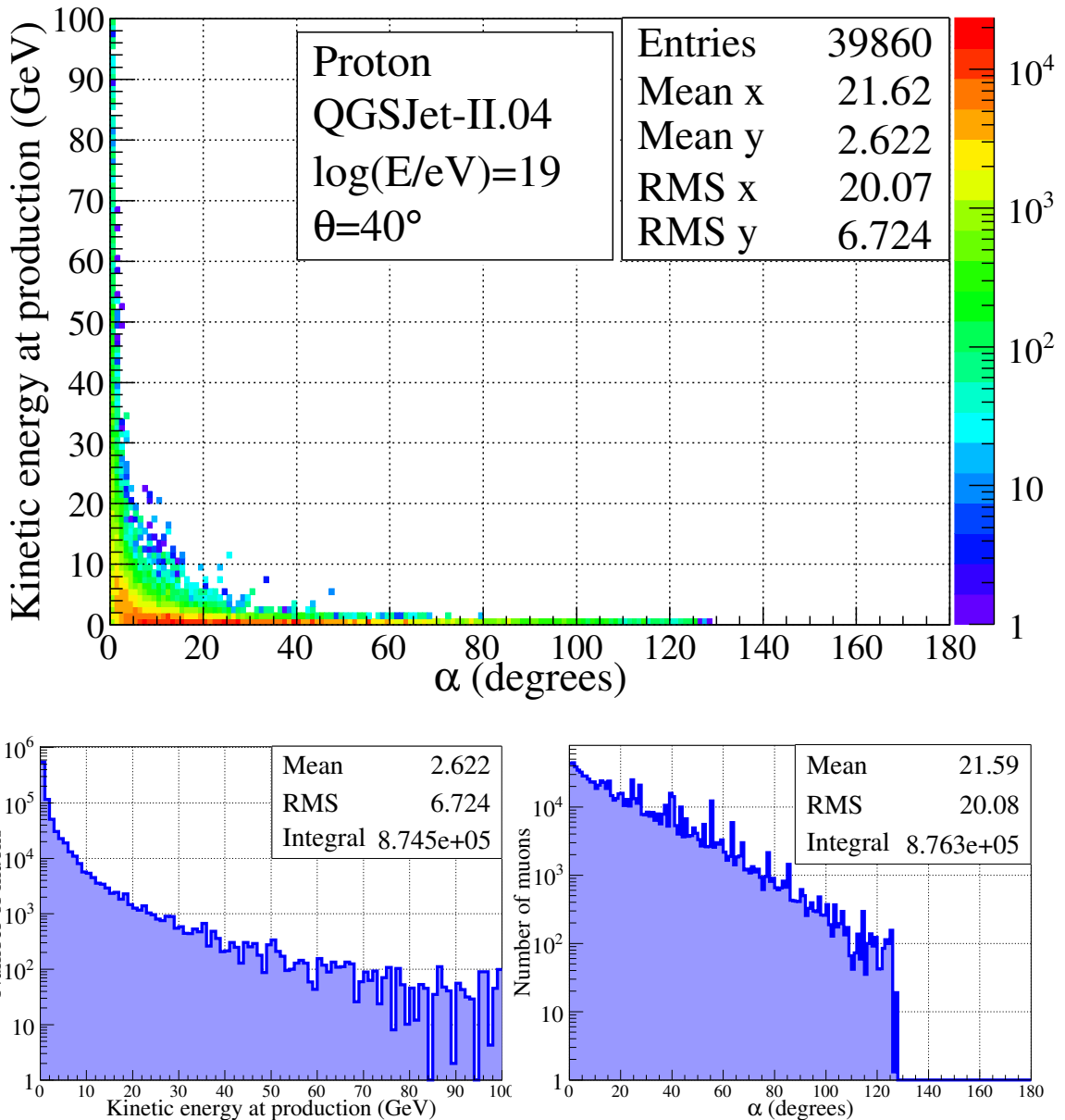


**Figure 6.5:** (Top) The 2D distribution of opening angles and production energies for muons originating between 4000 m and 4050 m above the ground as measured along the shower axis. (Bottom) The associated one dimensional histograms of each axis of the 2D histogram. On the left is the production energies, on the right is the opening angles.

axis,  $\vec{S}$ . The opening angle,  $\alpha$ , of each muon was calculated using the dot product,

$$\alpha = \arccos \left( \frac{\vec{P} \cdot \vec{S}}{|\vec{P}| |\vec{S}|} \right) \quad (6.4)$$

whilst the kinetic energy at production was calculated via

$$E = \sqrt{\vec{P} \cdot \vec{P} + M_\mu^2} - M_\mu \quad (6.5)$$

where  $M_\mu$  is the mass of the muon in  $\text{GeV}/c^2$  and  $\vec{P}$  is in units  $\text{GeV}/c$ . An example 2D distribution is shown in Figure 6.5 together with the corresponding 1D histograms of each axis. The number of entries shown for the 2D histogram again represents the unweighted number of particles. The weighted number of particles is given correctly by the integral of the 1D opening angle histogram as roughly  $8.76 \times 10^5$  muons. The discrepancy between this value and the one stated in the 1D production energy histogram arises because there are muons which are produced with energies greater than 100 GeV which are not shown.

From the 2D histogram note how high energy muons are only ever produced with small opening angles, whilst low energy muons can be produced with a wide range of opening angles. This behaviour arises from the fact that

$$\sin \alpha \approx \frac{p_t}{E} \quad (6.6)$$

where  $p_t$  is the transverse momentum of the muon [86]. The 1D histogram of production energies can give us an idea of what fraction of muons will reach the ground. As a very rough approximation, if every muon was produced on the shower axis at the mean slant depth  $\approx 637 \text{ g cm}^{-2}$  (as given in Figure 6.4) and travelled parallel to the shower axis until reaching ground, then the slant depth traversed by each muon would be  $\approx 510 \text{ g cm}^{-2}$ . Approximating the energy loss of each muon as  $2 \text{ MeV/g cm}^{-2}$  means any muon produced with less than 1 GeV of kinetic energy would not reach ground. This equates to the number of particles in the first bin of the production energy histogram in Figure 6.5, roughly  $5.5 \times 10^5$  muons. This is more than 60% of the total number of muons produced at this position (4000-4050 m up along the shower axis). Assuming other distance bins have similar production energy distributions, we thus expect that when the Monte Carlo simulation is performed in full a large fraction of muons will attenuate before reaching ground.

### 6.3 The Monte Carlo model

With the required distributions constructed for this single CORSIKA shower, it was now possible to create a simple Monte Carlo simulation to study how geometrical and attenuation effects contribute to the asymmetry in muon particle density. In

all Monte Carlo simulations the “shower” was made to arrive from the positive  $x$  direction (magnetic north in CORSIKA conventions) with a zenith angle equivalent to that of the CORSIKA shower the distributions were from.

The Monte Carlo was performed as follows. Starting from the first bin in the muon production histogram (Figure 6.2), the number of muons in each bin,  $N_\mu(h)$ , was simulated to be produced at the distance along the shower axis corresponding to the middle of that bin. For example, the first set of muons was simulated at 25 m from the ground as measured along the shower axis. Secondly, the 2D opening angle and energy distribution for that bin was randomly sampled to assign to each muon an opening angle,  $\theta_\mu$ , and kinetic energy, which together with the muon rest mass made up the total energy,  $E_\mu$ . Each muon was also given a random azimuthal angle,  $\phi_\mu$ , between 0 and  $2\pi$ . These properties were all that was needed to define every muon’s direction and probability of hitting the ground. For a muon produced at location  $\vec{p} = (x_\mu, 0, z_\mu)$ , measured in the ground frame with respect to the shower core, and momentum vector  $\vec{P} = (P_x, P_y, P_z)$ , its ground location,  $\vec{g}_\mu$ , was given by

$$\vec{g}_\mu = \vec{p} - (z_\mu/P_z)\vec{P} \quad (6.7)$$

To get  $\vec{P}$  itself, the values of  $\theta_\mu$  and  $\phi_\mu$  were used to define the momentum vector of the muon in spherical coordinates, with the  $\theta$  axis in the same direction as the shower axis. This vector was given by

$$\vec{P}' = \begin{bmatrix} 1 \\ \pi - \theta_\mu \\ \phi_\mu \end{bmatrix} \quad (6.8)$$

which can be expressed in Cartesian coordinates (of the shower plane coordinate system) as

$$\vec{P}' = \begin{bmatrix} \sin(\pi - \theta_\mu) \cos(\phi_\mu) \\ \sin(\pi - \theta_\mu) \sin(\phi_\mu) \\ \cos(\pi - \theta_\mu) \end{bmatrix} \quad (6.9)$$

To transform this vector to the regular ground based coordinate system, the vector was simply rotated about the  $y$  axis clockwise by the shower zenith,

$$\vec{P} = \begin{bmatrix} \cos \theta & 0 & -\sin \theta \\ 0 & 1 & 0 \\ \sin \theta & 0 & \cos \theta \end{bmatrix} \vec{P}' \quad (6.10)$$

At this stage the final ground position,  $\vec{g}_\mu$ , was recorded for each muon. This made up the list of particles at ground with no decay process implemented. In the case of considering attenuation affects, the possible decay of each muon had to be accounted for. This was done by first, finding the total distance,  $d$ , and total slant depth,  $X_\mu$ , the muon had to travel through to hit the ground (assuming a straight

line trajectory),

$$d = |\vec{p} - \vec{g}_\mu| \quad (6.11)$$

$$X_\mu = \frac{M(1.452) - M(1.452 + z_\mu)}{\cos \theta_\mu} \quad (6.12)$$

where again we have used the atmospheric profile of Malargue,  $M(h)$ , to calculate the slant depth. The value of 1.452 km corresponds to the height above sea level of the observation level (ground) of the CORSIKA shower. The muon's path was then broken up into  $n$  intervals of length  $I = d/n$ . At the start of each interval, the *total* energy of the muon at that point was used to define its gamma factor and hence velocity,

$$\gamma_\mu = E_\mu/M_\mu \quad (6.13)$$

$$v = c\sqrt{1 - 1/\gamma_\mu^2} \quad (6.14)$$

These values were then used to calculate the boosted lifetime of the muon,  $L_B$ , and the time needed to traverse the interval based on the muons velocity,  $T_I$ ,

$$L_B = \tau \times \gamma_\mu = 2.2\gamma_\mu \times 10^{-6} \text{ s} \quad (6.15)$$

$$T_I = I/v \quad (6.16)$$

This allowed for the calculation of the number of lifetimes an individual muon would need to survive in order to traverse the interval,

$$N_L = T_I/L_B \quad (6.17)$$

The probability the muon would survive traversing the interval was thus

$$P = e^{-N_L} \quad (6.18)$$

The decay process was then simulated by generating a random number between 0 and 1. If the result was less than  $P$  then the muon continued to the next interval, now with an energy

$$E'_\mu = E_\mu - aX_I \quad (6.19)$$

where  $X_I$  is the slant depth traversed by the muon in the interval,

$$X_I = X_\mu - \frac{M(1.452) - M(1.452 + z_\mu - n_i I \cos \theta_\mu)}{\cos \theta_\mu} \quad (6.20)$$

and the ionisation energy loss,  $a$ , is given by the Bethe-Bloch formula. We have used the same parameterisation for  $a$  as in [86], where

$$a = \left( 2.06 + 0.5453\xi + \frac{0.0324}{(\xi + 1.0312)^2} \right) \times 10^{-3} \text{ GeV/g cm}^{-2} \quad (6.21)$$

for  $\xi = \log_{10}(E_\mu)$ . Note in Equation 6.20  $n_i$  is simply referring to the interval number,  $n_i = 1, 2 \dots n$ . Also  $X_\mu$  was updated to be the remaining slant depth,  $X'_\mu = X_\mu - X_I$ . Radiative losses were not included in the energy loss process as these only appear above 50 GeV [86], an energy at which relatively few muons were produced.

If the survival probability was less than the randomly generated number then the muon was set to decay and its final intended ground position would not be added to the list of particles surviving the attenuation Monte Carlo. The reason for performing the decay process in a step-wise fashion rather than trying to come up with an analytical expression was that such an expression would have only been possible by making additional approximations regarding the atmospheric profile and muon speed. Considering we were not accounting for other small effects such as scattering and magnetic deflection, we continued with the above approach. An example of an analytical expression is given in [86] and although faster, when we tested it the results were no better than when using the step-wise method.

Weights were also incorporated into the Monte Carlo, for the purpose of reducing run-time. This meant only some fraction  $1/w$  of the particles in each bin were simulated. Particles which survived and reached the ground would be assigned a weight of  $w$ , which would be used when filling the relevant histograms. Using  $w = 10$  allowed the run-time of the program to be sufficiently fast whilst also maintaining enough statistics, provided the number of intervals the muon's trajectory was broken into,  $n$ , wasn't overly large e.g.  $> 100$ .

## 6.4 Results

The results from CORSIKA directly and the Monte Carlo simulations (with and without decay) for the asymmetry in muon particle density are shown in Figures 6.6 and 6.7 respectively. The asymmetry was measured for an annulus between 950 m and 1050 m in the shower plane, as per usual, and the decay process set to 20 intervals. The density was also calculated as done previously, by dividing the weighted number of muons by the area of the section *on the ground* which corresponded to the annular region in the shower plane. To estimate the asymmetry in CORSIKA truth and the results from our model, Equation 5.1 has been fit to the histograms, as done in the previous chapter for EM particle density. The errors bars on each bin were calculated using the method described in Section 5.3.

For this example shower, the histogram without a decay process shows a clear asymmetry, with an asymmetry amplitude of roughly  $0.170 \pm 0.002$ . This value is slightly below the CORSIKA amplitude of  $0.19 \pm 0.01$ . The shape of the profile is close to symmetric about  $\zeta = 0^\circ$  and the absolute value of the density is roughly 4

times larger than that from CORSIKA. This is not surprising as no decay process has been implemented here.

For the asymmetry profile with attenuation, the shape appears slightly narrower than without attenuation and the absolute value of the density is now nearly identical to that of the CORSIKA output. The asymmetry amplitude is larger than the CORSIKA value however, with  $k = 0.216 \pm 0.004$ . Although the values of  $k$  for the attenuation MC and CORSIKA truth do not agree to within uncertainty, there is only  $\sim 10\%$  difference between them. The discrepancy is likely due to the combination of assumptions/approximations made in both the geometrical and attenuation aspects of our model. Taking the attenuation MC value of  $k$  as our final value, this means geometrical effects alone are responsible for the initial 0.17 increase in asymmetry amplitude, and attenuation effects responsible for a further (additive) 0.0416 increase. In short, geometrical effects are contributing  $0.17/0.0416 \approx 4$  times more to the final asymmetry than attenuation effects in this particular example. One additional note is that the non-symmetric nature about  $\zeta = 0^\circ$  of the CORSIKA result, in comparison to the Monte Carlo simulations, is probably due to the random components of the additional factors that CORSIKA accounts for e.g. scattering and off axis production. The use of larger weights, up to several thousand for some muons, may also play a role.

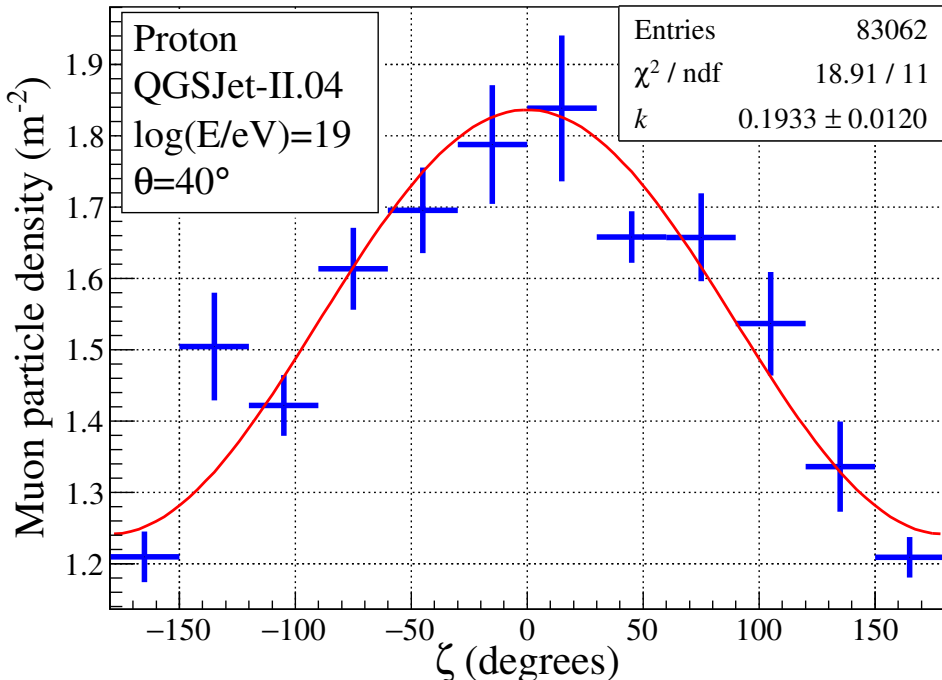


**Figure 6.6:** Asymmetry in muon particle density measured from the output of CORSIKA ground particles. Results from fitting Equation 5.1 to the data are shown in the top right.

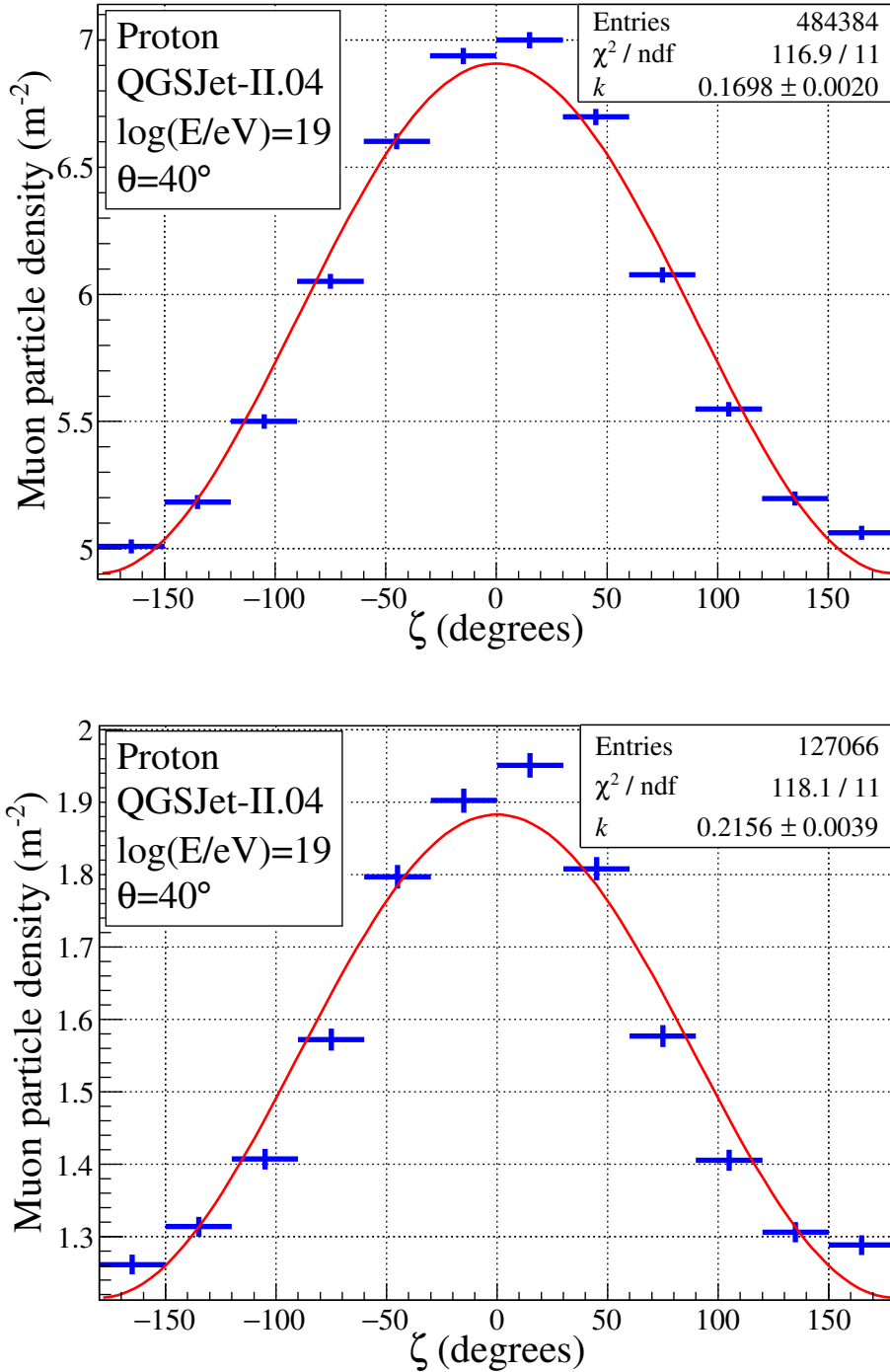


**Figure 6.7:** Asymmetry in muon particle density generated from the Monte Carlo outlined in Section 6.3. The top plot is the geometry only Monte Carlo, the bottom plot also includes attenuation. Results from fitting Equation 5.1 to the data are shown in the top right of each plot.

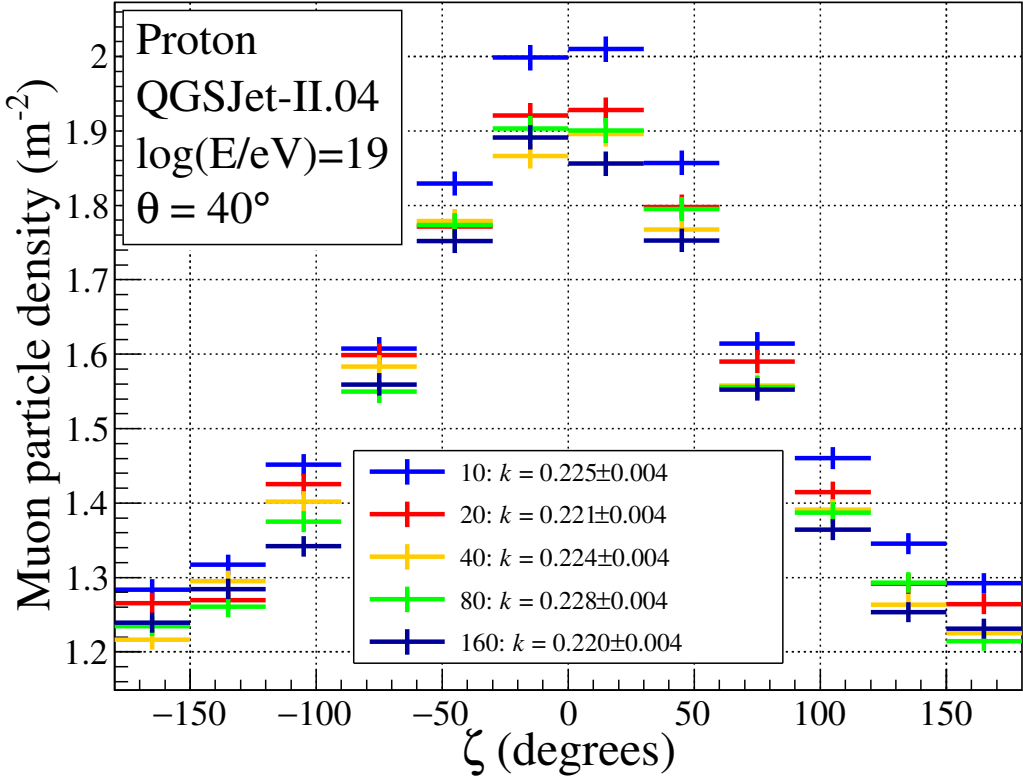


**Figure 6.8:** Measurements of the muon particle density from the attenuation Monte Carlo for different numbers of intervals used in the decay calculation. The legend at the bottom of the figure indicates which histogram corresponds to which number of intervals, with the values of  $k$  alongside representing the asymmetry amplitude for that histogram.

To briefly investigate the discrepancy in the asymmetry amplitude between CORSIKA and our attenuation inclusive Monte Carlo, specifically whether it could be decreased, we tried increasing the number of intervals in the decay simulation. Figure 6.8 shows the asymmetry in muon particle density, measured as before, for the attenuation Monte Carlo run on the same shower with varying numbers of intervals. The shower used is the same as in the previous plots, however due to the random nature of the Monte Carlo the asymmetry amplitude for the  $n = 20$  case is slightly different to that shown in Figure 6.7. Also note that the properties of the muons sampled in each histogram are exactly the same, meaning the only difference between the histograms is the number of decay intervals used in the simulation of attenuation. At the bottom of the figure the asymmetry amplitudes for the different histograms are shown, with the number of intervals used in the decay simulation given before each  $k$  value. We can see that the asymmetry amplitudes are all within uncertainty of one another and the shapes of the histograms are largely the same, the only noticeable difference being for the  $n = 10$  histogram with increased densi-

ties at  $\pm 15^\circ$ . Collectively, this indicates that increasing the number of intervals in the decay simulation beyond 20 should not give significantly different results, and that the cause of the discrepancy between CORSIKA and our model lies elsewhere.

To see how the contributions of geometrical and attenuation effects differed with zenith angle, 20 proton and 20 iron showers of the same energy,  $10^{19}$  eV, and varying zenith angles,  $30\text{--}60^\circ$ , were simulated with CORSIKA. For each shower, the same process of generating the required distributions, sampling from these distributions to simulate the muon component of the shower and then measuring the asymmetry at ground with and without attenuation, was performed. In addition to checking how the contributions varied with zenith angle, comparing the resulting asymmetry amplitudes also provided checks of whether the discrepancy between our attenuation Monte Carlo and CORSIKA was zenith dependent, and whether the magnitude of the geometrical asymmetry would continue to be lower (as expected) than the CORSIKA output. Figure 6.9 shows the three asymmetry amplitudes; CORSIKA, no attenuation MC and attenuation MC, for the two sets of showers as a function of zenith angle. All showers were simulated with the same incoming azimuthal direction (magnetic north), with the number of intervals set to 20, based on the results in Figure 6.8.

Both primaries show an increase in the magnitude of the asymmetry with zenith angle up to approximately  $50 - 55^\circ$  before dropping slightly. This is simply demonstrating what was learnt in Chapter 4. The attenuation Monte Carlo overestimates the asymmetry when compared to CORSIKA in nearly all cases, however the discrepancy appears to decrease at larger zenith angles, particularly for iron primaries. In fact the CORSIKA and attenuation MC values for  $k$  tend to be closer for iron primaries overall. The reason for this is not clear and could very well be a coincidence, considering the small number of showers analysed. As for the geometry only Monte Carlo, the asymmetry amplitudes are generally lower than the CORSIKA result, though in some cases they do agree to within uncertainty with both CORSIKA and the attenuation MC. Again these instances occur at large zenith angles. It is not known whether this is a success of the model or some cancelling out of factors which haven't been accounted for, such as scattering and off-axis production. Overall, it is evident that geometrical effects are the dominant cause of asymmetry in the muon component of extensive air showers.

For low zenith angles the additive contributions of geometry and attenuation to the total asymmetry measured by the attenuation Monte Carlo are approximately 0.15 & 0.05, and 0.14 & 0.04 for proton and iron respectively. At zenith angles between  $50\text{--}55^\circ$  these contributions change to roughly 0.23 & 0.035, and 0.2 & 0.02. Taking the ratios of these pairs tells us the how much larger the contribution from geometrical effects is to the asymmetry than attenuation effects. For proton showers, the ratio of the geometrical contribution to attenuation contribution goes from being roughly 3 times larger at  $30^\circ$  to 6-7 times larger around  $50^\circ$ . For iron showers, the

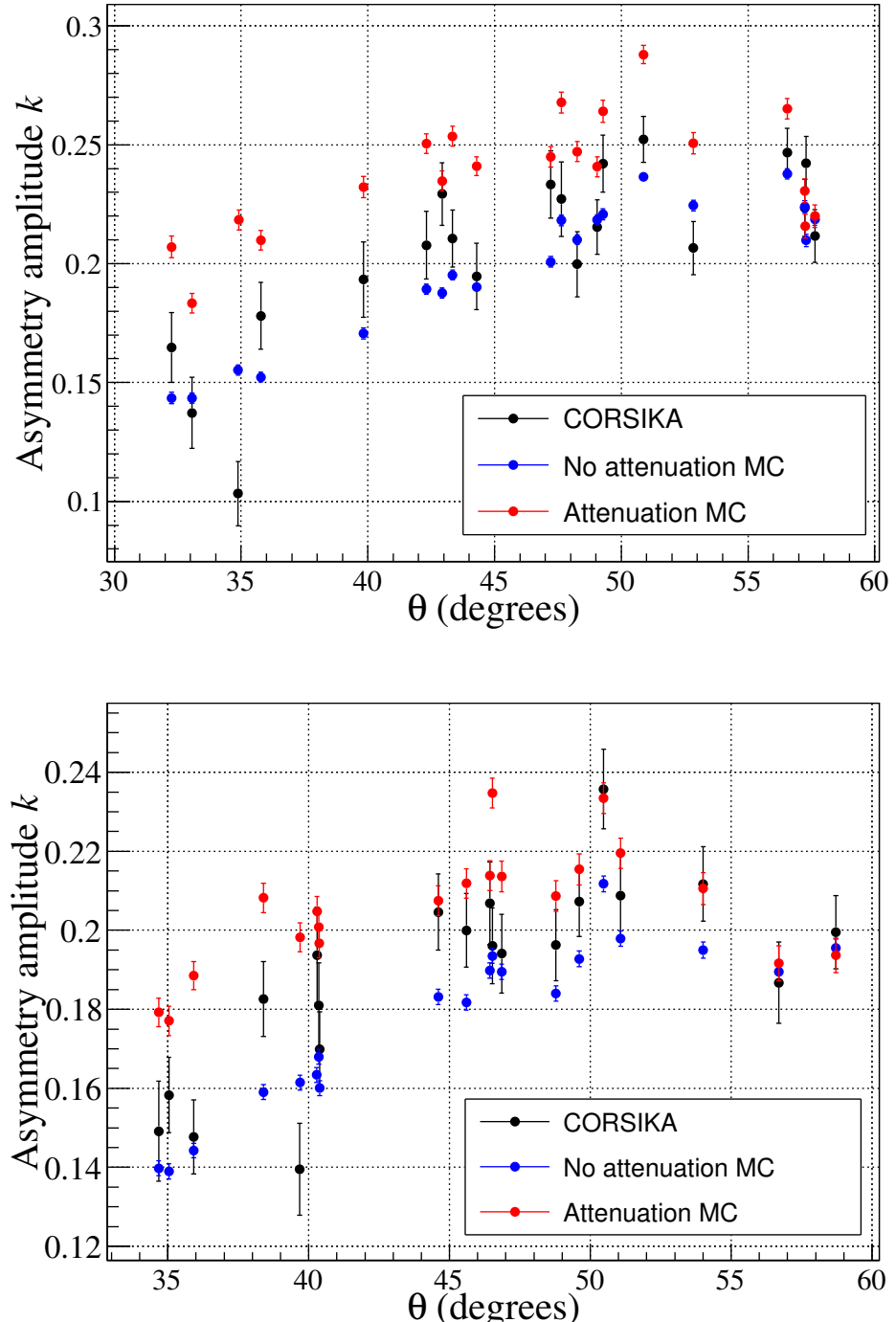


**Figure 6.9:** Asymmetry amplitudes,  $k$ , for 20 proton (top) and 20 iron (bottom) showers from each type of asymmetry profile (CORSIKA, MC without attenuation, MC with attenuation), plotted as a function of shower zenith angle.

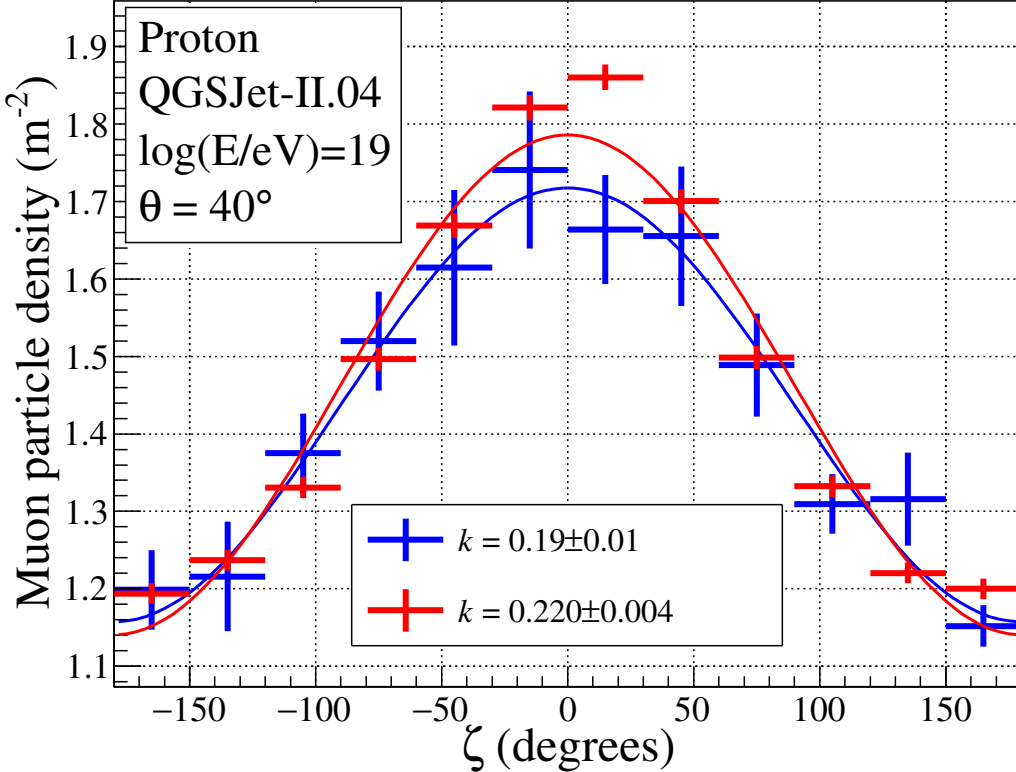


**Figure 6.10:** The asymmetry in muon particle density predicted by the attenuation Monte Carlo (red) and CORSIKA truth (blue) for a CORSIKA shower simulated without the presence of earth's magnetic field.

same ratio increases from  $\sim 3.5$  at  $35^\circ$  to  $\sim 10$  near  $50^\circ$ . Thus, in addition to being the primary cause of asymmetry in muon particle density, geometrical effects appear to become more dominant at larger zenith angles.

As a simple, though certainly not comprehensive, check of whether or not accounting for magnetic deflection alters our model's result, a CORSIKA shower with no magnetic field (magnetic field strength values set to  $10^{-6}$ ) was simulated. The CORSIKA asymmetry and attenuation Monte Carlo predicted asymmetry are shown together in Figure 6.10. The difference in asymmetry amplitude is similar to what has already been observed, indicating that the source of the difference between CORSIKA and our Monte Carlo model is likely in the other factors not accounted for e.g. scattering and off-axis production. On the whole, we are satisfied with our Monte Carlo's results as they match the initial expectation of the asymmetry in muon particle density being predominantly caused by geometry and are not overly dissimilar from CORSIKA truth.

## 6.5 Conclusions

This chapter has attempted to separate the geometrical and attenuation components of asymmetry in muon particle density. This was achieved by constructing a Monte Carlo model of muon production and propagation, which assumed that muons are produced on the shower axis and travel in straight lines, to produce two estimates of the asymmetry - one based on solely geometrical effects and the other including both geometrical and attenuation effects. The model took data from individual CORSIKA showers as input and built distributions of production height (measured along the shower axis) and opening angle/production energy to sample from to generate the asymmetry profiles. Results from the model showed that geometry is the primary factor in producing asymmetry in muon particle density. Quantitatively, we showed that geometry can contribute anywhere from 3 to 10 times more than attenuation for showers with zenith angles  $> 30^\circ$ .

Regarding the attenuation inclusive Monte Carlo, it decreased the number of muons which reached the ground significantly compared to the geometrical only simulation. This brought the resulting particle density values very close to the CORSIKA output, although there was generally a slightly larger asymmetry amplitude for our model. Tests using an increased number of intervals in the decay simulation process and without magnetic fields to deflect muons in the CORSIKA simulation did not alter the discrepancy. However the difference is small enough that we are relatively confident that a more robust and thorough treatment of all the factors entering the production and propagation of muons in air shower, as done in [86], would bring the model results into agreement with CORSIKA. Moreover, the purpose of this model was to be a simple and easy to understand method of checking the contributions of geometry and attenuation to the asymmetry in muon particle density - exact agreement was never expected. Effects such as scattering and off axis production, if included in the model, may make it difficult to fully separate geometry and attenuation. This is because these effects depend on the inclination of the shower (large scale) and on the energy of individual muons involved in them (small scale). Fully investigating these additions is beyond the scope of this thesis but is certainly a recommendation for future work.

A natural extension to this study would be to average the distributions of production height and opening angle/energy over many showers and use the results to build a true model of muon propagation (rather than relying on individual CORSIKA showers as input). This could then be used to study how changing each component of the model impacts the overall asymmetry. The first part of this suggestion has already been accomplished in [86], so perhaps utilising that work would be useful in further probing the underlying causes of asymmetry in muon particle density.



---

# Using asymmetry to improve $X_{\max}$ estimates from LDF slope parameters

---

The previous chapters have focused on building an understanding of asymmetry and how it could potentially be used for mass composition studies. However there are other methods which utilise the ground detectors of the Pierre Auger Observatory to learn about mass composition. These typically involve trying to indirectly measure  $X_{\max}$ . Examples include,

- Applying machine learning algorithms, such as deep neural networks, to the signals induced by secondary particles in the WCDs [87]
- Using the principles of air shower universality to decompose signal traces into the contributions from different shower components [88]
- Using correlations between the risetimes of signals in the WCDs [89]

Another method is correlating the slope parameters of the lateral distribution function, or LDF (see Section 3.2.4), with  $X_{\max}$ , as done by Alex Hervé in his PhD thesis [90] and Mary Diaz [91], another member of the Pierre Auger Collaboration. The goal of this chapter is to use the parameterisations of the asymmetry magnitude found in Chapter 4 to improve event by event LDF fits, and then see whether the corrected slope parameters provide better estimates of  $X_{\max}$  via this technique. Since the asymmetry parameterisations were performed on simulations, the following analysis will necessarily also rely on simulated data. Should the method be viable, it could be applied to real data, assuming a parameterisation of the asymmetry in real data could be found.

## 7.1 LDF slope parameters versus distance to $X_{\max}$

To understand the method of extracting  $X_{\max}$  from the slope parameter of an LDF, simulations with dense rings placed every 100 m between 500-2500 m were initially used to obtain the best possible estimate of the LDF for several showers. Using

dense rings also eliminated any effects related to asymmetry. These simulations were in fact a subset of the data used in Section 4.4 for the parameterisations of the asymmetry amplitude. Specifically, we only used showers which had a Monte Carlo energy between  $19.1 \leq \log(E/\text{eV}) \leq 19.4$ . This corresponded to 568 proton showers and 508 iron showers.

For each dense ring the mean signal and standard error of the 12 stations was found and plotted as a function of radius in the shower plane. Similar to the asymmetry studies, only dense rings which had all 12 stations triggering were included in the fit. Compared to an LDF which is fit using only stations triggered in the regular Auger SD array, these “dense ring LDFs” were highly constrained, thanks to the accuracy and precision of the mean signal measurements. To further simplify the process, the function initially fitted to the distribution of signals was the *original* Nishimura-Kamata-Greisen (NKG) function,

$$\rho_{\text{NKG}}(r, s, N_e) = \frac{N_e}{(r_M)^2} \frac{\Gamma(4.5 - s)}{2\pi\Gamma(s)\Gamma(4.5 - 2s)} \times \left(\frac{r}{r_M}\right)^{s-2} \left(1 + \frac{r}{r_M}\right)^{s-4.5} \quad (7.1)$$

which has only one slope parameter,  $s$ . This is in contrast to the *modified* NKG function used in normal event reconstruction (see Section 3.2.4) which has two slope parameters,  $\beta$  and  $\gamma$ . In Equation 7.1  $s$  is a fitted slope parameter, known as the “shower age”,  $N_e$  is a fitted normalisation parameter, approximately representing the number of electrons at ground level,  $r$  is the distance from the detector to the shower axis and  $r_M$  is the radius inside which, on average, 90% of the shower’s energy is deposited. This is known as the Moilre radius and in our case  $r_M \approx 100 \text{ m}$  [92]. An example LDF as measured by the dense rings with the original NKG function fitted is shown in Figure 7.1. In order to get a good fit with the original NKG function the  $N_e$  and  $s$  parameters were given initial guesses of  $10^{10}$  and 1.5 respectively. Note also that the Monte Carlo geometry was used for these fits, so that every station in each dense ring had a radius  $r$  equal to an exact multiple of 100 m.

For our first attempt at trying to find a correlation between  $X_{\text{max}}$  and the slope parameter of the original NKG LDF,  $s$  was compared to the difference between  $X_{\text{ground}}$  and  $X_{\text{max}}$ , where  $X_{\text{ground}}$  is the atmospheric slant depth of the ground as measured along the shower axis. This quantity is known as the distance to  $X_{\text{max}}$  or DX. The atmospheric profile used in the simulated showers was that of Malargüe during April (parameters given in Table B.1 in Appendix B) where the average vertical atmospheric depth  $X_{\text{vert}} \approx 880 \text{ g cm}^{-2}$ . Thus, for our calculations, DX was given by

$$\text{DX} = X_{\text{ground}} - X_{\text{max}} = \frac{X_{\text{vert}}}{\cos \theta} - X_{\text{max}} = \frac{880 \text{ g cm}^{-2}}{\cos \theta} - X_{\text{max}} \quad (7.2)$$

The idea was that for some measured values of  $s$  and  $\theta$ , from either the WCD or SSD, one could estimate DX via  $s$  and then convert this value to  $X_{\text{max}}$  via Equation

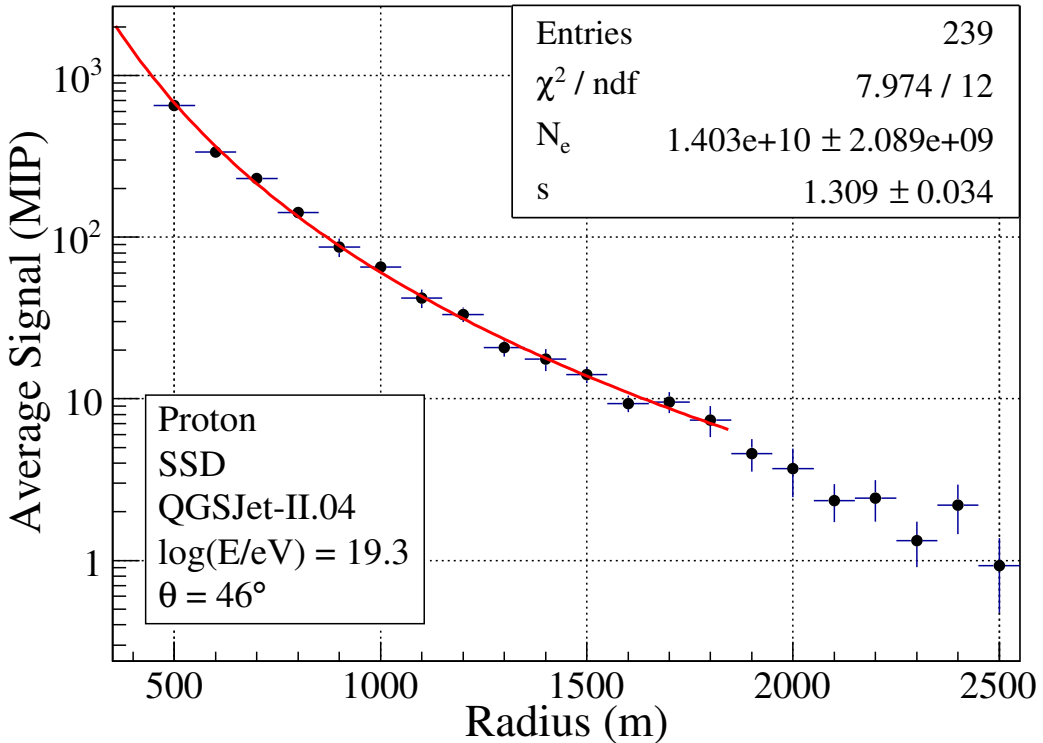


**Figure 7.1:** The original NKG LDF fitted to the average signals measured by dense rings at radii spaced by 100 m. The error bars are the standard error on the mean. Past 1800 m, not all stations in each dense ring were triggered, thus they were not used in the fit.

**7.2.** If this method was applied to real showers, then although  $X_{\text{vert}}$  at Auger does vary day to day, as long as the correct value is measured at the time of the event, the calibration between  $s$  and DX could still be used to determine  $X_{\text{max}}$ .

Figure 7.2 shows  $s$  plotted against DX for every shower in the data set, for both the WCD and SSD. No cuts have been applied to the quality of the LDF fits or the geometry of the showers. The blue points represent iron showers and the red points proton showers. There is considerable overlap between the two, however at low values of DX there is a slight average separation, with iron showers generally having a higher value of  $s$  (corresponding to a flatter LDF) for a given DX than proton showers. At higher DX values the difference appears to reduce. The additional muon content in iron showers relative to proton showers is likely responsible for this effect, as the LDF of purely muons is flatter than the LDF of the electromagnetic component of air showers. Another simple observation is that the uncertainties in the values of  $s$  are larger for the SSD than the WCD. This is ultimately a result of the smaller detecting area of the scintillator, resulting in greater signal fluctuations and subsequently a more uncertain value for the slope parameter of the LDF.

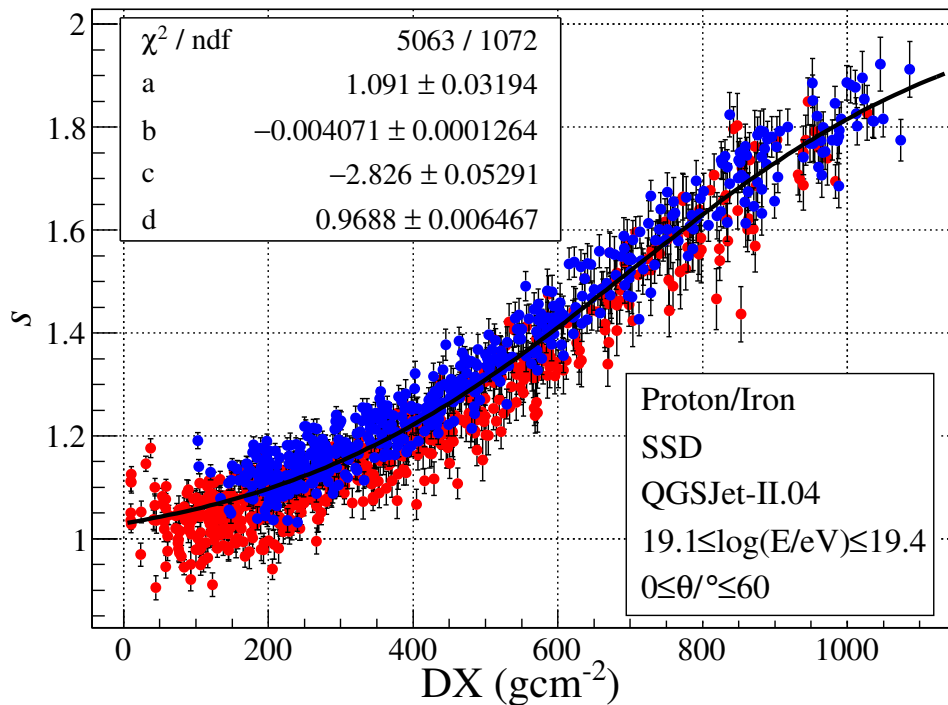
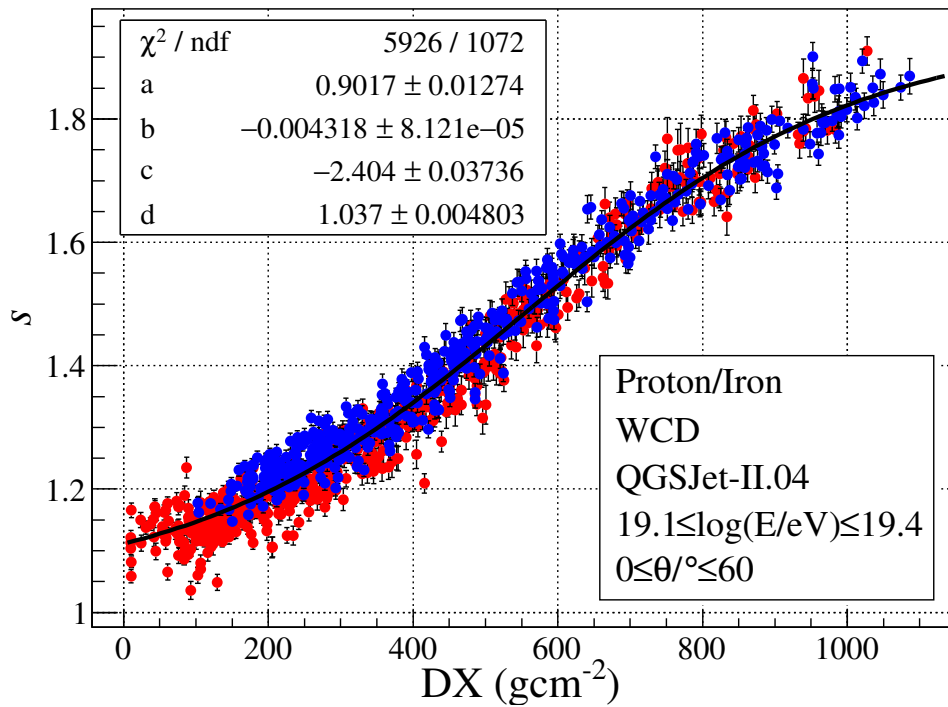


**Figure 7.2:** Calibrations of the correlation between the age parameter of the original NKG function,  $s$ , and the distance to  $X_{\max}$ ,  $DX$ , for both the WCD (top) and SSD (bottom). Values of the fit parameters are shown in the top left of each plot.

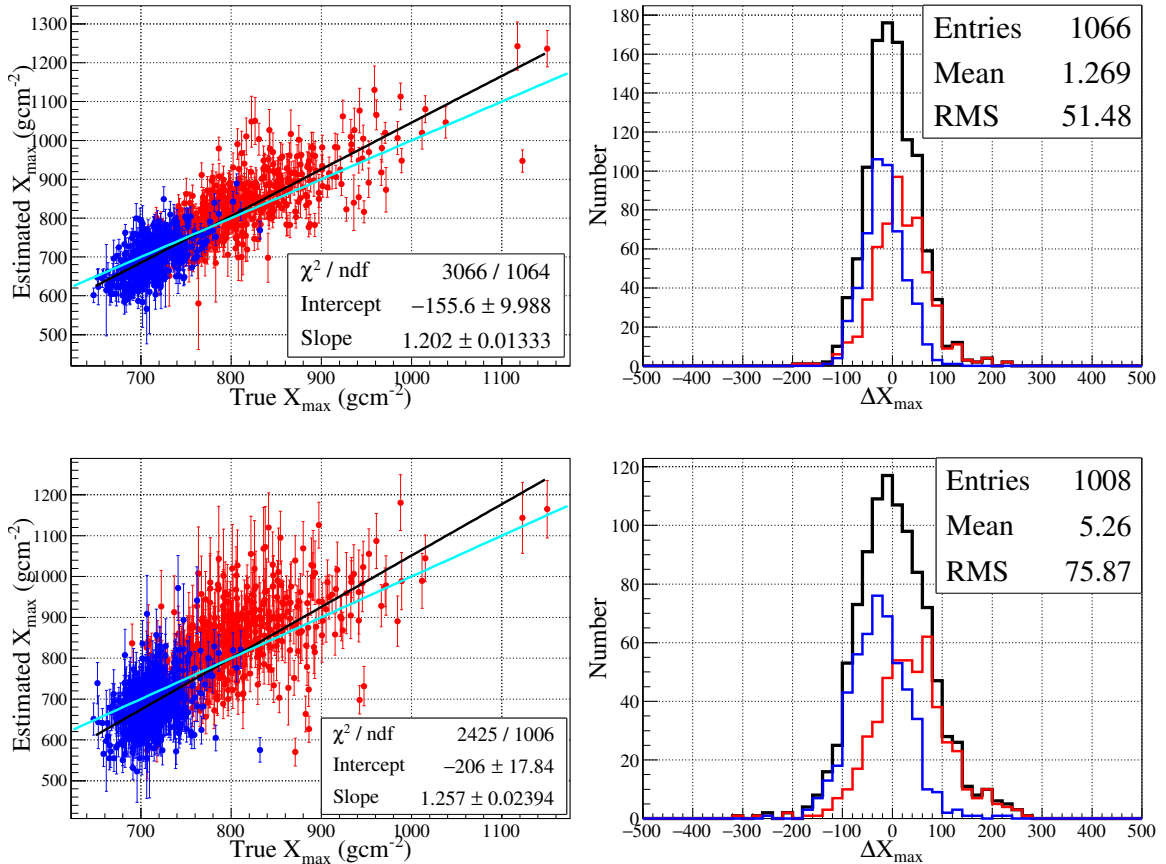


**Figure 7.3:** Plots checking the calibration in Figure 7.2 using the same data. The top panels show, from left to right, a graph of the true  $X_{\max}$  against the estimated  $X_{\max}$  and a histogram of the residuals  $\Delta X_{\max} = (\text{estimated } X_{\max} - \text{true } X_{\max})$  for the WCD. These residuals correspond to the difference between the data points and the cyan line, representing the 1-1 correlation. In the left hand plots, the black line is an overall linear fit to the set of red (proton) and blue (iron) points. In the right hand plots, the black histogram is the sum of the red and blue histograms and has its statistics shown. The bottom plots are the same but for the SSD.

If this calibration between  $s$  and  $\text{DX}$  is to be used in reality, then since we do not know apriori the primary mass of a cosmic ray, the proton and iron points must be fit to together. This has been done in Figure 7.2 with a sigmoid function of the form

$$s(\text{DX}) = \frac{a}{1 + \exp(-b \times \text{DX} + c)} + d \quad (7.3)$$

where  $a$ ,  $b$ ,  $c$  and  $d$  are free parameters. This type of function was chosen as there seemed to be a flattening off of the data at both low and high values of  $\text{DX}$ . These flatter regions have little sensitivity to  $\text{DX}$  i.e. a single value of  $s$  could correspond to many different values of  $\text{DX}$ , meaning there will be a greater spread in the estimated value of  $X_{\max}$  for low/high values of  $s$ . Another consequence of the shape of this correlation is that any functional form which adequately fits the data will necessarily

have to flatten at extreme DX values. For the chosen function in Equation 7.3, this manifests in the range of  $s(\text{DX})$  being limited to within  $d$  and  $d + a$ . Therefore,  $s$  values measured outside this range cannot be assigned a value of DX and in turn  $X_{\max}$ . Additionally,  $s$  values that are very close to the horizontal asymptotes may be assigned extremely low/high values of DX, leading to poor estimates of  $X_{\max}$ .

Performing a check of this calibration on the same data set yields the results shown in Figure 7.3. On the left we have plotted the estimated  $X_{\max}$  against the true  $X_{\max}$  to observe whether there is a bias as a function of true  $X_{\max}$ . This has been done for both the WCD (top row) and SSD (bottom row). Once again the red/blue points correspond to proton/iron respectively. The error bars on these points come from the error in  $s$  and the error in the calibration to convert  $s$  to DX. As the Monte Carlo shower parameters were used there was no uncertainty in the zenith angle of the shower. A linear fit has been performed on the overall set of points, shown in black, with a one to one line (cyan) plotted for reference. Also shown are histograms of  $\Delta X_{\max} = (\text{estimated } X_{\max} - \text{true } X_{\max})$ . The individual proton and iron histograms are shown in red/blue, with their sum shown in black. The statistics box containing the number of entries, mean and RMS corresponds to the black histogram. Note that to avoid extremely low/high values of DX being transformed into poor estimates of  $X_{\max}$  we have placed a cut on the showers selected in this checking process, namely that  $d+0.05a < s < (a+d)-0.05a$  for the respective fit parameters of the WCD and SSD. Recall from Equation 7.3 that  $d$  is the value of the lower asymptote and  $a$  is the difference between the high asymptote and low asymptote. The cut removes around 10 points for the WCD and 68 points from the SSD, the majority of these being proton points at low DX values.

Immediately we notice a bias is present in both the WCD and SSD cases, where iron primaries generally have their  $X_{\max}$  underestimated and proton primaries have their  $X_{\max}$  overestimated. This can be seen in the graphs via the misalignment of the best fit line and 1-1 line, and in the histograms from the separation in the central values of proton and iron, which are either side of 0. The bias is caused by the original calibration having to “split the middle” between the proton and iron points, meaning for a particular value of  $s$  the estimated DX for a proton shower will generally be lower than the true value, and for an iron shower it will generally be higher. The overall residual histograms (black) hide this offset, showing only a small bias towards larger estimates for  $X_{\max}$ . A final note is the RMS of the WCD histogram is roughly  $25 \text{ g cm}^{-2}$  smaller than the SSD, due to having less spread in DX for any particular value of  $s$ .

These results are not ideal for taking this method to the next step - applying the calibration to regular (simulated) showers, that is those without dense rings, to estimate  $X_{\max}$ . Given that we are dealing with what is essentially the best possible estimate of the LDF, we would like to be able to achieve a calibration which is not biased based on the primary particle and has a somewhat tighter

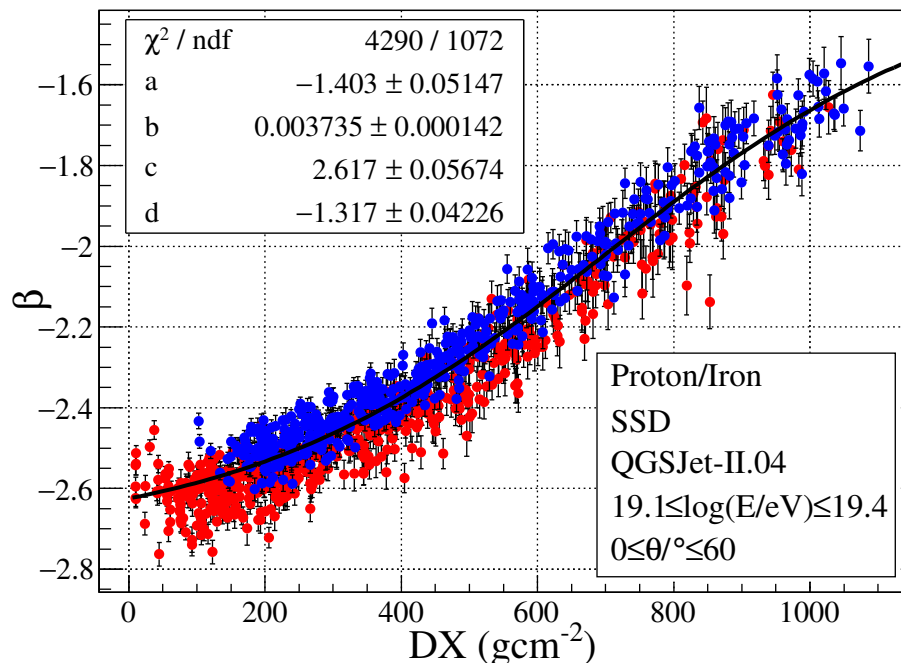
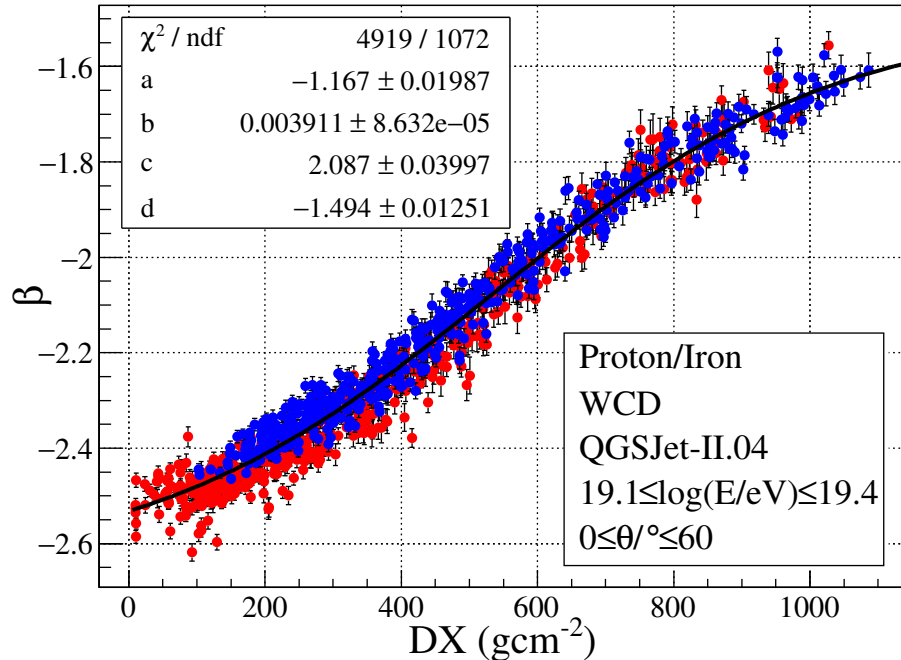


**Figure 7.4:** Calibrations of the correlation between  $\beta$ , a slope parameter of the modified NKG function, and the distance to  $X_{\max}$ ,  $DX$ , for the WCD (top) and SSD (bottom). Note the fits of the modified NKG function were performed with  $\gamma = 0$ . Values of the fit parameters are shown in the top left of each plot.

residual distribution (smaller RMS) when tested on the same data. To this end, we re-performed the LDF fits to the dense ring data but now using the modified NKG function. Our hope was that using different slope parameters would not give the bias seen using the original NKG function. The initial test allowed  $\beta$  and  $\gamma$  to be freely fit. However this resulted in no correlation between either  $\beta$  or  $\gamma$  and DX, a result believed to be caused by the degeneracy in  $\beta$  and  $\gamma$ . To remove this degeneracy,  $\gamma$  was set to a fixed value of zero and the fits performed once again. The resulting calibration curves are shown in Figure 7.4.

The calibration is extremely similar to the previous result in terms of shape and spread. The only real difference is the range of values taken by  $\beta$  compared to  $s$ . Unfortunately the slight separation between proton and iron points at low values of DX also remains, causing a similar bias issue as before. To solve this bias problem, a different technique had to be used. In the following section we describe a slightly more complicated method where  $X_{\max}$  and  $\theta$  are used directly to parameterise the slope parameter of the LDF. The resulting function is then used to estimate  $X_{\max}$ . Importantly, we chose to advance using the modified NKG function with  $\gamma$  set to zero as the LDF to fit. This decision was made primarily because the modified NKG function is currently used in the Offline reconstruction of real and simulated events, and performing the same check of the estimated  $X_{\max}$  using the calibration curves in Figure 7.4 gave very similar results to Figure 7.3.

## 7.2 Parameterising $\beta$ as a function of $\theta$ and $X_{\max}$ using dense rings

Let us start by taking a step back from our initial attempt at finding a correlation between  $s$  and some variable associated with  $X_{\max}$ . We know that the slope of the LDF will depend primarily on two things; the zenith angle of the shower and  $X_{\max}$  itself. To understand why, first consider the case of a fixed  $X_{\max}$  and varying zenith angle. The greater the inclination of the shower, the more spread out particles reaching the ground become, leading to a flatter LDF. For the modified NKG function with  $\gamma$  set to 0, this corresponds to a larger value of  $\beta$ . This same dependence was shown indirectly by the calibration curves of  $\beta$  against DX, as larger values of DX typically corresponded to larger zenith angles. On the other hand, for a given zenith angle, showers with deeper  $X_{\max}$  values will have a steeper LDF.

Both of these facts can be observed directly by plotting the value of  $\beta$  against either  $\sin^2 \theta$  for different bins of  $X_{\max}$ , or  $X_{\max}$  for different bins of  $\sin^2 \theta$ . Example plots for the SSD, using the same dense ring data as in the previous section, are shown in Figures 7.5 and 7.6. In Figure 7.5, the data have been split into 7 equally sized bins in  $\sin^2 \theta$ . We can see that for a fixed  $X_{\max}$ , the more inclined the shower, the greater the value of  $\beta$ . As for Figure 7.6, the data have been split into 4 equally sized bins of  $X_{\max}$ , ranging from 680 to 880 g cm<sup>-2</sup>. This choice covered the majority

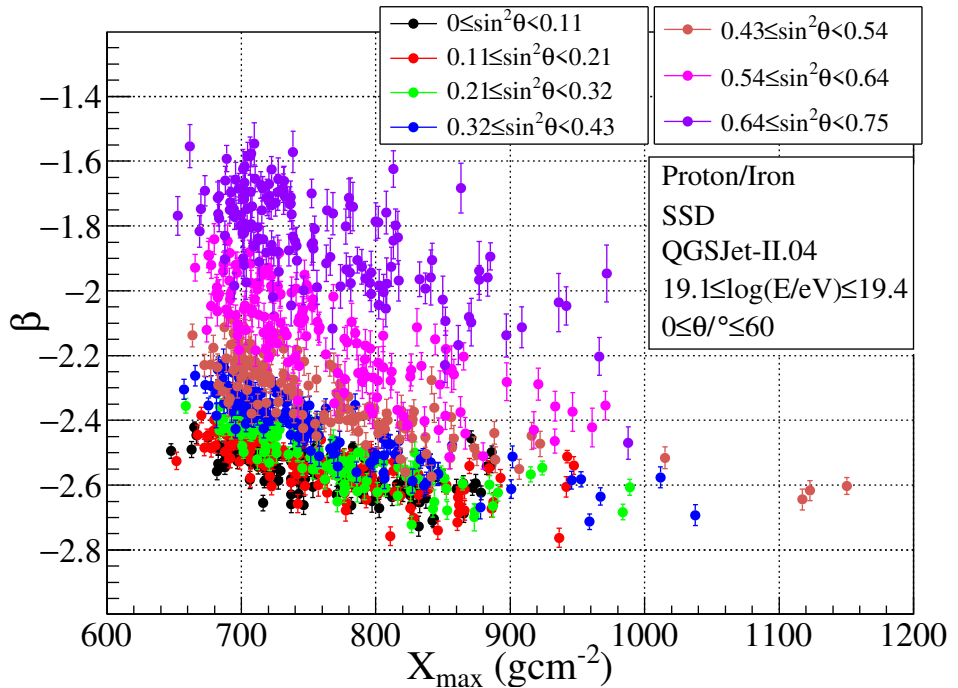


**Figure 7.5:** The slope parameter  $\beta$  of the modified NKG function (with  $\gamma$  set to 0) versus  $X_{\max}$ , for different bins of  $\sin^2 \theta$ . Results are for the SSD

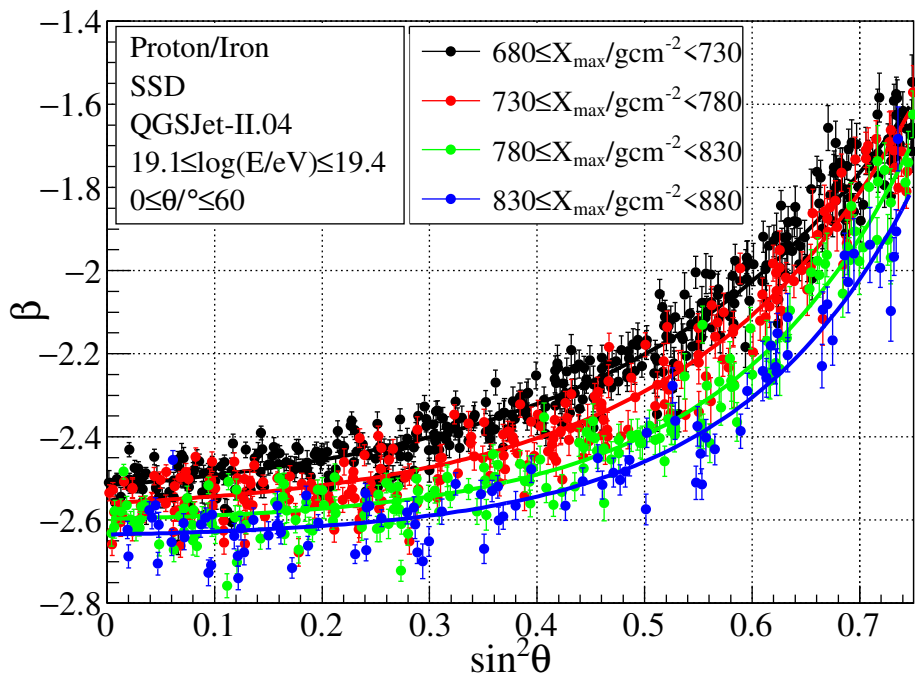


**Figure 7.6:** The slope parameter  $\beta$  of the modified NKG function (with  $\gamma$  set to 0) versus  $\sin^2 \theta$ , for different bins of  $X_{\max}$ . Exponential functions have been fit to each set of points. The colour of each fitted line corresponds to the data points of the same colour. Results are for the SSD.

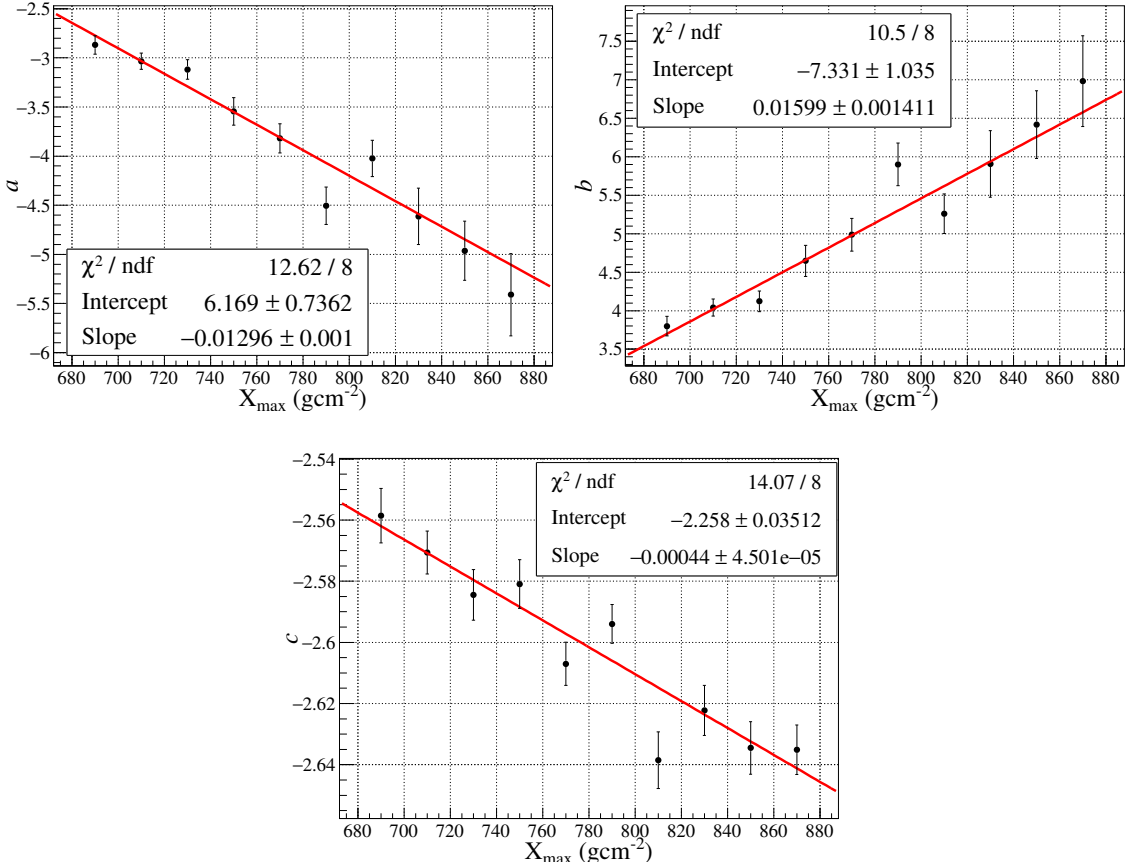


**Figure 7.7:** Parameterisations of the parameters of the exponential fits (Equation 7.4) to  $\beta$  versus  $\sin^2 \theta$  as a function of  $X_{\max}$  for the SSD.

of the  $X_{\max}$  data, as can be seen in Figure 7.5. Again, our initial intuition is shown to be correct, as for a given zenith angle, greater  $X_{\max}$  values correspond to smaller values of  $\beta$ . Each bin in this plot has also been fit to with an exponential of the form

$$\exp(a + b \sin^2 \theta) + c \quad (7.4)$$

where again  $a$ ,  $b$  and  $c$  are free parameters. This is the method with which  $\beta$  was parameterised. Specifically, the parameters of the exponential fits were parameterised as a function of  $X_{\max}$ . This meant an estimate of  $\beta$  could be obtained based solely on a measurement of  $X_{\max}$  and  $\theta$ . Of course though, our interest was in reversing this relationship so that  $X_{\max}$  could be estimated from a measurement of  $\beta$  and  $\theta$ . By fitting to different  $X_{\max}$  regions, we naturally fit to different primaries, with low values of  $X_{\max}$  being dominated by iron showers and larger values dominated by proton showers. This allows for much more information to be captured about the relationship between the LDF slope parameter and  $X_{\max}$  than in our initial calibration using DX, where we fitted over the whole  $X_{\max}$  distribution. It should be stated that there was no physical reason why an exponential was chosen, it simply appeared to fit the data reasonably well. In future studies involving a similar

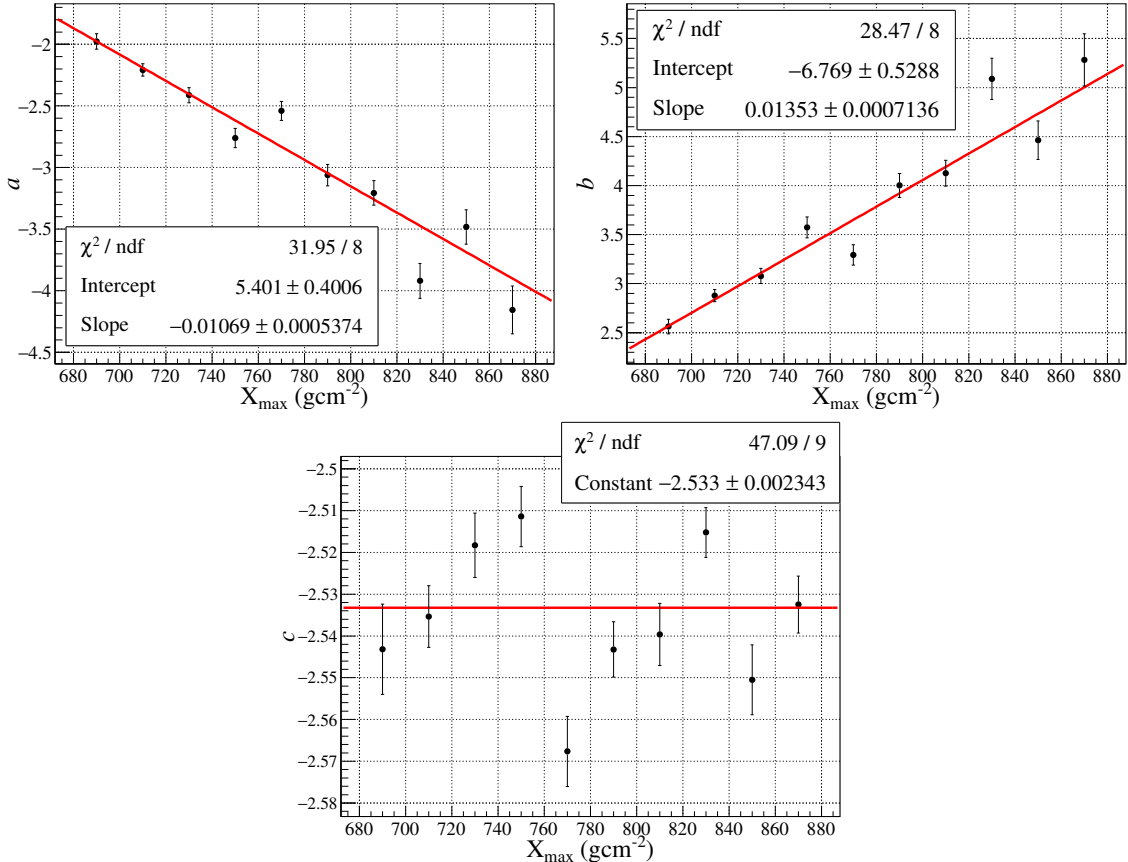


**Figure 7.8:** The same type of plots as in Figure 7.7 but for the WCD. Note the fitting of a constant function to the  $c$  parameter, as opposed to the linear fit used for the SSD.

method, a search for a more physically motivated function should be attempted. For now, we continue with a demonstration of the technique.

Plotting the parameters of the exponential fit as a function of  $X_{\max}$  for the SSD results in the plots shown in Figure 7.7. In these plots the data have been split into 10 bins of  $X_{\max}$ , each of size  $20 \text{ g cm}^{-2}$ , ranging from  $680$  to  $880 \text{ g cm}^{-2}$ . The smaller sized bins were chosen so as to capture any small scale behaviour. Conveniently, the parameters appear to follow simple linear trends, at least to a first approximation. Similar parameterisation plots are shown for the WCD in Figure 7.8, the only difference being a constant function was fitted to the  $c$  parameter rather than a linear one. Here, the  $y$ -axis scale has been kept similar to the  $c$  vs.  $X_{\max}$  graph for the SSD. This is to emphasize the need for a linear relationship in the SSD plot, and how the WCD appears “flat” in comparison.

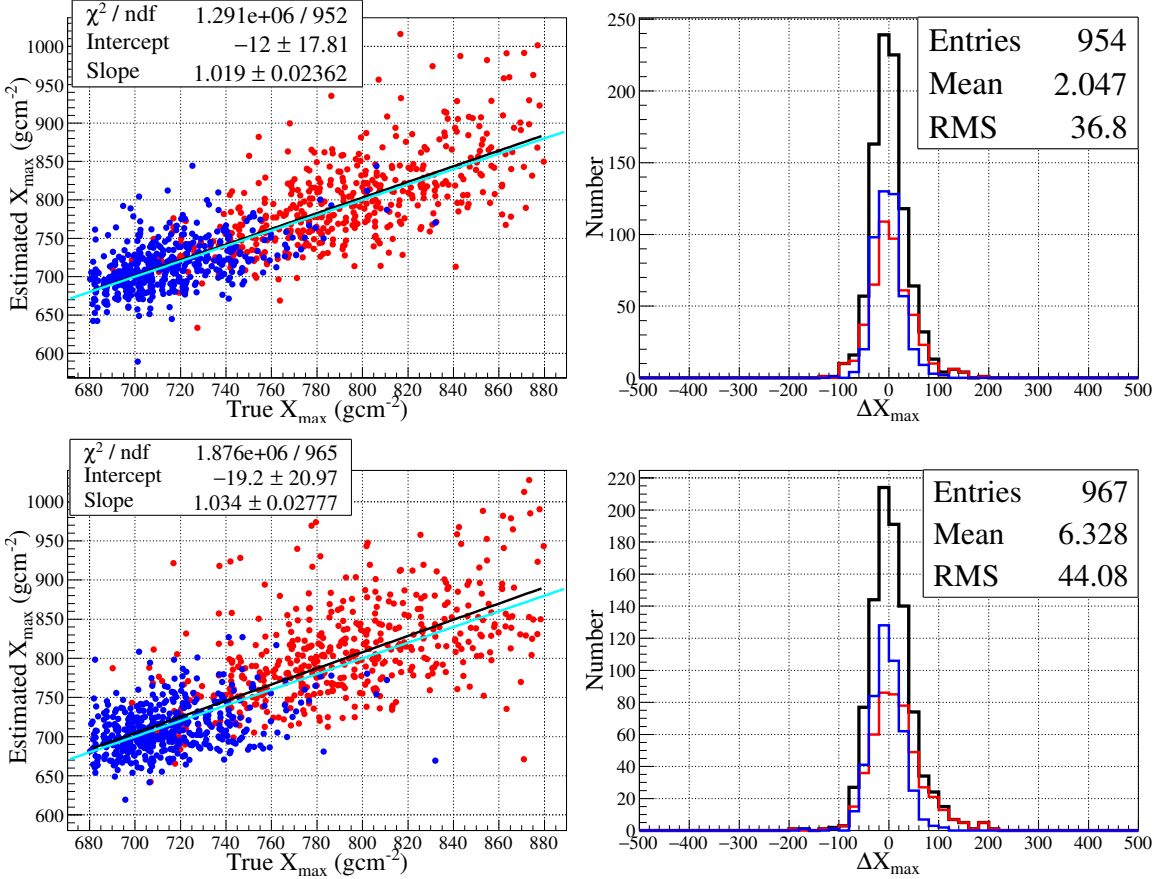


**Figure 7.9:** Results from checking the dense ring calibration of  $\beta$ ,  $\theta$  and  $X_{\max}$  on the same data. Red/blue represents proton/iron. The top row shows results for the WCD, the bottom row for the SSD. Linear fits have been applied to the combined set of proton and iron points in the right hand plots. The black histogram is the sum of the proton and iron histograms and has its statistics shown.

Thus, the functions

$$\beta_{\text{WCD}} = \exp((5.4 - 0.0107X_{\max}) + (-6.8 + 0.0135X_{\max}) \sin^2 \theta) - 2.533 \quad (7.5)$$

$$\beta_{\text{SSD}} = \exp((6.2 - 0.013X_{\max}) + (-7 + 0.016X_{\max}) \sin^2 \theta) - 2.26 - 0.00044X_{\max} \quad (7.6)$$

make up our new, two dimensional, calibration curves. These calibrations were then tested similarly to before - by running over the same data set and calculating  $X_{\max}$  from the measured  $\beta$  and  $\theta$ . Note that when checking the calibration only showers with an  $X_{\max}$  between the range used in the parameterisations were considered i.e.  $680 \leq X_{\max} / \text{g cm}^{-2} \leq 880$ . Also, any showers with an estimated value of  $\beta < -2.51$  for the WCD and  $\beta < -2.7$  for the SSD were cut. This simply removed some noticeably poor  $X_{\max}$  estimates, similar to what was done when checking the initial DX versus  $s$  calibration. The cuts on  $\beta$  removed 14 data points from the WCD and 8 data points from the SSD. Plotting the same graphs of true  $X_{\max}$  against esti-

mated  $X_{\max}$  and histograms of  $\Delta X_{\max}$  for the WCD and SSD gave the results shown in Figure 7.9. There is now no longer a bias in the estimated  $X_{\max}$  as a function of true  $X_{\max}$ , in either the WCD or SSD. This is shown by the fitted linear functions being consistent (or nearly consistent in the case of the SSD) with the 1-1 lines. These results are reflected in the  $\Delta X_{\max}$  histograms for proton and iron, both of which now appear to be centred at 0. The RMS values of the overall histograms are also significantly smaller, around  $37 \text{ g cm}^{-2}$  for the WCD and  $44 \text{ g cm}^{-2}$  for the SSD. This level of quality is what we initially hoped to achieve with the dense ring method.

There is a small anomaly in the SSD  $\Delta X_{\max}$  histogram, namely the tail in the proton  $\Delta X_{\max}$  distribution stretching to the right. Ideally, the results should be symmetric around 0. This can be achieved by increasing the severity of the  $\beta$  cut for the SSD to be  $\beta < -2.6$ , removing the tail. This changes the mean of the overall histogram to -0.4 and reduces the overall RMS to  $\approx 36 \text{ g cm}^{-2}$ . Doing this does introduce a small acceptance bias towards deeper proton showers, however. As this work is primarily a demonstration utilising simulations rather than a practical application, no actions will be taken to correct/account for this. However, if the calibration were to be applied to real data and a similar cut introduced, then the relative acceptance of the SSD to different  $X_{\max}$  values could in principle be estimated and used to account for the acceptance bias in the reconstructed  $X_{\max}$  distributions.

## 7.3 Applying the dense ring calibration to regular showers

With the check of the dense ring calibration on the same data being successful, the calibrations were then tested on regular simulated showers, that is those without dense rings. It is in this section where we attempt to correct the signals measured by the WCD and SSD using our asymmetry parameterisations from Chapter 4. Specifically, along with performing a standard LDF fit, we will correct the measured signals of each detector to the average signal which would be measured by a dense ring at the detector's radius, before fitting an LDF to the corrected data. The Monte Carlo shower parameters were used when analysing these events. This allowed us to select showers within the same energy, zenith angle and  $X_{\max}$  range as used in the dense ring calibration. It also meant the correct core location and station radii/azimuth could be used when performing our own LDF fits as well as the asymmetry corrections, which were applied based on the type of detector and primary particle being considered (WCD/SSD, proton/iron). Lastly, note that the severity of the shower zenith angle cut was increased to  $\theta < 55^\circ$  for this test. This was because above this zenith single events would occasionally give  $\beta$  values well above those used to create the dense ring calibration, around -1.1.

To ensure each LDF fit gave a reasonable value of  $\beta$ , strict cuts were placed on the stations included in the fits. The stations included had to...

- Have an expected signal  $>10$  VEM in the WCD. In other words, based on the fit of the LDF performed by `Offline`, if the signal predicted by this LDF at the radius of the station was  $< 10$  VEM, then the station would not be included in the fit. This was a conservative cut to avoid upward fluctuations. Note this cut isn't perfectly valid when using the Monte Carlo geometry, as the `Offline` LDF fit uses the reconstructed core.
- Be identified by `Offline` as a “candidate” station (a station which is part of the event). This cut excludes triggered stations which have no neighbouring stations that triggered, known as lonely stations.
- Not be saturated, for both the WCD and SSD.

Additional criteria were required for the distribution of stations, namely the Billoir criteria. These are the same criteria that were outlined in Section 3.2.4 which define the showers with which  $\beta$  is parameterised (for real events). To reiterate, to pass the Billoir criteria there must be at least 2, 3 or 4 stations in the range 400-1600 m, with at least two of the stations separated by a distance of at least 900, 800 or 700 m respectively. These conditions provide a satisfactory number of stations and lever arm with which to fit  $\beta$ .

As for the asymmetry correction, it was performed as follows. A dense ring at 1000 m was simulated for each event and used to estimate  $\log(S(1000))$ . Then, for a station at a particular radius in an event with a certain  $\log(S(1000))$  and zenith angle, our parameterisations of the asymmetry were used to estimate  $b$  for both the WCD and SSD, depending on whether the primary was proton or iron. The value of  $\zeta$  for the station was then used to get the relative signal at this station position, defined as per our original asymmetry fits,  $1 + b \cos \zeta$ . Dividing the measured signal by this value gave the asymmetry-adjusted signal.

Fitting LDFs to the showers which passed all these cuts, and then using the fitted value of  $\beta$  to estimate  $X_{\max}$  via Equations 7.5 and 7.6 (done numerically for Equation 7.6), yielded the  $\Delta X_{\max}$  histograms in Figure 7.10. There is a clear difference between the number of proton and iron showers present in these plots. Since the total number of proton showers and iron showers which were analysed was within 10% of each other, this must be due to the cuts implemented. A table of the cuts for the shower criteria and how they affected the initial collection of proton and iron showers is shown in Table 7.1. Follow up Tables 7.2 and 7.3 show the effect of applying the same  $\beta$  cut that was used in the dense ring calibration check on the  $\beta$  values for the uncorrected WCD/SSD LDF fits.

We can see that the cut on  $X_{\max}$  reduces the relative number of proton events more than iron events. This is simply due to the inherent proton  $X_{\max}$  distribution.

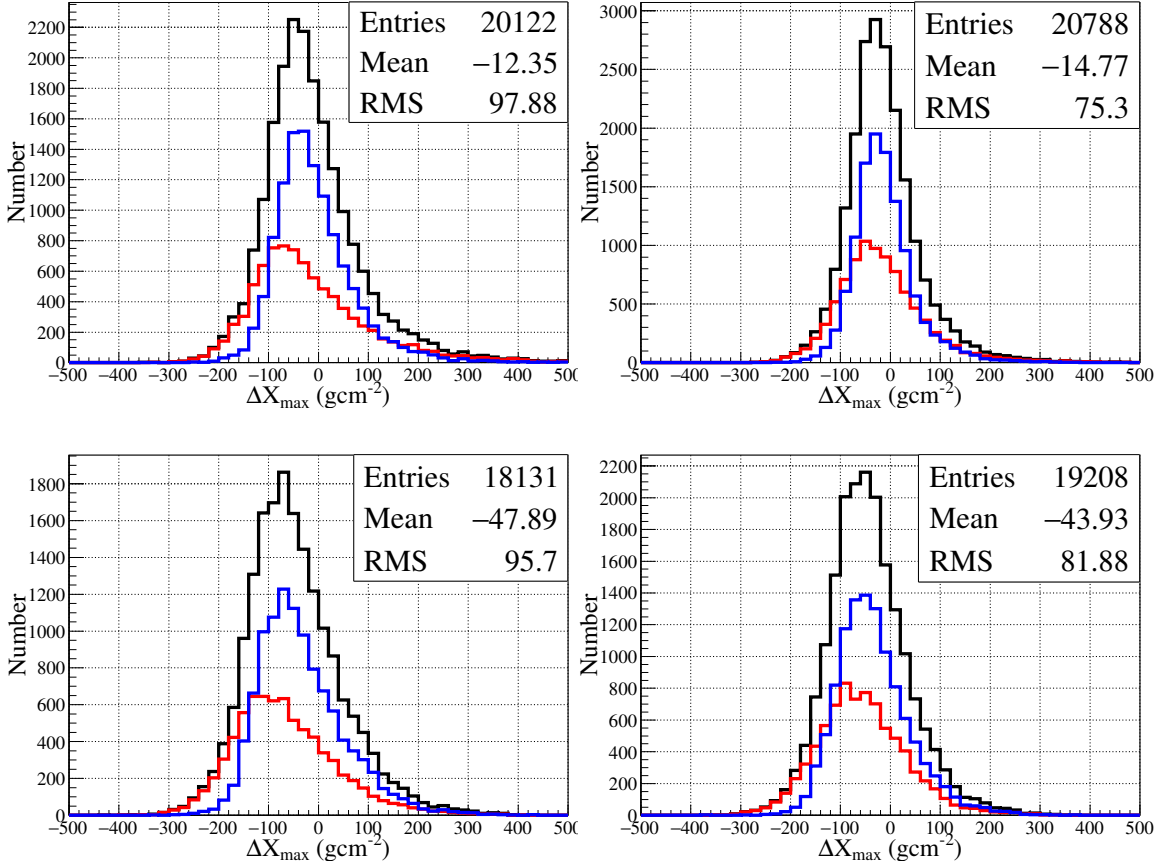


**Figure 7.10:** Histograms of  $\Delta X_{\max} = (\text{reconstructed } X_{\max} - \text{true } X_{\max})$  using the dense ring calibration for regular showers. The top row shows the results for the WCD, with the  $X_{\max}$  estimates from the uncorrected LDF fits shown on the left and the asymmetry-corrected fits shown on the right. The bottom row is the same but for the SSD. The black histograms are the sum of the red and blue histograms, given by proton and iron events respectively. Statistics are shown for the black histogram.

Cut	Proton Events	% remaining	Iron Events	% remaining
-	25,236	100%	27,384	100%
$\theta < 55^\circ$	20,664	82%	22,620	83%
$680 < X_{\max} < 880$	17,964	72%	20,700	76%
Billoir criteria	9,880	39%	11,925	44%

**Table 7.1:** A table showing the number of events analysed when checking the dense ring calibration on regular showers and how the various cuts implemented reduced the initial number. The % remaining columns show what percentage of the original number of events (25,236 and 27,384) remained after each cut.

Cut	Proton WCD	% remaining	Iron WCD	% remaining
$\beta > -2.51$	8567	34%	11555	42%

**Table 7.2:** An extension of Table 7.1 showing how many events were removed after applying our  $\beta$  cut on the uncorrected WCD LDF fits for proton and iron showers.

Cut	Proton SSD	% remaining	Iron SSD	% remaining
$\beta > -2.6$	7432	29%	10699	39%

**Table 7.3:** The same as Table 7.2 but for the SSD.

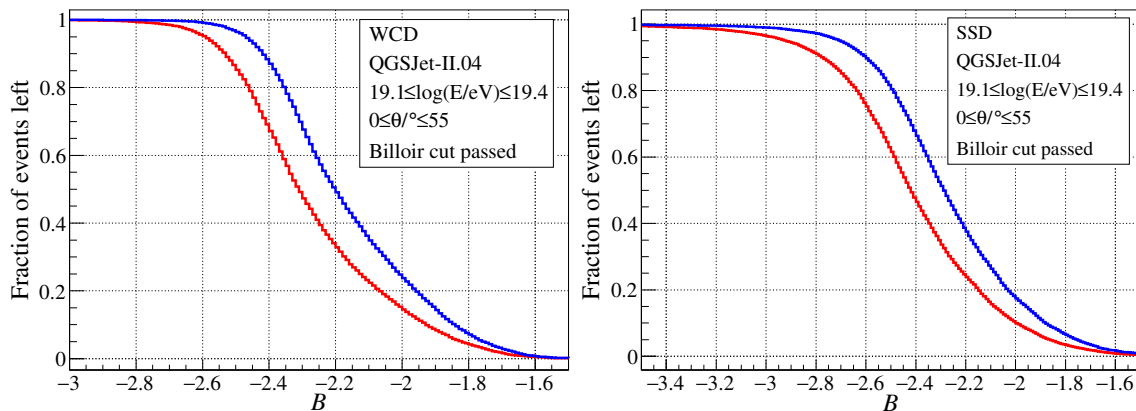


**Figure 7.11:** Histograms showing the fraction of events left after cutting events with a fitted value of  $\beta < B$  ( $\beta$  from the uncorrected LDF fits). On the left is the WCD, on the right is the SSD. The red and blue histograms correspond to proton/iron showers respectively.

The cuts for  $\theta < 55^\circ$  and the Billoir criteria meanwhile do not appear to favour either proton events or iron events. However, we do see a large difference in the relative number of proton/iron events removed due to the cut on  $\beta$ , for both the WCD and SSD. It has already been noted that for the SSD the acceptance to proton showers would be lower due to this cut. However the fact we see the same phenomenon in the WCD may indicate that the  $\beta$  values are, on average, more negative for the regular event fits than the dense ring fits. For completeness, acceptance plots showing the fraction of events left after requiring  $\beta$  values from the uncorrected LDF fits be larger than some number  $B$ , measured with respect to the number of showers which passed all the cuts in Table 7.1, are shown in Figure 7.11. The left/right hand plot corresponds to the WCD/SSD, with the proton/iron histograms being coloured red/blue as usual. These plots are effectively the normalised cumulative distribution of fitted  $\beta$  values and show that for any given  $B$  a greater number of proton events will be cut than iron events.

As for the shape of the distributions in Figure 7.10, there is a systematic shift to underestimating  $X_{\max}$  in each instance, by roughly  $15 \text{ g cm}^{-2}$  for the WCD and

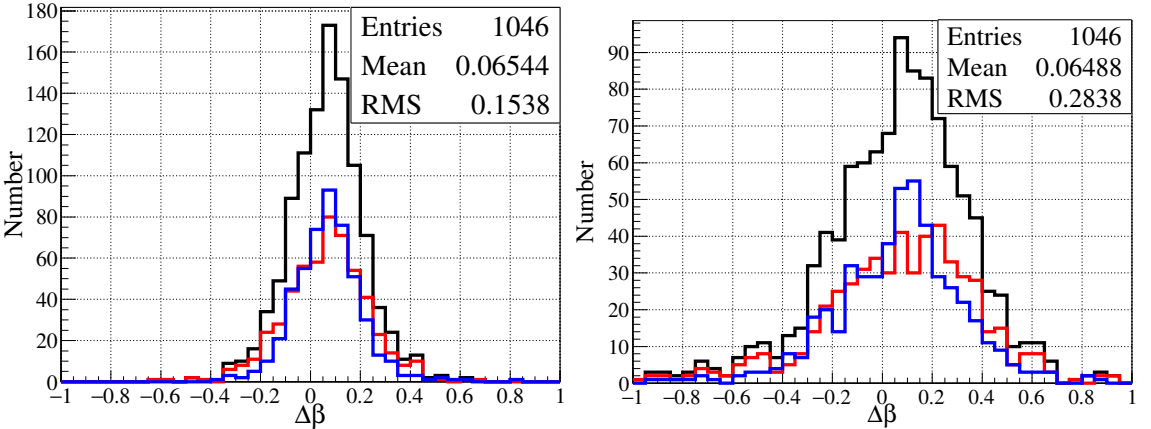


**Figure 7.12:** Histograms of the difference in  $\beta$  when estimated using dense rings vs. the regular number/distribution of triggered stations in a standard event (not corrected for asymmetry). The left panel shows the result for the WCD, the right for the SSD. The black histogram, with statistics shown in the upper right corner, is the sum of the red (proton events) and blue (iron events) histograms.

44 g cm<sup>-2</sup> for the SSD (taking the mean values of the asymmetry corrected histograms). Comparing the left hand plots to the right hand plots, there is a noteworthy improvement in the alignment of the centres of the proton and iron distributions when going from  $X_{\max}$  estimates from fits without the asymmetry correction to those with it. The RMS values of the asymmetry corrected histograms are also noticeably smaller, and a sizeable portion of the tails in the distributions are removed. The improvements here are encouraging and perhaps indicate a potential application of asymmetry for the improvement of LDF fits, similar to Luce’s work [82] correcting the position of the shower core. Again though, this is all being performed in simulations where the asymmetry correction is based on the primary particle. In real data the parameterisation would likely be to some unknown mixed composition, and the correction would be affected by other imperfections in the reconstructed shower parameters.

Regarding the bias in  $\Delta X_{\max}$ , this is, at least in part, believed to be from the different radial distributions of stations used in the calibration. Explicitly, for a uniform array of stations, as is the case with Auger, the probability of finding a station between  $r$  and  $r + dr$  is proportional to  $2\pi r dr$ . Hence, for real events, the radial distribution of tanks is proportional to  $r$  (up to some radius where stations no longer trigger). Alternatively, for the dense ring calibration, where there were exactly 12 stations every 100 m, the radial distribution of stations was flat in  $r$ . We can see how this affects our estimate of  $\beta$  by plotting the difference between the fitted  $\beta$  from sets of dense rings vs. that from regular stations in the Auger array for the same simulated shower. This gives the histograms in Figure 7.12. Note  $\Delta\beta = \beta_{\text{Normal}} - \beta_{\text{Dense ring}}$ . In both the WCD and SSD the estimate of  $\beta$

using the regular station distribution is larger than when utilising dense rings, by approximately 0.065. This supports the earlier hypothesis made when observing the larger than expected number of showers being cut based on their value of  $\beta$ . The difference in  $\beta$  indicates the functional form being used is probably not correct. If it were, then no matter the distribution of stations, the value of  $\beta$ , on average, shouldn't change.

To see whether this difference in fitted  $\beta$  could feasibly give the bias we see in Figure 7.10, Tables 7.4 and 7.5 below show the change in estimated  $X_{\max}$  when changing initial values of  $\beta$  by the mean of the histograms in Figure 7.12, for different zenith angles. These calculations were done using the dense ring calibration Equations 7.5 and 7.6. For example, for a starting (dense ring) value of  $\beta = -1.665$ , the difference between the corresponding value of  $X_{\max}$  and the  $X_{\max}$  estimated using a  $\beta$  value of -1.6 was found.

Starting $\beta$	$0^\circ$	$15^\circ$	$30^\circ$	$45^\circ$
-1.665	-6	-7	-10	-18
-1.865	-9	-9	-13	-24
-2.065	-12	-13	-18	-33
-2.265	-20	-22	-30	-55
-2.465	-63	-69	-92	-171

**Table 7.4:** A table showing the change in  $X_{\max}$  (all values in  $\text{g cm}^{-2}$ ) when increasing  $\beta$  by 0.065 for different starting values of  $\beta$  and zenith angles. These results are for the WCD calibration curve.

Starting $\beta$	$0^\circ$	$15^\circ$	$30^\circ$	$45^\circ$
-1.565	-5	-6	-7	-13
-1.815	-7	-7	-10	-16
-2.065	-10	-11	-14	-22
-2.315	-19	-20	-24	-33
-2.565	-66	-65	-62	-60

**Table 7.5:** The same as Table 7.4 but for the SSD

The values in the tables are all negative, which agrees with the systematic change in underestimating  $X_{\max}$ . It isn't immediately clear though whether the values calculated match the expected bias, as this would depend on the relationship between the dense ring and regular distributions of fitted  $\beta$ . However the larger spread in the SSD  $\Delta\beta$  histogram and lower  $\beta$  values overall may explain the difference in the magnitude of the bias between the WCD and SSD seen in Figure 7.10. In the hope of fixing the bias in  $\Delta X_{\max}$ , we decided to attempt a new calibration which utilised a more realistic radial distribution of stations.

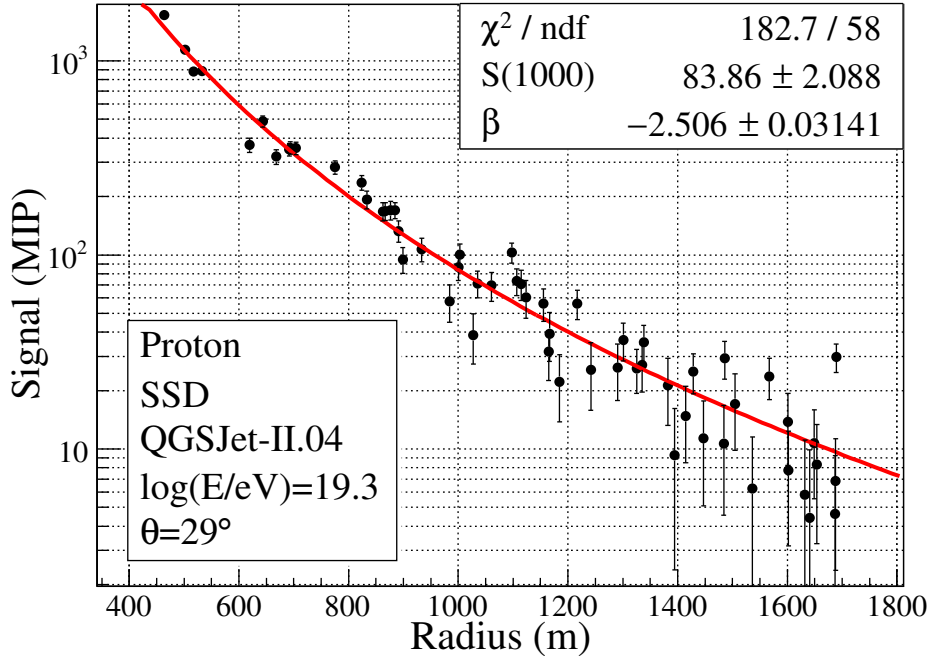


**Figure 7.13:** An example of an ensemble LDF, made with stations from 12 instances of the same shower. Signals are from the SSD.

## 7.4 Calibrating using ensemble LDFs

To properly check our hypothesis that the bias seen is due to the different radial distribution of stations used in the dense ring calibration, we formed a new calibration made with the same radial distribution of stations as would be found in a regular shower. This was achieved by simulating the same shower to be incident on the Auger array 12 times, with each instance having a different core location, and then using any stations which triggered from any instance in one large LDF fit. For example, if 5 stations triggered in each of the 12 instances, then the LDF would be fit to 60 stations, each at different radii and with different signals. Such LDFs will be referred to as “ensemble LDFs”. An example is shown in Figure 7.13. These ensemble LDFs give a distribution of station core distances that is similar to that in a real event (but with a higher station multiplicity). The large number of stations allows for an accurate and precise measure of  $\beta$ .

The same parameterisation steps performed in Section 7.2 were used to parameterise the parameters of the exponential fits (Equation 7.4) to the values of  $\beta$  obtained from ensemble LDFs. Note that the same shower criteria listed in Table 7.1, excluding the Billoir criteria, were required for an ensemble LDF to be included in the calibration ( $\theta < 55^\circ$ ,  $680 \leq X_{\max} / \text{g cm}^{-2} \leq 880$ ). Approximately 1500 proton and 1700 iron ensemble LDFs were used in the calibration.

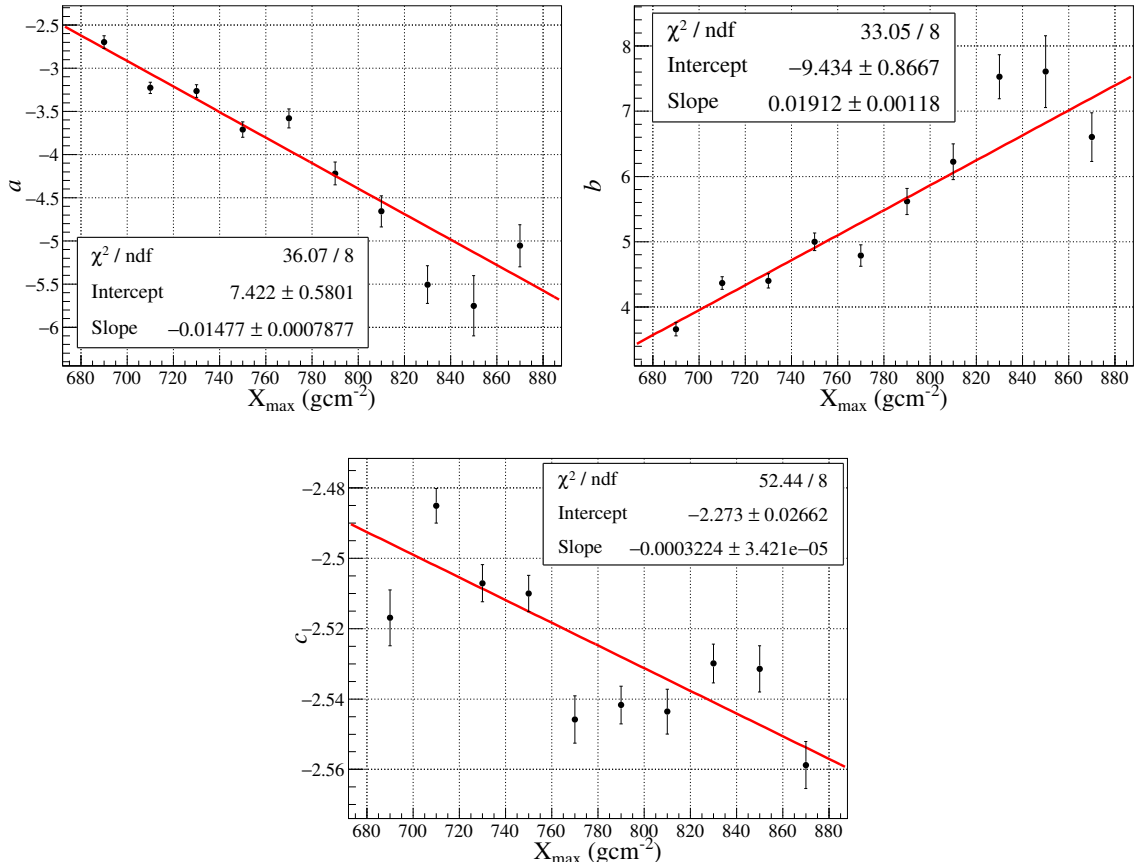


**Figure 7.14:** Parameterisations of the parameters of the exponential fits to  $\beta$  versus  $\sin^2 \theta$  as a function of  $X_{\max}$  for the SSD. The values of  $\beta$  came from ensemble LDF fits.

The parameterisation results for the SSD and WCD are given in Figures 7.14 and 7.15 respectively. Using the new calibration functions for our estimates of  $X_{\max}$  for regular showers, we obtain the results in Figure 7.16. Initially, the cuts placed on the allowed  $\beta$  values were the same as in the dense ring calibration. However these were not strict enough to remove all of the unrealistic  $X_{\max}$  estimates e.g.  $>1800 \text{ g cm}^{-2}$ . This, of course, is because the calibration had changed. To accommodate the change in calibration and remove the majority of the bad estimates, the severity of the cuts was increased, to  $\beta > -2.42$  for the WCD and  $\beta > -2.55$  for the SSD. This corresponded to removing  $\sim 25\%$  of proton and  $\sim 10\%$  of iron showers for the WCD, and  $\sim 30\%$  of proton and  $\sim 15\%$  of iron showers for the SSD. The showers removed were predominantly those with large true  $X_{\max}$  values.

Focusing on the plots themselves, the bias is now much smaller for the SSD and the WCD, with the mean of the overall histograms being around  $-1 \text{ g cm}^{-2}$  for both (taking the asymmetry-corrected results again). The asymmetry corrected plots maintain their improved RMS and alignment of proton and iron histograms

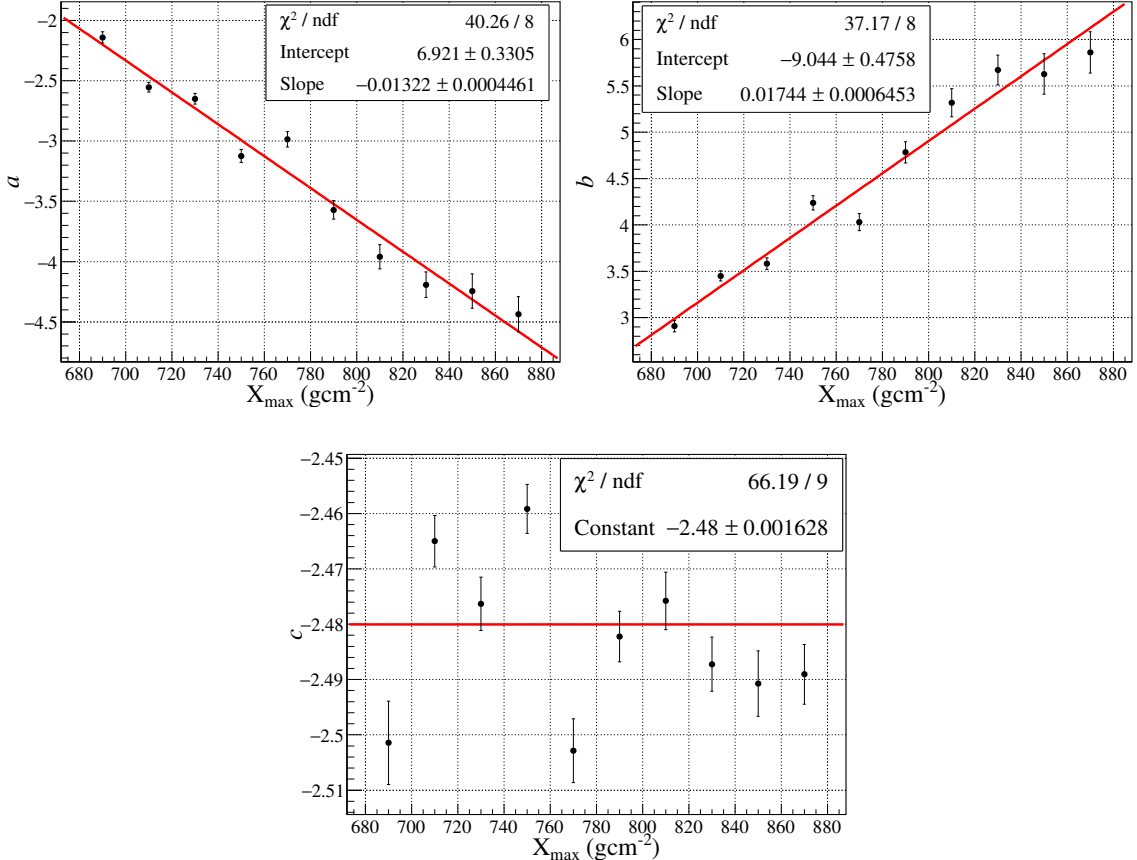


**Figure 7.15:** Parameterisations of the parameters of the exponential fits to  $\beta$  versus  $\sin^2 \theta$  as a function of  $X_{\max}$  for the WCD. The values of  $\beta$  came from ensemble LDF fits.

over the uncorrected ones, as well as smaller tails. Overall, this is a significant improvement and reinforces our point that the radial distribution of stations in the LDF fit changes the values of  $\beta$ .

The obvious next step in this process would be to test the calibration on reconstructed data from simulated events i.e. not using any Monte Carlo properties, and subsequently real data. The asymmetry correction in this case would be more difficult, due to not knowing the primary particle. One option may be to simply take the average of the proton and iron correction, assuming a 50:50 mix. Here however we come to an issue with parameterising asymmetry in general. If we would like to discern the primary particle based on asymmetry alone then the parameterisations must be done on different primaries and results compared. However if we want to correct for asymmetry then the parameterisations must be done using some mix of primaries. Tackling these issues is beyond the scope of this work, but is certainly a potential for future studies. Another natural extension would be to

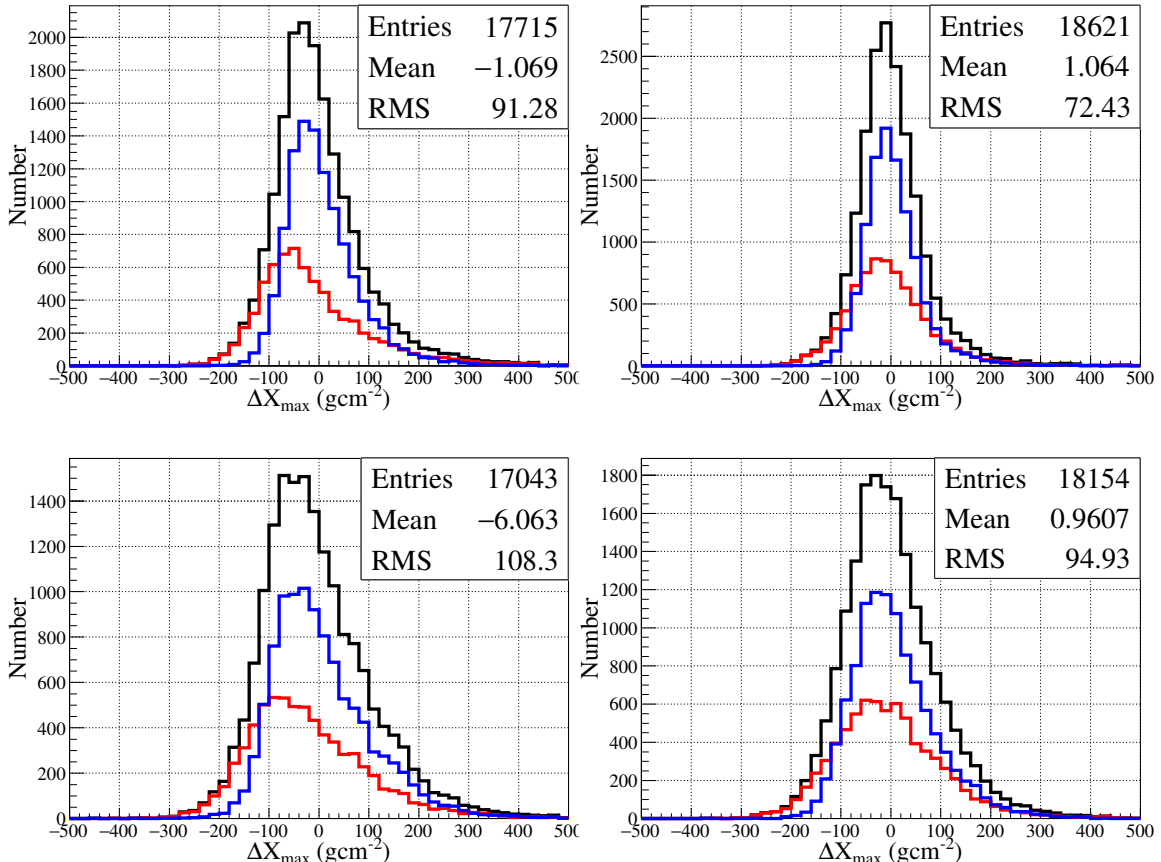


**Figure 7.16:** Histograms of  $\Delta X_{\max} = (\text{reconstructed } X_{\max} - \text{true } X_{\max})$  using the ensemble LDF calibration for regular showers. The top row shows the results for the WCD, with the  $X_{\max}$  estimates from the uncorrected LDF fits shown on the left and the asymmetry corrected fits shown on the right. The bottom row is the same but for the SSD. The black histograms are the sum of the red and blue histograms, given by proton and iron events respectively. Statistics are shown for the black histogram.

perform the techniques demonstrated above for different energy bins and different hadronic models.

## 7.5 Conclusions

In this chapter we have demonstrated a possible application of asymmetry, in this case to the improvement of LDF fits with the goal of extracting mass composition information. These fits were performed with LDFs which utilised only one slope parameter. Specifically, we primarily utilised the modified NKG function with  $\gamma$  set to 0, leaving  $\beta$  as the one fitted slope parameter. Initial results showed that fitting to the whole  $X_{\max}$  distribution through an intermediate variable,  $\text{DX}$ , gave a bias where the  $X_{\max}$  of proton showers would be underestimated and the  $X_{\max}$  of iron showers overestimated. This was corrected by breaking down the zenith dependence

of  $\beta$  into different  $X_{\max}$  bins and parameterising  $\beta$  directly with these variables.  $X_{\max}$  was then able to be calculated based on a measurement of  $\beta$  and  $\theta$  alone. This method was shown to work well when making use of dense rings to measure the LDF.

Checking the dense ring calibration on regular events showed a difference between the fitted values of  $\beta$  when compared to dense rings and a subsequent bias in the  $X_{\max}$  estimates. For normal showers,  $\beta$  was on average 0.065 units larger, with the  $X_{\max}$  estimates of the WCD and SSD being underestimated by approximately  $12 \text{ g cm}^{-2}$  and  $48 \text{ g cm}^{-2}$  respectively. The magnitude of the bias did not change significantly when correcting for asymmetry in the LDF fits, however the RMS values of the distributions and the offset between the centres of the proton and iron histograms were both reduced. This showed a definitive improvement for this technique when correcting for asymmetry.

The calibration was then re-performed using the newly labelled “ensemble LDFs”. These LDFs constituted a large number of stations from many instances of the same shower, and importantly had the same radial distribution of stations as a regular event. Checking this new calibration removed the majority of the bias in the  $\Delta X_{\max}$  plots. The asymmetry-corrected plots retained their improvements over the uncorrected ones with this calibration. If these calibrations could be extended to include additional realistic aspects and maintain an unbiased  $X_{\max}$  reconstruction for both proton and iron primaries, then they may be sufficient for calculating the mean  $X_{\max}$  as a function of energy. However the large RMS values in  $\Delta X_{\max}$ , approximately  $70 \text{ g cm}^{-2}$  for the WCD and  $95 \text{ g cm}^{-2}$  for the SSD, even when using Monte Carlo parameters, mean the calibrations are probably not appropriate for studying the true  $X_{\max}$  RMS. This is clear when comparing these values to the resolution obtained in other mass composition studies, such as  $45 \text{ g cm}^{-2}$  when utilising the risetimes of signals in the WCDs [89], or around  $20 \text{ g cm}^{-2}$  at the same energy as studied here when using hybrid data [25].

The natural next step is to perform this type of analysis on real events, with reconstructed cores, zenith angles, energies etc. The calibrations performed here with ensemble LDFs could certainly be used for such studies, at least as a first estimate. However it will be a more challenging task and one where correcting for asymmetry will be more difficult, due to not knowing the mass of the primary particle. If asymmetry is to be corrected for, then a parameterisation of the asymmetry in real data will be required.



---

## Summary and outlook

---

This thesis has explored asymmetry in extensive air showers, a phenomenon where detectors/regions of equal distance from the core of an inclined shower will have different signals/particle densities depending on their azimuthal angle in the shower plane,  $\zeta$ . We have demonstrated that, at least in simulations, asymmetry has the potential to be used in aiding the prediction of mass composition, whether this is by using it directly or by correcting for it to improve the precision of other analyses.

In Chapter 4, the amplitude of the signal asymmetry in the water Cherenkov and scintillator detectors of the Pierre Auger Observatory was parameterised in simulations. It was found that the asymmetry differs in magnitude depending on the detector type, primary, zenith angle, average signal at 1000 m in the shower plane, and radius in the shower plane. The results of the parameterisations can be found in Tables 4.3 - 4.6. The parameterisations showed the asymmetry in the SSD, for both proton and iron primaries, to be larger than in the WCD. Another key observation was that, for both the WCD and SSD, at  $r=1000$  m, asymmetry was seen to be primarily dependent on zenith angle, with changes in  $\log(S(1000))$  only causing minor deviations in comparison. To see whether asymmetry could be used for studying mass composition, the phase space in which the difference between the proton and iron parameterisations at  $r=1000$  m was a maximum was found. The greatest difference was for the SSD at large zenith angles  $\approx 55^\circ$  and primary energies around  $2 \times 10^{19}$  eV. The asymmetry amplitude,  $b$ , of proton/iron showers in this phase space was calculated with the parameterisations to be 0.36 and 0.25 respectively.

This difference is certainly large enough to distinguish between simulated ensembles of proton and iron showers in said phase space based on asymmetry alone. The same however cannot necessarily be said for real data. Even if averages of showers in bins of  $\log(S(1000))$  and  $\theta$  were used to obtain decent precision in the mean value of  $b$ , the challenge would be to interpret the result, given that the asymmetry in real data has been shown by Luce [83] to be different to that of simulations, and in reality the composition of UHECRs is likely some mix of light and heavy elements. In order to use asymmetry directly for mass composition studies, it is recommended that future work focus on understanding the differences between the asymmetry measured in simulations and in real data.

The causes of asymmetry in electromagnetic particle density were investigated in Chapter 5. The goal was to understand how geometrical and attenuation effects contributed to the overall asymmetry and whether differences in these contributions could be exploited for mass composition studies. We found that, for showers with a zenith angle of  $38^\circ$ , the electromagnetic attenuation of air shower particles is a non-trivial component of asymmetry, and in the case of showers with shallow  $X_{\max}$  values, it may be the dominant factor. This was shown by predicting the asymmetry for a  $38^\circ$  shower based on density measurements at different vertical atmospheric depths. Although no methods of determining mass composition were discovered which directly utilised this result, performing the technique on a number of proton and iron showers with varying  $X_{\max}$  values showed that proton showers of the same  $X_{\max}$  as iron showers may have slightly higher asymmetry amplitudes. This could point to a future method utilising asymmetry measurements from the SSD (which, due to its shape and equal response to electromagnetic/muonic particles, gives a signal closer to representing a density than the WCD) and FD to constrain the mass composition of an ensemble of showers. Obviously many challenges would have to be overcome to achieve this, such as addressing any discrepancies between asymmetry in simulations and real data, as well as determining whether the same effect is observed in the asymmetry of SSD signals. Extending the analysis to address this second concern whilst also investigating different zenith angles and utilising a greater number of simulated showers is recommended for future work.

The other techniques presented in Chapter 5 which attempted to separate geometrical and attenuation based asymmetry effects were unsuccessful, in so far as neither a qualitative or quantitative measure for how each factor contributes to asymmetry was assigned. This is because, if the results *were* to be taken as valid, it would imply geometrical asymmetry effects actually cause there to be larger particle densities downstream, which contradicts our fundamental understanding of how geometry contributes to asymmetry. We believe the main assumptions made in both methods, that electromagnetic particles can be traced back along their momentum vector to some intersection point (i.e. ignoring scattering), and that the possible production of new particles can be ignored, are likely the cause of failure.

To check our understanding of the causes of asymmetry, a simple case was studied in Chapter 6 - the asymmetry in muon particle density. This was achieved by using individual CORSIKA simulations to extract the information required to build a model of muon production and propagation. Specifically, the production profile of muons as a function of height along the shower axis and the distributions of opening angles and production energies for each bin of height was obtained from CORSIKA. These were then used to simulate the production of muons, their propagation to ground and their potential decay in flight. Results showed our full Monte Carlo model, which included both attenuation and geometrical effects, overestimated the true asymmetry given by CORSIKA. However the difference was small enough that we believe it can be attributed to the assumptions made in the model, namely that muons are produced on the shower axis and travel in straight lines. When the

decay section of the simulation was not included in our Monte Carlo, removing any attenuation-based asymmetry effects, it was found that the geometrical component of asymmetry in muon particle density is by far the dominant factor, contributing anywhere from 3 to 10 times more to the overall asymmetry than attenuation for showers with  $\theta > 30^\circ$ . The difference in contribution may be even larger at zenith angles approaching  $60^\circ$ , though at these angles contributions from the effects which were not accounted for, such as off axis production and scattering, likely play a bigger role in forming the final asymmetry. Thus, we believe a more robust muon model, such as that in [86], should be used to properly analyse the different contributions at these large zenith angles.

Finally, by applying the asymmetry parameterisations in Chapter 4 to correct the station signals used in LDF fits (again in simulations), the technique of reconstructing  $X_{\max}$  from LDF slope parameters was shown to improve. The initial correlation found between DX and a single LDF slope parameter, either for the original NKG function or the modified NKG function, was found to introduce a mass dependent bias when reconstructing  $X_{\max}$ . This bias was removed by parameterising the modified NKG slope parameter  $\beta$ , fitted to the average signal obtained from dense rings, in bins of  $\theta$  and  $X_{\max}$ . Note that  $\beta$  was fitted with the second slope parameter of the modified NKG function,  $\gamma$ , fixed to zero. However, when checking the dense ring calibration on regular events, the reconstructed  $X_{\max}$  values were, on average smaller than the true  $X_{\max}$  values. This was due to the radial distribution of tanks in a real event being different to that when using dense rings. To fix this issue, “ensemble LDFs” were constructed and used to calibrate the relationship between  $\beta$ ,  $\theta$  and  $X_{\max}$ . These ensemble LDFs were LDFs containing a large number of stations coming from multiple simulations of the same shower incident on the Auger array with different core locations. Using the new calibration to reconstruct the  $X_{\max}$  values of the same set of regular events, which had an initial proton/iron mix of  $\sim 50:50$ , the majority of the bias in the combined  $\Delta X_{\max}$  distributions was corrected. Also, the asymmetry-corrected LDF fits were shown to give better reconstructed  $X_{\max}$  values, with the RMS values of the combined  $\Delta X_{\max}$  histograms reducing from 90 and  $110 \text{ g cm}^{-2}$  to 70 and  $95 \text{ g cm}^{-2}$  for the WCD and SSD respectively. The bias was also slightly improved, from  $-1 \text{ g cm}^{-2}$  for the WCD and  $-6 \text{ g cm}^{-2}$  for the SSD to  $1 \text{ g cm}^{-2}$  for both.

Despite containing unrealistic elements, namely the inclusion of Monte Carlo parameters and the use of a simulation based asymmetry-correction, the success of both this method and that of Luce [82] demonstrates that asymmetry can be used to improve different analyses, in this case for the purpose of determining mass composition. Assuming a parameterisation of asymmetry in real data can be found, then performing this type of analysis on real events with reconstructed parameters could allow for the mean  $X_{\max}$  as a function of energy to be estimated. Future work should investigate whether alterations to the parameterisation could improve the resolution in reconstructed  $X_{\max}$  and how introducing reality affects the results.



## Residual/WCD asymmetry parameterisation plots from Chapter 4

---

Figures A.1 and A.2 show the residual distributions for the fits to the proton SSD/WCD asymmetry data from Chapter 4 respectively. Figures A.3 and A.4 are the same but for iron. In these figures, labels containing  $\log(S_{1000}/\text{MIP})$  for the SSD and  $\log(S_{1000}/\text{VEM})$  for the WCD have been replaced by simply  $\log(S)$  for readability. Finally, Figures A.5 and A.6 show the asymmetry parameterisations for proton and iron showers detected by the WCD. Recall that polynomial functions of the form  $a + bx + cx^2$  have been fit, where the polynomial degree is chosen based on the shape of the data.

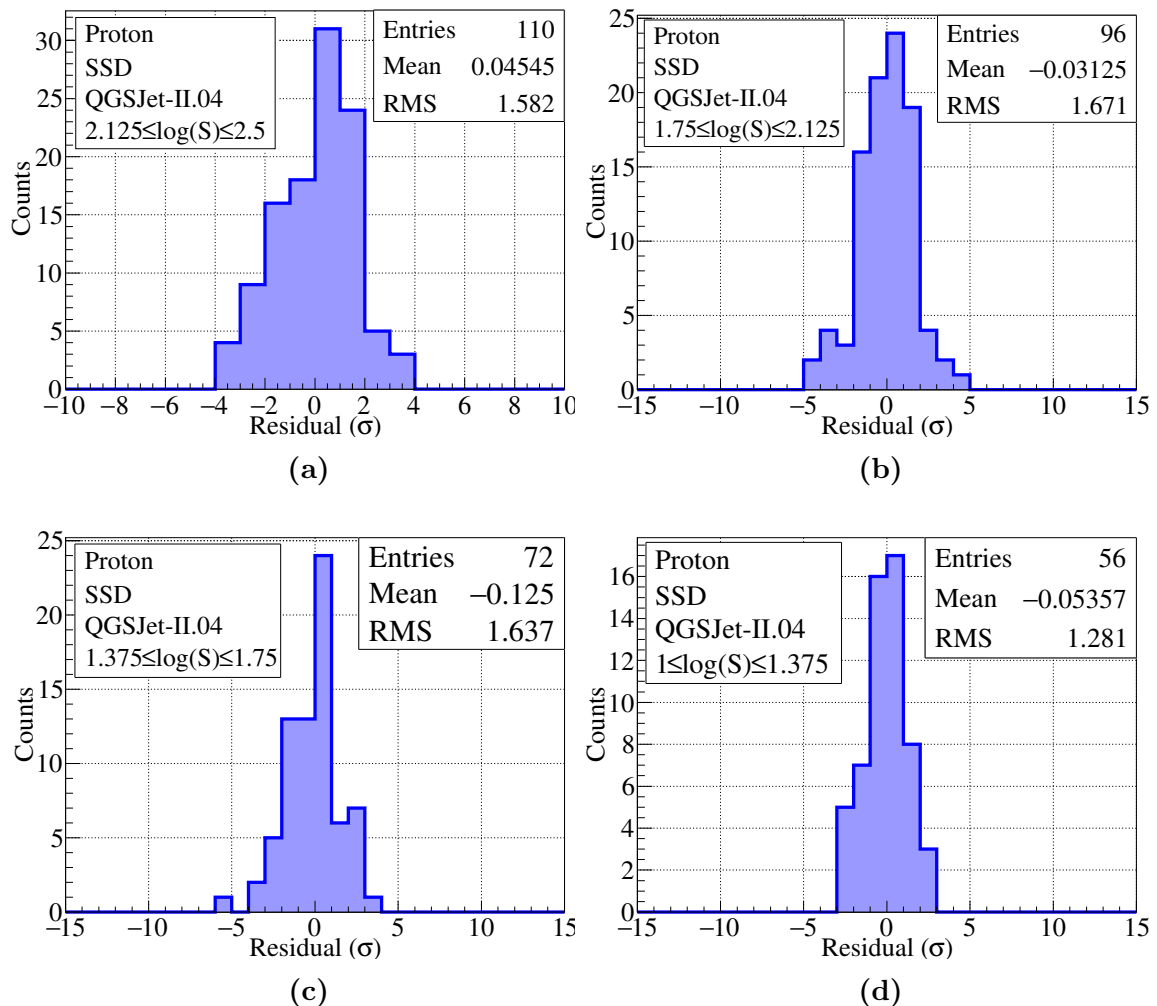


**Figure A.1:** Residuals for the fits to the asymmetry data from proton showers measured by the SSD.

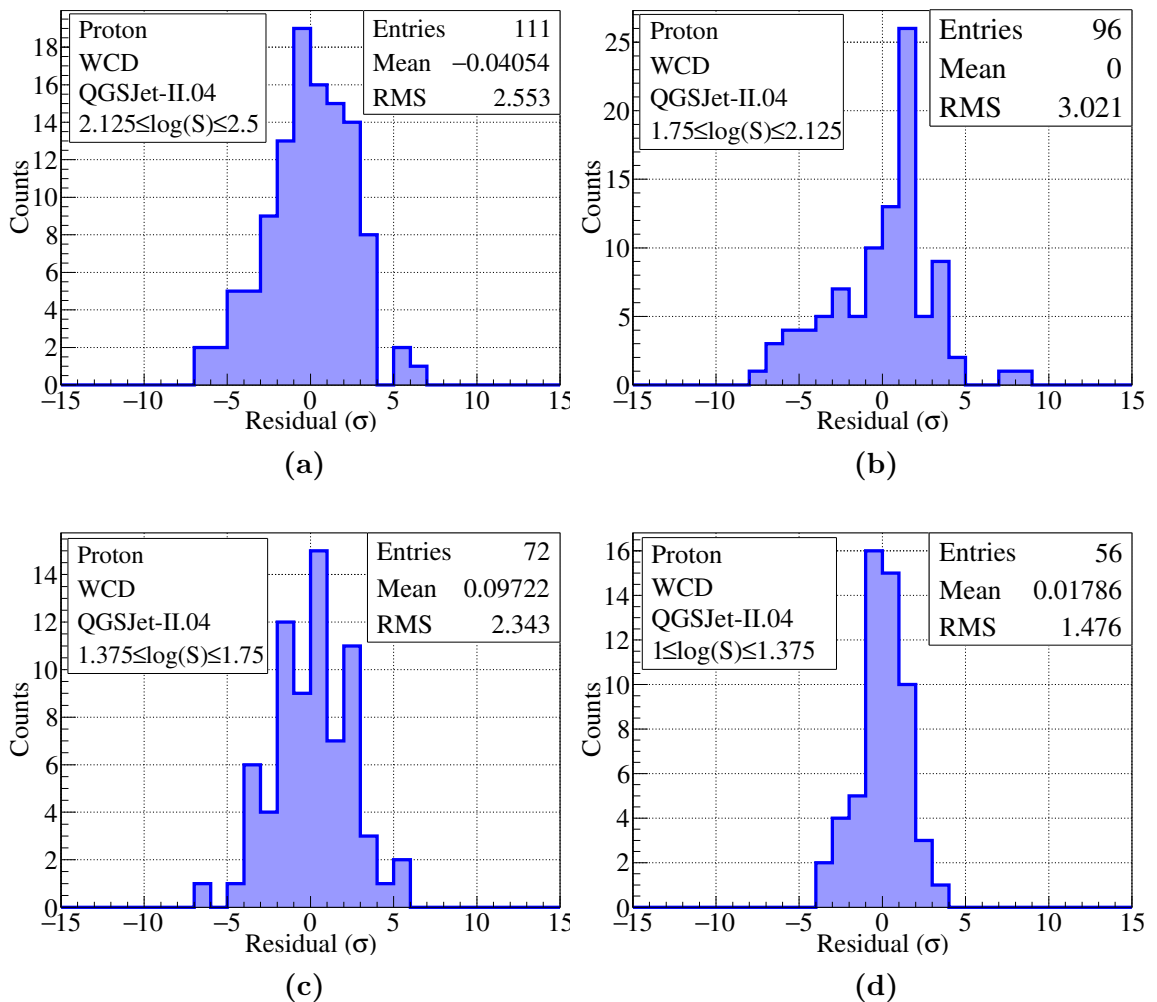


**Figure A.2:** Residuals for the fits to the asymmetry data from proton showers measured by the WCD.

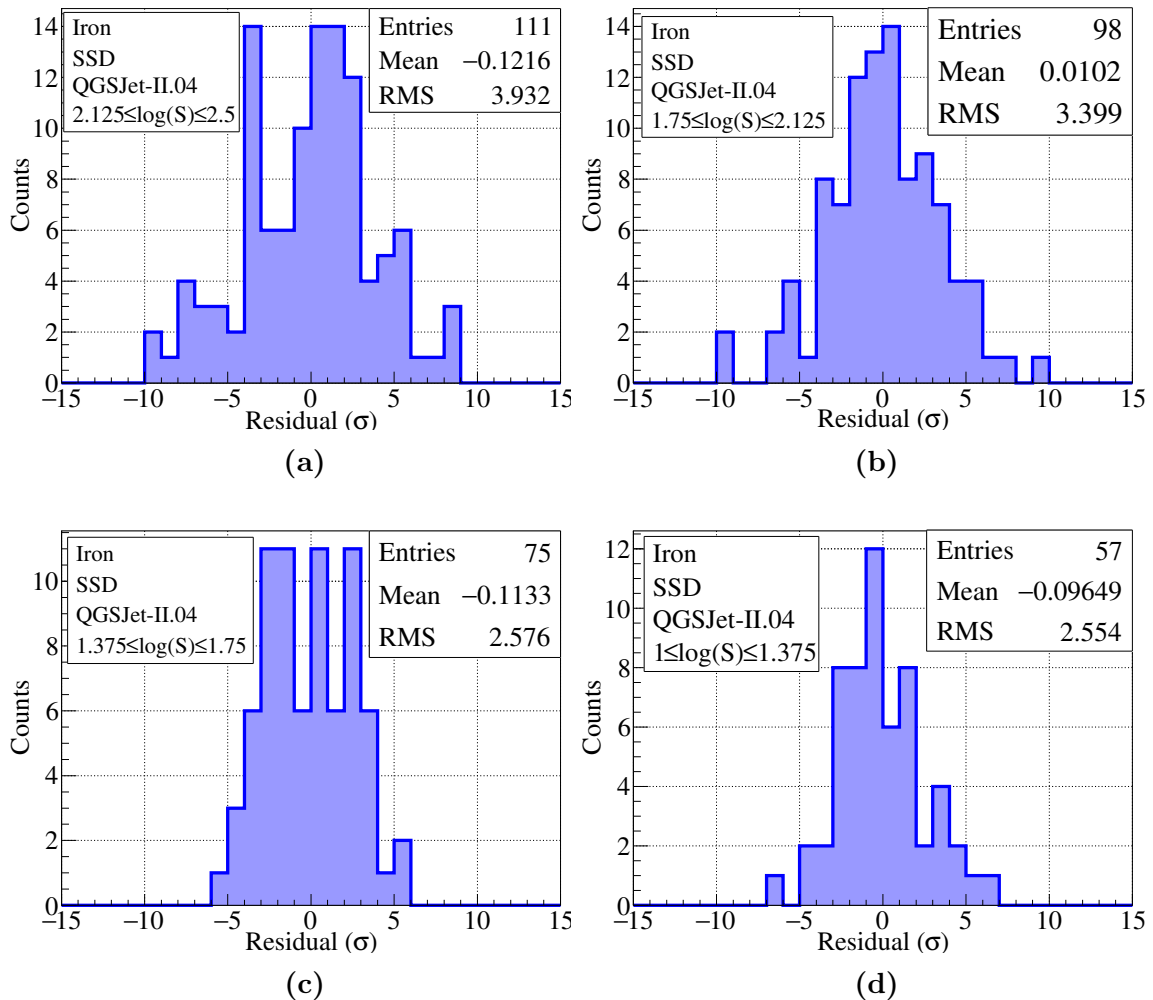


**Figure A.3:** Residuals for the fits to the asymmetry data from iron showers measured by the SSD.

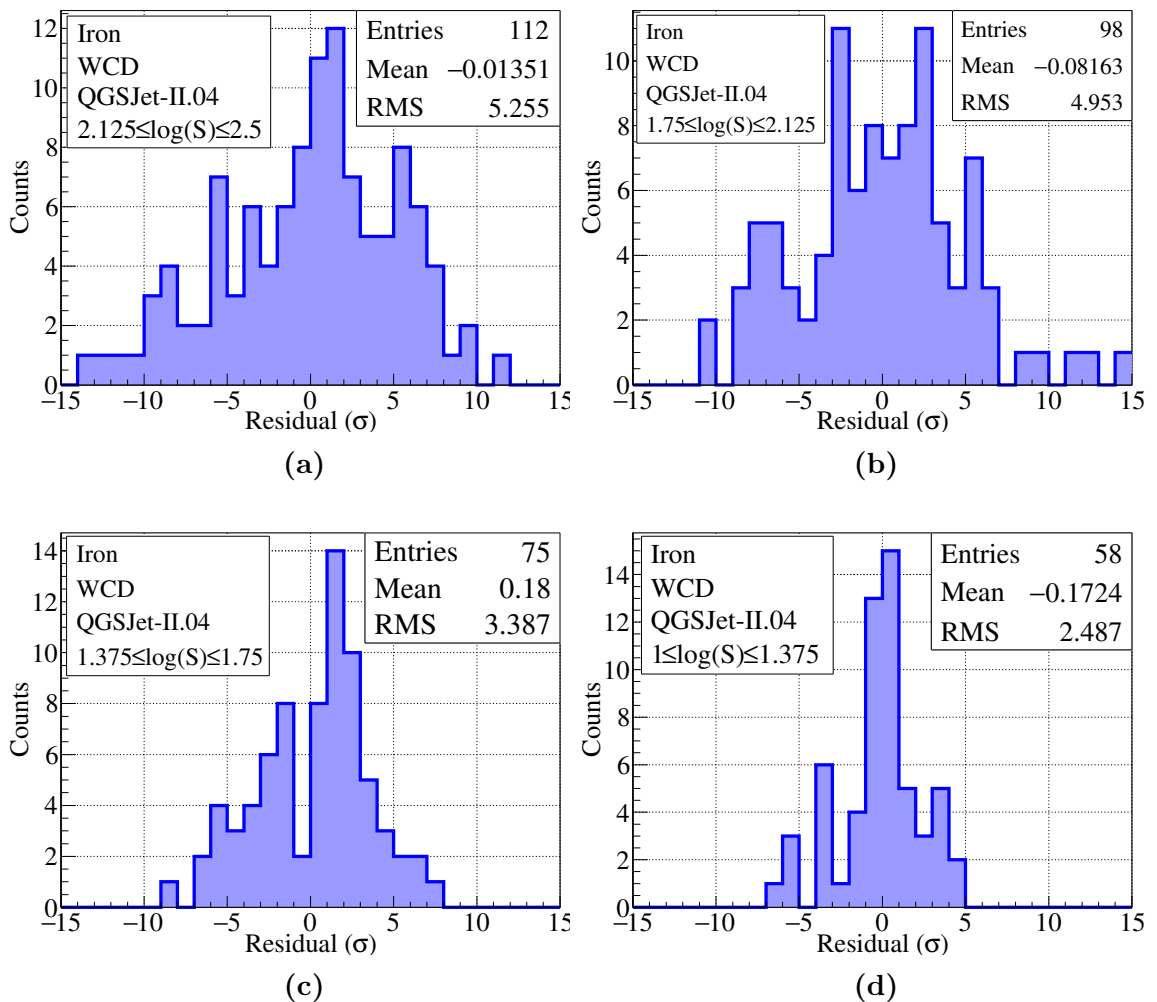


**Figure A.4:** Residuals for the fits to the asymmetry data from iron showers measured by the WCD.

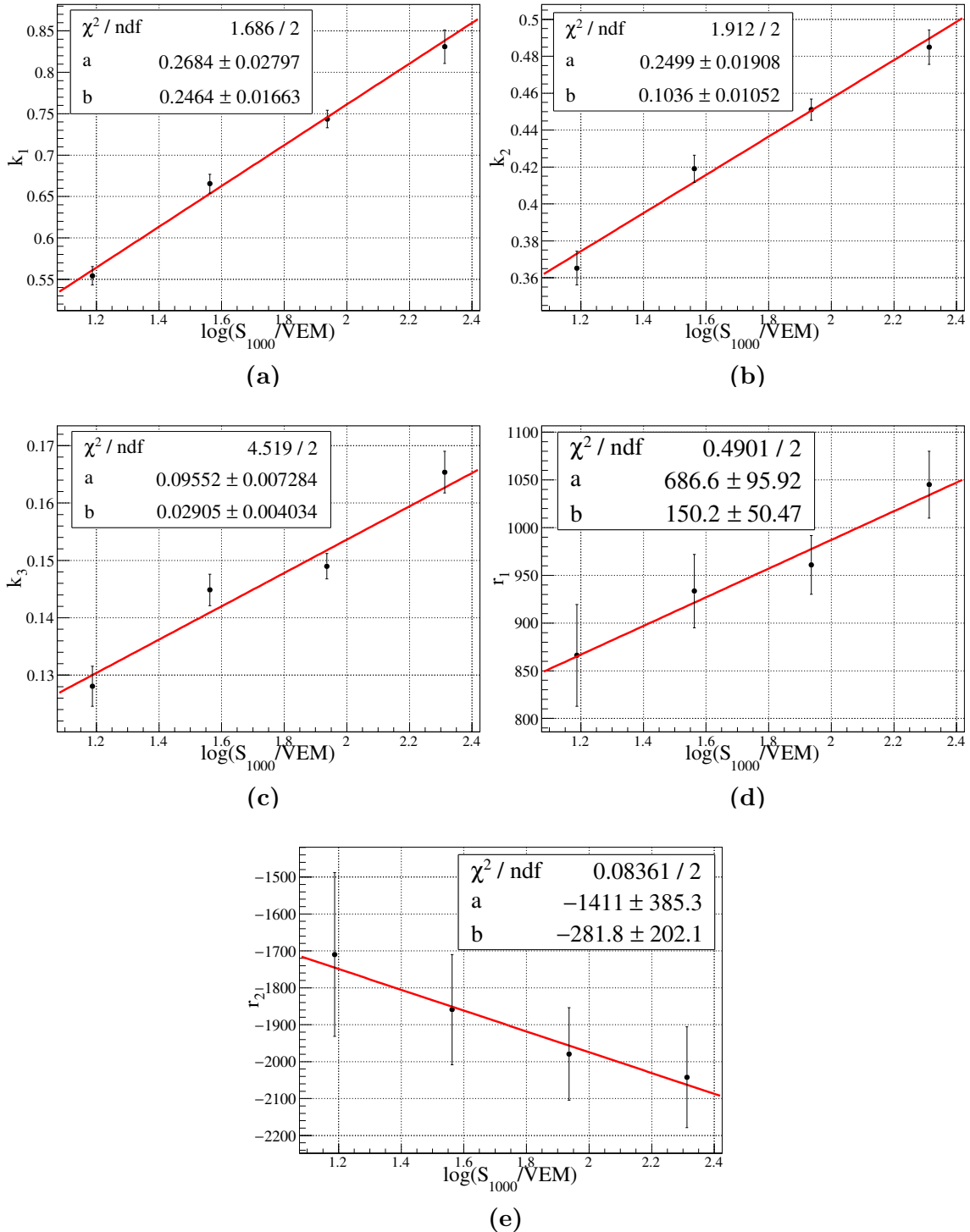


**Figure A.5:** Parameterisations of the parameters of the function  $b(r, \theta, \log(S_{1000}))$  for proton showers as measured by the WCD.

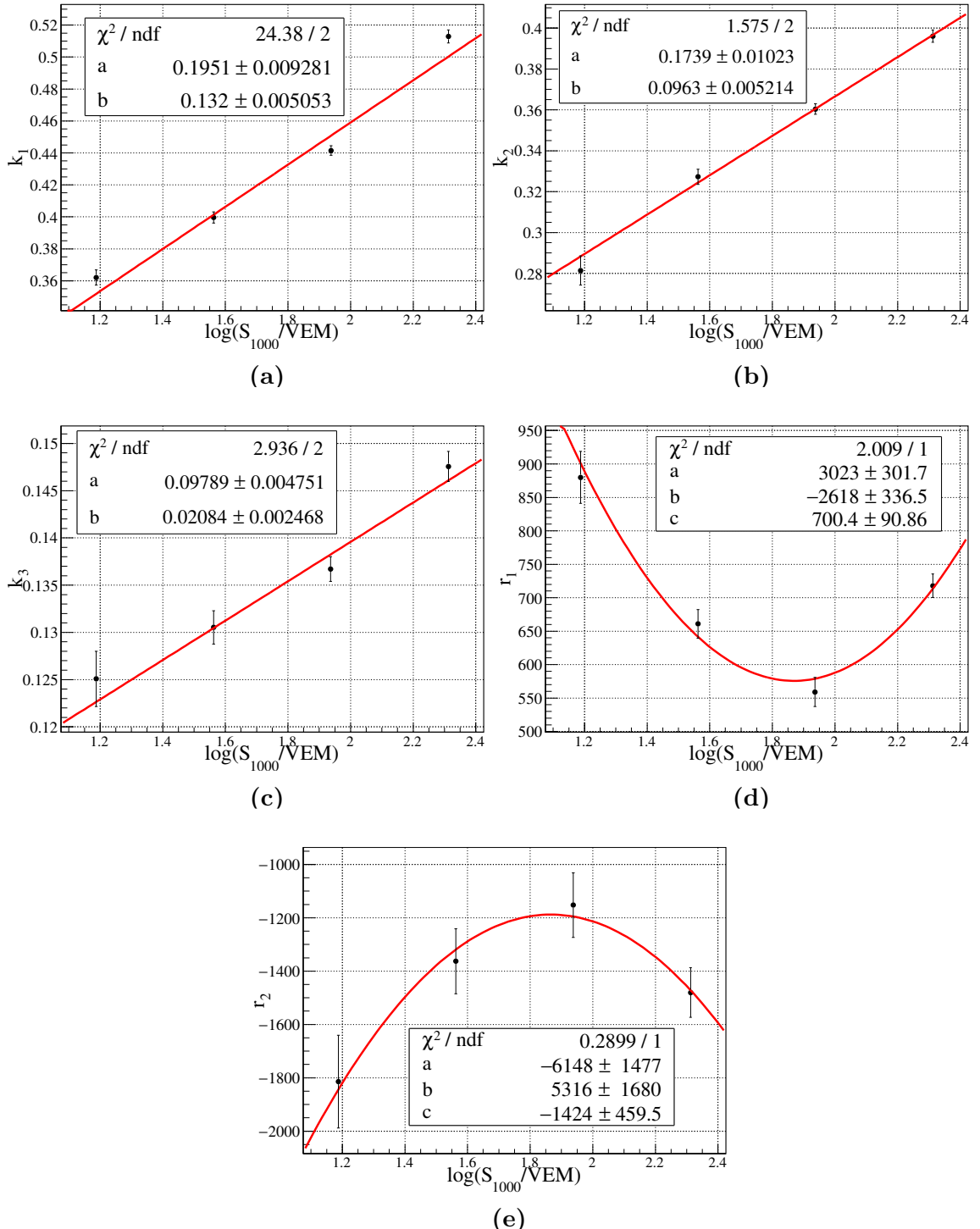


**Figure A.6:** Parameterisations of the parameters of the function  $b(r, \theta, \log(S_{1000}))$  for iron showers as measured by the WCD.



## Inclined atmospheres

When using CORSIKA to simulate an air shower the user must decide whether to use one of the many predefined atmospheres or define their own. Each predefined atmosphere typically corresponds to a different geographical location, with that location possibly having a number of different predefined atmospheres depending on the time of year, as is the case for Malargüe. Typically, each atmosphere contains five layers of varying height ranges. The first four layers are defined by the functional form

$$T_i(h) = a_i + b_i e^{-h/c_i}, \quad (\text{B.1})$$

where  $h$  is the vertical height above sea level,  $T(h)$  is the number of  $\text{g cm}^{-2}$  above  $h$ , and  $a_i$ ,  $b_i$  and  $c_i$  (for  $i = 1 \dots 4$ ) are fitted parameters. The fifth layer is described by a linear function

$$T_5(h) = a_5 - b_5 \times \frac{h}{c_5} \quad (\text{B.2})$$

where  $b_5$  is set to 1. Thus the parameters  $a_i$ ,  $b_i$  and  $c_i$  define the layers of every atmosphere. Note also that the functions  $T_i(h)$  are such that their piece-wise union,  $T(h)$ , which defines the entire atmosphere, is continuous and smooth. An example parameter table for the atmosphere at Malargüe in April is shown in Table B.1. Throughout this thesis  $M(h)$  represents the piece-wise function which combines the parameters in Table B.1.

The ability to define one's own atmosphere is particularly useful. Chapter 5 for example contains multiple instances where the atmospheric profile of an inclined

Layer $i$	Altitude $h$ (km)	$a_i (\text{g cm}^{-2})$	$b_i (\text{g cm}^{-2})$	$c_i (\text{g cm}^{-2})$
1	0 .. 10.0	-129.9930412	1172.3291878	962396:5521
2	10.0 .. 14.9	-21.847248438	1250.2922774	711452.06673
3	14.9 .. 32.6	1.5211136484	1542.6248413	603480.61835
4	32.6 .. 100.0	$3:9559055121 \times 10^{-4}$	713.1008285	735460.83741
5	> 100.0	0.01128292	1.	109

**Table B.1:** Parameters describing the atmospheric column density profile in Malargüe in April from GDAS [79].

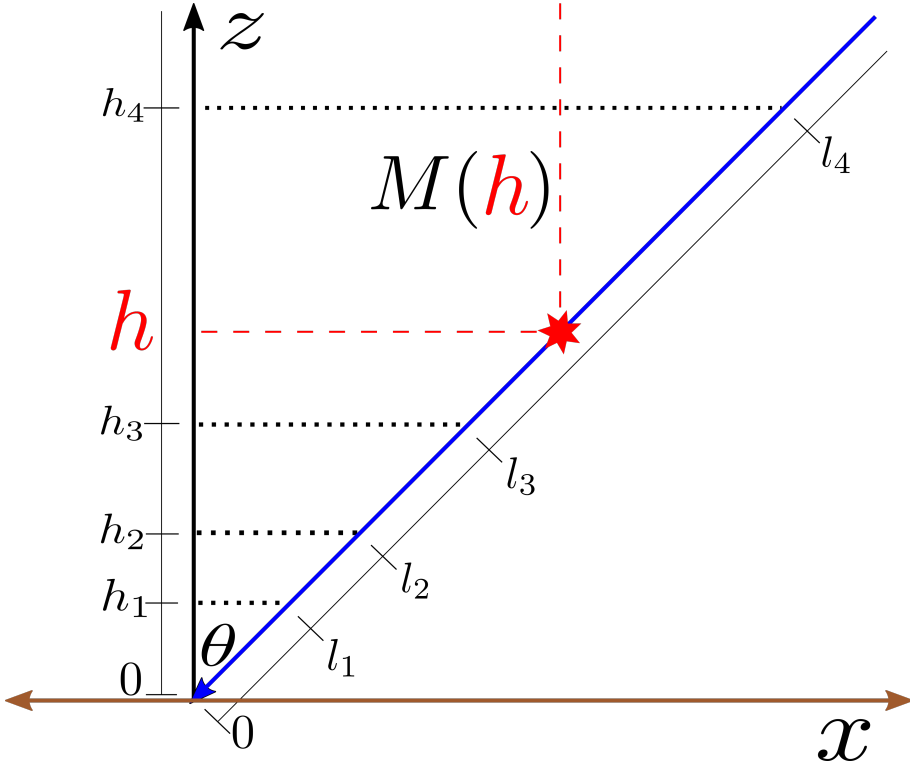


**Figure B.1:** Schematic showing how the layers for the inclined atmosphere are defined. Also shown is an example sample point at height  $h$  above sea level. The value of  $M(h)/\cos \theta$  gives the slant depth above the red point along the shower axis.

shower is desired. In creating an inclined atmosphere, we are essentially trying to answer the following question,

“If we begin at the shower core and move up along the shower axis of an inclined shower, what are the parameters  $a_i, b_i$  and  $c_i$  that define the atmosphere we see (as we move up the axis)?”

To solve this problem we break the process down into two steps:

- Find the ranges along the shower axis corresponding to each layer in the vertical profile of some predefined atmosphere. These ranges will form the layers of the inclined atmosphere.
- For each inclined layer, find the parameters  $a_i, b_i$  and  $c_i$ .

To find the layer altitudes for the inclined atmosphere consider Figure B.1. The distance along the shower axis corresponding to the beginning height of each layer in the vertical profile will be the height of the vertical layer multiplied by  $\sec \theta$ . From the diagram,

$$l_i = h_i \times \sec \theta \quad (\text{B.3})$$

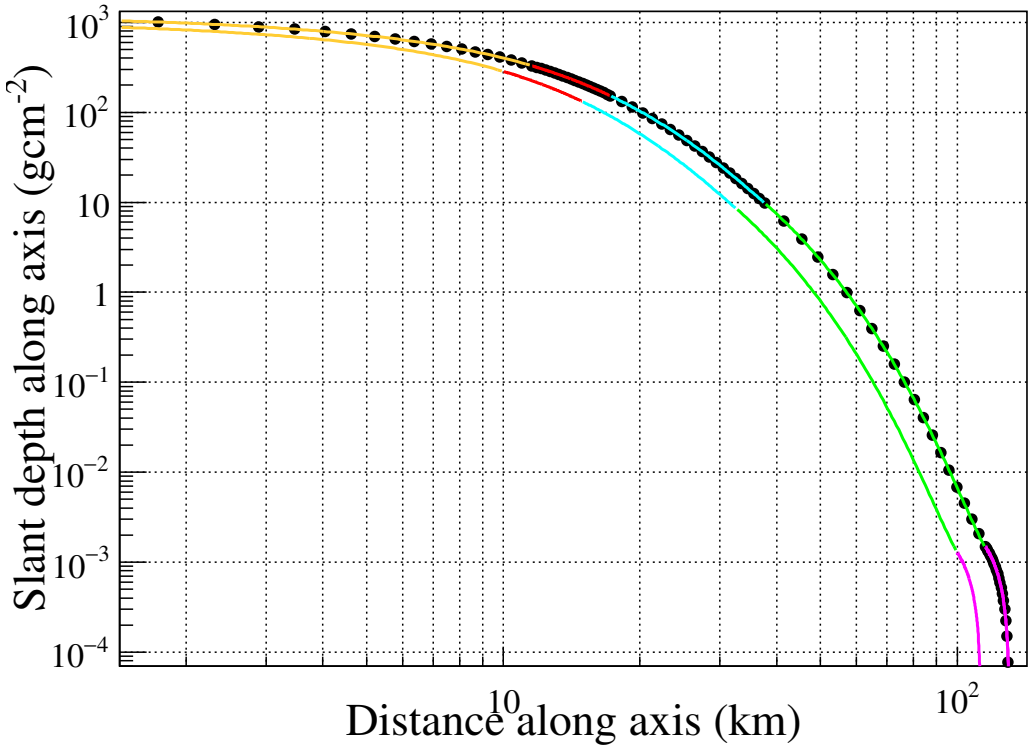


**Figure B.2:** The function  $T(h)$  for the Malargüe standard atmosphere (bottom curve) and the atmospheric profile which would be seen by a shower inclined by  $30^\circ$  (top curve). “Axis” here refers to either the vertical axis (for the Malargüe atmosphere) or the axis inclined by  $30^\circ$ . The different colours denote the separate layers. The black points are fit to generate the atmospheric parameters  $a_i$ ,  $b_i$  and  $c_i$  for each inclined layer.

For a  $30^\circ$  shower, using the Malargüe standard atmosphere in April, the layer heights for the inclined atmospheric profile are 0, 11.55, 17.21, 37.64 and 115.47 km.

To find the parameters  $a_i$ ,  $b_i$  and  $c_i$  which will define the atmosphere in each of our inclined layers, each layer is split into 20 equally sized intervals. The vertical height above ground of the endpoints of each interval is then calculated. This is done by taking the distance along the shower axis to the endpoint and multiplying by  $\cos \theta$ . Evaluating the Malargüe standard atmospheric profile at each of these heights then gives the vertical atmospheric depth above that point. These values can then be converted to slant depths along the shower axis by multiplying by  $\sec \theta$ . Finally, for each layers set of 20 points, the functional forms in Equation B.1 (for the first 4 layers) and B.2 (for the 5<sup>th</sup> layer) are fit, giving the  $a_i$ ,  $b_i$  and  $c_i$  parameters for each layer of the inclined atmosphere.

An example of this process is shown in Figure B.2. The corresponding parameter table is shown in Table B.2. The different coloured segments represent the different

Layer $i$	Altitude $h$ (km)	$a_i$ ( $\text{g cm}^{-2}$ )	$b_i$ ( $\text{g cm}^{-2}$ )	$c_i$ ( $\text{g cm}^{-2}$ )
1	0...11.547	-150.103	1353.69	1111280
2	11.547...17.205	-25.2298	1443.7	821523
3	17.205...37.6432	1.75642	1781.27	696839
4	37.6432...115.47	$3.89821 \times 10^{-4}$	823.352	849245
5	>115.47	0.0130176	1.	100.076

**Table B.2:** The  $a_i$ ,  $b_i$  and  $c_i$  parameters which define the atmosphere a  $30^\circ$  shower would see when incident on the Malargüe standard atmosphere in April. Values are from the fits performed on the five different groups of black points (denoted by different line colours for the fits) in Figure B.2.

layers. The bottom curve shows the standard Malargüe atmosphere in April, whilst the top curve corresponds to the atmospheric profile as seen by a shower inclined by  $30^\circ$  (incident on the same Malargüe atmosphere).

With this method, inclined atmospheres can be easily generated, with the only input needed being a zenith angle  $\theta$ . The parameters of each layer can then be used to define a new atmosphere in CORSIKA by setting the ATMOS option in the CORSIKA input file to a value of 10. This allows the user to provide CORSIKA a list of beginning layer heights (excluding 0 km) and lists of the parameters  $a_i$ ,  $b_i$  and  $c_i$  to generate a new atmosphere. An example of a CORSIKA input file with this option utilised, using the parameters for a  $30^\circ$  inclined atmosphere, is shown in Figure B.3.

## B.1 Using an inclined atmosphere to calculate slant depths

If one assumes that particles travel parallel to the shower axis, then an inclined atmosphere can be used to estimate the atmospheric slant depth travelled through by particles which land either side of the shower core in an inclined shower. Let  $G(h)$  represent the function describing the atmosphere of an inclined shower, approaching from the positive  $x$  direction, with zenith angle  $\theta$ . If, for example, a particle lands on the ground with  $x$  coordinate 1000 m, then compared to particles travelling along the shower axis it will have travelled  $1000 \sin \theta$  m less. If  $h_g$  is the height above sea level, as measured along the shower axis, of the observation level then this particle will have travelled through  $G(h_g + 1000 \sin \theta) \text{ g cm}^{-2}$ . Similarly, for particles on the downstream side at 1000 m they will travel through  $G(h_g - 1000 \sin \theta) \text{ g cm}^{-2}$ . Thus, more generally, the difference in atmospheric slant depth travelled by two particles landing upstream ( $0^\circ$ ) and downstream ( $180^\circ$ ) at the same distance  $r$  (measured on the ground) from the shower core will be

$$G(h_g - r \sin \theta) - G(h_g + r \sin \theta) \text{ g cm}^{-2} \quad (\text{B.4})$$

These types of calculations are used in this thesis to estimate slant depths which can be used when considering attenuation-based asymmetry effects.

```

RUNNR 200000
NSHOW 1
PRMPAR 14
ESLOPE -1.0
ERANGE 1.00e+10 1.00e+10
SEED 200000 0 0
SEED 400000 0 0
SEED 600000 0 0
DIRECT /LocalHome/auger/corsika/100397/
THIN 1.000000E-06 10365 10000
THINH 1.000E+00 1.000E+02
THETAP 0. 180.
PHIP -180. 180.
ATMOD 10
ATMA -150.103 -25.2298 1.75642 0.000393821 0.0130284
ATMB 1353.69 1443.7 1781.27 823.352
ATMC 1111280. 821523. 696839. 849245. 1.00E+9
ATMLAY 1154700. 1720500. 3764320. 11547000.
OBSLEV 1.6766E+05
MAGNET 2.010E+01 -1.420E+01
ECUTS 1.000E-01 1.000E-01 2.500E-04 2.500E-04
MUADDI T
MUMULT T
ELMFLG F T
STEPFC 1.0
RADNKG 5.0E+05
LONGI T 5. T T
ECTMAP 2.5E+5
MAXPRT 1
DATABAS T
USER durso
PAROUT T T
EXIT

```

**Figure B.3:** Example of a CORSIKA input file with the ATMOD option set to 10 (user defined atmosphere). The commands ATMA, ATMB and ATMC are used to define the parameters  $a_i$ ,  $b_i$  and  $c_i$  respectively, with the order of the values corresponding to the layer number. The layer heights (excluding zero) are defined by the ATMLAY command. Note the change to the regular observation level to ensure the ground is located at the usual Auger height above sea level, 1.452 km.

---

# Acronyms

---

**AGASA** Akeno Giant Air Shower Array.

**AGN** Active Galactic Nuclei.

**AMIGA** Auger Muon and Infilled Ground Array.

**CDAS** Central Data Acquisition System.

**CMB** cosmic microwave background.

**CORSIKA** COsmic Ray SImulations for KAscade.

**DSA** diffusive shock acceleration.

**EAS** extensive air shower.

**EM** electromagnetic.

**FADC** flash analog to digital converter.

**FAST** Fluorescence detector Array of Single-pixel Telescopes.

**FD** fluorescence detector.

**GDAS** Global Data Assimilation System.

**GZK** Greisen–Zatsepin–Kuz’min.

**HEAT** High Elevation Auger Telescopes.

**ISM** interstellar medium.

**LDF** lateral distribution function.

**MC** Monte Carlo.

**MIP** minimum ionising particle.

**NKG** Nishimura-Kamata-Greisen.

**PMT** photomultiplier tube.

**SD** surface detector.

**SNR** supernova remnant.

**SSD** scintillator surface detector.

**SUGAR** Sydney University Giant Air-shower Recorder.

**TA** Telescope Array.

**ToT** time over threshold.

**UHECRs** Ultra High Energy Cosmic Rays.

**UUB** upgraded unified board.

**UV** ultraviolet.

**VEM** vertical equivalent muon.

**WCD** water Cherenkov detector.

**WLS** wavelength-shifting.

---

# References

---

- [1] Qiaozhen Xu and Laurie M Brown. “The early history of cosmic ray research”. In: *American journal of physics* 55.1 (1987), pp. 23–33.
- [2] Michael Faraday. *Experimental Researches in Electricity*. Number v.2 in Experimental Researches in Electricity. Richard, John Edward Taylor, printers, and publishers to the University of London, 1844.
- [3] Yataro Sekido and Harry Elliot. *Early history of cosmic ray studies: Personal reminiscences with old photographs*. Vol. 118. Springer Science & Business Media, 2012.
- [4] Charles Thomson Rees Wilson. “On the ionisation of atmospheric air”. In: *Proceedings of the Royal Society of London* 68.442-450 (1901), pp. 151–161.
- [5] Per Carlson. “Discovery of cosmic rays”. In: *AIP Conference Proceedings*. Vol. 1516. 1. American Institute of Physics. 2013, pp. 9–16.
- [6] Viktor F Hess. “Über Beobachtungen der durchdringenden Strahlung bei sieben Freiballonfahrten”. In: *Phys. Zeits.* 13 (1912), pp. 1084–1091.
- [7] Johannes Blümer, Ralph Engel, and Jörg R Hörandel. “Cosmic rays from the knee to the highest energies”. In: *Progress in Particle and Nuclear Physics* 63.2 (2009), pp. 293–338.
- [8] Pierre Auger et al. “Extensive cosmic-ray showers”. In: *Reviews of modern physics* 11.3-4 (1939), p. 288.
- [9] Thomas K Gaisser, Todor Stanev, and Serap Tilav. “Cosmic ray energy spectrum from measurements of air showers”. In: *Frontiers of Physics* 8.6 (2013), pp. 748–758.
- [10] Jörg R Hörandel. “Cosmic rays from the knee to the second knee:  $10^{14}$  to  $10^{18}$ eV”. In: *Modern Physics Letters A* 22.21 (2007), pp. 1533–1551.
- [11] AM Hillas. “Can diffusive shock acceleration in supernova remnants account for high-energy galactic cosmic rays?” In: *Journal of Physics G: Nuclear and Particle Physics* 31.5 (2005), R95.
- [12] Alan Coleman et al. “Measurement of the cosmic ray flux near the second knee with the Pierre Auger Observatory”. In: *36th International Cosmic Ray Conference (ICRC2019)*. Vol. 36. 2019, p. 225.
- [13] T Abu-Zayyad et al. “The knee and the second knee of the cosmic-ray energy spectrum”. In: *arXiv preprint arXiv:1803.07052* (2018).

- [14] J Abraham et al. “Measurement of the energy spectrum of cosmic rays above  $10^{18}$ eV using the Pierre Auger Observatory”. In: *Physics Letters B* 685.4-5 (2010), pp. 239–246.
- [15] Dariusz Gora, Pierre Auger Collaboration, et al. “The Pierre Auger observatory: review of latest results and perspectives”. In: *Universe* 4.11 (2018), p. 128.
- [16] James W Cronin. “Cosmic rays: the most energetic particles in the universe”. In: *More Things in Heaven and Earth* (1999), pp. 278–290.
- [17] Enrico Fermi. “On the origin of the cosmic radiation”. In: *Physical review* 75.8 (1949), p. 1169.
- [18] Roger D Blandford and James P Ostriker. “Particle acceleration by astrophysical shocks”. In: *The Astrophysical Journal* 221 (1978), pp. L29–L32.
- [19] RJ Protheroe. “Acceleration and interaction of ultra high energy cosmic rays”. In: *arXiv preprint astro-ph/9812055* (1998).
- [20] Kumiko Kotera and Angela V Olinto. “The astrophysics of ultrahigh-energy cosmic rays”. In: *Annual Review of Astronomy and Astrophysics* 49 (2011), pp. 119–153.
- [21] Anthony M Hillas. “The origin of ultra-high-energy cosmic rays”. In: *Annual review of astronomy and astrophysics* 22.1 (1984), pp. 425–444.
- [22] Diego F Torres and Luis A Anchordoqui. “Astrophysical origins of ultrahigh energy cosmic rays”. In: *Reports on Progress in Physics* 67.9 (2004), p. 1663.
- [23] Thomas K Gaisser and Todor Stanev. “High-energy cosmic rays”. In: *Nuclear Physics A* 777 (2006), pp. 98–110.
- [24] Thomas K Gaisser, Ralph Engel, and Elisa Resconi. *Cosmic rays and particle physics*. Cambridge University Press, 2016.
- [25] Alexey Yushkov, Pierre Auger Collaboration, et al. “Mass Composition of Cosmic Rays with Energies above  $10^{17.2}$ eV from the Hybrid Data of the Pierre Auger Observatory”. In: *36th International Cosmic Ray Conference*. Vol. 358. SISSA Medialab. 2019, p. 482.
- [26] William Hanlon. “Telescope Array 10 year composition”. In: *arXiv preprint arXiv:1908.01356* (2019).
- [27] Frank G Schröder. “News from Cosmic Ray Air Showers (ICRC 2019–Cosmic Ray Indirect Rapport)”. In: *arXiv preprint arXiv:1910.03721* (2019).
- [28] Paul Sommers and Stefan Westerhoff. “Cosmic ray astronomy”. In: *New Journal of Physics* 11.5 (2009), p. 055004.
- [29] Alexander Aab et al. “Large-scale cosmic-ray anisotropies above 4 EeV measured by the Pierre Auger Observatory”. In: *The Astrophysical Journal* 868.1 (2018), p. 4.

- [30] RU Abbasi et al. “Search for Large-scale Anisotropy on Arrival Directions of Ultra-high-energy Cosmic Rays Observed with the Telescope Array Experiment”. In: *The Astrophysical Journal Letters* 898.2 (2020), p. L28.
- [31] Peter Tinyakov et al. “The UHECR dipole and quadrupole in the latest data from the original Auger and TA surface detectors”. In: *arXiv preprint arXiv:2111.14593* (2021).
- [32] Lorenzo Caccianiga, Pierre Auger Collaboration, et al. “Anisotropies of the highest energy cosmic-ray events recorded by the Pierre Auger Observatory in 15 years of operation”. In: *36th international cosmic ray conference*. Vol. 358. SISSA Medialab. 2019, p. 206.
- [33] Kawata, Kazumasa, et al. “Updated Results on the UHECR Hotspot Observed by the Telescope Array Experiment”. In: *PoS ICRC2019* (2020), p. 310. DOI: [10.22323/1.358.0310](https://doi.org/10.22323/1.358.0310).
- [34] Ralph Engel, Dieter Heck, and Tanguy Pierog. “Extensive air showers and hadronic interactions at high energy”. In: *Annual review of nuclear and particle science* 61 (2011), pp. 467–489.
- [35] Alexander Aab et al. “Azimuthal asymmetry in the risetime of the surface detector signals of the Pierre Auger Observatory”. In: *Physical Review D* 93.7 (2016), p. 072006.
- [36] A Haungs et al. “Kcdc—the kascade cosmic-ray data centre”. In: *Journal of Physics: Conference Series*. Vol. 632. 1. IOP Publishing. 2015, p. 012011.
- [37] James Matthews. “A Heitler model of extensive air showers”. In: *Astroparticle Physics* 22.5-6 (2005), pp. 387–397.
- [38] Walter Heitler. *The Quantum Theory of Radiation, third ed.* London: Oxford University Press, 1954, p. 386.
- [39] Ralf Ulrich, Ralph Engel, and Michael Unger. “Hadronic multiparticle production at ultrahigh energies and extensive air showers”. In: *Physical Review D* 83.5 (2011), p. 054026.
- [40] The Auger Collaboration. *The Pierre Auger Observatory Design Report, Second Edition*. Fermi National Lab, Chicago. 1997.
- [41] Ingo Allekotte et al. “The surface detector system of the Pierre Auger Observatory”. In: *Nuclear Instruments and Methods in Physics Research Section A: Accelerators, Spectrometers, Detectors and Associated Equipment* 586.3 (2008), pp. 409–420.
- [42] Fernando Arqueros, Jörg R Hörandel, and Bianca Keilhauer. “Air fluorescence relevant for cosmic-ray detection—Summary of the 5th fluorescence workshop, El Escorial 2007”. In: *Nuclear Instruments and Methods in Physics Research Section A: Accelerators, Spectrometers, Detectors and Associated Equipment* 597.1 (2008), pp. 1–22.

- [43] Jorge Abraham et al. “The fluorescence detector of the Pierre Auger Observatory”. In: *Nuclear Instruments and Methods in Physics Research Section A: Accelerators, Spectrometers, Detectors and Associated Equipment* 620.2-3 (2010), pp. 227–251.
- [44] Fermilab History and Archives Project. *Finding Aid to the John Linsley Papers, c.1946-2002 (bulk 1950-2002)*. URL: [https://history.fnal.gov/findingsaids/Linsley\\_ibatf2012001.html](https://history.fnal.gov/findingsaids/Linsley_ibatf2012001.html).
- [45] J Linsley. “Primary cosmic rays of energy  $10^{17}$  to  $10^{20}$  eV, the energy spectrum and arrival directions”. In: *International Cosmic Ray Conference*. Vol. 4. 1963, p. 77.
- [46] John Linsley. “Evidence for a primary cosmic-ray particle with energy  $10^{20}$  eV”. In: *Physical Review Letters* 10.4 (1963), p. 146.
- [47] RM Tennent. “The Haverah Park extensive air shower array”. In: *Proceedings of the Physical Society (1958-1967)* 92.3 (1967), p. 622.
- [48] MA Lawrence, RJO Reid, and AA Watson. “The cosmic ray energy spectrum above  $4 \times 10^{17}$  eV as measured by the Haverah Park array”. In: *Journal of Physics G: Nuclear and Particle Physics* 17.5 (1991), p. 733.
- [49] MM Winn et al. “The cosmic-ray energy spectrum above  $10^{17}$  eV”. In: *Journal of Physics G: Nuclear Physics* 12.7 (1986), p. 653.
- [50] JA Bellido et al. “Muon content of extensive air showers: Comparison of the energy spectra obtained by the Sydney University Giant Air-shower Recorder and by the Pierre Auger Observatory”. In: *Physical Review D* 98.2 (2018), p. 023014.
- [51] N Chiba et al. “Akeno giant air shower array (agasa) covering  $100 \text{ km}^2$  area”. In: *Nuclear Instruments and Methods in Physics Research Section A: Accelerators, Spectrometers, Detectors and Associated Equipment* 311.1-2 (1992), pp. 338–349.
- [52] P Sokolsky and GB Thomson. “Highest energy cosmic-rays and results from the HiRes experiment”. In: *Journal of Physics G: Nuclear and Particle Physics* 34.11 (2007), R401.
- [53] RM Baltrusaitis et al. “The Utah Fly’s eye detector”. In: *Nuclear Instruments and Methods in Physics Research Section A: Accelerators, Spectrometers, Detectors and Associated Equipment* 240.2 (1985), pp. 410–428.
- [54] DJ Bird et al. “Results from the fly’s eye experiment”. In: *AIP Conference Proceedings*. Vol. 338. 1. American Institute of Physics. 1995, pp. 839–854.
- [55] RU Abbasi et al. “Monocular measurement of the spectrum of UHE cosmic rays by the FADC detector of the HiRes experiment”. In: *Astroparticle Physics* 23.2 (2005), pp. 157–174.

- [56] RU Abbasi et al. “A study of the composition of ultra-high-energy cosmic rays using the high-resolution fly’s eye”. In: *The astrophysical journal* 622.2 (2005), p. 910.
- [57] H Kawai et al. “Telescope array experiment”. In: *Nuclear Physics B (Proceedings Supplements)* 175-176 (2008), pp. 221–226.
- [58] Toshihiro Fujii et al. “Latest results of ultra-high-energy cosmic ray measurements with prototypes of the Fluorescence detector Array of Single-pixel Telescopes (FAST)”. In: *arXiv preprint arXiv:2107.02949* (2021).
- [59] Toshihiro Fujii et al. “A next-generation ground array for the detection of ultrahigh-energy cosmic rays: the Fluorescence detector Array of Single-pixel Telescopes (FAST)”. In: *EPJ Web of Conferences*. Vol. 210. EDP Sciences. 2019, p. 06003.
- [60] Alexander Aab et al. “The Pierre Auger Observatory upgrade-preliminary design report”. In: *arXiv preprint arXiv:1604.03637* (2016).
- [61] Pierre Auger Collaboration. “The Pierre Auger cosmic ray observatory”. In: *Nuclear Instruments and Methods in Physics Research Section A: Accelerators, Spectrometers, Detectors and Associated Equipment* 798 (2015), pp. 172–213.
- [62] J Abraham et al. “Properties and performance of the prototype instrument for the Pierre Auger Observatory”. In: *Nuclear Instruments and Methods in Physics Research Section A: Accelerators, Spectrometers, Detectors and Associated Equipment* 523.1-2 (2004), pp. 50–95.
- [63] Ingo Allekotte et al. “The surface detector system of the Pierre Auger Observatory”. In: *Nuclear Instruments and Methods in Physics Research Section A: Accelerators, Spectrometers, Detectors and Associated Equipment* 586.3 (2008), pp. 409–420.
- [64] Xavier Bertou et al. “Calibration of the surface array of the Pierre Auger Observatory”. In: *Nuclear Instruments and Methods in Physics Research Section A: Accelerators, Spectrometers, Detectors and Associated Equipment* 568.2 (2006), pp. 839–846.
- [65] J Abraham et al. “Trigger and aperture of the surface detector array of the Pierre Auger Observatory”. In: *Nuclear Instruments and Methods in Physics Research Section A: Accelerators, Spectrometers, Detectors and Associated Equipment* 613.1 (2010), pp. 29–39.
- [66] Álvaro Taboada Núñez. “Analysis of the First Data of the AugerPrime Detector Upgrade”. PhD thesis. Karlsruher Institut für Technologie (KIT), 2020.
- [67] Pierre Auger Collaboration et al. “Reconstruction of inclined air showers detected with the Pierre Auger Observatory”. In: *Journal of Cosmology and Astroparticle Physics* 2014.08 (2014), p. 019.

- [68] Alexander Aab et al. “Reconstruction of events recorded with the surface detector of the Pierre Auger Observatory”. In: *Journal of instrumentation* 15.10 (2020), P10021.
- [69] J Hersil et al. “Observations of extensive air showers near the maximum of their longitudinal development”. In: *Physical Review Letters* 6.1 (1961), p. 22.
- [70] Alexander Aab et al. “Measurement of the cosmic-ray energy spectrum above  $2.5 \times 10^{18}$  eV using the Pierre Auger Observatory”. In: *Physical Review D* 102.6 (2020), p. 062005.
- [71] Thomas K Gaisser and A Michael Hillas. “Reliability of the method of constant intensity cuts for reconstructing the average development of vertical showers”. In: *International Cosmic Ray Conference*. Vol. 8. 1977, pp. 353–357.
- [72] Bruce Dawson, Pierre Auger Collaboration, et al. “The energy scale of the Pierre Auger Observatory”. In: *36th International Cosmic Ray Conference*. Vol. 358. SISSA Medialab. 2019, p. 231.
- [73] Jose Bellido, Pierre Auger Collaboration, et al. “Depth of maximum of air-shower profiles at the Pierre Auger Observatory: Measurements above  $10^{17.2}$  eV and Composition Implications”. In: *35th International Cosmic Ray Conference*. Vol. 301. SISSA Medialab. 2018, p. 506.
- [74] Alexander Aab et al. “Measurement of the average shape of longitudinal profiles of cosmic-ray air showers at the Pierre Auger Observatory”. In: *Journal of Cosmology and Astroparticle Physics* 2019.03 (2019), p. 018.
- [75] P Abreu et al. “The Pierre Auger Observatory V: Enhancements”. In: *arXiv preprint arXiv:1107.4807* (2011).
- [76] *Auger Maps*. 2021. URL: <https://maps.auger.org.ar/erosion.php>.
- [77] David Schmidt. “Sensitivity of AugerPrime to the masses of ultra-high-energy cosmic rays”. PhD thesis. Karlsruher Institut für Technologie (KIT), 2018.
- [78] KURARAY CO. *Wavelength Shifting Fibres*. URL: <http://kuraraypsf.jp/psf/ws.html>.
- [79] Dieter Heck et al. “CORSIKA: A Monte Carlo code to simulate extensive air showers”. In: *Report fzka* 6019.11 (1998).
- [80] Stefano Argiro et al. “The offline software framework of the Pierre Auger Observatory”. In: *Nuclear Instruments and Methods in Physics Research Section A: Accelerators, Spectrometers, Detectors and Associated Equipment* 580.3 (2007), pp. 1485–1496.
- [81] T Schulz. “Enhanced UHECR Event Reconstruction by means of Sampling Lateral Distributions with Multiple Surface Sub-Detectors”. B.S. Thesis. Karlsruhe Institute of Technology, 2018.
- [82] Q. Luce. *LDF-Asymmetries - What you always wanted to know*. 2021. URL: <https://indico.nucleares.unam.mx/event/1692/session/2/contribution/44>.

- [83] Quentin Luce. *SD signal asymmetries in data*. Auger Collaboration Foundation Task Meeting. 2021.
- [84] Pierre Billoir, Pierre Da Silva, and Xavier Bertou. *Checking the Origin of the Asymmetry of the Surface Detector Signals*. Tech. rep. Pierre Auger Observatory Internal Note 2002-074, 2002.
- [85] Xavier Bertou and Pierre Billoir. *On the Origin of the Asymmetry of Ground Densities in Inclined Showers*. Tech. rep. Pierre Auger Observatory Internal Note 2000-017, 2000.
- [86] L Cazon et al. “A model for the transport of muons in extensive air showers”. In: *Astroparticle Physics* 36.1 (2012), pp. 211–223.
- [87] Alexander Aab et al. “Deep-learning based reconstruction of the shower maximum X max using the water-Cherenkov detectors of the Pierre Auger Observatory”. In: *Journal of instrumentation* 16.07 (2021), P07019.
- [88] M Ave et al. “A generalized description of the signal size in extensive air shower detectors and its applications”. In: *Astroparticle physics* 87 (2017), pp. 23–39.
- [89] Alexander Aab et al. “Inferences on mass composition and tests of hadronic interactions from 0.3 to 100 EeV using the water-Cherenkov detectors of the Pierre Auger Observatory”. In: *Physical Review D* 96.12 (2017), p. 122003.
- [90] Alexander Edward Hervé. “Measurement of the mass composition of the highest energy cosmic rays with the Pierre Auger observatory.” PhD thesis. 2013.
- [91] Mary Díaz Castro, Bruce Dawson, and José Bellido. *Evaluating the use of the measured LDF (slope -  $\beta$ ) for mass composition studies*. Tech. rep. Pierre Auger Observatory Internal Note 2017-030, 2017.
- [92] Paul Sommers. “Extensive air showers and measurement techniques”. In: *Comptes Rendus Physique* 5.4 (2004), pp. 463–472.